

LITHIUM-FED ARC MULTICHANNEL AND
SINGLE-CHANNEL HOLLOW CATHODE:
EXPERIMENT AND THEORY

LEONARD DENNIS CASSADY

A DISSERTATION
PRESENTED TO THE FACULTY
OF PRINCETON UNIVERSITY
IN CANDIDACY FOR THE DEGREE
OF DOCTOR OF PHILOSOPHY

RECOMMENDED FOR ACCEPTANCE
BY THE DEPARTMENT OF
MECHANICAL AND AEROSPACE ENGINEERING

SEPTEMBER 2006

© Copyright by Leonard Dennis Cassady, 2006.

All Rights Reserved

Prepared By:

Leonard Dennis Cassady

Dissertation Advisor:

Professor Edgar Y. Choueiri

Dissertation Readers:

Professor Robert G. Jahn

Professor Samuel A. Cohen

Abstract

Lithium-fed arc multichannel hollow cathode (MCHC) and single-channel hollow cathode (SCHC) physical processes, including the current conduction mechanism and the conditions that determine the plasma penetration depth, cathode temperature, and cathode voltage drop, are investigated experimentally and theoretically. The ability of the MCHC to conduct high current was previously not understood. Knowledge of the SCHC and MCHC physical processes is required for informed cathode design, especially for that of the lithium Lorentz force accelerator (LiLFA).

Experiments were conducted to measure the plasma penetration depth, cathode temperature, and plasma potential at the cathode tip of four lithium-fed SCHCs (with inner diameters of 2, 4, 6, 8 mm) and an MCHC (19 - 1 mm channels in a 10 mm diameter rod) at mass flow rates of 0.2 - 4.0 mg/s and currents of 5 - 210 A. It was found that the plasma penetration depth decreases with mass flow rate, increases with channel diameter, and increases with current. The peak cathode temperature was found to depend on current and channel diameter, but not mass flow rate. From the new findings, it was determined that (1) the arc penetrates to a location of optimum plasma density that depends on current and channel diameter, (2) the arc attaches to the cathode in an annulus of width equal to three times the wall thickness, and (3) the plasma density can be determined from the cathode temperature.

The theoretical models predict the cathode voltage drop, cathode temperature, and plasma penetration depth as a function of mass flow rate, cathode material type, cathode geometry, and current. The MCHC model also includes the differences of the multichannel configuration - the thermal interaction of adjacent channels and the division of current and mass flow. The models are validated by the experimental data. They lead to the physical insight that thermal radiation and thermionic cooling are the most significant power loss mechanisms, and that the MCHC operates at a lower voltage than the SCHC because of lower thermal radiation losses due to less exposed surface area, and a reduced temperature due to a larger arc attachment area. Finally, a procedure for the design of an MCHC is presented, which is applied to the cathode of an LiLFA.

Acknowledgements

This dissertation and my tenure at graduate school could not have been successfully completed without the support, friendship, and guidance of many people. I gratefully acknowledge that I would not have made it without them.

Amy, my wife, has been my most fervent supporter. She willingly accepted the long hours while we lived together and the many years we spent apart. But, always, she encouraged me to keep going, and even helped me with grading homework, editing this dissertation and other papers, as well as being a sounding board for my ideas. Most importantly, she brought joy and love into my life every day. Amy, I love you very much.

My family gave their support throughout this entire process. Dennis and Evilo, my parents, have always believed their children can accomplish anything they set their mind to and encouraged them along the way. My parents were always there to listen during the difficult times, but never faltered in their belief that I would finish. The rest of my family, Kalena (and Jon), Patrick, Grandma Behler, and Grandpa Nelson, never failed to ask how I was doing and offer encouragement.

The students that I was fortunate enough to share my time with at EPPDyL made my life at Princeton both challenging and enjoyable. Andrea forced me to arrive at the lab early and leave late through her example as a tireless researcher of the lithium lorentz force accelerator and its thrust stand. Luckily, she also “forced” me to drink coffee perpetually. (As a side note, I would like to thank Small World Coffee and Diedrich Coffee for fueling my research.) I am glad to have gone through classes, general exams, research, and our weddings with Slava, Jack, and Kurt. They and Andrea challenged me to be a better researcher, but they also made life enjoyable by having parties and playing basketball, volleyball, and softball. The younger guys, Jimmy, Luke, and Peter, always offered a new perspective on life and research, which I definitely needed. I also thank them for housing me at various points during my 6th year.

Without Bob Sorenson I would not have been able to successfully accomplish the experiments conducted in the lab. He always encouraged me to build apparatus correctly the first time, and was eager to teach me how to do it myself.

I would like to thank many professors at Princeton University that taught me so much - Prof. Jeremy Kasdin, Tim Baker, Prof. Szymon Suckewer, and Prof. Samuel Cohen. I would especially like to thank Prof. Robert Jahn for teaching me the physics of electric propulsion and attending the EPPDyL lab meetings. Your vast stores of knowledge and experience always helped me to find the crux of the problem.

Last, but not least, I would like to thank my advisor, Prof. Edgar Choueiri, for his guidance and support. The level of scientific rigor he holds himself and his students to

is exceptionally high - I hope that I can maintain those standards. He taught me how to conduct solid scientific research and accurately convey the results of that work. He helped create a scientist from an engineer, and I am grateful.

Professional Acknowledgements: I am extremely honored to have been selected for the National Defense Science and Engineering Graduate Fellowship, which is funded by the Department of Defense and managed by the American Society for Engineering Education, and as a Francis Upton Fellow by the School of Engineering and Applied Sciences at Princeton University. These two generous fellowships funded the first four years of my graduate education. This research was also supported by the Program in Plasma Science and Technology, which is directed by the Princeton Plasma Physics Laboratory, and NASA's Jet Propulsion Laboratory, both of which supplied salary and equipment.

This dissertation carries the designation 3154T in the records of the Department of Mechanical and Aerospace Engineering.

To set foot on the soil of the asteroids, to lift by hand
a rock from the Moon, to observe Mars from a
distance of several tens of kilometers, to land on its
satellite or even on its surface, what can be more
fantastic? From the moment of using rocket devices
a new great era will begin in astronomy: the epoch
of the more intensive study of the firmament.

- Konstantin E. Tsiolkovsky

Contents

Abstract	iv
Acknowledgements	v
Nomenclature	xv
1 Introduction	1
1.1 The LiLFA	5
1.2 The Multichannel Hollow Cathode	8
1.2.1 The Single-channel Hollow Cathode	9
1.2.2 Arc Hollow Cathode Discharge Operation	10
1.3 Goal of the Lithium-fed MCHC Theoretical Modeling	11
1.4 Goal of the Experiments	12
1.5 Organization	12
2 Review of Arc Hollow Cathode Research	14
2.1 Review of MCHC Research	15
2.1.1 <i>Laboratoire de Physique des Plasmas</i> (1969-1974)	16
2.1.2 Babkin's Research Group (1976-1979)	18
2.1.3 Ogarkov's Research Group (1976-1979)	20
2.1.4 Other Research Groups	22
2.2 Review of SCHC Research	24
2.2.1 MIT and Oak Ridge National Laboratory (1962)	24

2.2.2	<i>Institut d'Electronique Fondamentale</i> (1972)	25
2.2.3	<i>Office National d'Études et de Recherches Aérospatiales</i> (1973-1977)	26
2.2.4	<i>Laboratoire de Physique des Plasmas</i> (1968-1978)	27
2.2.5	Grishin's Research Group (1977)	31
2.2.6	<i>A.F. Ioffe Physicotechnical Institute</i> (1978-1981)	32
2.2.7	Baikov Institute of Metallurgy (1979)	33
2.2.8	Moscow Aviation Institute (1996)	34
2.2.9	Princeton University (1976-2002)	35
2.2.10	<i>Centrosazio</i> - University of Pisa (2002-2005)	36
2.2.11	Other Research	38
2.3	Review of Orificed Hollow Cathode Research	38
2.4	Summary of Relevant Research	39
2.4.1	Experimental Observations	40
2.4.2	Theoretical Model Components	41
3	Apparatus and Diagnostics	43
3.1	Experimental Layout	43
3.2	Lithium Experimental Facility	44
3.3	Electrode Set-up	47
3.4	Cathode Specifications	47
3.4.1	Material Selection	47
3.4.2	SCHC Dimensions	48
3.4.3	MCHC Dimensions	50
3.4.4	Cathode Interface with Evaporator	50
3.5	Lithium Physical Properties	50
3.5.1	Vapor Pressure	51
3.5.2	Thermal Conductivity	52
3.5.3	Surface Tension and Capillary Effect	54

3.5.4	Compatibility and Contamination	56
3.5.5	Lithium Handling and Safety	57
3.6	Lithium Feed System	58
3.7	Lithium Evaporator	59
3.8	Optical Access	62
3.9	Power Systems	64
3.10	Data Acquisition System	65
3.11	Diagnostics	65
3.11.1	Current and Total Voltage Measurement	66
3.11.2	Langmuir Probe	66
3.11.3	Multi-color Video Pyrometry	67
3.11.4	Emission Spectroscopy	68
4	Experimental Results and Analysis	73
4.1	SCHC Results	74
4.1.1	SCHC Temperature Results	75
4.1.2	SCHC Plasma Potential Results	82
4.1.3	Total Discharge Voltage	85
4.2	MCHC Results	88
4.3	Analysis of the SCHC Results	91
4.3.1	Cathode Temperature and Voltage Drop Dependence on Current Density	91
4.3.2	Active Zone Width	92
4.3.3	Ion Pressure in the Active Zone	94
4.3.4	Plasma Penetration Depth	98
4.4	Analysis of MCHC Results	100
4.5	Summary of Experimental Results	100

5	Lithium-fed Hollow Cathode Theoretical Model	103
5.1	Gas Flow Through a Channel	105
5.1.1	Molecular Flow Conductance	108
5.1.2	Viscous Flow Conductance	109
5.1.3	Pressure and Velocity at the Channel Exit	110
5.1.4	Pressure Profiles Within Channels	111
5.2	Plasma Penetration Depth	111
5.3	Active Zone Width	113
5.4	Particle Conservation	113
5.5	Non-equilibrium Excitation/Ionization	114
5.5.1	Lithium Excitation Model	115
5.5.2	Excitation and Ionization Via Thermionic Electrons	116
5.5.3	Excitation and Ionization Via Thermal Electrons	117
5.6	Thermionic Electron Cascade	117
5.6.1	Energy Exchange within the Active Zone	118
5.6.2	Direct Loss from the Active Zone	120
5.7	Current Conduction at the Cathode Wall	122
5.7.1	Thermionic Electron Current	122
5.7.2	Ion Current	123
5.7.3	Thermal Electron Current	123
5.8	Electric Field at the Cathode Surface	124
5.9	Cathode Material Heating	126
5.9.1	Ion Heating	127
5.9.2	Thermal Electron Heating	127
5.9.3	Heating via Spontaneous Radation	128
5.9.4	Cooling via Thermal Radiation and Conduction	128
5.9.5	Cooling via Thermionic Electron Emission	129

5.10	Plasma Electron Heating	130
5.11	MCHC Model Components	130
5.12	Neglected Processes	132
5.12.1	Axial Electric Field	132
5.12.2	Electron-ion Three-Body Recombination	133
5.12.3	Bremsstrahlung Radiation and Radiative Capture	134
5.12.4	Collisional Deexcitation	134
5.13	Solution Procedure	135
5.14	Validation	137
5.15	Effect of Non-equilibrium Excitation and Ionization	145
5.16	Theoretical Results and Insights	146
5.17	Summary of Theoretical Results	151
6	Design Procedure for an MCHC	152
6.1	Optimum Channel Cross Section	153
6.2	MCHC Design Procedure	154
6.3	Application to an LiLFA	159
6.4	Comments	162
7	Conclusions	163
7.1	Summary of Findings	164
7.2	Future Work	165
7.3	Application to the LiLFA	167
A	PROPULSION OPTIONS FOR MISSIONS TO MARS	168
A.1	Introduction	169
A.1.1	Review of Previous Studies	170
A.1.2	Outline	171
A.2	Mission Description	171

A.2.1	Trajectory Calculations	172
A.3	Propulsion Options	173
A.3.1	Selection Criteria	173
A.3.2	Piloted Mission	174
A.3.3	Cargo Mission	178
A.4	Mission Analysis	182
A.4.1	Assumptions	182
A.4.2	Calculations	183
A.4.3	Results	184
A.4.4	Cargo Mission	185
A.4.5	Piloted Mission	187
A.5	Other Viable Candidates	187
A.6	Concluding Remarks	189
B	Least-squares Multi-color Pyrometry	191
B.1	Introduction	192
B.1.1	Review of Previous Research	192
B.1.2	Motivation	194
B.2	Fundamental Relations	194
B.3	Method Comparison	197
B.3.1	Discussion	198
B.3.2	Recommendations	200
B.4	Effect of errors associated with noise and calibration	201
B.4.1	Discussion	202
B.4.2	Recommendations	207
B.5	Complementary Measurements	207
B.6	Conclusions	208

C	Spectroscopy Data	210
D	Lithium Surface Coverage	221
E	Double Sheath Derivation	225
E.1	Thermionic Electrons	226
E.2	Ions	227
E.3	Thermal Electrons	228
E.4	Sheath Relations	228

Nomenclature

α	Transmission probability through a short duct
α_i	Ionization fraction
α_p	Specific mass of the power supply
α_t	Specific mass of the thruster
β_s	Normalized sheath voltage
γ	Ratio of specific heats
γ_t	Surface tension of a liquid
$\Delta\epsilon_{b,\kappa}^e$	Energy thermionic electrons in energy group κ lose in collisions with plasma electrons
$\Delta\epsilon_k^{\hat{p}}$	Energy difference between states k and \hat{p}
Δv	Change in spacecraft velocity during a maneuver
δ	Molecular diameter
δ_{Ar}	Diameter of argon atoms
δ_{Li}	Diameter of lithium atoms
δ_{Li-Ar}	Common diameter of lithium and argon atoms
ϵ	Energy of impacting electrons
ϵ_0	Permittivity of free space
$\epsilon_{b,\kappa}$	Energy of thermionic electrons in energy group κ

$\epsilon_{b,o}$	Initial energy of the thermionic electrons
$\bar{\epsilon}_c$	Average energy of thermal electrons at cathode wall
ϵ_λ	Emissivity of a surface
ϵ_W	Emissivity of tungsten
η_s	Spitzer resistivity
η_T	Thrust efficiency
η_v	Fluid viscosity
Θ	Factor that relates active zone width to wall thickness
θ	Weighting factor used in transitional flow calculations
θ_c	Contact angle of a liquid with a surface
λ	Wavelength of electromagnetic radiation
λ_{Li}	Mean free path of lithium vapor
λ_a	Average mean free path
λ_D	Debye length
$\lambda_{ex,\kappa}$	Mean free path for energy exchange collisions for thermionic electrons
λ_m	Mean free path
$\lambda_{t,\kappa}$	Total mean free path for thermionic electrons
$\nu_{b,\kappa}^{in}(\epsilon)$	Total inelastic collision frequency of thermionic electrons with lithium atoms
$\nu_{b,\kappa}^{ex}(\epsilon)$	Total energy exchange collision frequency for thermionic electrons with energy ϵ
$\nu_{b,\kappa}^e(\epsilon)$	Collision frequency of thermionic electrons with energy ϵ with thermal electrons
$\nu_{b,\kappa}^i(\epsilon)$	Thermionic electron-ion collision frequency
$\nu_{b,k}^{\hat{p}}(\epsilon)$	Inelastic collision frequency for process \hat{p} of thermionic electrons with lithium atoms in state k

$\nu_{e,i}^{3b}$	Electron-ion three-body recombination frequency
$\hat{\nu}_i$	Normalized ion density
$\bar{\nu}_{th,k}^{\hat{p}}$	Average collision frequency for inelastic process \hat{p} of thermal electrons atoms in state k
$\nu_{t,\kappa}$	Total collision frequency of thermionic electrons
ξ	Normalized distance
ϱ	Normalized space charge density in sheath
ρ_a	Average gas density
ρ_c	Space charge density
σ_{SB}	Stefan-Boltzmann constant
τ_s	Normalized cathode temperature
Υ	Volume of the active zone
Φ	Ratio of the cross section of the channels to the total area encircled by the MCHC
Φ^*	Optimum ratio of the cross section of the channels to the total area encircled by the MCHC
ϕ_{eff}	Effective work function
ϕ_i	Ionization potential
ϕ_o	Work function of cathode material
χ_{th}	Normalized thermionic electron current
ψ_x	Fraction of electrons colliding inelastically in the channel
ω_{Li}	Pre-exponential coefficient for desorption
ω_{mn}	Frequency of emitted line radiation
$n_{b,\kappa}$	Number density of thermionic electrons with energy ϵ
a	First coefficient in linear emissivity model

a'	First coefficient in natural logarithm emissivity model
A_A	Antoine equation coefficient
A_{eff}	Exposed area effectively seen by an individual channel
$A_{M,e}$	Area of the exposed outer surface of the MCHC
A_{nm}	Transition probability coefficient
A_{os}	Outer surface area of cathode
A_R	Empirical thermionic electron emission constant of cathode material
A_{xs}	Cross sectional area
A_{xs}^{Li}	Cross sectional area of the lithium
A_{xs}^{SS}	Cross sectional area of the stainless steel tube
A_z	Area of the inner cathode wall exposed to plasma
$A_{z,M}$	Area of arc attachment in an MCHC
$A_{z,M}^*$	Optimal area of arc attachment in an MCHC
B	Magnetic Induction
b	Second coefficient in linear emissivity model
b'	Second coefficient in natural logarithm emissivity model
B_A	Antoine equation coefficient
b_o	Impact parameter
C	Conductance
C_1	First radiation constant
C_2	Second radiation constant
C_A	Antoine equation coefficient
C_a	Aperture conductance for molecular flow
C_m	Molecular conductance

c_n	Coefficient in emissivity polynomial
C_v	Viscous conductance
$C_{v,a}$	Viscous conductance through aperture
C_z	Conductance term in viscous flow
d_c	Inner diameter of the cathode channel
d_o	Depth of plasma as viewed by spectrometer
$D_{\bar{V}}$	Denominator of average energy calculation
E	Electric field
e	Electron charge
E_c	Electric field at the cathode surface
E_d^{Li}	Desorption energy
E_m	Energy of the initial state
$f(V)$	Maxwellian distribution function
f_D	Darcy friction factor
$F(\lambda)$	Calibration factor of spectrometer intensity
f_{Li}	Fractional surface coverage of lithium
g_m	Degeneracy of state m
g_o	Acceleration of gravity at the Earth's surface
\hbar	Planck's constant divided by 2π
I	Intensity of thermal radiation
I_m	Measured intensity of calibration lamp
i_{nm}	Intensity of line emission
I_p	Published intensity of calibration lamp
I_{sp}	Specific impulse (u_e/g_o)

j	Current per unit area (vector)
J	Total current
j	Current density
J_d	Current thermionic electrons carry from volume
$J_{d,\kappa}$	Current thermionic electrons in energy bin κ carry from volume
$J_{e,x}$	Current conducted by electrons at the channel exit
j_i	Ion current density
j_{min}	Optimal (minimum) current density on cathode surface
j_{pe}	Plasma electron current density
j_{th}	Thermionic electron current density
Kn	Knudsen number
k_a	Condensation rate coefficient
k_B	Boltzmann constant
k_d	Desorption rate coefficient
k_s	Empirical constant in flow weighting factor
k_{th}	Thermal conductivity
k_{th}^{Li}	Thermal conductivity of lithium
k_{th}^{SS}	Thermal conductivity of stainless steel
$\ln \Lambda$	Coulomb logarithm
l	Plasma penetration depth
\dot{m}	Mass flow rate
m	Molecular mass
M	Mach number
M_x	Mach number at the upstream location x

m_{Ar}	Mass of argon atom
\dot{m}_c	Mass flow rate through a single channel of an MCHC
m_e	Mass of the electron
m_{Li}	Mass of lithium atom
M_{pl}	Payload mass
M_{prop}	Propellant mass
n	Number density
n_{Ar}	Number density of argon molecules
n_b	Number density of thermionic electrons
N_c	Number of channels in an MCHC
n_e	Electron number density
$n_{e,o}$	Electron density at the sheath/presheath boundary
n_i	Ion number density
$n_{i,o}$	Ion density at sheath/presheath boundary
$n_{i,s}$	Ion density at the sheath/presheath boundary
n_k	Number density of lithium atoms in state k
N_{Li}	Surface density of lithium
N_m	Population of state m
N_{min}^{Li}	Surface density with the minimum work function
N_t	Total population
$N_{\bar{V}}$	Numerator of average energy calculation
p_i	Ion pressure
P_{br}	Power of <i>bremsstrahlung</i> radiation
P_c	Power conducted along the cathode upstream of the plasma

$P_{c,v}$	Thermal power conduction in the evaporator
$P_{c,v}^{Li}$	Power conducted through liquid lithium
$P_{c,v}^{SS}$	Power conducted through stainless steel
p_d	Downstream pressure
P_d	Power thermionic electrons carry directly from channel
$P_{d,\kappa}$	Power thermionic electrons in energy bin κ carry directly from channel
P_e	Input electrical power to thruster
p_e	Pressure within the channel at the exit
P_{ex}	Power thermal electrons lose to inelastic collisions
P_{fb}	Power associated with radiative capture
P_h	Power transferred from thermionic electrons to thermal electrons
P_i	Power delivered by the ions to the cathode
p_l	Liquid phase pressure
P_{pe}	Power delivered by thermal electrons to the cathode
p_r	Required pressure estimated for MCHC design
P_{rad}	Power radiated from the cathode surface
P_{sp}	Power lost to spontaneous radiation
$P_{sp,t}$	Power from spontaneous radiation trapped by the cathode walls
P_{th}	Power removed from cathode walls by thermionic electrons
p_u	Upstream pressure
p_v	Vapor phase pressure
p_{vp}	Vapor pressure
\dot{Q}	Flow throughput
$Q_k^{\hat{p}}(\epsilon)$	Cross section of inelastic process \hat{p} for atom in state k

\dot{Q}_m	Molecular gas flow throughput
\dot{Q}_t	Total gas flow throughput
\dot{Q}_v	Viscous gas flow throughput
r	Radius
Re	Reynolds number for pipe flow
r_c	Cathode inner radius
$r_{M,o}$	Outer radius of the MCHC
R_{sp}	Ratio of trapped to total spontaneous radiation
S_κ	Rate thermionic electrons enter group κ
\mathcal{T}	Thrust
T	Temperature
t_c	Effective thickness of a channel wall in an MCHC
T_c	Temperature of the inner wall of the cathode
T_e	Electron Temperature
T_{max}	Maximum cathode operating temperature
T_r	Brightness temperature
u	Thermal speed of gas molecules
u_e	Exhaust velocity
V	Voltage
$v_{b,\kappa}$	Velocity of thermionic electrons in state κ
v_a	Average gas speed
V_B	Voltage associated with Bohm velocity
v_B	Bohm velocity
v_b	Velocity of thermionic electrons within a sheath

$V_{B,m}$	Voltage associated with modified Bohm velocity
$v_{B,m}$	Modified Bohm velocity
V_c	Cathode voltage drop, plasma potential at the cathode tip
V_f	Floating potential
$v_{g,x}$	Velocity of the gas at the channel exit
v_i	Velocity of ions within the sheath
$v_{i,o}$	Velocity of ions as they enter the sheath
V_s	Sheath voltage (excluding presheath)
\bar{V}_{V_c}	Average energy of thermal electrons with energy greater than V_c
w	Active zone width
x	Distance upstream of channel exit
x_e	Effective distance upstream of exit for molecular flow
y	Normalized intensity of line emission
Z_a	Partition function

Chapter 1

Introduction

Humans will soon venture far beyond the safety of Earth-orbit on multi-year missions to the Moon, asteroids, and Mars. It is an inevitable continuation of our natural drive to explore the universe around us. Presently, NASA's vision for space exploration (VSE) includes a return mission to the Moon that will include long duration missions on the surface as early as 2015 [1]. NASA will then extend a human presence to Mars and asteroids after 2020. With demanding missions beyond the Moon on the horizon, new technologies must be developed in the near future. Among the most crucial technologies are the advanced propulsion systems that will enable these missions by providing a reasonable travel time while utilizing minimal propellant.

A combination of three characteristics render the VSE missions more demanding than those accomplished in the past: a large energy requirement to reach the destination, a severe upper limit on mission duration, and a payload mass on the order of 100,000 kg (100 metric tons). The energy, which is characterized by the change in velocity, Δv , of these missions is approximately 7-20 km/s. This value is on par with some of NASA's interplanetary missions such as Voyager, Pioneer, Galileo, and Cassini, however, those missions required years to reach their destinations and their payloads weighed at least an order of magnitude less than the VSE missions. The maximum mission duration with humans on board will be

on the order of a few months because of the negative health effects of exposure to radiation and weightlessness for extended periods of time. Finally, for perspective, a 100 metric ton payload is 17 times more massive than the heaviest interplanetary mission ever launched (Cassini) [2] and four times more massive than the spacecraft that were sent to the Moon during the Apollo program [3]. A large payload mass requires a large amount of propellant to accomplish the mission and thus a much larger mass must be launched at the beginning of the mission.

High-power electric propulsion (HiPEP) is one advanced propulsion technology that can enable VSE missions and has long been recognized as being among the most promising options [4, 5, 6, 7, 8] (one study that the author contributed to is presented in Appendix A). Electric propulsion (EP) is defined as “the acceleration of gases for propulsion by electrical heating and/or by electric and magnetic body forces.” [9] These thrusters utilize electricity as the source of power rather than the energy released in the chemical reactions of conventional liquid and solid rockets. HiPEP thrusters are in a class of EP devices that operate with more power than that available on today’s spacecraft (approximately 10 kW).

Here we outline how HiPEP can accomplish a piloted mission to Mars with a relatively small propellant mass in a short period of time. We first address the issue of propellant mass and compare the performance of EP devices to that of a state-of-the-art chemical rocket, the Space Shuttle Main Engine. The ratio of propellant to payload mass can be found from the rocket equation, which was first derived by Tsiolkovsky in 1903 [10],

$$\frac{M_{prop}}{M_{pl}} = \exp \frac{\Delta v}{u_e} - 1,$$

where M_{prop} is the mass of the propellant, M_{pl} is the payload mass (including the power generation system), Δv is the characteristic velocity change the thruster is required to produce for a given mission, and u_e is the exhaust velocity of the rocket. It can be seen that small propellant fractions are only possible if the exhaust velocity of the rocket is a few

times greater than the characteristic velocity change of the mission, which is 7 km/s for a one-way mission to Mars. The Space Shuttle Main Engine has an exhaust velocity of 4.5 km/s while EP thrusters suitable to VSE missions have a range of 30 to 100 km/s (we take 50 km/s for the following analysis). The chemical rocket requires 374 metric tons of propellant while an EP thruster consumes only 15 metric tons. It can be seen that EP devices are capable of reducing the propellant mass by an order of magnitude, which translates to tens of thousands of kilograms. This mass savings enables large payload missions by reducing the costs associated with launching the propellant mass into low Earth orbit (presently, approximately \$20,000 per kilogram).

Most EP thrusters have a high exhaust velocity, but only those that operate at high power can also deliver a payload in a reasonable time. Here, we demonstrate approximately how much power is required for the mission above when we set a five month duration. We can determine the thrust, \mathcal{T} , required from the relation

$$\mathcal{T} = \dot{m}u_e, \quad (1.1)$$

where \dot{m} is the mass flow rate and u_e is the exhaust velocity, which we again take as 50 km/s. A mass flow rate of 1.2 g/s is determined from the total propellant mass found above divided by the mission duration. The resulting thrust is 60 N. The electrical power, P_e , required is given by

$$P_e = \frac{1}{2} \frac{\mathcal{T}u_e}{\eta_{\mathcal{T}}}, \quad (1.2)$$

where $\eta_{\mathcal{T}}$ is the thruster efficiency, which we take as 50%. Thus, a 3 MW HiPEP device is capable of accomplishing a human Mars mission.

We have shown that HiPEP devices that process on the order of a few megawatts and produce an exhaust velocity of many 10s of km/s can fulfill demanding mission requirements, but have not given a specific example of such a thruster. This is because there are few devices capable of operating at powers greater than 100 kW and none have been proven

to meet the lifetime requirements. Some of those that are being developed are the magnetoplasmadynamic thruster (MPDT), lithium Lorentz force accelerator (LiLFA), variable specific impulse magnetoplasma rocket (VASIMR), and pulsed inductive thruster (PIT).¹

The Electric Propulsion and Plasma Dynamics Laboratory (EPPDyL) at Princeton University has been involved in research on MPDTs, including the LiLFA, for decades. The recent work on LiLFAs has been accomplished in collaboration with NASA’s Jet Propulsion Laboratory and the Moscow Aviation Institute [11]. The focus has been to demonstrate that the performance and lifetime of LiLFAs exceed the requirements of the missions they would be used for. Lifetime is of prime importance since the thruster must operate for months, as demonstrated above. The cathode generally is the component that fails first due to erosion via evaporation [12, 13]. The LiLFA is designed to reduce cathode material evaporation through the implementation of a multichannel hollow cathode and a lithium vapor propellant (explained in more detail in sections 1.1 and 1.3). Tungsten evaporates at $1 \mu\text{g}\cdot\text{cm}^{-2}\text{s}^{-1}$ ($0.03 \mu\text{m/hr}$ surface material loss) for the current densities of $\mathcal{O}(100 \text{ A/cm}^2)$ that MPDTs are operated at. Both implementations have been shown experimentally to improve the performance [14] and lifetime of the LiLFA over a standard gas-fed MPDT, but the fundamental operation of such a cathode configuration is poorly understood. Therefore, the goal of this dissertation is to develop an understanding of the fundamental physics of the lithium-fed MCHC with a detailed theoretical model that has been validated with experimental results.

This chapter provides the motivation, goals, and methodology for studying the multichannel hollow cathode. The next section describes the LiLFA. Section 1.2 describes the multichannel hollow cathode. The goals of the theoretical modeling and experimental

¹NASA recently began a focused effort of developing the in-space power systems that harness nuclear reactions to generate power at the megawatt level and the thrusters to utilize that power. The program, Project Prometheus, re-invigorated research into high-power EP systems after decades of minimal funding due the lack of near-term applications. Unfortunately, Project Prometheus is on hold until the next generation of human-rated launch vehicles are operational and NASA is closer to a human Mars mission. The goal of Project Prometheus is to develop nuclear power and propulsion systems for the demanding space missions outlined in the NASA vision.

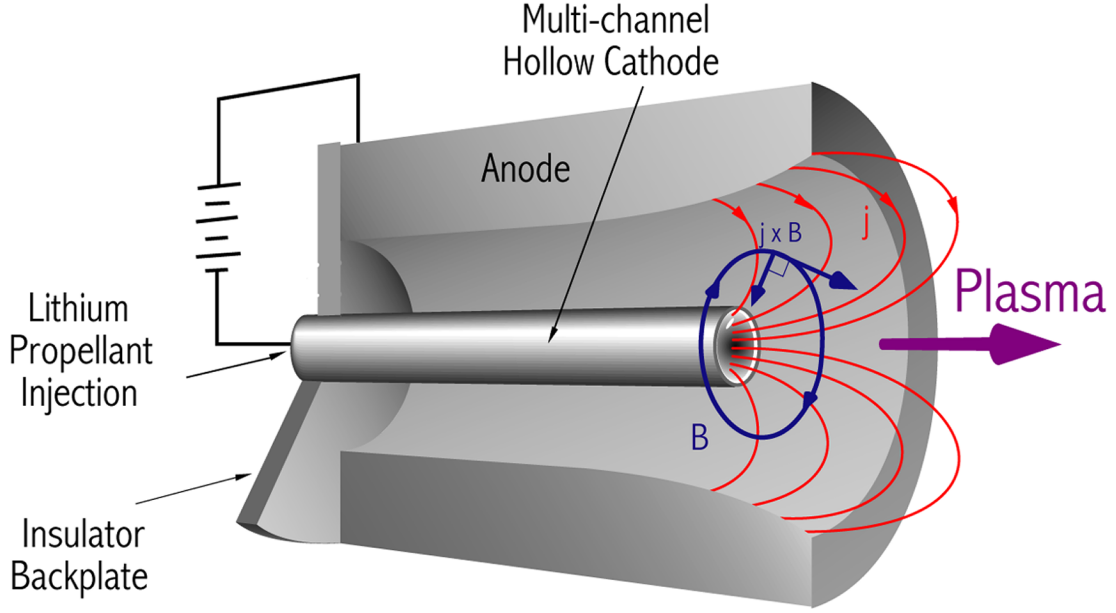


Figure 1.1: Schematic of the LiLFA

study are outlined in sections 1.3 and 1.4, respectively. Finally, we outline our research on the MCHC in section 1.5.

1.1 The LiLFA

As discussed above, the lithium Lorentz force accelerator is a candidate for demanding space missions. The LiLFA, shown in figure 1.1, is considered the next-generation MPDT [15] because the geometry is similar and thrust is produced with the same physical mechanisms but has improvements that make it a superior thruster. In an MPDT, a voltage is applied between concentric electrodes that breaks down a propellant gas, creating a quasi-neutral plasma within the thruster chamber (see figure 1.1). A high current ($10^2 - 10^4$ A) that is carried by the plasma between the electrodes induces an azimuthal magnetic field, causing a Lorentz force ($\mathbf{j} \times \mathbf{B}$) to accelerate the plasma out of the thruster at velocities of $\mathcal{O}(10 \text{ km/s})$ [9]. This body force accelerates the fluid in the direction perpendicular to both the current and the magnetic field. The radial current and azimuthal magnetic field produce

a force in the axial direction, while the axial current and azimuthal magnetic field interact to “pump” the plasma towards the axis of the thruster, which produces a pressure on the cathode and a resulting force on the thruster.

However, two major differences between the LiLFA and the MPDT bring about performance and lifetime improvements that truly enable the thruster to be applied to demanding missions. First is the choice of propellant. Whereas the MPDT traditionally uses inert gas propellants, such as argon, helium, and hydrogen, the LiLFA, as its name indicates, uses lithium. Furthermore, the central electrode of the LiLFA differs from the single rod design common to most gas-fed MPDTs. Instead, the LiLFA employs the multichannel hollow cathode (MCHC), small rods tightly packed within a hollow tube. Liquid lithium is injected into the upstream end of the cathode body where it is vaporized with power from a heater and the discharge. The vapor then flows into the channels between the rods of the MCHC where it is ionized and exits to the thruster chamber.

These two differences address some of the fundamental limitations of the MPDT. First, lithium is an ideal propellant for plasma thrusters where frozen flow losses are important, such as MPDTs, because of a low first ionization potential (5.4 eV), a high second ionization potential (75.6 eV), and a high first excitation level (59.0 eV) of the lithium ion [16]. The use of lithium also precludes the need for high-voltage ignition capacitors and hardware required to achieve breakdown in inert gas systems. Moreover, lithium can be stored in solid form onboard the spacecraft, leading to potential mass savings. Second, the multiple channel design for the central cathode, combined with the lithium propellant, has been shown to improve efficiency and increase thruster lifetime by reducing the near-cathode voltage fall and electrode erosion, respectively [17]. As stated previously, erosion is primarily due to evaporation of cathode material due to the extreme temperatures. The upper bound of mass loss rate per unit surface area, Γ^W , is described by [13]

$$\Gamma^W = \left(\frac{m_W}{2\pi k_B T_c} \right)^{1/2} p_{vp}^W(T_c), \quad (1.3)$$

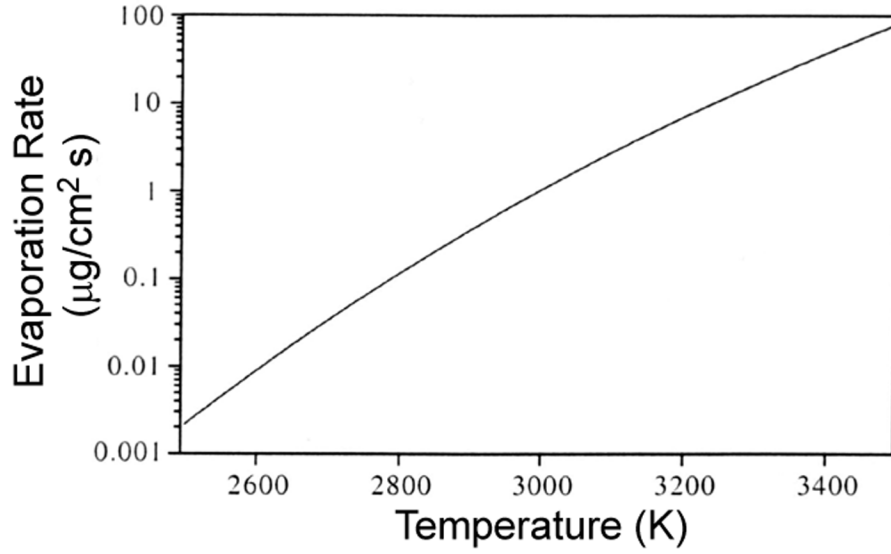


Figure 1.2: The evaporation rate of tungsten as function of temperature (from [12, 18]).

where m_W is the molecular mass of tungsten, k_B is Boltzmann's constant, T_c is the cathode temperature, and $p_{vp}^W(T_c)$ is the vapor pressure of tungsten as a function of the surface temperature. The vapor pressure can be approximated as [18]

$$p_{vp}^W(T_c) = 10^{\left(\frac{42000}{T_c} + 0.146 \ln(T_c) - 0.164 \times 10^{-3} T_c + 9.84\right)}, \quad (1.4)$$

which gives evaporation rate shown in figure 1.2. It can be seen that the evaporation rate and lifetime depend strongly on cathode temperature. The role of the electrode design in increasing efficiency and lifetime is, however, poorly understood. The MCHC is critical to the LiLFA due to its dual purpose role of plasma source and discharge cathode, yet there is no model that describes its operation.

From this we derive our motivation for studying the MCHC: *to enhance the lifetime and performance of the LiLFA by developing and validating a model that describes the operation of a lithium-fed MCHC.*

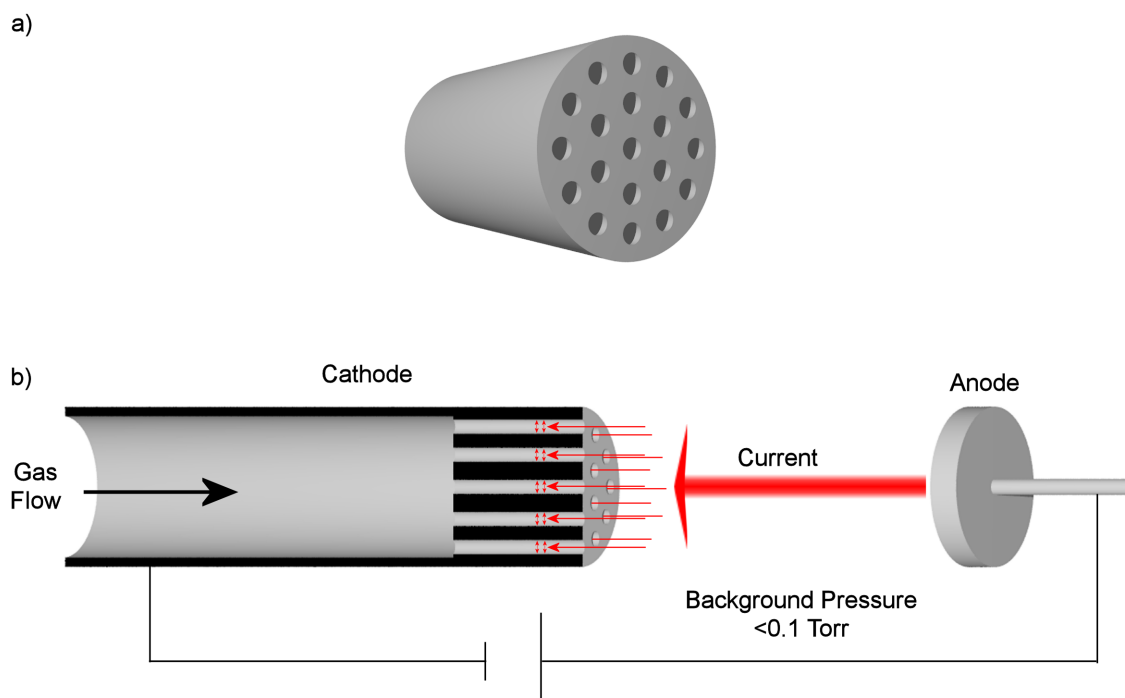


Figure 1.3: a) A perspective view of an example MCHC tip. b) A schematic of MCHC operation, including current penetration into the channels, gas flow through the channels, and low background pressure.

1.2 The Multichannel Hollow Cathode

Multichannel hollow cathodes conduct high current at low voltage while having a longer lifetime than other cathode types operating at similar conditions. They differ from planar or solid cathodes in that they have many channels that are open to the plasma in the inter-electrode space, as shown in figure 1.3. Generally, gas flows through the channels and plasma penetrates into the cavities under many operating conditions, which causes the arc to attach to the cathode through the confined volume within the channels. Discharges utilizing the MCHC are normally arcs, which are characterized by surface temperatures great enough to cause significant thermionic electron emission and low voltages that are less than a few times the ionization potential. Here we address only MCHCs that operate with arc discharges.

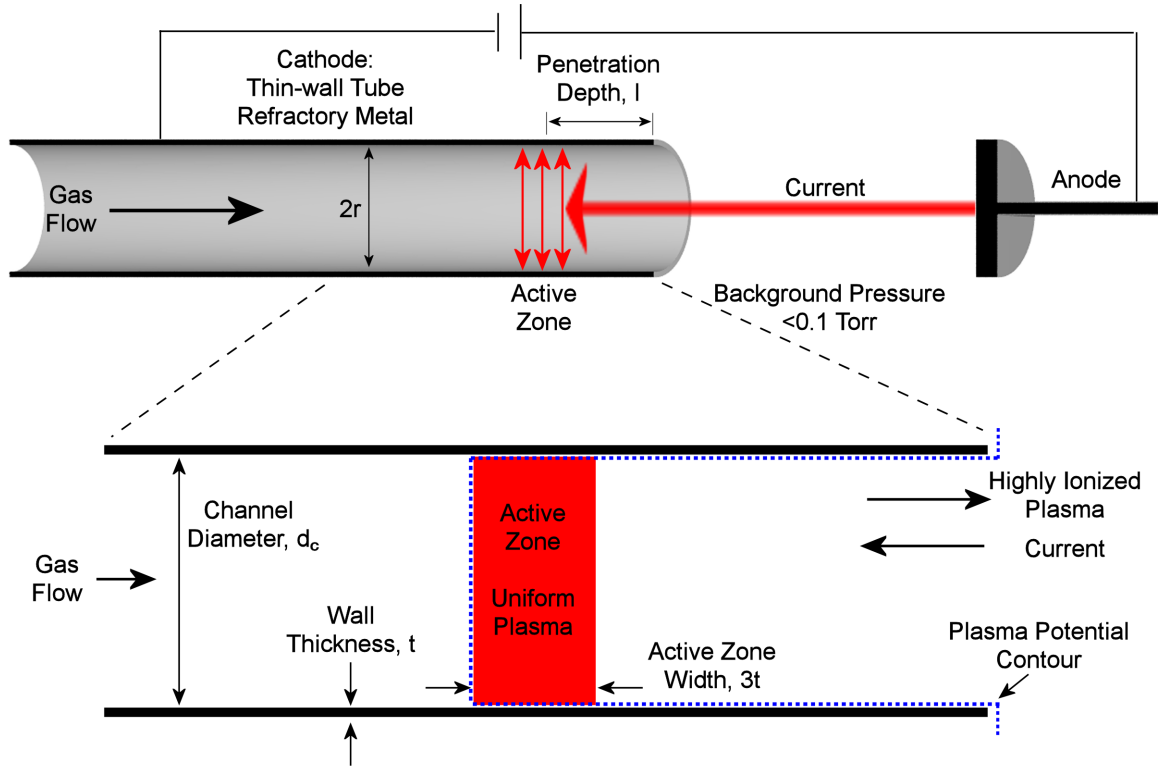


Figure 1.4: Schematic of an SCHC discharge.

Delcroix et al. developed the multichannel hollow cathode to conduct a relatively large current at an extended range of mass flow rate [19]. They demonstrated that the MCHC indeed delivered more current while maintaining a lower voltage. Although no detailed model was presented, they demonstrated that the division of mass flow rate and current between channels reduces voltage and cathode temperature.

1.2.1 The Single-channel Hollow Cathode

Each channel in an MCHC is similar to a single-channel hollow cathode (SCHC), shown in figure 1.4, which is better understood and provides a basis for our research (see Chapter 2). However, no complete model of SCHC operation had been previously developed. Physically, a high current density ($10 - 10^3$ A/cm²) SCHC is normally a thin-walled (0.01-1 mm) tube manufactured from a refractory material such as tantalum, tungsten, and graphite, so that it can withstand the extreme temperatures of the arc discharge. The working gas flows

through the channel of the cathode, which creates a relatively high pressure within the channel (a few Torr) because the flow is choked as it exits into the inter-electrode space. The arc attaches to the interior surface of the channel at a distance from the tip, called the penetration depth, that depends upon mass flow rate, channel diameter, wall thickness, and current. Electrons are thermionically emitted from the cathode material. The region where most of the current is drawn from the cathode surface is called the “active zone.” The cathode voltage drop (or fall), which is relevant to LiLFA efficiency, is defined in this dissertation as the difference in potential between the material surface and the plasma at the exit of the cathode channel. We demonstrate in this dissertation that plasma potential in the active zone is approximately the same as that at the cathode tip.

The characteristics of an arc hollow cathode operating in the regime that we are researching are [20]

- high current ($>10 \text{ A/cm}^2$ at the channel exit plane)
- a highly ionized ($>50\%$), dense plasma flowing from the channel
- arc attachment upstream of cathode tip
- low erosion
- operation independent of background pressures less than 0.1 Torr.

1.2.2 Arc Hollow Cathode Discharge Operation

The controllable parameters of an arc hollow cathode discharge are the channel diameter and length, the cathode wall thickness and material, the gas mass flow rate and type, and the current. The discharge adjusts plasma potential at the channel exit, the temperature profile of the cathode (including the distance the plasma penetrates), the ionization fraction of the gas within the channel, and the electron temperature inside the channel to provide the current demanded by the external circuit.

1.3 Goal of the Lithium-fed MCHC Theoretical Modeling

The lithium-fed MCHC is a very important component of the LiLFA: it impacts the lifetime of the device because of erosion during operation; it affects efficiency because power is dissipated by the arc in the cathode voltage drop; it provides plasma to the discharge chamber as the gas passes through the channels. Yet no complete, predictive model of its operation exists. As part of the design of an LiLFA, the radius of the cathode, range of mass flow rate and current, and propellant type are specified. The size and number of channels of the MCHC may be chosen to give both the best possible overall efficiency and lifetime required. The model should predict the plasma potential at the cathode tip (which is equal to the cathode voltage drop), which affects efficiency, as a function of the operating parameters, including number of channels and channel size. The issue of lifetime can be translated directly to cathode temperature. The hotter the cathode, the shorter the lifetime because the cathode erodes primarily due to evaporation [12]. By setting the lifetime to that required by the thruster mission, a maximum temperature can be determined. The MCHC model should be able to predict the temperature so that it can be part of the LiLFA design process.

Also, as explained in the previous section, the discharge adjusts certain parameters (plasma potential, cathode temperature profile, electron temperature, and ionization fraction) to provide the current required by the external circuit and the physical conditions dependent on geometry and gas flow rate and type. It is logical to develop a model that predicts the same parameters that the discharge adjusts to. Therefore, the goal of this research was: *to develop an experimentally validated theory of the lithium-fed multichannel hollow cathode that predicts cathode voltage drop, temperature and plasma penetration depth utilizing the physical conditions of:*

- *gas mass flow rate*
- *cathode material type*

- *cathode outer radius*
- *number of channels*
- *diameter of channels*
- *current,*

and to use that theory to develop an MCHC design procedure.

As alluded to previously, the MCHC is essentially many SCHCs bundled together, which is also how we approach the development of the theoretical model in this work. Therefore, the methodology of the research presented here was to develop and validate a theory of the lithium-fed SCHC and then build that into an MCHC model.

1.4 Goal of the Experiments

The experiments were designed especially to characterize the physical processes of the lithium-fed SCHC and MCHC, and were used to validate the theoretical models. A review of published data, described in Chapter 2, determined that their was limited direct measurement of the relevant parameters of cathode temperature, plasma potential at the cathode tip, and the plasma penetration depth for arc hollow cathode, especially lithium-fed ones. The goal of the experimental study was to measure those properties in lithium-fed SCHCs operated at a range of currents, mass flow rates, and channel diameters and an MCHC operated at a range of currents and mass flow rates.

1.5 Organization

The remainder of this dissertation presents the SCHC and MCHC theoretical models, and the experimental studies carried out to verify them, followed by an optimal design strategy for the MCHC. In chapter 2, the previous experimental and theoretical work on high-current

hollow cathodes is summarized and evaluated. In chapter 3, the apparatus and diagnostics of the experiments conducted on lithium-fed hollow cathodes are described. In chapter 4, the results of those experiments are summarized and explanations of the findings are presented. A theoretical model of the operation of the SCHC and MCHC, its validation against the experimental results, and the insights it provides are presented in chapter 5. In chapter 6, a procedure for designing the optimum lithium-fed hollow cathode is outlined. Finally, the conclusions are presented in chapter 7.

Chapter 2

Review of Arc Hollow Cathode Research

This chapter reviews past theoretical and experimental research on subjects related to the arc hollow cathode; including the multichannel hollow cathode, single-channel hollow cathode, and orificed hollow cathode. All three cathode types operate in a similar manner, by extracting current from the material surface via thermionic electron emission and conducting it to the outside through a high pressure [$\mathcal{O}(1 \text{ Torr})$] plasma confined within the channel, therefore the study of the physical processes in those cathodes aids in the understanding of the MCHC. Since our goal is to characterize how the cathode voltage drop and temperature are affected by the operational parameters of current, mass flow rate, and channel diameter, this review is focused on those issues. Overall, there is a lack of experimental data of internal properties of any hollow cathode because of difficulties in diagnosing such a small, dense plasma. The results of experiments that used lithium are presented to illustrate important trends that should be captured by our model and measured in our experiments.

Hollow cathode research generally includes glow and pulsed discharges, however these subjects are not discussed here because the current conduction mechanisms are sufficiently

different from a steady-state arc to warrant exclusion. Often, the term *hollow cathode* implies a glow discharge, but this cathode type is disregarded here because the electrons are extracted via secondary electron emission, the current is lower, and the voltage is higher. Pulsed hollow cathodes, such as the one studied by Krishnan et al. [21], are generally cold and therefore electron emission is due to spot attachment, secondary electron emission, or photoelectric emission, all minor processes in a steady-state hollow cathode [20].

Some researchers utilized a solenoidal magnetic field to confine the external plasma between the anode and cathode. The magnetic field does not affect the plasma inside of the hollow cathode channels because the ion Hall parameter is very small ($< 1 \times 10^{-3}$). This allows the ions to move radially toward the cathode wall along the electric field. The electron Hall parameter is ≤ 1 , which also indicates that the magnetic field has a limited affect on electron transport. Therefore, the magnetic field can be neglected in the study of the discharge within the channels of a hollow cathode.

The small body of published MCHC research is presented in section 2.1, followed by a summary of relevant SCHC research in section 2.2. The research on orificed hollow cathodes is mentioned in section 2.3 because the fundamental physical processes are similar to those of the SCHC and MCHC. The research is grouped by laboratory or primary author (since in some cases there is no laboratory or institution acknowledged).

2.1 Review of MCHC Research

Three primary research groups developed the foundation of MCHC knowledge through theoretical and experimental work and, therefore, are the focus of the first three subsections below. Other researchers have utilized the MCHC in the context of applications (such as MPD thrusters) or focused on erosion, and that work is presented in the forth subsection.

2.1.1 *Laboratoire de Physique des Plasmas (1969-1974)*

The multichannel hollow cathode was invented by Delcroix et al. [19, 20] while developing a hollow cathode that could conduct more current and operate at a lesser gas flow rate than a single-channel hollow cathode; in fact, the term *multichannel* was coined by those researchers. Their seminal work presented no detailed theoretical model, instead an insightful analysis compared MCHC operation to that of an SCHC. The analysis was based upon data from experiments of 9 and 3.6 mm outer diameter tantalum cathodes operating with currents from 20 to 80 A and argon mass flow rates from 0.9 to 8.9 mg/s. Approximate quantitative explanations of the dependence of plasma penetration depth on the number of channels, the ignition of a fraction of channels, the reduced voltage (the use of the term *voltage* without reference to the cathode fall indicates total discharge voltage) due to thermal coupling between channels, and the benefit of a hotter surface were presented.

They associated a reduction in plasma penetration depth with improved cathode operation because data from SCHC experiments conducted by their group suggested a direct relation to reduced voltage. They asserted that the plasma extends upstream to a location where the pressure is an optimum that is dependent on the gas and cathode material type - 2 Torr for argon gas and tantalum cathode. (Although, they also stated two different opinions in other works - that the optimum pressure depended on channel diameter [22] and that its dependence was not understood well enough to be predicted [20].) Poiseuille's law, corrected for transitional flow, was utilized to predict the pressure within the channel. Assuming a fixed cathode outer diameter and that the flow was evenly divided between the channels, it was shown that the plasma penetration depth decreases with an increasing number of channels, because the pressure increases. They presented data of decreased penetration depth in an MCHC compared to an SCHC, but did not quantitatively compare the results to their model. They also presented data of decreased voltage and temperature with multiple channels when compared to an SCHC at the same operating conditions.

An MCHC operated at a high flow rate or low current was shown to not utilize all

of the channels to conduct current because some of the channels failed to ignite. They presented an analysis of gas flow through channels of different temperatures that showed gas preferentially flows through the unlit (cold) channels. They contended that this had a negative effect on cathode voltage drop because the penetration depth would increase in the ignited channels. The cathode voltage fall as a function of the number of ignited channels was not presented, so this assertion was not verified. They did present the fraction of ignited channels as a function of current (the experiment was conducted with an 8.6 mm tube diameter with 6 internal channels of 3 mm diameter), but they did not attempt to predict the fraction of ignited channels as a function of current or flow rate.

Qualitative arguments explaining the benefits of a higher cathode temperature at the arc attachment region, and locating channels near to one another, were also presented. The argument for a hotter surface temperature depended on the reduction of the plasma penetration depth because of the increase in viscosity, and therefore increase in pressure, with temperature. They discussed two methods for increasing the temperature: (1) reducing thermal conduction and radiative losses by utilizing small wall thicknesses and radiation shields and (2) increasing the power transferred to the cathode wall from the plasma by reducing the channel size to increase the current density. They also noted that when channels of an MCHC were located closer to each other the voltage decreased. This effect was also attributed to the increase in surface temperature. The results of SCHC experiments with and without radiation shields demonstrated the importance of reducing radiation because it leads to a lower discharge voltage. Three MCHCs consisting of 2 channels (2 mm diameter) at varying distances (0.2, 0.8, 1.0 mm) from each other were tested at a range of currents from 20 to 80 A to demonstrate the effects of channel thermal interactions. The results demonstrated a 10% to 20% decrease in voltage as the distance between channels decreased.

Comments

The experimental results of Delcroix et al. definitively demonstrated that the MCHC can operate at a lower voltage and temperature than an SCHC and that thermal interactions between the channels can reduce voltage. The improved operation was attributed to a reduction in the thermal radiation power loss mechanism. The experimental data presented in this dissertation show that a short plasma penetration depth is not necessarily an indicator of lower voltage operation and, therefore, the above arguments based on penetration depth are not included in our model.

2.1.2 Babkin's Research Group (1976-1979)

The plasma parameters of a lithium-fed MCHC were measured experimentally by Babkin et al. [23]. The MCHC outer wall was a 16 mm inner diameter tungsten tube with a 2 mm wall thickness. The 2 mm diameter channels were made from 19 rolled pieces of 0.05 mm thick tungsten foil, which were not sealed axially. The foil channels extended 5 mm past the end of the tube. The vapor flowed within and between the cylindrical channels, making the actual number of channels greater than 19. The flow rate was 10 mg/s for most of the experiments and the current was varied between 50 and 500 A. To gain optical access to the cathode tip, a low flow rate of argon was introduced into the vacuum chamber near a window as a buffer to keep lithium vapor from the window. Spectroscopic data were analyzed to determine both the neutral and electron density and temperature within the channels. The electron and neutral temperatures were measured to be constant at 5500 K and 3000 K, within the uncertainties of 30% and 20%, respectively. The ionization fraction was measured to increase from 75% to 90% as the current increased, but the uncertainty in the neutral and electron density was significant, 40% and 20%, respectively. The total voltage and the plasma potential near the cathode tip were measured, however, the latter were not specifically presented, but were given to be 80% of the total voltage. The total voltage ranged from 10 to 15 V. The plasma potential was measured with a "floating sensor", which

was not described except that it was located 2 mm from the end of the cathode.

Babkin et al. [24] also investigated a “critical point” in the operation of a lithium arc with an MCHC. The research was focused primarily on measuring the change of the profiles of the plasma properties *external* to the cathode as the current increases through a certain value where the rate of voltage change with current increases dramatically. No model of the MCHC is discussed, but a double probe was used to measure the electron temperature and plasma density 1 and 2 cm downstream of the cathode tip. The cathode temperature was measured to be 2800 to 2900 K at currents from 200 to 1200 A and a flow rate of 10 mg/s, but no plasma potential measurements were reported.

Babkin and Potapov [25] also presented an analysis of the effect of oxygen on the erosion and operation of a tungsten MCHC. The experimental results from a previous investigation [24] were used to demonstrate that the surface current density was greater than could be accounted for with a pure tungsten surface and that contamination of the lithium with oxygen was a likely cause. No detailed calculations were presented, but an experiment was set up in which increased oxygen density reduced the cathode temperature.

Comments

These experiments demonstrated that lithium-fed MCHCs can operate over a very wide range of current and that useful measurements of plasma parameters can be obtained. The use of a tube with flowing argon to block lithium flux onto an optical window was the inspiration of an apparatus utilized to maintain optical access in our experiment. Also, the successful use of a probe in a lithium arc plasma indicated that a probe can survive such a harsh environment.

The neutral density measurements [23] do not follow the expected trends of stable or decreasing value with increasing current. One would expect the neutral density to decrease as current increases because the ionization fraction would increase and, since the mass flow rate was constant, there was no source for more neutrals. The neutral and electron density

measurements obtained using spectroscopy were likely influenced by background pressure because the vacuum facility was small and did not have significant cooling of the chamber walls. The background pressure of lithium could have easily risen when the chamber walls were heated from thermal radiation, as we observed in our early experiments, and could have caused particles in the line of sight to be measured. Even though Babkin's experimental investigations had many diagnostics and gave general insight to their uses, the limited amount and inconsistencies of the published quantitative results do not allow for an independent analysis of their data.

2.1.3 Ogarkov's Research Group (1976-1979)

Ogarkov et al. [26] tested a lithium-fed MCHC and developed a model that predicts the maximum possible current. The model included a power balance at the cathode surface, but did not attempt to model the plasma discharge within the channel. The model included thermal radiation, thermal conduction, surface ionization, tungsten evaporation, heat conduction from the plasma, resistive heating within the tungsten, thermionic electron emission, and the kinetic/potential energy of ion impact. It was assumed that the sheath voltage was equal to the ionization potential of neutral lithium, the plasma was fully ionized, and that the penetration depth was indirectly determined by a maximum axial electric field within the channel. The model was extended to include adsorption of lithium on the tungsten surface [27]. The maximum current conducted from an MCHC was shown to increase as the channel size decreases.

Unfortunately, there was no description of the diagnostics. All that was reported was that the cathode consisted of a 26 mm inner diameter tube holding tungsten rods of 1, 2, and 3 mm diameter. The lithium mass flow rate was set at 50 mg/s and the current varied between 900 and 2600 A. Total discharge voltage versus current was presented and they measured the plasma temperature away from the cathode to be 5000 K via spectroscopic methods. They took the current at which there is change in slope of current versus voltage to

be the maximum current the MCHC could conduct and compared that to their predictions.

Comments

The power balance at the cathode surface presented by Ogarkov has many components that are used in our cathode model:

- thermionic electron emission
- kinetic and potential energy delivered when the ions impact the wall
- thermal radiation
- thermal conduction
- heat conduction from the plasma.

We treat heat conduction from the plasma in terms of each source of energy, rather than Ogarkov's approximate model. Our calculations showed that tungsten evaporation and resistive heating were small in most cases, so we neglect those terms. Ionization of the neutrals on the surface was modeled with contact ionization, a process where an electron can be stripped from a neutral when the work function of the surface is approximately the same or greater than the ionization potential. This model is not consistent for these cathodes because any ions created by surface ionization would be stuck there due to the force caused by the electric field, hence we do not include it. It is unclear how lithium evaporation from the surface was accounted for in the adsorption model, and therefore we do not use their model, but one developed by other researchers [12, 6].

The current at which the rate of increase of voltage with current changes to a greater rate was likely influenced by the geometry of the discharge because the discharge was operated in an MPDT and the total voltage was measured. The voltage due to the back-electromotive force of the thruster and the sheath voltage of the anode could have affected

the measured value. Therefore, the voltage measurements and inferred maximum current were not accurate, but, nonetheless, provided qualitative agreement with their model.

2.1.4 Other Research Groups

The utility of the MCHC in high-current MPDTs was realized early, and many researchers studied how cathode configuration and location affected thruster performance. Grishin et al. [28] designed and tested a high-power (operated up to 100 kW) thruster that utilized lithium as propellant and had many different cathode outer diameters. The details of the cathodes, such as outer tube thickness and rod size, were not given. No measurements of the cathode temperature or voltage drop were presented, only discharge voltage and thrust.

Thruster research demonstrated that pure tungsten hollow cathode erosion was a formidable problem if lifetime was to be greater than hundreds of hours. Dyuzhev et al. [29] studied alkali metal (specifically cesium) coatings on MCHCs as a method of increasing lifetime. Alkali metals have a low work function, which can reduce the cathode temperature, hence evaporation, if they coat the cathode surface and reduce the effective work function. The temperature exponentially depends on the work function, as described by the Richardson equation, therefore a small reduction in work function (0.1 eV) can greatly reduce the surface temperature. There was no gas flow through the cathode; instead a background fill was utilized to sustain the discharge, which was a mixture of argon and cesium. The use of argon and cesium, combined with zero flow through the cathode, makes it difficult to use these results in our research. A detailed model explaining the temperature reduction was not given, only the fact that complete coverage of the surface with an alkali metal can reduce the work function to that of the coating material.

Ageyev et al. [17] presented results of high power (500 kW) lithium-fed MPDT experiments. The thruster utilized an MCHC that consisted of a 70 mm diameter hollow tungsten cone with an unspecified number of holes drilled through it. The cathode operated at temperatures between 3000 and 3100 K during pure lithium propellant operation, and 1000 K

lower with barium additive. The high temperature operation indicated that there was no lithium coverage of the cathode during lithium-only operation, although no significant erosion was measured.

Vaulin et al. [30] presented a theoretical analysis of cathode material erosion, which included basic power balances of the cathode wall and plasma. The calculation of erosion included sputtering, evaporation and the possible recycling of the cathode material back onto the surface. The power balances were too approximate to benefit our research and no data were presented.

Semenikhin and Tikhonov [31] presented experimental data regarding the influence different MCHC configurations and locations on lithium-fed thruster performance. There was no cathode theoretical model or data presented.

Most recently, Rossetti et al. created a numerical model of the MCHC [32, 33] based upon their SCHC model discussed in section 2.2.10. The components that are added to the SCHC model are calculations of (1) the flow rate through each channel based on the channel size and shape and (2) heat conduction between and around the circumference of the channels. The model captures the overall reduction in cathode temperature of an MCHC compared to an SCHC, but, as explained below, is not capable of predicting high-current operation.

Comments

The above research emphasized the importance of understanding the MCHC in order to develop higher efficiency and longer lifetime thrusters, but cannot be directly applied to the development of our theoretical model.

2.2 Review of SCHC Research

A wide range of research has been accomplished on SCHCs, but because of the complexities of modeling all of the relevant physical processes and the difficulties of making measurements, no previous work had developed a complete understanding of the SCHC. This section describes and evaluates the work of ten groups that studied the SCHC.

2.2.1 MIT and Oak Ridge National Laboratory (1962)

The first peer-reviewed work describing the SCHC was authored by Lidsky et al. [34], with contributing authors from the Nuclear Engineering Department and Research Laboratory of Electronics at MIT and Oak Ridge National Laboratory. The SCHC was developed as a high-density, steady-state plasma source for fusion research. Experimental results using different types of cathodes (graphite and tantalum tubes of 3 and 12.4 mm inner diameter) were presented. Many experiments with gas flows of 0.09 to 3.6 mg/s argon and low background pressure (<1 mTorr) were accomplished, but limited data were presented. Proper hollow cathode operation was distinguished by the presence of a “hot spot” upstream of the cathode tip, which Delcroix later called the “active zone,” which is the term we use. The pressure at the upstream end of the cathode was measured to be 5-20 Torr for a 3 mm inner diameter tube for “typical” argon flow rates. The total discharge voltage and cathode tip temperature were presented. Experimental data presented in a figure demonstrated the advantage of radiation shielding by reducing the discharge voltage, even though this effect was not explicitly discussed. The investigators noted that the discharge was not affected by anode location or geometry.

A general estimate of the current conduction mechanism was also presented. Field-enhanced thermionic electron emission was discussed, as well as the fact that the atoms were likely ionized and struck the cathode wall many times before exiting the cathode. They also asserted that the plasma penetrated to a location where the product of the pressure

times the diameter would be approximately 1 cm·Torr. No calculations were presented, although the value was determined from the ionization mean free path being comparable to the tube diameter, as is often done for glow discharges [35].

Comments

This early work experimentally demonstrated many of the important characteristics of the SCHC:

- arc attachment upstream of the cathode tip
- high current
- highly ionized, dense plasma
- cathode operation independent of anode location and geometry
- low erosion.

Because this work was a general presentation of a new device, there were no detailed calculations or analyses of cathode operation. The assertion that the plasma penetrated to a depth where the product of the pressure and diameter is 1 cm·Torr was not supported by experimental data or detailed calculations, therefore this conclusion must be verified.

2.2.2 *Institut d'Electronique Fondamentale (1972)*

Lorente-Arcas [36] presented an explanation of the experimentally observed pressure rise in the vacuum vessel just after hollow cathode arcs are extinguished. The upstream boundary of the active zone was shown to be a sheath through which the electron pressure is transferred to the neutral gas, and, therefore, a small amount of extra gas can be trapped within the cathode during the discharge. The dominant processes within the sheath were considered to be ambipolar diffusion and electron-ion recombination. The ions were assumed to be created by inelastic collisions of thermal electrons with neutrals. The energy

the electrons gained by accelerating through the cathode sheath was assumed to transfer directly to thermal electron energy, without inelastic collisions. The ionization model was approximate, relying on a population of metastable argon atoms that were assumed to exist without explanation of their creation mechanism. Furthermore, their density was determined by a free parameter.

Comments

This research does not relate directly to ours because it applies only to the upstream boundary of the plasma, a very small component of the discharge. In addition, the location of the upstream boundary of the active zone was not predicted. However, this model could supplement the one presented in chapter 5 because it is a likely description of the upstream plasma boundary, but we did not take that step.

2.2.3 *Office National d'Études et de Recherches Aéronautiques (1973-1977)*

Brunet measured the plasma potential and density, electron temperature, and cathode temperature of a tantalum SCHC with an inner diameter of 5.6 mm and a wall thickness of 0.2 mm [37, 38]. Argon was introduced through the cathode at 1.2 and 3.5 mg/s and the current was set to 10 and 15 A. Langmuir probes were positioned along the axis of the cathode downstream to 6 cm upstream of the tip. The gas was measured to be not fully ionized and, therefore, the cathode was not operating in the optimal hollow cathode mode. The plasma potential at the cathode tip was approximately 40 V for the three operating conditions and the peak cathode temperature was 2100 K.

Comments

The measurement of plasma potential and temperature within the cathode provided valuable information, but because the cathode was operated at low current and the plasma did

not fully penetrate the channel, the data cannot be generalized for an SCHC operating in the optimal range.

2.2.4 *Laboratoire de Physique des Plasmas (1968-1978)*

Delcroix and Trindade authored a review of arc hollow cathode research conducted prior to 1974 [20]. The review discussed experimental results of the cathode region and the external plasma, including operation at a wide range of background pressures, gas flow rates, and currents. Most of the research on the cathode region operating in optimum hollow cathode mode was conducted at the *Laboratoire de Physique des Plasmas*, and, therefore, the publications from that group prior to 1974 [39, 40, 41, 42, 43] were the primary sources for that portion of the review article.

Their analysis of a wide range of experimental conditions allowed them to identify the optimal regime of arc hollow cathode operation; which is when gas is injected through the cathode channel into a discharge vessel of pressure less than 0.1 Torr and there is an extensive “active zone” located some distance upstream of the cathode tip. This regime corresponds to the cathode being able to draw the greatest current at the lowest voltage. It was not known why the plasma penetrated to a certain location, but it was thought that the gas pressure there must be optimum for the experimental conditions, which were estimated to be a few Torr. The minimum current density at the cathode tip was determined to be a few tens of A/cm^2 and the flow rate a few tenths of mg/s ; the upper limits depend on cathode material properties.

The plasma penetration depth and maximum temperature were measured as a function of gas flow rate and channel diameter at a constant current of 15 A. The penetration depth increased with increasing channel diameter and decreasing flow rate. The increase in penetration depth with channel diameter was partially attributed to the change in current density. Their conclusion was that the penetration depth decreases with increasing current. Using an approximate theoretical model of the gas flow, the pressure at the active zone was

determined to be a few Torr. The temperature increased from 2200 to 2400 K as the channel radius decreased from 3.3 to 1.8 mm. A small ($\leq 5\%$) reduction in the peak cathode temperature was measured as the penetration depth increased from 0 to 6 cm for a given channel radius.

The cathode voltage drop was estimated from the total discharge voltage and power loss calculations and calorimetry measurements. The cathode voltage fall was calculated from experiments where the mass flow rate and channel diameter were constant. They estimated that the electric field of the internal plasma was quite large (1 V/cm), based upon their interpretation of total discharge voltage and active zone location. The active zone was determined to have the same voltage (10-14 V) independent of mass flow rate. A reduction in total discharge voltage was measured when radiation shielding was added around the cathode; this was attributed to less power lost via thermal radiation from the cathode wall.

The outline of a cathode model was presented in Delcroix and Trindade's review, but it became the focus of a later paper by Ferreira and Delcroix [44], therefore we only describe the more detailed theoretical model here. They presented a one-dimensional model of the SCHC, however it required the experimentally measured cathode temperature profile, which implicitly includes total current, and potential at the cathode tip as inputs. Differential equations of the plasma potential and electron energy plus a plasma density equation are solved to find the internal plasma properties. The differential equations utilize the inputs from detailed models of

- gas flow within the channel
- excitation and ionization
- radial transport of ions
- axial transport of current and energy.

Gas flow was modeled as transitional flow through a tube, following the semi-empirical model presented by Dushman [45]. The predicted pressure at the upstream end of the cath-

ode matched experimental measurements fairly well. The high-energy electrons emitted from the wall and accelerated by the sheath were assumed to lose energy through multiple collisions. The model of this process, called the “cascade,” was presented as a general model including collisions with ions, electrons, and neutrals in any excited state. A numerical solution for electrons with initial energies from 15 to 40 V entering an argon gas was presented, but only collisions with ground state neutral argon were included. The solution gave the number of ions created by each injected electron. A fundamental description of radial transport of ions was also presented, from which the plasma density across the channel radius was determined. The electron power balance included resistive heating, ion heating, losses due to inelastic collisions with excited neutrals, and the power delivered by the thermionic electrons.

Comments

The early work at this laboratory determined many of the important trends and limits of arc hollow cathodes, such as

- an upper limit to background pressure
- minimum current densities and flow rates
- the increase of plasma penetration depth with decreasing flow rate
- the increase of plasma penetration depth with increasing channel diameter,

but some of the other conclusions must be critically evaluated. The conclusion regarding plasma penetration depth decreasing as a function of current was based upon ambiguous experimental results: The plasma penetration depth experiments were all accomplished at a current of 15 A; only the current density was altered by changing the channel diameter. The change in channel diameter simultaneously affected the gas pressure profile and the circumferential area for the arc to attach to, but this was not considered in their analysis.

Indeed, at a constant flow rate and channel diameter we would expect the plasma to penetrate further upstream with increasing current due to either the greater density or surface area available, of which the former was borne out by our experiments.

The analysis regarding the cathode voltage fall and internal electric field was not based upon direct experimental measurements. The total discharge voltage was measured and estimates of some power loss mechanisms were accomplished to calculate the voltage for different portions of the discharge. The cathode voltage estimates only included the heat conducted to the cathode base or radiated from the outer cathode surface, but not both, and other mechanisms such as ionization and thermionic cooling were neglected entirely. The heat conducted to the base is a relatively small portion of the power loss and is nearly independent of operational conditions if the active zone is far enough from the cathode base, which their measurements supported. The estimate of power lost via radiation is more representative of cathode power loss [40] and trends from those calculations show that the fraction of power lost in cathode processes decreases with increasing mass flow rate, an estimate that was ignored in their final analysis of cathode voltage drop trends. Changes in total discharge voltage as the penetration depth increased were attributed to the internal electric field, but it is also possible that the anode voltage increased because of the lower external plasma density that occurred when the flow rate was decreased.

The theoretical model had limitations that did not allow it to predict cathode operation, the most important being the use of plasma potential at the cathode tip and temperature profile (which also determines the thermionic current profile) as boundary conditions. The physical processes that were components of Ferreira and Delcroix's model and were considered for our model are

- ion transport to the sheath
- power balance of thermal electrons, including resistive heating, ion heating, and inelastic collisions

- an ionization model
- “cascade” of thermionic electrons as their energy decreases through inelastic collisions.

Although the “cascade” model was presented in great detail, they utilized only a small fraction of what was presented because they included only electron collisions with neutral, unexcited argon. This limited ionization mechanism probably reduced the predicted ionization fraction. We modified their implementation of the cascade model by including collisions with electrons, ions, and the excited states of the neutrals.

2.2.5 Grishin’s Research Group (1977)

Many experiments with a 3 mm inner diameter tantalum SCHC with a 0.1 mm wall thickness were accomplished by Grishin et al. [46]. Many cathode temperature profiles were measured, but only three were presented. Nine maximum temperature measurements, which were between 2640 and 3040 K, were presented as a function of current (10-160 A) and argon mass flow rate (0.16-3.6 mg/s). The cathode voltage drop was estimated from energy balances at the near-cathode plasma and cathode, which included radiation, thermionic emission, and resistive heating measurements. Analysis of the data determined that the electron current was solely due to thermionic emission.

Comments

The cathode voltage drop estimates were not reliable enough to utilize as a basis for our theoretical model because the energy balances from which it was calculated were approximate and they were less than physically possible values at high current. The cathode temperature data were too sparse to clearly demonstrate trends, but if the high mass flow rate data are neglected, the cathode temperature increased with current. (The high mass flow rate temperature profile showed that the active zone was at the tip; Therefore, the cathode was

likely not operating in optimum mode and the results can be ignored.)

2.2.6 *A.F. Ioffe Physicotechnical Institute (1978-1981)*

Hollow cathodes operated with cesium vapor were studied theoretically and experimentally by Baksht and Rybakov [47, 48, 49] and Dyuzhev et al. [50], respectively. Models of an externally heated hollow cathode with a fully ionized cesium plasma, with and without gas flow, were presented [47, 48]. The emitted electron current density was set by the assumed wall temperature and cesium work function, thus separating the electron emission and plasma processes. The power of the electrons in the axial direction, current continuity, and, in the case of flowing plasma, pressure were modeled. The effect of cesium coating on an unheated cathode was studied theoretically in reference [49]. This model is similar to the others, except that a power balance of the cathode wall was included. The theories predicted current versus voltage and plasma potential versus depth as functions of pressure or flow rate and surface current density.

An externally heated, 3 mm inner diameter nickel hollow cathode operated with a mixture of stagnant cesium and argon gas was tested to determine plasma properties within the channel. Discharge pulses 1 ms long at currents between 9 and 40 A were applied to the 1050 K cathode with background pressures of cesium from 1 to 4 Torr. Measurements of plasma potential, density, and electron temperature were accomplished at locations up to 1 cm within the cathode with a Langmuir probe. The measurements demonstrated an increasing cathode voltage drop with current, that the internal electric field was significant (≈ 5 V/cm), and that the plasma penetration increased with increasing current. This was in general agreement with their model.

Comments

Although the theoretical model of preheated, non-flow-through cathodes only included current continuity and axial power carried by electrons, the model captured the trends mea-

sured in their experimental device. However, the model and experimental results cannot be directly applied to an unheated, flow-through hollow cathode; the plasma/surface interaction is different because the ions are not pulled toward the cathode wall by a strong electric field and are not recycled in order to heat the surface. The emitted electrons are different in a preheated cathode because they are not accelerated through a sheath and the model does not require that they ionize even once; they must only conduct current. The theoretical models are limited by the assumption of full ionization and, as such, are of limited applicability to our cathode model. The experiment demonstrated that plasma conditions could be measured within a pulsed, preheated hollow cathode, but this experiment is much different from steady-state operation with cathode temperatures of ≥ 2500 K, which was measured in our experiment and, therefore, much of their work does not apply directly to our research.

2.2.7 Baikov Institute of Metallurgy (1979)

A concise description of the dependence of the maximum cathode temperature and its location was presented by Rykalin et al. [51]. Tungsten cathodes with 0.4 to 2.0 cm inner diameters, 0.2 to 0.5 cm wall thicknesses, and 6 to 12 cm lengths were operated from 300 to 3000 A with argon mass flow rates of 0.09 to 0.46 mg/s. The background pressure was 0.4 Torr, which was greater than the 0.1 Torr limit for optimal operation, as found by Delcroix et al. [20]. The maximum temperature was between 2900 and 3300 K. It was noted that the position of maximum cathode temperature depended strongly on *both* current and gas mass flow rate. The active zone moved upstream with decreasing current and mass flow rate. It was also noted that the value of the maximum temperature was independent of gas mass flow rate. No plasma potential measurements were presented.

Comments

This paper presented the important trends of

- plasma penetration depth dependence on current
- plasma penetration depth dependence on mass flow rate
- maximum temperature independence of mass flow rate.

Rykalin's data was likely affected by the high background pressure, which could have affected the penetration distance and the pressure within the channel [20]. Therefore, care must be taken when comparing these trends to SCHCs operated at optimal conditions. At low mass flow rate and high current, it is possible that the flow was not choked at the cathode exit, and that the internal plasma density was affected.

2.2.8 Moscow Aviation Institute (1996)

A one dimensional model of the SCHC was presented by Vaulin et al. [52] that included differential equations describing the

- heat conduction along the cathode wall
- plasma electron power balance
- gas flow within the channel
- ion and neutral particle balances.

The terms of the heat conduction equation included resistive heating, electron cooling, ion bombardment, conduction to the neutral gas, and thermal radiation. The plasma electron relation included resistive heating, power from thermionic electrons accelerated through the sheath, and losses from atomic excitation and ionization. The ionization rate was assumed to be equal to the rate that ions recombine at the wall, which was determined by diffusion of ions to the sheath. The ionization inefficiency was determined from an approximation specific to argon and the gas flow was modeled as viscous laminar flow with an allowance for slip.

The model required cathode material, gas type and flow rate, cathode radius and length, current, and the temperatures at the cathode base and tip as inputs. The plasma potential, cathode temperature profile, gas pressure, ionization fraction, and electron temperature were predicted along the length of the cathode. The theoretical and experimental temperature profiles were compared and were in good agreement, but the upstream and downstream values were set to be the same so this result is not surprising. The prediction of plasma potential at the cathode tip was comparable to the measured value, but it was predicted to increase upstream of the cathode tip, which is not physically possible.

Comments

The model included most of the important processes that occur within an SCHC, although the flux of neutrals into plasma due to gas flow was neglected and ionization was solely due to thermal electrons. The calculated plasma potential profile was not physical because the electric field was predicted to be the reverse of the electron current direction along a relatively large length of the channel. This was a possible result because the axial current conduction model did not constrain the potential profile.

Because this model did not correctly calculate cathode voltage drop and used many approximations in order to be solved as a set of differential equations, we choose not to use this type of model in our analysis.

2.2.9 Princeton University (1976-2002)

Kennedy [53] developed a model of the SCHC that was solely based upon a power balance of the electrons along the length of the plasma within the channel. The pressure variation along the length of the channel was ignored because the model assumed no flow through the channel. Power was modeled as lost from the end of the channel via conduction and through collisions with heavy particles within the channel, while it was supplied from the electric field and electrons emitted from the wall. The current from the wall was determined

by the electron power balance. The ion loss rate was set so that the power delivered to the cathode exactly equaled that extracted by the electrons, neglecting thermal radiation and conduction. Ionization was assumed to be accomplished by the thermal electrons within the plasma at the rate of ion loss to the wall. The analysis required the electron temperature at the tip as a boundary condition. The electric field was assumed to be constant throughout the length. The surface current density predictions were compared to the results of a quasi-steady experiment conducted by Krishnan et al. [54].

Princeton University was also interested in the effect of alkali metals on the operation of solid cathodes, a precursor to the research presented in this dissertation, even though it is not hollow cathode research. The goal was to increase cathode lifetime by reducing the surface work function through the creation of an electropositive surface layer. Chamberlain [55, 56] and Fillmore [57] studied barium oxide and lithium dispenser cathodes, which are porous cathodes that allow the alkali to diffuse through pores to the surface, thus maintaining the electropositive surface layer. The results demonstrated that lithium alone could not be relied upon to provide adequate coverage, but that barium oxide could reduce the cathode temperature if there was a renewable supply.

Comments

Kennedy's work is not applicable to our analysis because it neglected the plasma-surface interaction and did not include gas flow through the channel. Ionization was assumed to be via inelastic collisions with thermal electrons, but no calculations or models of the process were presented. This model neglected many of the important processes that must be included for an accurate model, and therefore it was not utilized.

2.2.10 *Centrosazio* - University of Pisa (2002-2005)

A one dimensional theoretical model of the SCHC was presented by Rossetti et al. [58, 32, 33]. The model included differential equations describing the

- heat conduction of the cathode wall
- plasma electron power balance
- gas flow within the channel
- axial current conduction in the plasma.

The models of the heat conduction, plasma electron power balance, and gas flow were very similar to Vaulin et al. [52]. The ionization model included collisions by the primary electrons emitted by the cathode. Ionization via thermal electrons or through excited states was neglected and, therefore, was modeled as a perfectly efficient process. The ion current to the wall was set by the electron current because it was assumed that every emitted electron that collided with an atom created one ion that impacted the cathode. This relation also determined the plasma density and maintained the particle balances. This work was the first to consider the loss of high-energy, thermionic electrons before they have an inelastic collision with the neutrals. The total mean free path was calculated utilizing the theory of the random walk [59]. If that length was greater than the distance to the cathode tip, a fraction of the high energy electrons would escape.

This model required the cathode voltage drop as an input, in addition to the normal parameters of cathode material, gas type and flow rate, and cathode radius and length. The model predicted the plasma potential, cathode temperature, gas pressure, ionization fraction, electron temperature, and current along the channel. The temperature profile predictions matched the experimental trends of a peak temperature upstream of the tip and the peak moving downstream with increasing mass flow rate. The current was predicted to decrease with increasing voltage in a way not seen experimentally.

Comments

This model captured some trends of plasma penetration in hollow cathodes, but because voltage is required as an input, it cannot predict the voltage as a function of current. An

SCHC can draw a wide range of current at a given voltage and this model finds the lowest current because the plasma penetration depth is limited by the electric field model. We include the loss of high energy electrons from the channel before they collide inelastically in our model.

2.2.11 Other Research

The SCHC has been utilized in MPD thruster and cathode erosion research. Mantenieks and Myers [60] used four different SCHCs in an applied field MPD thruster in order to determine the difference in performance brought about by various cathode configurations. The cathodes had low work function inserts, and, in some cases, orifices. Fradkin et al. [61] and Ageyev et al. [62] separately measured the performance of lithium-fed, applied field MPDTs with SCHCs. No direct measurements of the cathode properties were attempted in any of these studies.

2.3 Review of Orificed Hollow Cathode Research

The physical processes that occur within orificed hollow cathodes are similar to those in SCHCs and MCHCs. This is because much of the current is extracted from the material surface via thermionic electron emission. Therefore, the analysis of the power balance and the current conduction at the surface is similar. The primary difference between the orificed hollow cathode and an SCHC is that the end of the channel is not open, but there is a plate with a small orifice in the middle, generally about 10 times smaller in diameter than the channel. Therefore, the flow velocity within the orificed hollow cathode is well below the sonic speed and the neutral gas pressure is nearly constant within the channel volume. The other differences, including the low work function inserts from which the current is extracted and the importance of an external heater in cathode wall, make the details of the experimental and theoretical results too different to apply directly to the SCHC and MCHC.

However, the physical processes included in the theoretical and numerical investigations of those cathodes are of interest.

The first model was presented by Siegfried and Wilbur [63], which was found to be in good qualitative agreement with experimental data [64]. The components of the model were

- current balance
- field-enhanced thermionic electron emission
- a double sheath model to determine the electric field at the cathode surface
- energy balance at the cathode wall
- energy balance of the ion production region
- ion flux to wall determined by Bohm criterion
- existence length for primary electrons
- gas pressure.

Salhi and Turchi also [65, 66, 67] presented a theoretical model with similar components, except ion flux was determined by the random thermal velocity and a Saha-type two-temperature equilibrium ionization was included. Recent research has included advanced, two-dimensional numerical models of the plasma region, combined with separate thermal models of the insert [68, 69, 70]. The numerical models self-consistently solved for the ion, electron, and neutral mass continuity, momentum, and energy equations.

2.4 Summary of Relevant Research

Here we summarize the experimental observations and components of the theoretical models reviewed in this chapter. We also discuss the lack of experimental measurements of the

important features of hollow cathode operation and how we address this issue. The components of previous researcher's theoretical models that we have included in our model, which are described in chapter 5, are also summarized. The limitations of the previously developed cathode models are also described to demonstrate the need for a new theoretical model.

2.4.1 Experimental Observations

Many important experimental observations provide insight into the physical processes occurring in MCHCs and SCHCs. The unambiguous observations are summarized here;

- The plasma penetration depth increases as mass flow rate decreases.
- The plasma penetration depth increases as channel diameter increases.
- The peak cathode temperature increases with current.
- The peak cathode temperature is weakly dependent on penetration depth and flow rate.
- Thermal radiation shielding reduces the discharge voltage.
- An MCHC has a lower discharge voltage than an SCHC at identical current and flow rate.
- All MCHC channels do not all ignite at low current.
- Thermal coupling between channels in an MCHC reduces discharge voltage.
- Lithium-fed hollow cathodes can operate with temperatures up to 3000 K.
- Oxygen contamination can influence the surface work function in lithium discharges.

There are many experimental measurements required in order to develop a general MCHC model or, specifically, a lithium-fed one. In general, the cathode voltage drop was not measured under enough operational conditions to determine its characteristics. Also, no experimental effort has successfully resolved the conditions that determine the location of the active zone. In the case of lithium-fed cathodes, there are also not enough cathode temperature profile measurements to determine the plasma penetration depth.

We address the lack of experimental data by carrying out a series of experiments that directly measure cathode voltage drop and surface temperature profile over a wide range of operating conditions with a lithium-fed MCHC and four lithium-fed SCHCs, and presenting the results in this dissertation. The harsh (high temperature and density) environment within the active zone makes it impossible to directly measure plasma conditions, and therefore it is understandable that they had not been accomplished. However, we demonstrate in this dissertation that the conditions within the active zone can be indirectly determined through an analysis of the operating conditions and cathode temperature profiles.

2.4.2 Theoretical Model Components

The previous MCHC and SCHC research did not provide an individual model that predicts plasma penetration depth, accurately determines cathode voltage drop, and includes non-equilibrium ionization via both thermal electrons and thermionically emitted electrons. The models did demonstrate which processes are significant and should be modeled, such as:

- a gas flow model that includes transitional flow
- ionization and excitation
- radial ion transport using the Bohm sheath criterion
- axial transport of electron energy
- axial current

- “cascade” of thermionic electrons
- axial heat transport along cathode wall
- thermal radiation
- field-enhanced thermionic electron emission
- electric field at the cathode wall calculated from double sheath theory
- thermionic cooling of cathode
- energy of ion impact and recombination at the wall
- high-energy electrons lost from cathode channel before colliding inelastically.

Our model includes these components and was developed to predict cathode voltage and temperature as a function of current without experimental measurements required as boundary conditions. We also modeled the ionization process differently than any other researcher.

Chapter 3

Apparatus and Diagnostics

This chapter describes the apparatus, including the facility, and the diagnostics utilized in the lithium-fed hollow cathode experiments. The experiments were conducted in the lithium experimental facility (LEF), which was specially configured to operate with lithium and high-temperature experiments, at the Electric Propulsion and Plasma Dynamics Laboratory. Using lithium presented unique challenges in the apparatus design and operation due to its high melting point (180°C), high boiling point ($\approx 900^\circ\text{C}$ at 10 Torr), and incompatibility with most materials. We discuss how these complications affected the design of the cathodes, the liquid lithium feed system, and the lithium evaporator. We also include a description of two methods for maintaining optical access to the cathodes while working with a vapor that condenses on room temperature surfaces, such as view ports.

3.1 Experimental Layout

The primary components of the experimental apparatus were the cathode, anode, lithium feed system, lithium evaporator, vacuum facility, and the apparatus that maintained optical access. The general layout is illustrated in figure 3.1 and pictures are shown in figure 3.2.

The cathode was located near the vertical and horizontal centers of the cylindrically-shaped facility at the axial location of the 30 cm access ports. This location allowed optical

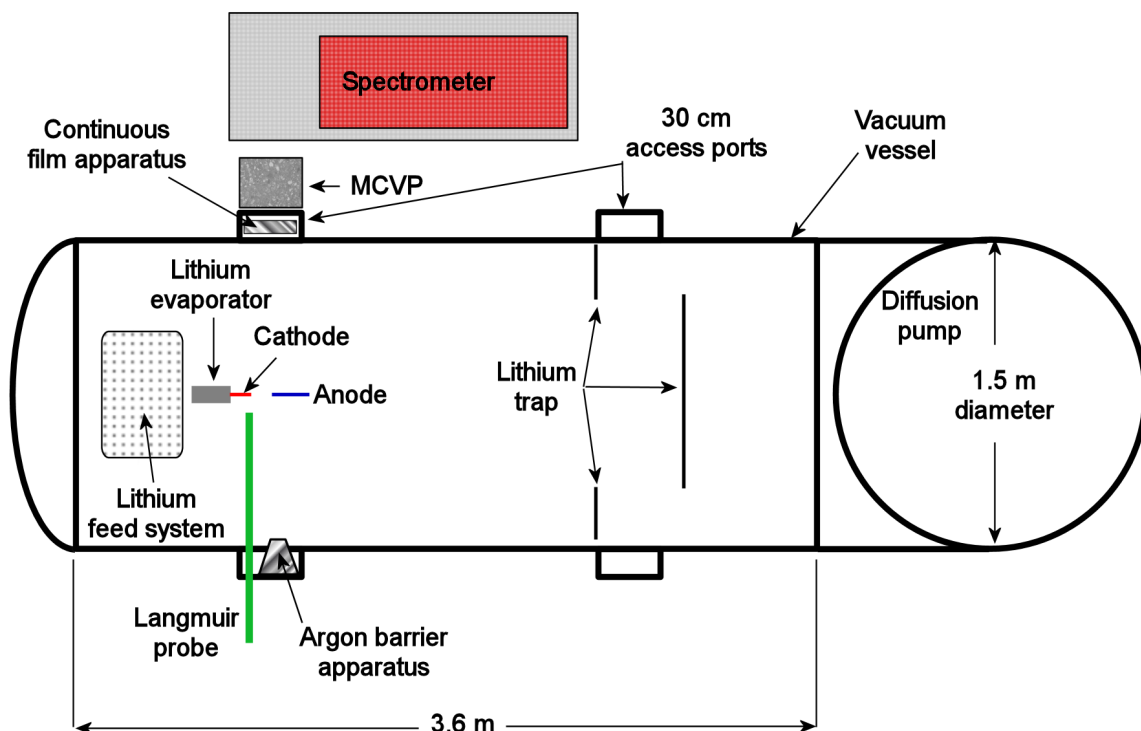


Figure 3.1: General Facility Layout of the LEF

access for the multi-color video pyrometer (MCVP) and spectrometer, as well as physical access with the Langmuir probe. The two apparatus designed to maintain optical access (continuous film and argon gas barrier) were located on the access ports near the cathode, one on each side. The MCVP and spectrometer utilized the same port, so the MCVP was removed when spectroscopy data were acquired.

3.2 Lithium Experimental Facility

The vacuum tank, pumping systems, and chilled-water systems that cool the experimental components and tank walls are parts of the LEF. The vacuum tank is a 1.5 m diameter, 3.6 m long steel vacuum chamber capable of withstanding the high temperatures of the lithium discharge apparatus and is compatible with lithium vapor. The ultimate pressure was 1×10^{-5} Torr, obtained with a 1.22 m CVC Type PMC-48C 95,000 l/s diffusion pump

backed by a Leybold Vacuum Products Inc. RUVAC WSU-2000 1342 CFM (630 l/s) roots pump in series with a 150 CFM (71 l/s) Stokes Microvac Pump. A set of water-cooled aluminum baffles were mounted approximately 1 m upstream of the diffusion pump to block direct flow of lithium into the pumping system. Pressure was measured with a Terranova Model 906 convection gauge at pressures above 1 mTorr and a MKS 943 cold cathode gauge below 1 mTorr.

Since lithium condenses on any room-temperature surface, it is pumped from the facility by the chamber walls and baffles. Therefore, it does not add load to the facility pumps and high mass flow rates could be utilized in the experiment. In order to simplify the post-experiment clean-up, the inside of the chamber was covered with aluminum foil, held to the walls by magnets, to capture the lithium as it condensed. The contaminated foil was disposed of after each experiment.

There were two separate cooling systems for the facility, one for the chamber walls and one for the rest of the apparatus. The chamber was cooled by 0.6 l/s (10 gallons per minute) chilled-water system capable of removing 100 kW of heat. Thermal control of the apparatus was achieved with a separate closed-loop chilled water system. Power dissipated by current conductors and thermal radiation was continuously removed with the water to prevent overheating of low-temperature components such as plastic and fiberglass insulators. Two components of the feed system, the lithium freezing valve and the cylinder, also relied on cooling to prevent the flow of liquid lithium where and when it was not desired. Overall, the closed-loop chilled-water system included five separate circuits that supplied water to the different components of the experiment at up to 125 ml/s each. A high-head pressure model Sta-Rite centrifugal pump supplied up to 630 ml/s at 240 kPa. The heat was rejected to the building chilled-water system using SWEP North America Inc. models 10046-030 and 10002-026 water-water heat exchangers.

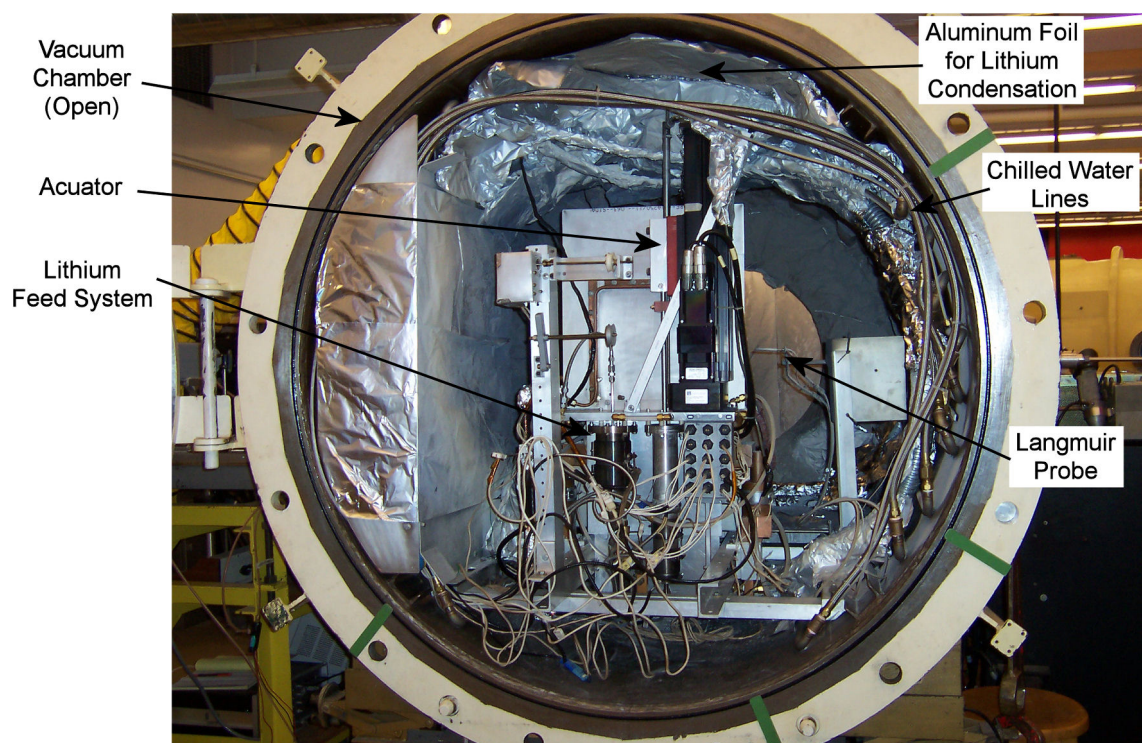
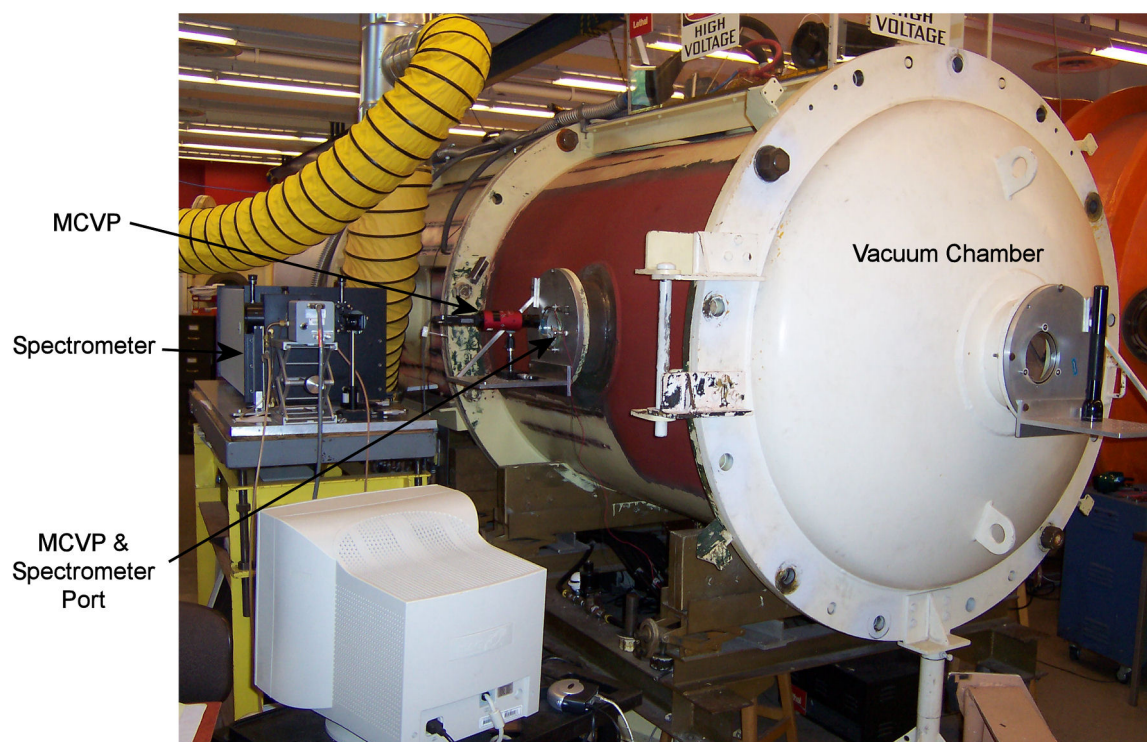


Figure 3.2: Pictures of the LEF.

3.3 Electrode Set-up

The anode was located approximately 3 cm from the cathode tip and aligned with the cathode axis. An experiment accomplished by us, as well as by previous researchers [19], demonstrated that the location of the anode has little affect on the cathode portion of the discharge, therefore we arbitrarily positioned the anode for the primary experiments. The anode was a 3/4" (1.9 cm) diameter tungsten rod with a hemispherical tip. Its copper support was water-cooled during high-current experiments.

The electricity for the arc was provided by two DC power supplies, one for high (>50 A) and one for low current. The arc would ignite at the open circuit voltage of the respective power supplies if sufficient lithium vapor was present in the space between the electrodes and the cathode temperature was greater than 1100 K. This eliminated the need for capacitors or high-voltage supplies.

3.4 Cathode Specifications

Five cathodes were designed and built specifically to explore the operation of lithium-fed hollow cathodes. The goal was to create cathodes that could be simply diagnosed, exchanged, and modeled. As described in chapter 5, the cathode affects the discharge through its thermionic electron emission, thermal radiation, and thermal conduction properties. The first two properties are inherent to the material and are shown in section 3.4.1 to be limited to tungsten for these experiments. The desire to limit axial thermal conduction and to make diagnosing the internal plasma easier drove the cathode design to a thin wall, $\mathcal{O}(0.1$ mm), and long length, $\mathcal{O}(10$ channel diameters).

3.4.1 Material Selection

Cathodes utilized in arc discharges are commonly made of refractory metals because of their extremely high melting temperatures; this is also the case for hollow cathodes. Cur-

rent densities range from 30 A/cm^2 to 1.2 kA/cm^2 , which corresponds to temperatures from 2000 to 3000 K for materials that have work functions of approximately 4 eV. Only the refractory metals tungsten, tantalum, and rhenium have melting temperatures high enough to ensure a reasonable lifetime. We considered only pure metals so that the material properties could be accurately determined.

A concern when selecting a pure refractory metal from which to make a cathode is the machinability of the material. None of the materials are well suited to machining, but Rhenium is much more brittle and hard than tungsten or tantalum and is rarely machined as a pure metal. Therefore, we did not consider it for our cathodes. We attempted to use thin-walled $\mathcal{O}(0.1 \text{ mm})$ tantalum tubes for the single-channel experiments without success. The poor thermal conductivity of tantalum caused the temperature at the cathode tip to be less than the lithium condensation temperature. Since we did not externally heat the cathode, no lithium vapor exited the cathode and an arc could not be struck. Therefore, tungsten was the only viable material to manufacture the cathodes from.

3.4.2 SCHC Dimensions

The cathode length and wall thickness play an important role in the discharge because thermal conduction from the active zone is affected by those dimensions. The active zone must be far enough removed from the cathode base to limit axial conduction, which implies that the cathode length should be many channel diameters to allow for significant plasma penetration. A thin wall allows for easy determination of plasma penetration depth and internal temperature, in addition to reducing heat conducted axially along the cathode. We also attempted to utilize cathodes similar to those used by previous researchers, most of which were thin-walled tantalum tubes. However, as explained in section 3.4.1, we were unable to successfully use tantalum tubes with lithium vapor. Due to the extremely brittle nature of tungsten, we were only able to manufacture tubes with a minimum wall thickness of 0.3 mm.

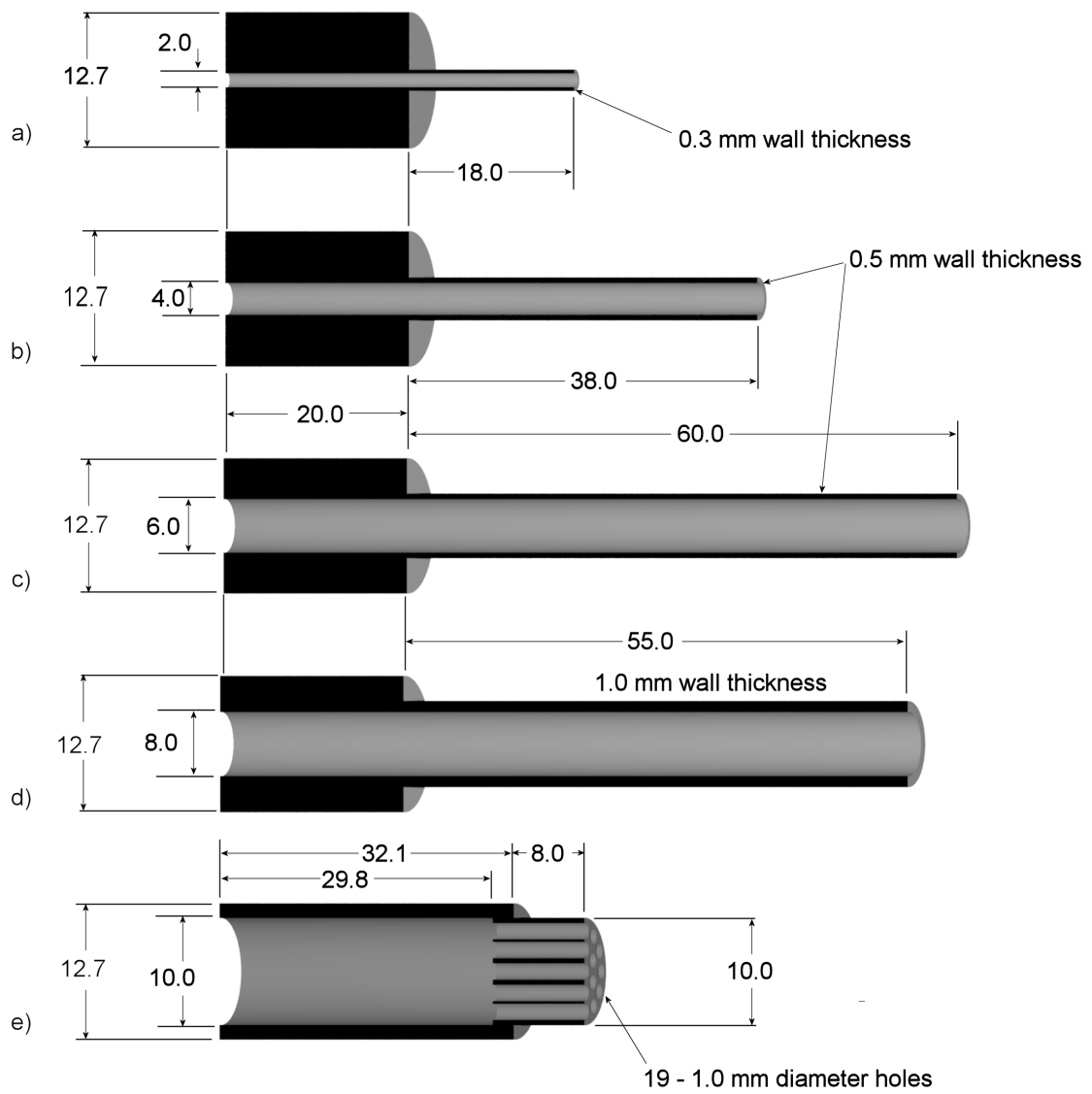


Figure 3.3: Schematic of cathodes used in the experiments (all dimensions in mm).

Four SCHCs with different inner diameters of 2, 4, 6, and 8 mm, shown schematically in figures 3.3a to 3.3d, were designed to demonstrate the dependence of the operating parameters on the channel diameter.

3.4.3 MCHC Dimensions

The MCHC was constructed from a single rod of tungsten, as shown in figure 3.3e. Nineteen 1 mm channels were drilled through the end of the rod machined to 10 mm in outer diameter. The channels open into a large volume upstream with an inner diameter of 10 mm and a length of 20 mm.

3.4.4 Cathode Interface with Evaporator

The cathode temperature had to be maintained above that at which lithium could condense on the surface, and the mechanical connection of the cathode to the evaporator had to have a small tolerance so that the lithium vapor would not leak. (In fact, it would have been optimal if the evaporator was inside the cathode, as in the LiLFA, but this was not feasible in this experiment where the goal was to test multiple cathodes.) A close tolerance ($\leq 0.001''$) fit was utilized for the mechanical, thermal, and electrical connection at the joint. The leak rate through this joint was more than 10 times smaller than the flow rate through the cathode based on estimates of molecular flow through a rectangular slit [71] and, therefore, was acceptable. Also, we did not notice any arc attachment or plasma near the interface during the experiments.

3.5 Lithium Physical Properties

Many physical properties that are usually neglected in experimental design of a gas discharge apparatus must be taken into account when utilizing a metal vapor. The controlled evaporation of a metal, which is solid at room temperature, requires operating components

of the apparatus at both the melting and boiling points. Also, stabilizing the evaporation point to maintain a constant and known flow rate requires an understanding of the surface tension, capillary forces, thermal conductivity, and vapor pressure of the liquid. In this section, we present the relevant lithium properties in the context of the experimental apparatus design.

3.5.1 Vapor Pressure

Lithium is an alkali metal that is solid with a silvery appearance below its melting point of 180°C . The boiling point within the liquid phase depends on the total pressure and on the partial pressure of the lithium vapor phase at the liquid/vapor interface. The pressure within the liquid phase must always be less than the lithium vapor pressure (at the local temperature) or lithium “bubbles” will form, changing the density of the lithium and making it impossible to accurately know the mass flow rate. The pressure of the liquid phase can be greater or less than the total gas pressure at the liquid/vapor interface depending of the capillary pressure, which is described below. Lithium will evaporate from the liquid/vapor interface if the lithium partial pressure is less than the vapor pressure. The rate of evaporation depends on power available for evaporation and the lithium vapor phase partial pressure.

The vapor pressure as a function of temperature is shown in figure 3.4. This figure is a plot of the Antoine equation [72],

$$\log_{10} p_{vp} = A_A - \frac{B_A}{T + C_A}, \quad (3.1)$$

where p_{vp} is the vapor pressure in bar, A_A , B_A , and C_A are the Antoine coefficients, and T is the temperature in Kelvin. The coefficients are determined by a fit of experimental measurements to equation (3.1). The coefficients for lithium are: $A_A = 4.98831$, $B_A = 7918.984$, $C_A = -9.52$ [73]. Since the facility pressure is 1×10^{-5} Torr, evaporation

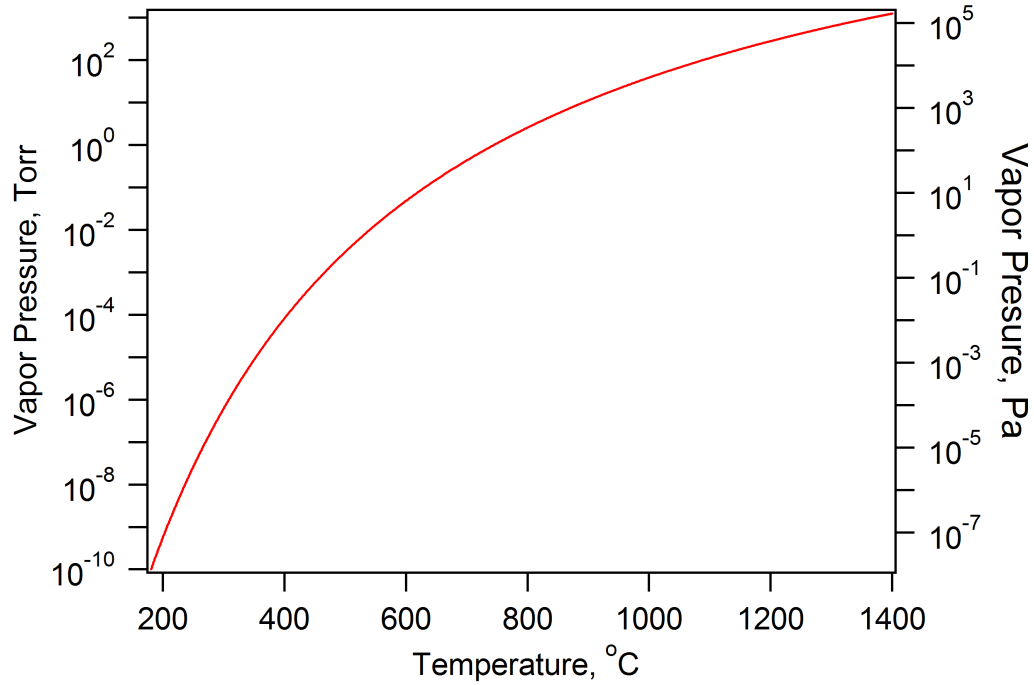


Figure 3.4: Vapor pressure of lithium as a function of temperature.

can occur at temperatures as low as 400°C and possibly even lower if the capillary effect reduces the pressure within the liquid.

The vapor pressure curve also shows that lithium condenses on cool surfaces. Lithium will condense on surfaces at a greater rate than it evaporates if the vapor pressure associated with the temperature of the surface is less than the partial pressure of the lithium. Lithium will coat the walls and optical access ports since they are kept near room temperature, therefore, special apparatus must be utilized to maintain optical access, as described in section 3.8.

3.5.2 Thermal Conductivity

Small channels were utilized in the tube at the lithium evaporation point so that thermal conduction through the lithium and the tube was appropriately controlled. A large temperature gradient should exist along the tube wall that transports the lithium in order to maintain

a stable evaporation point at low mass flow rate. The temperature should vary from well below to much greater than the evaporation temperature within a few millimeters. If the liquid lithium were to conduct large amounts of heat upstream of the liquid/vapor interface compared to that of the tube walls then an instability could develop and it would become difficult to control the location of the evaporation point. Therefore, the thermal conduction along the tube walls must be greater than that possible through the liquid lithium.

The thermal conductivity of liquid lithium varies from 40 to 60 $\text{W}\cdot\text{m}^{-1}\text{K}^{-1}$ in the range from the melting point to the boiling point at atmospheric pressure [74]. The thermal conductivity of stainless steel is approximately 20 $\text{W}\cdot\text{m}^{-1}\text{K}^{-1}$ at elevated temperatures [75]. The power conducted along a temperature gradient is

$$P_{c,v} = A_{xs} k_{th} \frac{\Delta T}{\Delta x}, \quad (3.2)$$

where A_{xs} is the cross-sectional area, k_{th} is the thermal conductivity, and $\frac{\Delta T}{\Delta x}$ is the temperature gradient. Since we desire the power conducted by the lithium to be much less ($\frac{1}{10}$) than that conducted by the stainless steel tube that must have an equal temperature gradient, the ratio of the cross-sectional areas can be calculated from

$$\frac{P_{c,v}^{Li}}{P_{c,v}^{SS}} = \frac{A_{xs}^{Li} k_{th}^{Li}}{A_{xs}^{SS} k_{th}^{SS}} < \frac{1}{10}, \quad (3.3)$$

where the superscripts Li and SS represent lithium and stainless steel, respectively. Therefore, the area ratio is

$$\frac{A_{xs}^{Li}}{A_{xs}^{SS}} < \frac{1}{10} \frac{k_{th}^{SS}}{k_{th}^{Li}} \approx \frac{1}{30}. \quad (3.4)$$

Using equation (3.4), the ideal channel size at the evaporation point was determined to be 1 mm for the 1/4" (6.35 mm) outer diameter tubes utilized in our experiment.

3.5.3 Surface Tension and Capillary Effect

The lithium evaporation point must be located in very small channels, as shown above, and, therefore, the capillary effect will be significant at that location. The capillary effect depends on the lithium surface tension, wetting of the channel wall, and channel radius. The capillary effect causes a pressure difference across a liquid/vapor interface created by surface tension and a curved meniscus. The difference between the pressure of the liquid phase, p_l , and the vapor phase, p_v , is proportional to the total curvature of the interface itself. For a spherical meniscus, this can be written as

$$p_v - p_l = \frac{2\gamma_t}{r} \cos \theta_c, \quad (3.5)$$

where γ_t is the surface tension of the liquid, θ_c is the contact angle with a surface, and r is the channel inner radius at the interface. If the contact angle is less than 90° (the liquid “wets” the tube walls), the liquid phase pressure is less than the pressure of the vapor. Lithium tends to wet tungsten [76], molybdenum [77, 78], and stainless steel [79] at high temperature, but the exact value of θ_c is not known. We assume the smallest possible contact angle ($\theta_c = 0$), which corresponds to full wetting of the surface. The pressure change at the interface is, therefore,

$$p_v - p_l = \frac{2\gamma_t}{r}. \quad (3.6)$$

The surface tension varies linearly with temperature from the melting point to the boiling point at atmospheric pressure, 0.4 to 0.2 N/m [74], respectively. The capillary pressure, assuming a mean value of 0.3 N/m, is shown in figure 3.5. For a 0.5 mm radius channel the capillary pressure is approximately 1200 Pa (10 Torr). Of course, the pressure cannot be negative in the liquid, so if the vapor’s pressure is less than capillary pressure the liquid

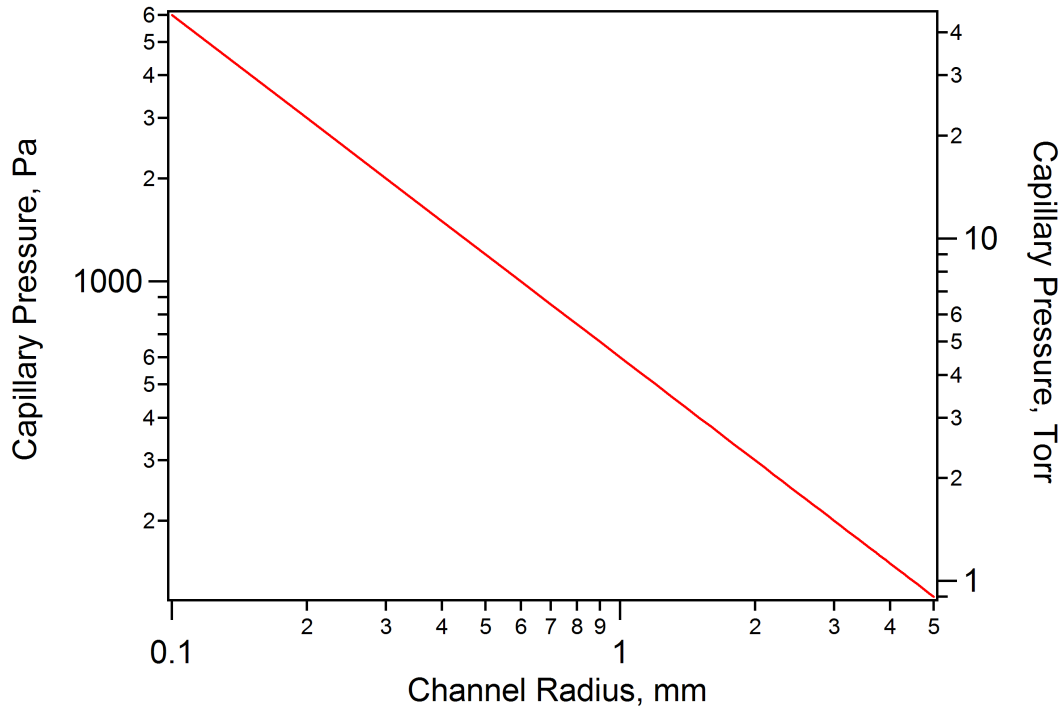


Figure 3.5: Pressure difference at a lithium liquid/vapor interface.

will boil. Therefore, the liquid's pressure must be greater than p_{vp} in order to maintain evaporation only at or near the interface.

The total pressure on the liquid/vapor interface must be greater than 10 Torr to overcome the capillary force. Since the facility pressure is 1×10^{-5} Torr, see section 3.2, at low flow rate, the pressure on the interface must be developed by constricting the vapor flow. The lithium vapor flow constriction, explained in section 3.7, ensures a pressure of lithium vapor that is greater than 20 Torr.

Since the partial pressure of lithium on the exposed liquid surface must be approximately 10 Torr, the temperature at the evaporation point can be determined utilizing the vapor pressure curve for lithium shown in figure 3.4. It can be seen that the lithium evaporator must operate at temperatures greater than 900°C .

To be conservative, it is desirable to maintain the vapor pressure of the liquid lithium in the feed system below the facility pressure, which corresponds to a maximum temperature of 375°C . The temperature of the feed system is kept below that of the evaporator by a ther-

mal control bar (see figure 3.7), which ensures heat from the evaporator is not conducted to the feed system.

3.5.4 Compatibility and Contamination

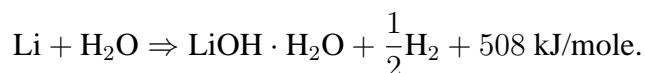
All aspects of experiment design and operation were affected by the necessity of keeping the lithium uncontaminated prior to use and the compatibility of lithium with any component it could contact, including the feed system and all exposed surfaces within the facility. Most importantly, lithium reacts strongly with water vapor and nitrogen in the air, making contamination before and during an experiment a concern. For this reason, lithium was continuously protected by an inert cover gas or vacuum. The procedures used to ensure uncontaminated lithium are outlined in the following subsection.

The concerns regarding lithium contact with facility components were: difficulty of cleaning, loss of electrical insulation by surface coatings or reactions, and material decomposition due to chemical reactions. Since the facility was exposed to small amounts of lithium vapor (less than 300 g over the entire facility) and most components were actively cooled, chemical reactions were not usually a concern. Aluminium and copper components at temperatures of hundreds of degrees Celsius react strongly with lithium and decompose, so those components were actively cooled to reduce the reaction rate. All hot components were made from stainless steel or refractory metals to eliminate this problem. The electrical insulation properties of alumina are greatly reduced by the reaction with and coating of the surface with lithium, therefore, alumina insulators were shielded or removed from the lithium vapor. Boron nitride maintains its electrical properties, but slowly decomposes when exposed to lithium at high temperatures. Therefore, it was used as the insulator of the Langmuir probe.

3.5.5 Lithium Handling and Safety

An extensive review of lithium handling and safety procedures identified the major hazards of operation to be: the handling of the pure lithium metal at room temperature during loading and transfer of the reservoir; the cleaning and disposal of lithium reaction products in the feed system and the testing facility; and the release of potentially hazardous gases, especially hydrogen, during facility venting and cleaning.

The hazards of lithium operation can be divided into two classes; 1) fire or explosion hazards due to the high reactivity of lithium; 2) the production of hydrogen during reactions with water and health hazards due to the corrosive and cancerous nature of the stable end products of lithium reactions. The first hazard was addressed through the controlled reaction of lithium with water, which is represented as



The buildup of hydrogen gas byproduct during lithium loading and cleaning, which is an explosion and fire hazard, was controlled with well ventilated facilities and proper hydrogen detection. The heat released was eliminated by a circulating water bath, which also controlled the reaction speed. The corrosive lithium hydroxide solution was handled with nitrile gloves and collected for proper disposal.

The 150-350 g lithium billets utilized in the experiments were individually packaged in argon by the supplier for ease of loading into the feed system. Special procedures and equipment were developed to get the lithium from the package into the lithium feed system [80]. The package was opened and placed in the feed system by hand, requiring a positive pressure argon environment in a glove box. The glove box, designated the Lithium Handling Facility (LiHF), consisted of an extensively re-conditioned 0.5 m³, stainless steel Blickmann glove box with a baseline facility pressure of less than 6.7 Pa (50 mTorr). The package of lithium was opened in an argon atmosphere and the billet was placed in the

reservoir. Argon flow through the reservoir was maintained as the reservoir was transferred from the LiHF to the LEF as well as while the facility was pumped down.

Once lithium was released in the LEF, most exposed surfaces in the vacuum vessel were coated with lithium. To reduce the effort of facility cleaning, the actively cooled chamber walls were covered by aluminum foil using magnets, as described in section 3.2. The thermal contact provided by the magnets maintained a low foil temperature and thus pumped lithium from the facility very effectively. Before venting the chamber, the pure lithium was reacted with water to create LiOH, which is less hazardous than the lithium nitride that would result from direct exposure to air. The incremental addition of small amounts of water controlled the reaction rate. Reaction gases were eliminated prior to opening the facility by pumping the facility after neutralization. To protect operators from any remaining hazardous gases, and also from inhaling the corrosive and toxic dust from the lithium reaction products, breathing apparatus gear was worn by operators during tank inspection and cleaning. Cleaning consisted of removing and disposing of the aluminum foil, vacuuming out any LiOH dust, and then scrubbing any surfaces that were exposed to lithium with paper towels and water. The feed system was soaked in water until the lithium dissolved.

3.6 Lithium Feed System

A mechanically-driven feed system controlled the mass flow rate of lithium [80]. It supplied liquid lithium to the vaporizer assembly, which is described in section 3.7. Flow was effected by the controlled movement of a piston within the cylinder filled with lithium. A servo motor and controller set the piston speed and allowed for continuous feedback of speed and position as the lithium was fed to the cathode. The lithium mass flow rate was directly proportional to piston speed and was verified by calibration. The ratio of mass flow rate to piston speed was determined to be 816 ± 17 mg/mm. Flow rates of 0.2-120 mg/s

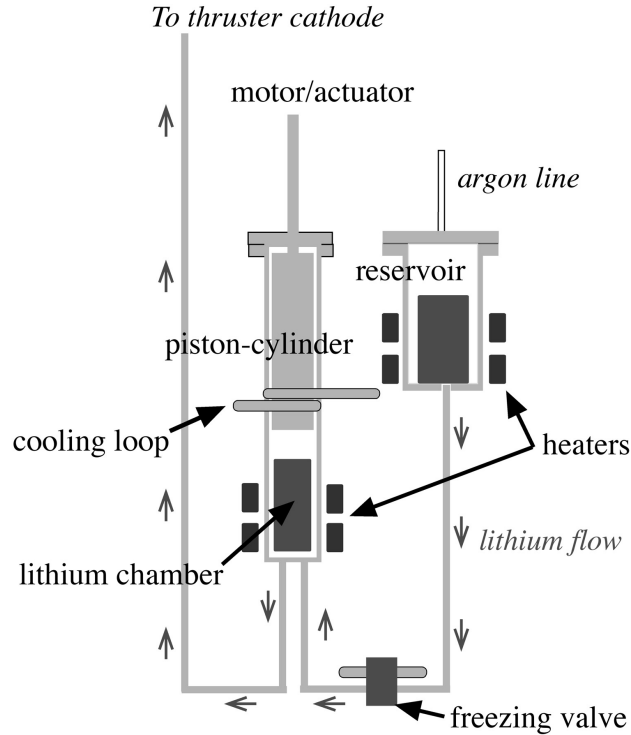


Figure 3.6: The lithium feed system.

were achievable with an error of 1% when averaged over a few minutes.

A schematic of the system is shown in figure 3.6 with arrows indicating the path of lithium flow through the system. Solid lithium was loaded into the vacuum facility under argon via the leak-tight reservoir. Under vacuum, the lithium was melted and fed into the cylinder via gravitational forces. Chilled water flowing through the freezing valve solidified the lithium within the feed system at that point, which formed a plug, and prevented back-flow to the reservoir during experimental operation. A chilled-water loop on the outside of the cylinder at the piston location prevented leakage during feeding. Liquid lithium temperatures were maintained between 200 and 350°C during operation.

3.7 Lithium Evaporator

The evaporator, shown in figure 3.7, had two functions; to evaporate lithium at a rate equal to the rate lithium flowed into it and to provide a mount for the cathode, which is presented

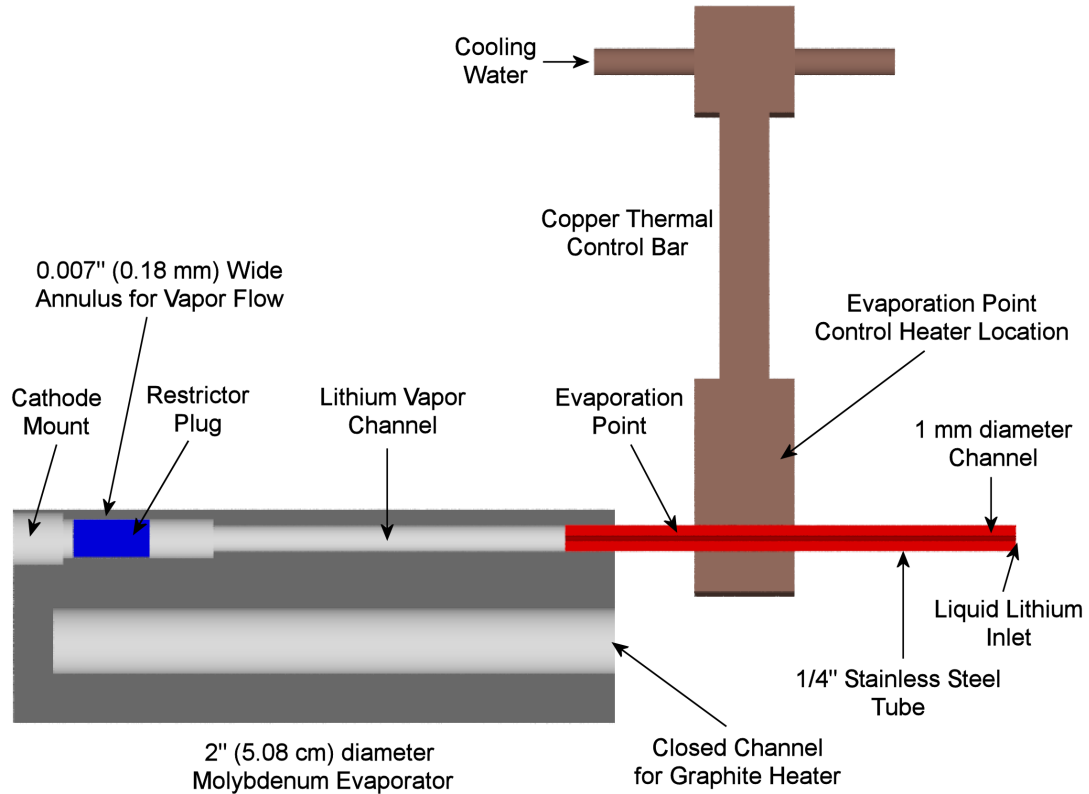


Figure 3.7: Schematic of the lithium evaporator.

in section 3.4.4. The evaporator was operated at approximately 1100°C to ensure that the evaporation point temperature was greater than 900°C . The temperature was maintained by a 1.3 kW graphite heater located within the evaporator, which was chosen because of our experience with such heaters and the limited availability of resistive heaters that operate at 1100°C .

Within the evaporator, heat must be conducted to a stable evaporation point from the heater. The evaporator must be constructed from a material that possesses a large enough thermal conductivity to maintain its temperature above the evaporation temperature, but not melt near the heater. Lithium has a high heat of evaporation [21200 kJ/kg or 21.2 W/(mg/s)], which requires a large amount of power to be delivered to the small evaporation point. Since the temperature must be above 900°C at the evaporation point and it must contact lithium, there are only a few materials to choose from: stainless steel, molybdenum, tungsten, and tantalum. Tungsten, tantalum, and stainless steel are not viable

options because of either machinability issues, poor conductivity, or the possibility of melting near the heater. Therefore, molybdenum, with a high melting temperature (2896 K) and thermal conductivity ($139 \text{ W}\cdot\text{m}^{-1}\text{K}^{-1}$), was chosen for the lithium evaporator material.

There must be a region of high temperature gradient at the interface between the liquid lithium feed system and the evaporator in order to maintain a stable evaporation point. The liquid lithium was supplied to the cathode in a 1/4" (6.35 mm) outer diameter tube with an inner diameter of 1 mm. Thermal control of the stainless steel tube was maintained with a copper bar clamped approximately 1 cm from the evaporator. The copper bar was chilled at the end furthest from the tube by the closed-loop water system and heated at the other end with a resistive heater, called the evaporation point control heater. By controlling the temperature at the heated end of the copper bar near the tube, we insured that the evaporation point was stable at the tube/evaporator interface.

The pressure of lithium vapor at the liquid/vapor interface was maintained above 10 Torr for all steady-state operating conditions, as explained in section 3.5.3. We chose to address this problem by adding a restriction in the vapor flow between the evaporation point and the cathode that increased the pressure. The restriction was made by a 25 mm long plug in the lithium vapor channel, which had a 3/8" diameter, that was undersized by 0.18 mm on the radius around most of the circumference. There were 3 lengthwise strips on the outer radial surface that gave the plug an overall 3/8" outer diameter so that it was pressure fit into the channel and, yet, still had a mostly open annulus for lithium to flow through. An annulus configuration was chosen because it was easy to manufacture and had a low chance of clogging. Using the theory of molecular flow through a rectangular cross section (because the annulus width is much smaller than its radius, this is a good approximation), it can be shown that the pressure difference from one side of the restriction to the other at the lowest flow rate (0.2 mg/s) and pressure (2 Torr) was 18 Torr. The Knudsen number, described in section 5.1, is 0.1, which indicates that the flow was transitional and that the pressure difference was actually somewhat lower, but still greater than 10 Torr.

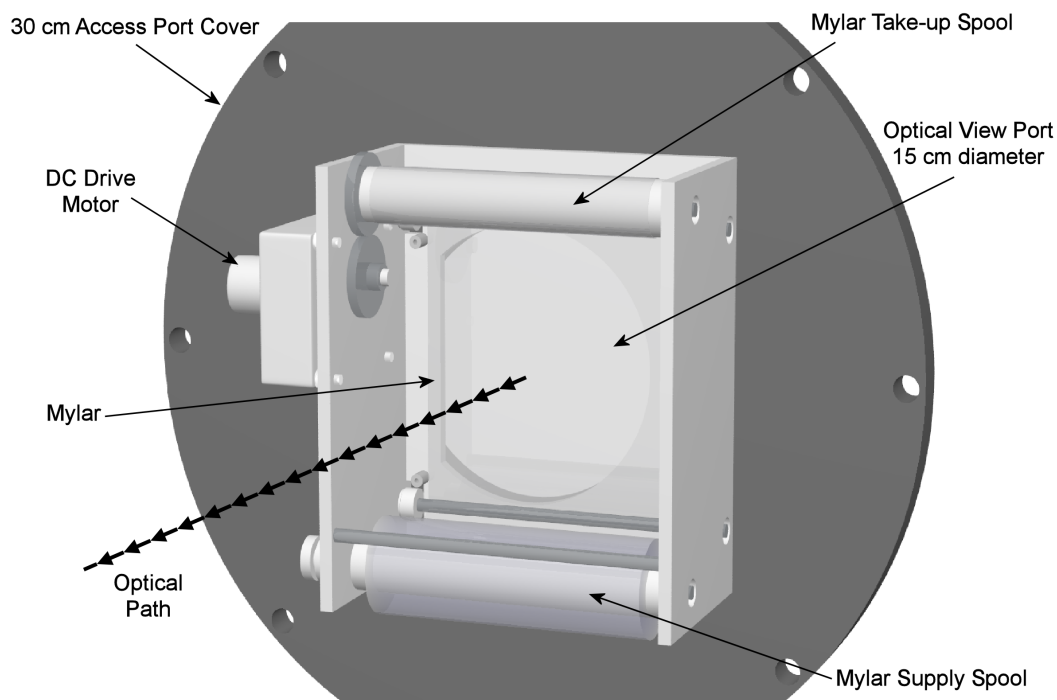


Figure 3.8: Schematic of continuous-film apparatus.

3.8 Optical Access

It is particularly difficult to maintain optical access through the view ports because lithium condenses on all surfaces below 1100°C. Two methods were employed to combat lithium deposition on optical ports: (1) a film of mylar placed inside the facility, near the optical port was continually replaced with new film and (2) an argon gas barrier was located within the volume in front of the port.

Method 1 is called the *continuous-film* method. The concept was based on the tear-away plastic coverings that NASCAR drivers wear on their visors. Mylar was selected based on its ability to survive contact with small amounts lithium vapor and transmit optical wavelengths. Measurements with a spectrometer demonstrated that the light (300 to 850 nm) was uniformly transmitted through the mylar. A long roll of film was used with the short dimension just wider than the optical port diameter (15 cm). The long dimension was determined by the length of film that could be wrapped around the spool that held it,

approximately 15 m. The virgin film was pulled from one spool onto a second spool that was connected to a DC motor, shown in figure 3.8. The rate of film travel was set by the voltage applied to the motor. We determined lithium coverage by visual inspection and adjusted the speed as necessary. Normally, the lowest possible rate (approximately 1 cm/s) of film motion was sufficient to limit lithium coverage.

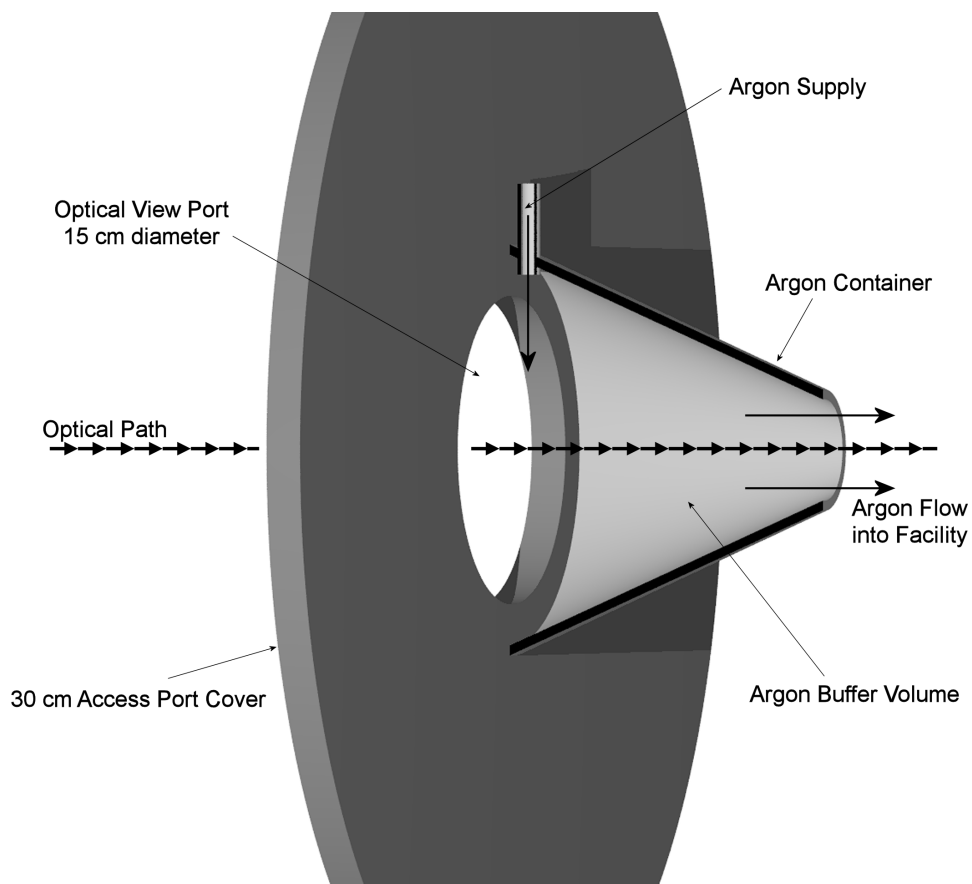


Figure 3.9: Schematic of the argon gas barrier method apparatus.

Method 2, or the *argon gas barrier* method, works by blocking the flux of lithium toward the view port through collisions with argon gas. A volume of relatively high pressure argon was located along the optical path inside the facility, shown in figure 3.9. The view port was located at one end of the volume and an opening just large enough to allow full view of the experiment was located at the other end (4 cm diameter). The argon carried the lithium from the volume and nearly eliminated the lithium coating on the view port. The

mean free path of the lithium traveling through argon can be calculated from

$$\lambda_{Li} = \frac{1}{\pi n_{Ar} \delta_{Li-Ar}^2 \sqrt{1 + (m_{Li}/m_{Ar})}}, \quad (3.7)$$

where $\delta_{Li-Ar} = (\delta_{Li} + \delta_{Ar})/2$ is the common diameter of interacting atoms and m_{Li}/m_{Ar} is their mass ratio [81]. To keep the lithium that enters through the open end from reaching the optical port the mean free path must be much less than the length of the argon container (20 cm), we take to be $\lambda_{Li} = 2$ cm. The density must be $1.1 \times 10^{20} \text{m}^{-3}$ (0.44 Pa or 3.3 mTorr), assuming $\delta_{Li} = 3.64 \text{ \AA}$, $\delta_{Ar} = 3.76 \text{ \AA}$ [82, 83], and $m_{Li}/m_{Ar} = 0.174$. Since the argon was flowing out of the opening into the chamber, the lithium was carried away from the optical port once it thermalized with the argon. The conditions described above resulted in a mass flow rate of argon of 0.4 to 1 mg/s. This apparatus allowed operation for tens of hours without noticeable contamination of the optical view port and the argon did not influence the experiment.

3.9 Power Systems

Since thermal control is effected through external heating of the different components of the feed system and evaporator, many power supplies are required to independently maintain the required temperatures.

Lithium Feed System Three variable voltage transformers (Variacs) supply AC power (one 1.0 kVA and two 1.4 kVA) to heat the three components of the feed system: the reservoir, piston-cylinder, and liquid lithium feed lines. The voltage was controlled by the experimenter to maintain the desired temperatures in open-loop control.

Evaporator Heater A current-controlled DC power supply manufactured by Rapid Power supplied 1.3 kW at approximately 115 A was used to maintain the evaporator temperature. The current was controlled by the experimenter and the operational parameters

were recorded by the data acquisition system.

Evaporation Point Control Heater The evaporation point control heater was controlled with a variable voltage transformer that could supply 1.4 kVA AC power.

High Current Arc Discharge A Miller constant current welding power source with the capability of 40 kW at up to 1000 A was utilized for the discharge. The voltage and current were recorded by the data acquisition system.

Low Current Arc Discharge An Electronic Measurements Incorporated current-limited power supply was utilized at currents less than 50 A. The voltage and current were recorded by the data acquisition system.

3.10 Data Acquisition System

The voltages, currents, and feed system temperature measurements were continuously recorded with a National Instruments analog to digital data acquisition system, which was controlled by a LabView VI. SCXI-1303 and SCXI-1300 modules multiplexed up to 32 thermocouple and voltage measurements each, respectively. Those measurements were routed through an SCXI-1000 chassis to an analog to digital converter housed in a G4-PowerMac. The actuator that effected the lithium mass flow rate was also controlled by the LabView VI. Data were recorded approximately once per second. The data from the other diagnostics were recorded separately and are discussed in their respective sections.

3.11 Diagnostics

A set of diagnostics were chosen to measure the independent operational parameters of cathode temperature profile, plasma potential at the cathode tip, and discharge voltage as well as the controlled settings of current and mass flow rate. Measurements of the cathode

temperature profile with the multi-color video pyrometer (MCVP) give both the peak temperature and penetration depth, as discussed in section 3.11.3. The cathode voltage drop was determined by measurement of the plasma potential with a Langmuir probe (see section 3.11.2) and the electron temperature near the cathode tip via emission spectroscopy (see section 3.11.4). The measurement of discharge current and total voltage is described in section 3.11.1.

3.11.1 Current and Total Voltage Measurement

Current was measured with a calibrated shunt resistor or a Hall-effect current sensor, the output of which was directly recorded by the data acquisition system during the experiment. A F.W. Bell closed-loop hall effect sensor (model QB-1687) was utilized at high current (>50 A), while a calibrated shunt-resistor was utilized at low current.

The total discharge voltage was measured with a 100:1 voltage divider. Oversized (4-0000 gauge) wires limited the voltage drop in the electrical conductors between the voltage divider, which was located outside of the chamber, and the cathode. The total voltage and current values for an experimental data point were determined from the average of at least one minute of data while the discharge was stable.

3.11.2 Langmuir Probe

A Langmuir probe was used to measure the floating potential relative to cathode ground near the cathode tip. While the probe survived when at the floating potential, it would have likely melted when biased due to the high plasma density. The Langmuir probe was a 0.01" tungsten wire with approximately 2 mm exposed at the tip of a boron nitride tube. The voltage was recorded with an oscilloscope for 20 s at 250 samples per second at each data point. The floating potential was determined as the average of that data.



Figure 3.10: A picture of the MCVP.

3.11.3 Multi-color Video Pyrometry

Pyrometry is based on the fact that all surfaces at temperatures above absolute zero emit thermal radiation. Planck's radiation law, modified to include surface emissivity, is the fundamental relation of thermal radiation:

$$I(\lambda, T) = \epsilon_{\lambda} \frac{C_1}{\lambda^5} \left(\frac{1}{e^{\frac{C_2}{T\lambda}} - 1} \right), \quad (3.8)$$

where I is the intensity, ϵ_{λ} is the emissivity, $C_1 = 1.191 \times 10^{16} \text{ W} \cdot \text{nm}^4 \text{cm}^{-2} \text{Sr}^{-1}$ and $C_2 = 1.4384 \times 10^7 \text{ nm} \cdot \text{K}$ are the first and second radiation constants, T is the absolute temperature in Kelvin, and λ is the wavelength of the radiation in nm. With knowledge of the emissivity, the temperature of any surface can be determined by fitting the intensities measured at various wavelengths to the above relation. We will take $\epsilon_{\lambda} = 0.44$, since the emissivity of tungsten is well known in the visible wavelengths at the temperatures we measured in our experiments [84].

The multi-color video pyrometer (MCVP), shown in figure 3.10, is a diagnostic developed at EPPDyL to measure the temperature of hot surfaces. The MCVP records the radiated intensity of a surface at four wavelengths (404.7, 514.5, 632.8, and 694.3 nm) on a single CCD. A single image is split with a prism to create four images that are passed

through narrow bandpass filters and focused on the CCD. An analysis routine then matched each pixel of the four images to the same location on the surface. The intensity of the pixels are fit to Planck's Law (equation (3.8)) to determine the temperature. The use of multiple wavelengths across the visible spectrum greatly reduces the uncertainty in the temperature determination. Utilizing a CCD to record the radiation allows the temperature to be determined over the entire surface.

To reduce the error in intensity measurements, data from ten images were included in the temperature determination routine. This technique is valid because the experiments were steady-state. The $\pm 50^\circ\text{C}$ uncertainty of the temperature was dominated by limitations of the calibration equipment. The MCVP was calibrated with a tungsten ribbon lamp and a separate optical pyrometer, which were calibrated by NIST.

3.11.4 Emission Spectroscopy

The plasma electron temperature, T_e , in the inter-electrode space, near the cathode tip, was measured through emission spectroscopy. This diagnostic was not used at every operating condition because it required 15 to 20 minutes to measure the intensity at all wavelengths, which consumed a large amount of lithium and mylar film.

Spectrometer and Camera

The spectrometer used in these observations was a Spex model 1702, which has a 0.75 m focal length and a grating of 1200 grooves/mm and was optimized for use in the visible (300 to 800 nm) range. The spectrometer grating was driven by a stepper motor, which was controlled by a Spex CD2A Compudrive system.

The camera used in these observations was a Princeton Instruments model ICCD-576 image-intensified CCD camera. A Princeton Instruments ST-138 Detector Controller served as the interface between the camera and the data collection PC. The camera was water-cooled to reduce thermal noise and was also flushed with dry nitrogen to prevent

water condensation.

Optics

A simple optical setup redirected light from the plasma location to the spectrometer. A mirror on a two-axis tilt stand and a single lens were positioned to image the plasma onto the entrance slit of the spectrometer. The internal spectrometer optics were configured such that any image falling on the entrance slit was also in focus on the detector at the exit slit.

Technique

The technique for analyzing spectroscopic data was taken from Markusic [85], who followed Griem [86]. The plasma was assumed to be optically thin, be in local thermodynamic equilibrium (LTE), and to have a depth d_o . The plasma can be considered to be LTE if the collisions dominate over radiative transitions. A rule-of-thumb for this condition is [87]

$$n_e \gg 10^{19} \sqrt{\frac{k_B T_e}{e}} \left(\frac{k_B (E_m - E_n)}{e} \right)^3, \quad (3.9)$$

where the electron number density is in m^{-3} and $(E_m - E_n)$ is the energy difference between levels m and n . The line radiation that was measured corresponded to a maximum energy level difference of 3 eV and the electron temperature at the tip of hollow cathodes can be estimated as 0.5 eV [38, 26]. This corresponds to $n_e \gg 2 \times 10^{20} \text{ m}^{-3}$. As we show in chapter 5, the ion pressure just inside the cathode tip is approximately 1 Torr, or $3 \times 10^{21} \text{ m}^{-3}$ (at 3000 K). The pressure external to the cathode will be much less than the internal pressure as the plasma expands into the vacuum facility, but likely not less than one order in the region immediately downstream of the cathode tip. Therefore, the electron density was slightly greater than the density specified by the rule-of-thumb relation and could be great enough to allow for the use of emission spectroscopy. The ultimate justification for the appropriate use of emission spectroscopy is that the experimental data (shown in appendix C) followed the trends predicted by the theory presented in this section.

The intensity of the emitted radiation due to the transition from energy level m to n , i_{nm} , is given by,

$$i_{nm} = \frac{\hbar\omega_{mn}}{4\pi} A_{nm} N_m d_o, \quad (3.10)$$

where ω_{mn} , A_{nm} , and N_m are the frequency of the emitted radiation, the transition probability coefficient, and the population of the m^{th} state, respectively, and \hbar is Planck's constant divided by 2π . Also, the plasma was assumed to be in local thermal equilibrium. Therefore, the population of the m^{th} energy level is described by the Boltzmann distribution,

$$\frac{N_m}{N_t} = \frac{g_m}{Z_a} \exp\left(\frac{-E_m}{k_B T_e}\right), \quad (3.11)$$

where k_B , N_t , g_m , E_m , Z_a are the Boltzmann constant, the total population, the degeneracy of the m^{th} state, the energy of the initial level, and the partition function, respectively. Combining equations (3.10) and (3.11) we find a linear equation of the form $y = ax + b$,

$$\ln\left(\frac{i_{nm}}{\omega_{mn} A_{nm} g_m}\right) = \frac{-1}{k_B T_e} E_m + \ln\left(\frac{\hbar N_t l}{4\pi Z_a}\right). \quad (3.12)$$

Using this equation, spectral line intensities can easily be used to determine electron temperature. E_m , ω_{mn} , A_{nm} , and g_m are known to a fair degree of accuracy for the lighter elements, including lithium [88, 89]. Thus, by measuring the intensities of the spectral lines of a plasma and using the known constants,

$$y = \ln\left(\frac{i_{mn}}{\omega_{mn} A_{mn} g_m}\right) \quad (3.13)$$

[from equation (3.12)] can be found as a function of E_m . The slope of the line fit to those data is $-\frac{1}{k_B T_e}$, from which electron temperature is easily obtained. Note that, given absolute intensities, the number density of the plasma could also be determined from the y -intercept of this line. Due to the problems with obtaining accurate absolute intensities, however, in most cases this is prohibitively difficult. In this study, only relative intensities

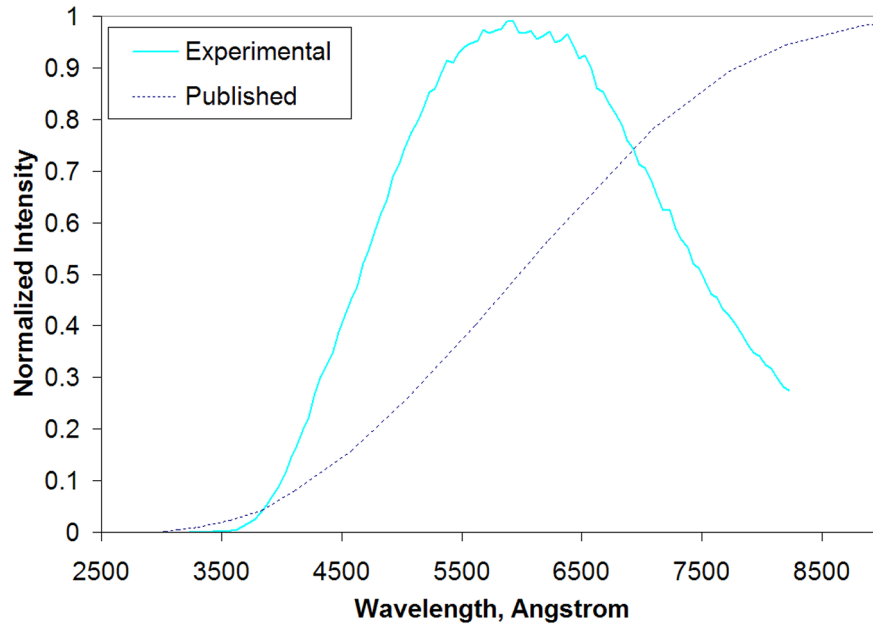


Figure 3.11: The measured and published intensity curves.

were obtained, and so only the slope of this line could be used.

Calibration

The spectrometer was calibrated for wavelength measurements so that the acquired measurements could be unambiguously correlated with tabular data. Wavelength calibration involved verifying that the wavelength set by the controller was actually what was measured at the center of the CCD. A mercury-argon Geisler tube and a HeNe laser were used in the wavelength calibration. These light sources have very narrow emission lines, allowing each line to be imaged on a single column of pixels.

The intensity calibration was accomplished to determine the response of the optics and CCD as a function of wavelength to a light source with a known intensity curve. To accomplish this, an Oriel 6337 Quartz-Tungsten-Halogen lamp was placed on a fixture in the vacuum chamber at the position of the lithium arc. Measurements of intensity were recorded at wavelengths from 3000 to 8500 Å at 50 Å intervals. These data were then compared to the published intensity versus wavelength curve provided by the manufacturer

of the lamp. Figure 3.11 shows the two curves, which were combined to find an intensity calibration factor as a function of wavelength,

$$F(\lambda) = \frac{I_p}{I_m}, \quad (3.14)$$

where I_p is the published intensity function and I_m is the measured intensity. The calibration factor, $F(\lambda)$, was integrated into the data analysis and applied to all data measurements. This calibration was only of relative intensity, and no attempt for absolute calibration was made.

We also characterized the affect of the continuous film apparatus on the repeatability of intensity measurements. As described in section 3.8, a moving film passes over the window in the vacuum tank to prevent the window from being coated with lithium. This introduces an element of variability into the measurement of intensities through this window due to variations in the film thickness and angle relative to the optical path. The effect was determined by taking many intensity measurements at the same wavelength throughout the visible spectrum. With the film moving across the window, ten readings were taken at five wavelengths throughout the visible spectrum. Error was taken as the difference from the mean intensity at each wavelength, which gave a maximum error among the fifty data points of 4.33% and a mean error of 1.86%.

Chapter 4

Experimental Results and Analysis

In this chapter we present the results and analysis of lithium-fed SCHC and MCHC experiments.¹ The primary goal of these experiments was to measure the cathode temperature profile, plasma potential at the cathode tip, and total discharge voltage of SCHCs and an MCHC operated over an extended range of mass flow rates and currents. These measurements were required to determine the dependence of plasma penetration depth, cathode voltage fall, and surface temperature on current, mass flow rate, and channel diameter; important relationships that had not been completely characterized by previous research, and are required for an accurate understanding of cathode operation. Lithium was selected so that the results would be directly applicable to the LiLFA MCHC described in chapter 1.

The data collected in our experiments provided a complete understanding of SCHC operation and significant insights into MCHC operation. We found the plasma penetration depth to be a function of mass flow rate, channel diameter, and current. An increase in depth with current was measured, for the first time, over an extended range of operational conditions. Also, the peak temperature was found to depend on current and channel diameter, but not mass flow rate, even though the location of the peak temperature depended on mass flow rate. Those two findings, in addition to the plasma potential measurements, give

¹Some of the results presented in this chapter were presented at the 29th International Electric Propulsion Conference at Princeton University [90].

significant insight into hollow cathode operation, such as the plasma density at the active zone, the width of the active zone, and the conditions that determine the penetration depth. The active zone and penetration depth are described in section 1.2.1. The measured peak temperature was taken to be the active zone temperature.

The SCHC results are presented first, in section 4.1. The MCHC data are presented in section 4.2. Finally, in section 4.3, an analysis of the experimental data is presented, which includes the determination of plasma density in the active zone, the width of the active zone, and the work function.

4.1 SCHC Results

Experiments with lithium-fed SCHCs were conducted because the plasma penetration depth and cathode temperature profile were readily measurable without the additional complications of interpreting multiple channel effects. As mentioned above, the results were required to develop an understanding of the physical processes of the MCHC and SCHC. The four SCHC cathodes, shown in figures 3.3a, 3.3b, 3.3c, and 3.3d, had the following dimensions, respectively,

- 2 mm inner diameter, 0.3 mm wall thickness
- 4 mm inner diameter, 0.5 mm wall thickness
- 6 mm inner diameter, 0.5 mm wall thickness
- 8 mm inner diameter, 1.0 mm wall thickness.

They were operated at currents from 2 to 140 A and lithium mass flow rates from 0.2 to 4.0 mg/s.

4.1.1 SCHC Temperature Results

The goal of the cathode temperature profile measurements was to determine the dependence on current, mass flow rate, and channel diameter. The cathode temperature profiles were measured using the MCVP, which is described in section 3.11.3. Axial temperature profiles along the vertical midline of the cathodes, as viewed with the MCVP, were extracted from the temperature image, an example data set is shown in figure 4.1. The increase in temperature downstream of the cathode tip is due to the pyrometer being able to view a small portion of the internal surface because the MCVP was a few centimeters downstream of the cathode tip plane. From the profile, we determined the maximum temperature and its distance from the cathode tip.

We adopted the definition of penetration depth used by Delcroix [20], which is the distance from the tip to the location of maximum temperature. This is appropriate because most of the current is conducted from the hottest region due to ion bombardment of the cathode wall and thermionic electron emission being the greatest at that location. We were unable to determine from an analysis of the measured temperature profiles how far upstream of the hottest spot significant current was conducted. This is because axial thermal conduction, radiation from the plasma, and ion impact affects the heating profile in complicated ways that cannot be determined only from the temperature measurements. Therefore, the definition of penetration depth with the least amount of subjective interpretation is that it is the location of the peak temperature. In addition, our model assumes the location of the peak temperature is the axial center of the “active zone,” as described in chapter 5 and shown in figure 5.2.

The maximum temperatures measured at different mass flow rates and currents are shown for the various SCHCs in figures 4.2, 4.3, 4.4, and 4.5. The most valuable insight provided by the data is that the maximum temperature at a given current and channel diameter is independent of mass flow rate, as seen in figures 4.3 and 4.4. Based on these data we conclude that the processes in the active zone are independent of the mass flow rate, a

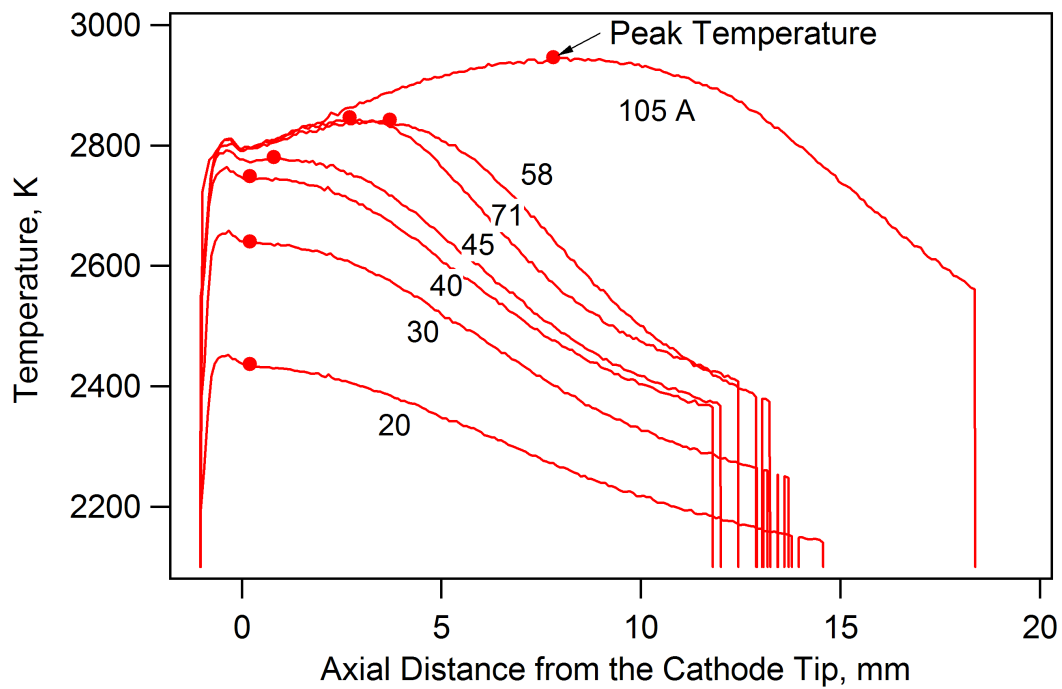


Figure 4.1: Temperature profiles of the 6 mm SCHC operating at 0.4 mg/s.

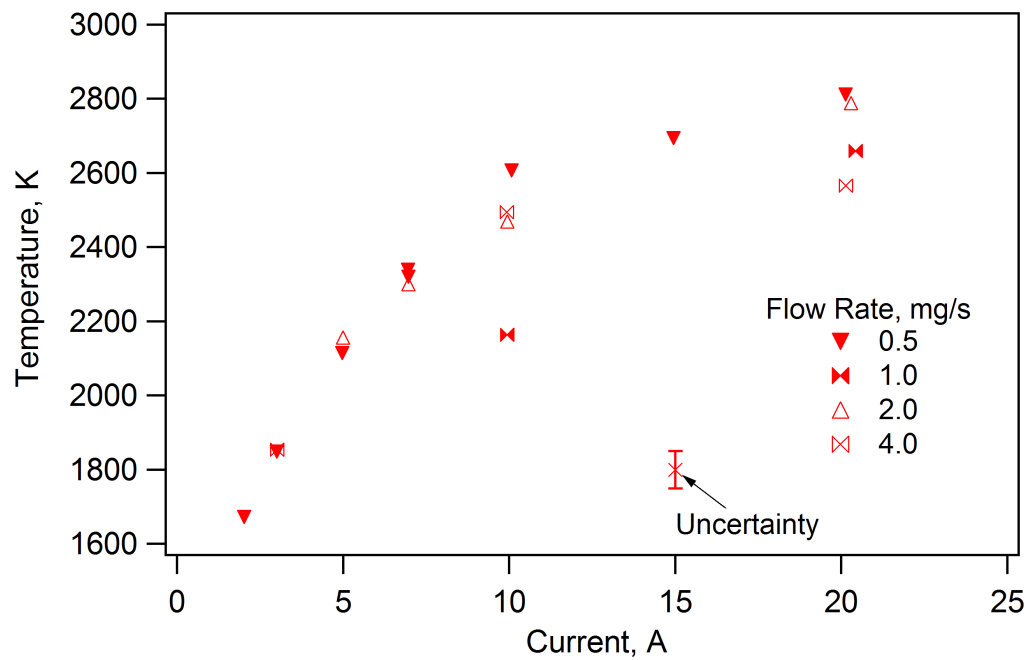


Figure 4.2: The maximum temperature of the 2 mm SCHC.

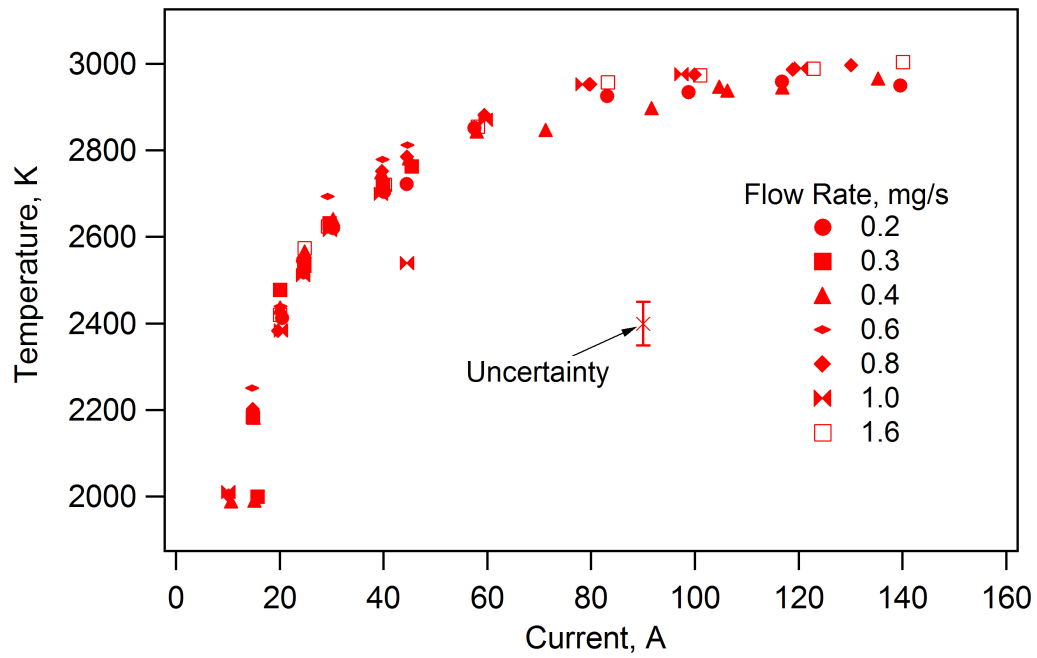


Figure 4.3: The maximum temperature of the 4 mm SCHC.

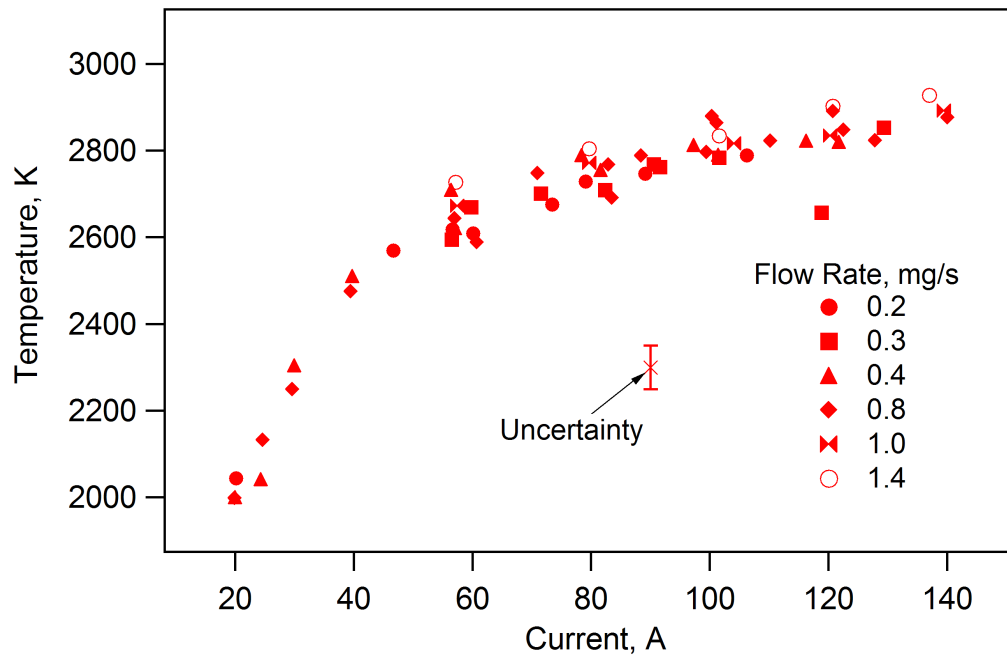


Figure 4.4: The maximum temperature of the 6 mm SCHC.

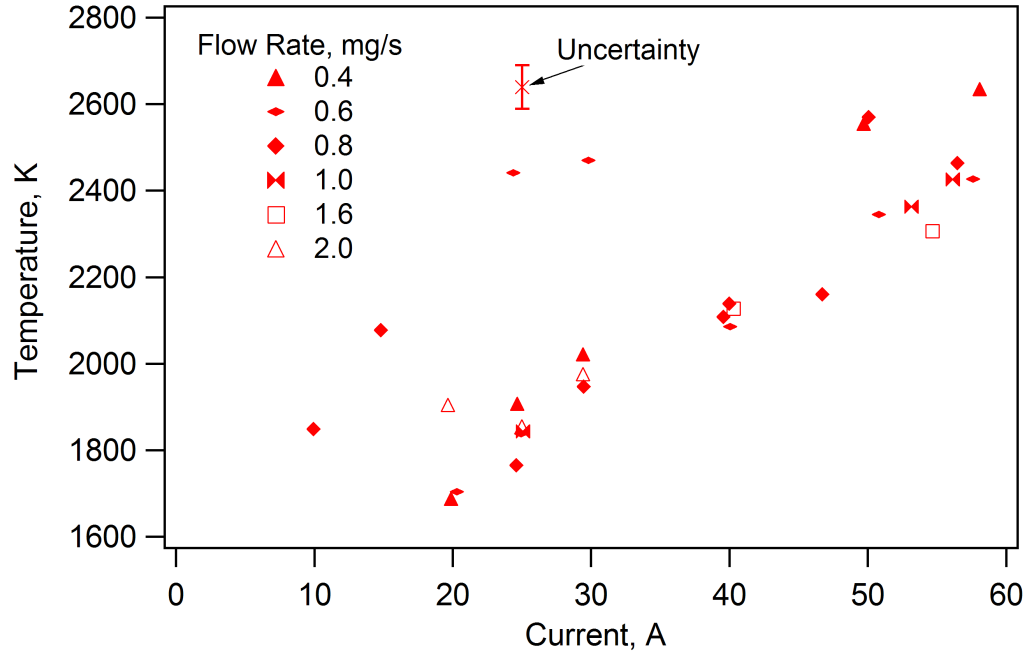


Figure 4.5: The maximum temperature of the 8 mm SCHC.

fact that will be used to physically describe that region (see section 4.3.3).

The plasma penetration depth is shown in figures 4.6, 4.7, 4.8, and 4.9, with an uncertainty of ± 0.5 mm, which was estimated from the accuracy of determining the location of the cathode tip by visual inspection of the temperature images. Generally, the penetration depth increased with current at a fixed mass flow rate and the rate of increase was inversely dependent on flow rate. The deviations from the trends in the penetration depth data can be attributed to small changes in the lithium mass flow rate. The calibration of the feed system determined that the mass flow rate averaged over many minutes was accurate to within 1%, because the calibration method averaged the total mass throughput over that period of time [80]. However, the calibration method was not able to measure variations in the flow rate on shorter timescales. The SCHC experimental results shown here suggest that at the flow rates we utilized, there could be small variations over short periods of time, since all other experimental conditions were unchanged and continuously monitored.

It was difficult to apply the 2 mm SCHC data to our study because the cathode was not operated in optimal hollow cathode mode, as indicated by the lack of plasma penetration

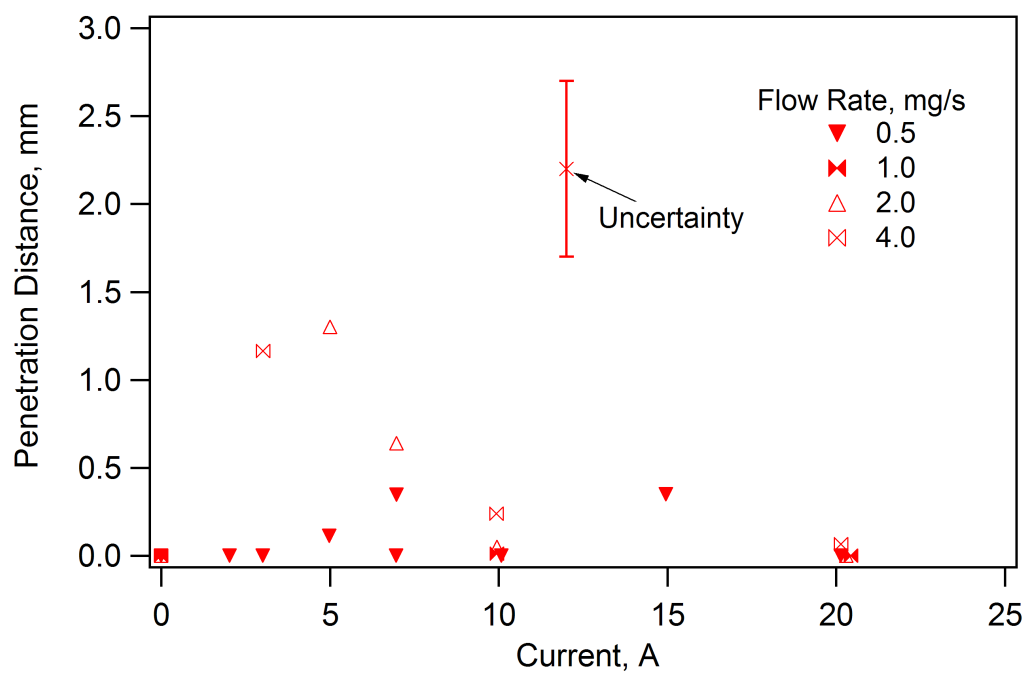


Figure 4.6: The location of the maximum temperature for the 2 mm cathode.

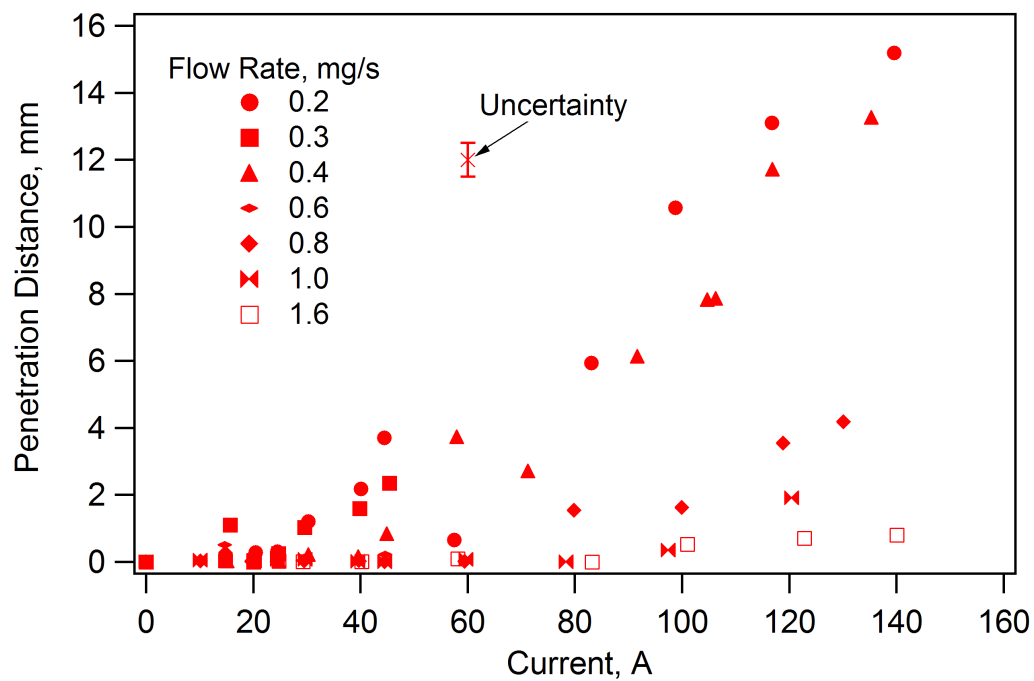


Figure 4.7: The location of the maximum temperature for the 4 mm cathode.

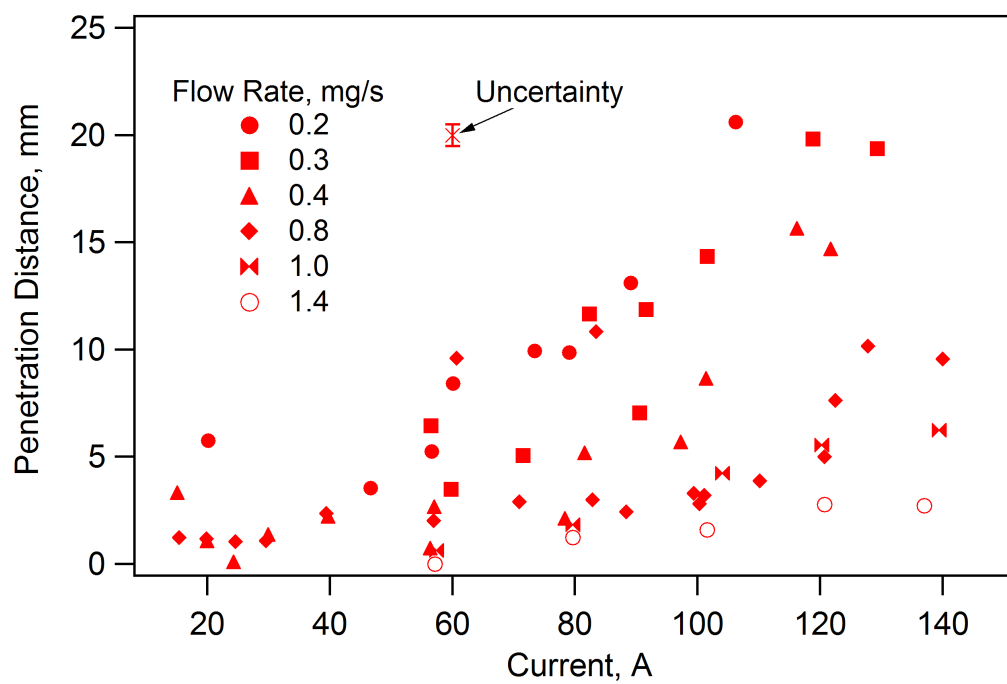


Figure 4.8: The location of the maximum temperature for the 6 mm cathode.

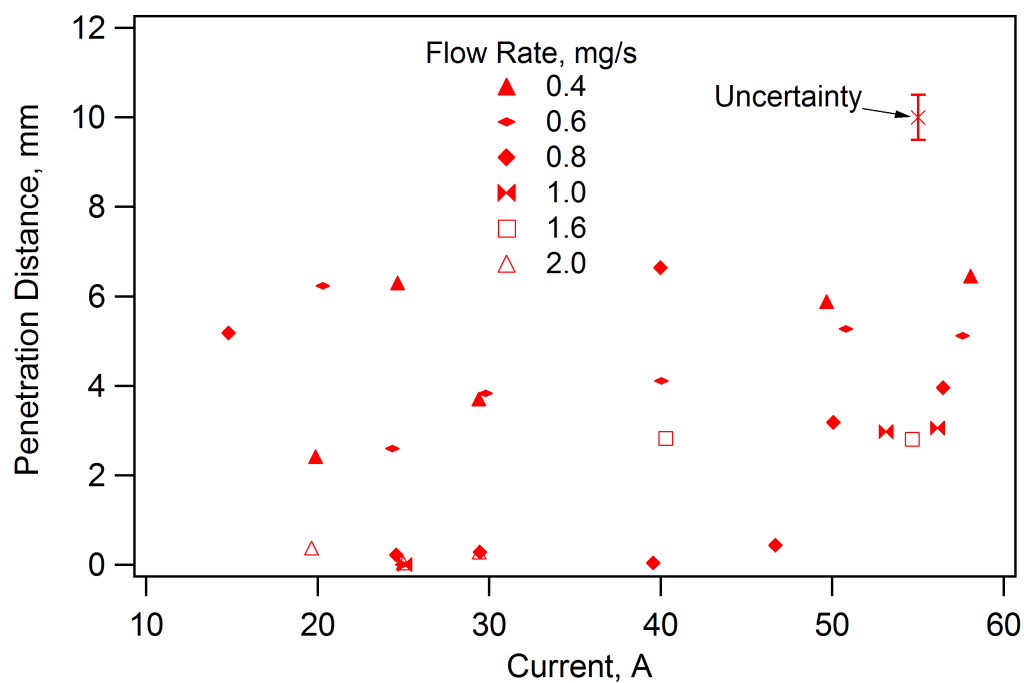


Figure 4.9: The location of the maximum temperature for the 8 mm cathode.

at high current (>10 A), as shown in figure 4.6. We did not operate at greater currents because, at the time of this experiment (our first successful one), we were wary of operating at higher power. Unfortunately, other constraints did not allow us to re-visit the 2 mm SCHC. However, at low current, we did measure penetration, but this was most likely due to the effects of lithium coating the relatively cool (<2500 K) cathode surface. We show in Appendix D that at temperatures less than 2500 K lithium can coat tungsten, which could influence cathode operation. Since we could not determine the location and extent of the active zone at high current, and the cathode tip was significantly eroded at the conclusion of these experiments, it was likely that the current was conducted from the cathode tip, rather than the internal surface, because the high flow rate and low current did not allow a highly ionized plasma to form within the channel.

The 8 mm SCHC temperature data were difficult to interpret because the peak temperature was below 2500 K at most operating conditions (see figure 4.5) and the plasma penetration depth had no clear trends (see figure 4.9). This SCHC had a wall thickness of 1 mm, which increased the thermal conduction through the cathode and reduced its temperature compared to that of the 4 and 6 mm SCHCs. Also, the cathode was operated at less than 60 A, a fairly low current for such a large cathode. (Higher current data were not obtained because we were still learning the operational ranges of the SCHC when this experiment was conducted.) The cathode operated in two modes that were distinguished by high or low temperatures (most clearly seen in the 0.6 and 0.8 mg/s data in figures 4.5 and 4.9), which indicated that the surface coating of lithium was unstable. Similar effects were found in lithium dispenser cathode experiments [57], where the surface coating would quickly evaporate and increase the cathode temperature. With this instability, it was difficult to determine if the location of the peak temperature was influenced by lithium surface coating, and, therefore, an unambiguous interpretation of the results was not possible. As a result, we did not use the data from the 2 or 8 mm experiments in our analysis of the SCHC because they were not operated in optimal mode.

4.1.2 SCHC Plasma Potential Results

The plasma potential at the cathode tip, V_c , which is equal to the cathode voltage fall, cannot be measured directly; it must be calculated from floating potential, V_f , and electron temperature, T_e , measurements at the cathode tip. The plasma potential is given by [91, 92]

$$V_c = V_f - \frac{k_B T_e}{e} \ln \left[4 \left(\frac{\pi m_e}{8 m_{Li}} \right)^{1/2} \right], \quad (4.1)$$

where m_e and m_{Li} are the masses of the electron and lithium atom, respectively, k_B is the Boltzmann constant, and e is the charge of an electron. This expression simplifies to

$$V_c = V_f + 3.8 \frac{k_B T_e}{e}. \quad (4.2)$$

Emission spectroscopy data were recorded at 20 operating conditions with 4 different cathodes, which are presented in Appendix C. The potential was calculated using the average electron temperature of all of the spectroscopy data, 0.37 ± 0.12 eV, because the electron temperature showed weak dependence on operating conditions, and the standard deviation of the temperatures was relatively small compared to that of the floating potential. A Langmuir probe measured the floating potential approximately 3 mm downstream of the cathode tip. The plasma potential calculated from the floating potential and electron temperature measurements are shown in figures 4.10, 4.11, 4.12, and 4.13.

Again, the potential measurements from the 2 and 8 mm SCHC experiments cannot be relied upon to demonstrate the trends because the cathodes did not operate in the optimal mode. Although, the 8 mm SCHC data appear to include both optimal and non-optimal modes of operation. The high voltage measurements corresponded to high peak temperature and low voltage corresponded to low peak temperature, which indicated that lithium was coating the cathode surface at low temperature and reduced the work function and, hence, the voltage.

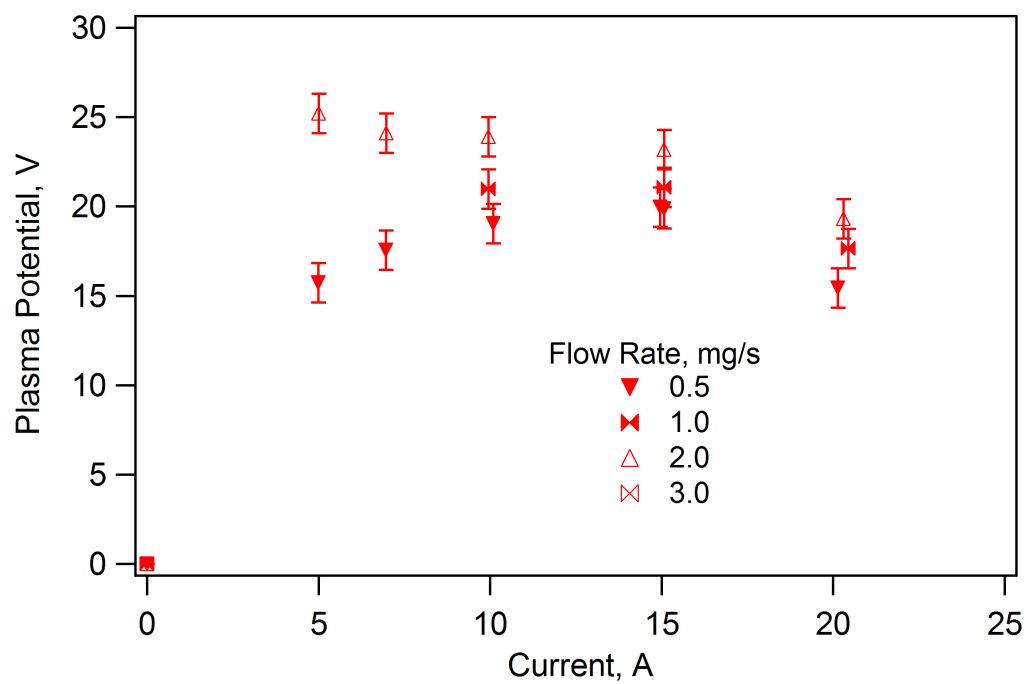


Figure 4.10: The plasma potential at the cathode tip of the 2 mm SCHC.

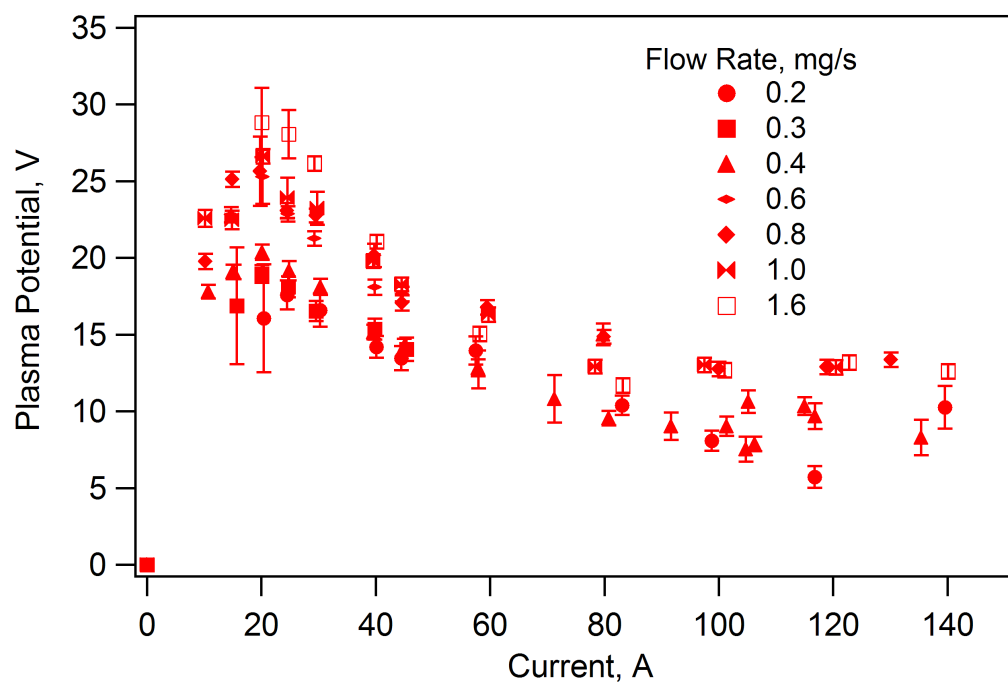


Figure 4.11: The plasma potential at the cathode tip of the 4 mm SCHC.

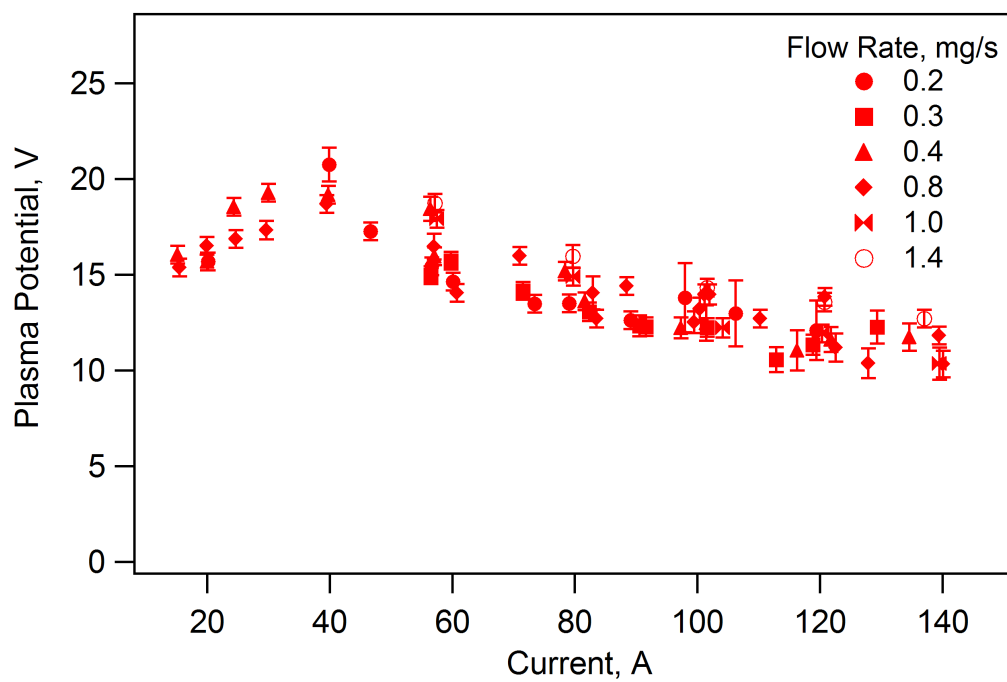


Figure 4.12: The plasma potential at the cathode tip of the 6 mm SCHC.

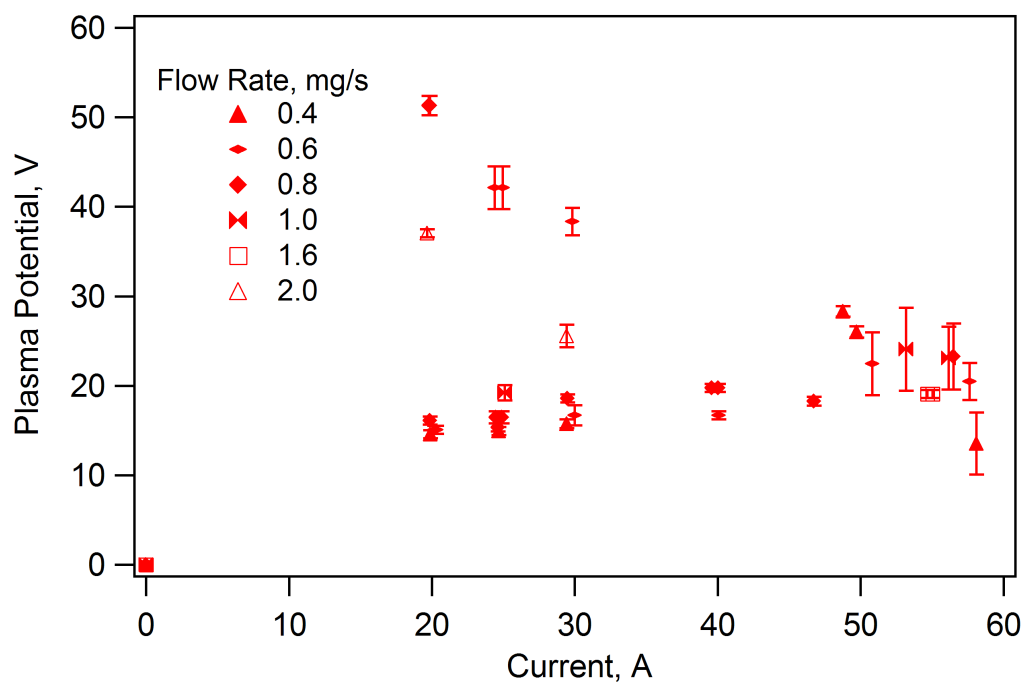


Figure 4.13: The plasma potential at the cathode tip of the 8 mm SCHC.

The plasma potential at the cathode tip decreased with current at currents greater than 30 A in the 4 mm SCHC experiment, as shown in figure 4.11. The trend reversed at lower currents, likely because of a coating of lithium on the surface, which reduced the power, hence, the voltage, required for thermionic emission. The small difference between the low flow rate (≤ 0.4 mg/s) and high flow rate potential measurements was likely due to measurement or experimental error, because the 6 mm SCHC data do not have the similar difference in high and low flow rate measurements. Also, the total discharge voltage measurements (see figure 4.15) do not have the same dependence on mass flow rate. Unfortunately, we could not determine the source of this discrepancy.

The plasma potential measured during the 6 mm SCHC experiment, shown in figure 4.12, has similar trends in voltage as a function of current as the 4 mm data. The voltage has a weak dependence on mass flow rate, with a higher voltage at greater flow rates. The most important trend is that the voltage asymptotes with increasing current, similar to the 4 mm SCHC data. This implies that the SCHCs could conduct more current than that supplied during our experiments without increasing the cathode voltage fall, making them more efficient as the current increases - the maximum current limited only by the evaporation or melting of the cathode material.

4.1.3 Total Discharge Voltage

The total discharge voltage data showed that they did not have the same dependencies as those of the cathode voltage. The data are presented in figures 4.14, 4.15, 4.16, and 4.17. At low current (< 50 A) the cathode voltage fall is approximately equal to the total voltage, but at high current the cathode voltage fall as a fraction of the total voltage decreases with increasing current. The high density plasma in the inter-electrode space and near the anode, which was supplied by the gas flow from the cathode directed at the anode, conducted the low currents without a strong electric field or high thermal conduction to the anode. Although, at high current, a significant amount of power was conducted to the anode or lost

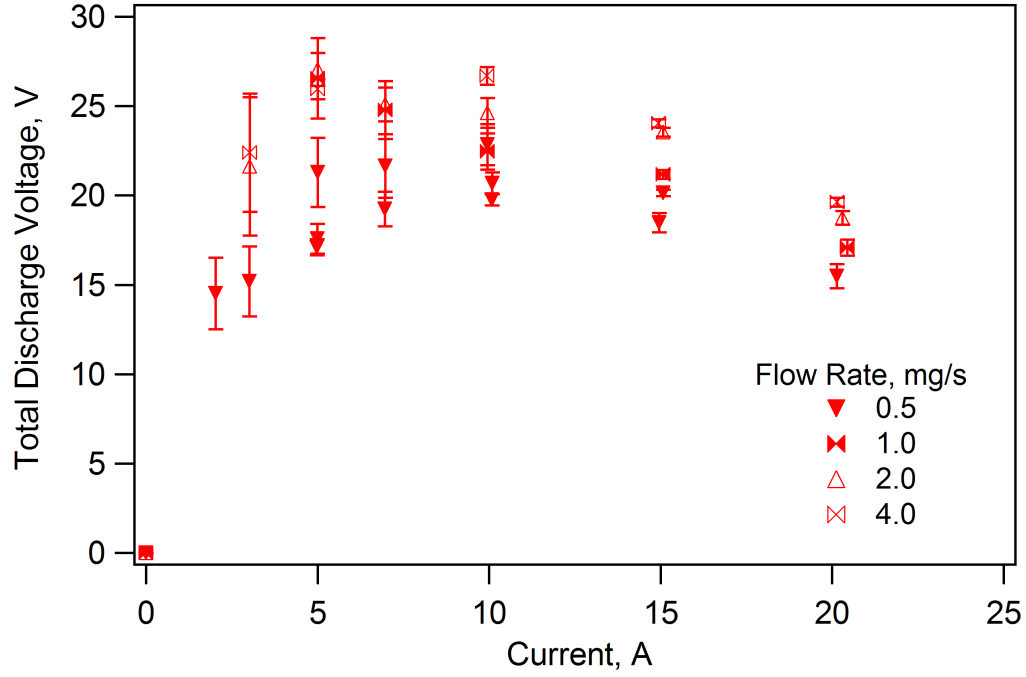


Figure 4.14: The total discharge voltage as a function of current of the 2 mm SCHC.

in resistive heating in the plasma column, as evidenced by the increased anode temperature and fraction of voltage not attributed to the cathode. (We did not measure the anode temperature, but at high current the anode had to be cooled to keep its support structure from melting.) The plasma density must also be a relevant parameter in this process because the total voltage depends on mass flow rate. The total voltage was measured to be greater at low mass flow rate (0.2-0.4 mg/s) than at high flow rate and high current in the 4 and 6 mm SCHC data.

The total voltage measurements did not indicate any dependence on cathode voltage fall at high current, therefore, we did not use these measurements in the analysis of cathode operation. The independence of the cathode voltage fall from the total voltage contradicts the conclusions of SCHC operation by Delcroix and Trindade [20], although their analysis was based on limited experimental data.

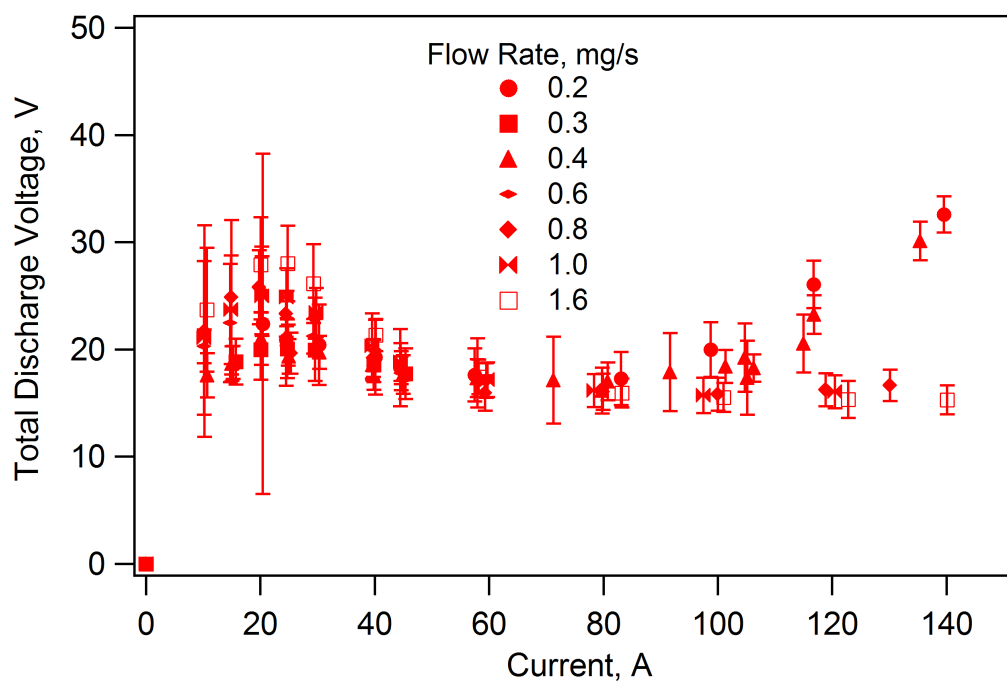


Figure 4.15: The total discharge voltage as a function of current of the 4 mm SCHC.

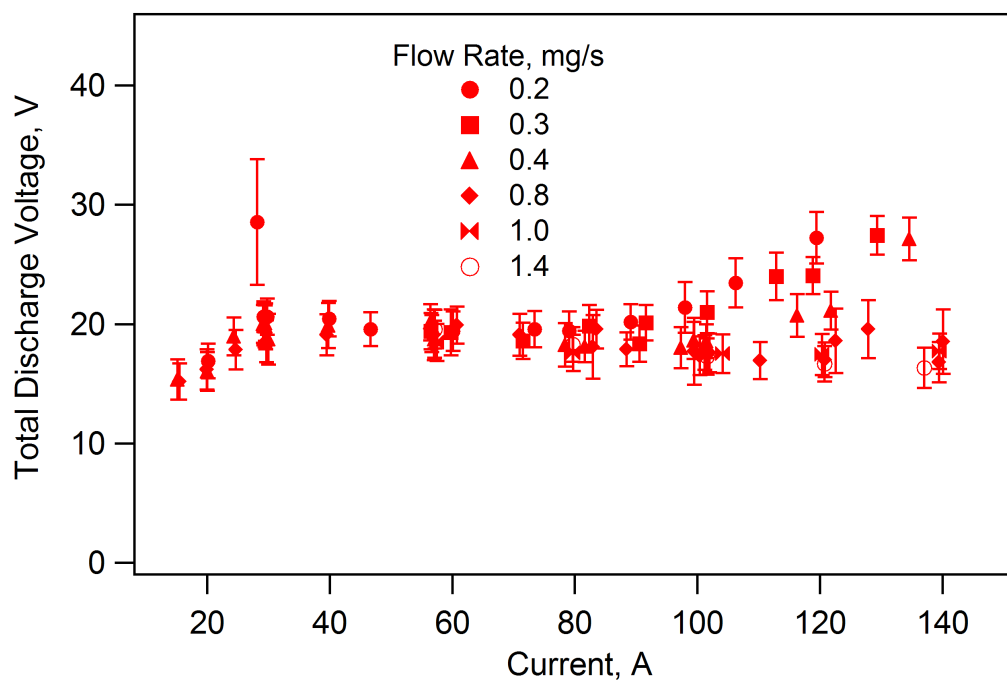


Figure 4.16: The total discharge voltage as a function of current of the 6 mm SCHC.

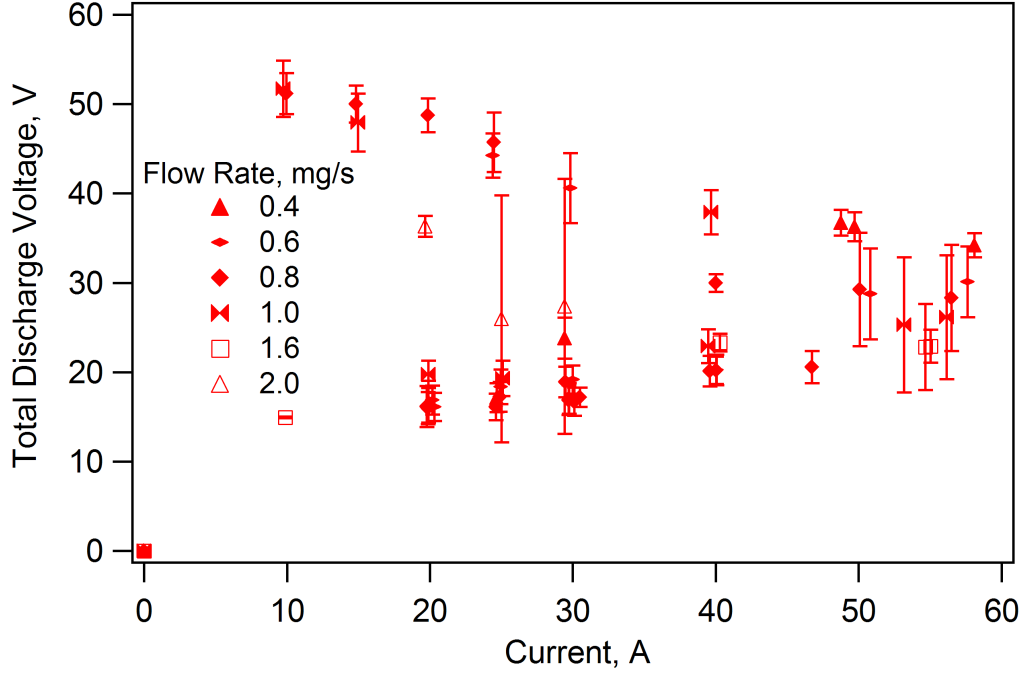


Figure 4.17: The total discharge voltage as a function of current of the 8 mm SCHC.

4.2 MCHC Results

An MCHC with 19 channels, illustrated in figure 3.3e, was operated at two mass flow rates of 0.4 and 1.0 mg/s and currents between 50 and 210 A. The results of the MCHC experiments demonstrate the advantage of utilizing multiple channels because the same current was conducted at a lower cathode voltage drop and temperature than in an SCHC, even though the MCHC was not operated in the optimal mode. We measured that the plasma did not penetrate the channel, which indicates that it was operated at or beyond the limits of the optimal mode, with too high of a flow rate and too low of a current. The 0.4 mg/s experiments are closer to optimal mode and will be considered to produce results more relevant to our analysis.

The peak cathode temperature increased with current, as shown in figure 4.18, but at a rate less than that measured in the SCHC experiments. This is because each channel conducted between 3 and 11 A due to the division of current between the channels. The temperatures measured in the 0.4 mg/s experiments were slightly greater than those of

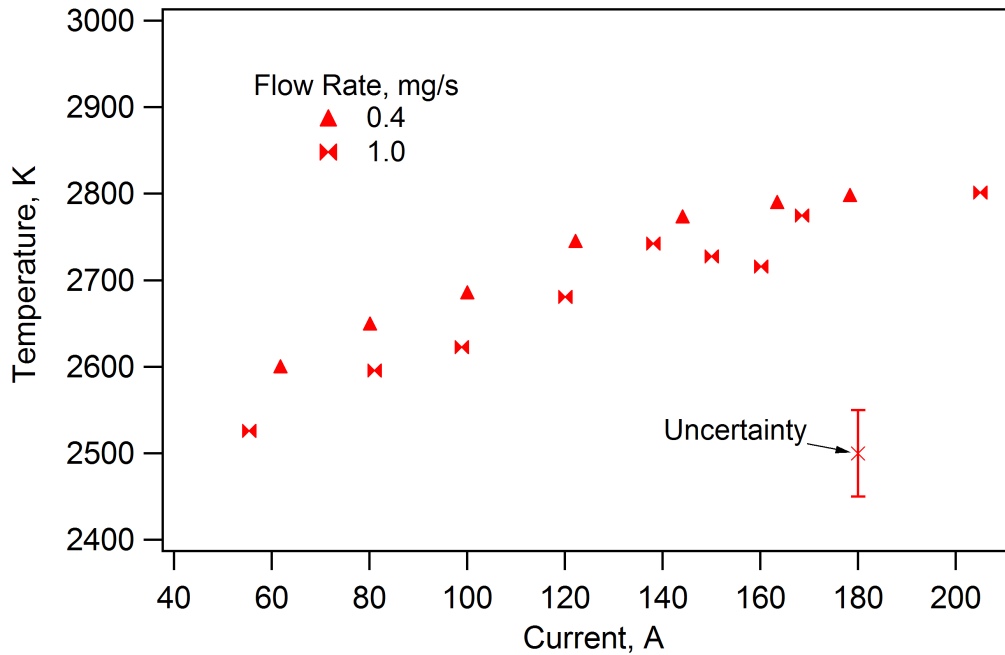


Figure 4.18: The maximum temperature of the MCHC.

the 1.0 mg/s data, because the low-flow-rate experiments were operated closer to optimal mode.

The plasma potential at the cathode tip of the MCHC decreased with current, as shown in figure 4.19. The voltage was lower at the 0.4 mg/s flow rate, again due to the high-flow-rate experiments operating further from the optimal mode. The limited amount of data do not allow us to comment on the minimum operational voltage that the data appear to be approaching asymptotically nor to find the maximum current. Although, the data demonstrate that the MCHC arc has a lower voltage than that of the SCHC when operating at similar currents and mass flow rates.

The total discharge voltage was approximately 40% greater than the cathode voltage drop, and decreased from 22 to 15 V with increasing current, as shown in figure 4.20. The total voltage data do not possess the same trends as the plasma potential because the former increase with current for values greater than 140 A for the 0.4 mg/s experiments; The former is also greater than the latter for the 1.0 mg/s experimental results. This confirms that the cathode voltage drop does not depend on the total voltage.

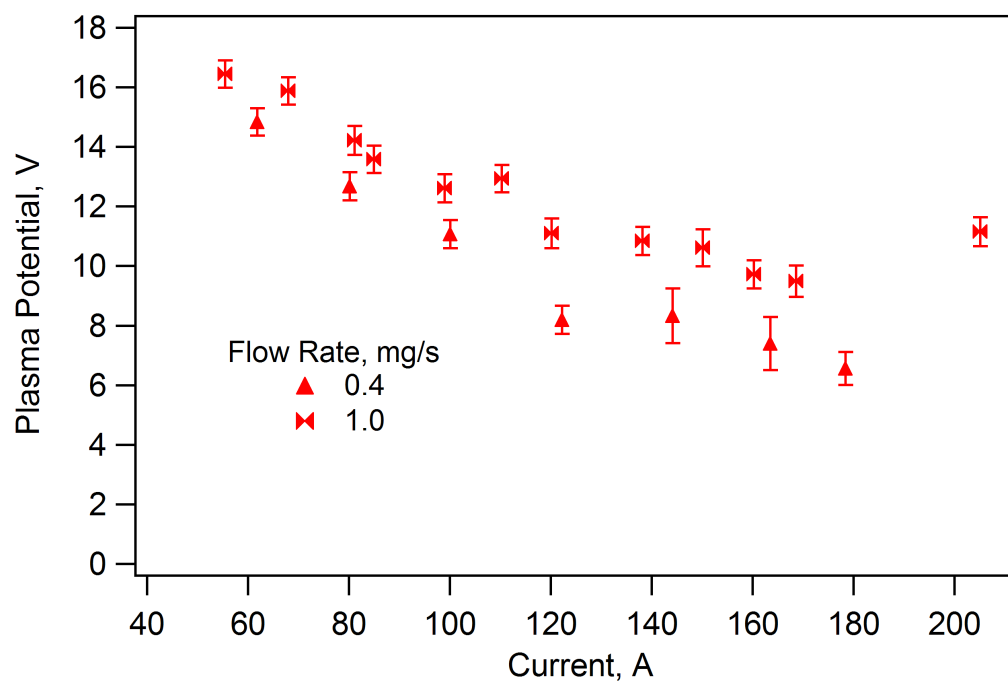


Figure 4.19: The plasma potential at the cathode tip of the MCHC.

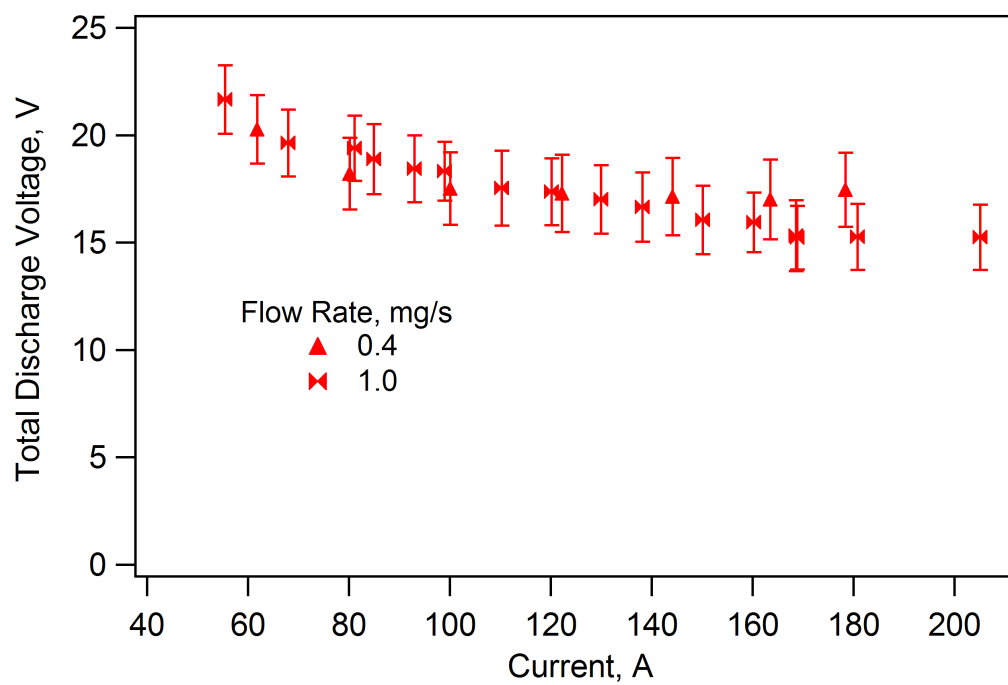


Figure 4.20: The total discharge voltage as a function of current of the MCHC.

4.3 Analysis of the SCHC Results

The extent of flow rates and currents utilized in the SCHC experiments provided a significant amount of data from which new insights were derived. These insights are important because the conditions within the active zone were determined, which allowed for an increased understanding of SCHC operation. The experimental data demonstrated that the cathode temperature was independent of flow rate, but dependent on the current density at the internal surface, as presented in section 4.3.1. We also determined the active zone width and the parameters that control it from the penetration depth and peak temperature data, as discussed in section 4.3.2. We present an estimation of the plasma pressure and cathode surface work function based upon the cathode temperature in section 4.3.3. Using the pressure estimation, the conditions that determine plasma penetration depth are explained in section 4.3.4.

4.3.1 Cathode Temperature and Voltage Drop Dependence on Current Density

The 4 and 6 mm SCHC peak temperature and plasma potential at the cathode tip measurements at all flow rates collapse onto the same curves when plotted as a function of current density on the internal cathode surface, as shown in figures 4.21 and 4.22. All of the current was assumed to be conducted from the plasma to the cathode wall in the active zone, the width of which was determined to be 1.5 mm based upon the cathode wall thickness, as described in section 4.3.2. However, the temperature of the 6 mm cathode was slightly lower than that of the 4 mm SCHC. This can be attributed to the increased heat conducted along the larger cross-sectional area of the 6 mm cathode wall, which requires a larger relative ion flux to heat the wall while simultaneously reducing the thermionic electron current, and, thus, temperature. Nonetheless, the cathode temperature and plasma potential show a clear dependence on current density, which indicates that the fundamental attachment

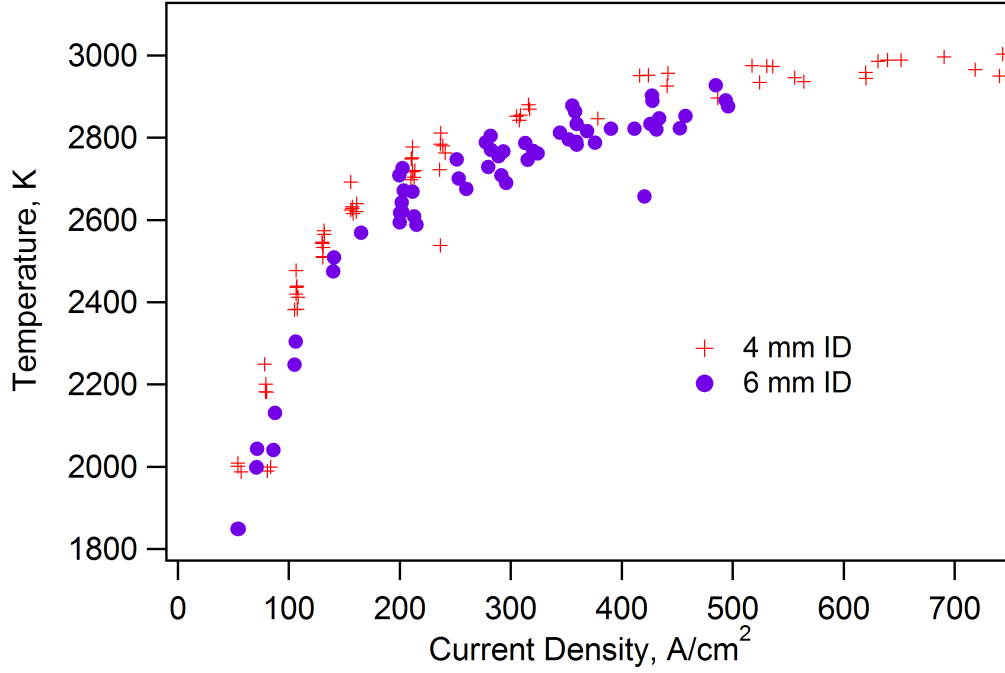


Figure 4.21: Maximum temperature as a function of current density for the 4 and 6 mm SCHCs.

processes are independent of penetration depth and mass flow rate, and also provides a useful tool for analyzing the data. This is one of the most important insights revealed by these measurements.

4.3.2 Active Zone Width

Here we present an analysis of the active zone width using the experimental results and a study of thermal conduction through a cathode wall. An arc prefers to attach to the smallest area possible in order to reduce thermal radiative losses. A smaller emitting surface gives a higher current density at a given current, but since the current density is exponentially dependent on temperature, the temperature will increase by a relatively small amount. This effect of weakly increasing thermal radiation power density, combined with the benefits of a smaller area drive the active zone to a small width.

There are two physical phenomena that could determine the minimum active zone width: the mean free path of the high-energy electrons and thermal conduction through

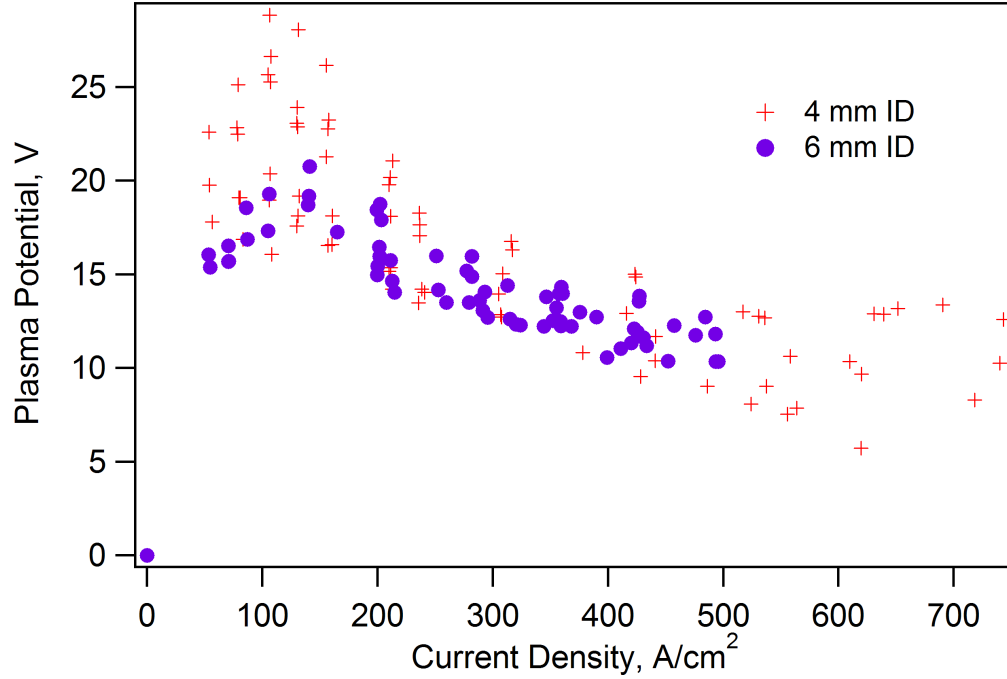


Figure 4.22: The plasma potential at the cathode tip as a function of current density for the 4 and 6 mm SCHCs.

the cathode wall. It is not physically possible for the active zone width to be less than the mean free path of the high energy electrons because the plasma is generated by those electrons. As mentioned above, the discharge adjusts to minimize power loss, of which the thermal conduction from the active zone is the dominant mechanism (excluding thermionic cooling, which cannot be minimized because it depends only on the work function). The minimal thermal power loss configuration only conducts heat radially from the inner surface of the active zone to the outer surface where it is radiated away; any heat conducted axially is an added power loss. A numerical solution of 2-dimensional heat conduction in a high-aspect-ratio plane demonstrated that 1-dimensional effects dominate with active zone widths of greater than 3 to 4 wall thicknesses, because the power loss increases linearly with active zone width, as shown in figure 4.23. The thermal modeling program FEMlab was used to calculate the heat drawn from a 2900 K active zone surface of varying width centered on the long dimension of a plane 100 mm long and 0.5 mm wide. The outer surfaces radiated with an emissivity of 0.45 and the thermal conductivity was that of tungsten.

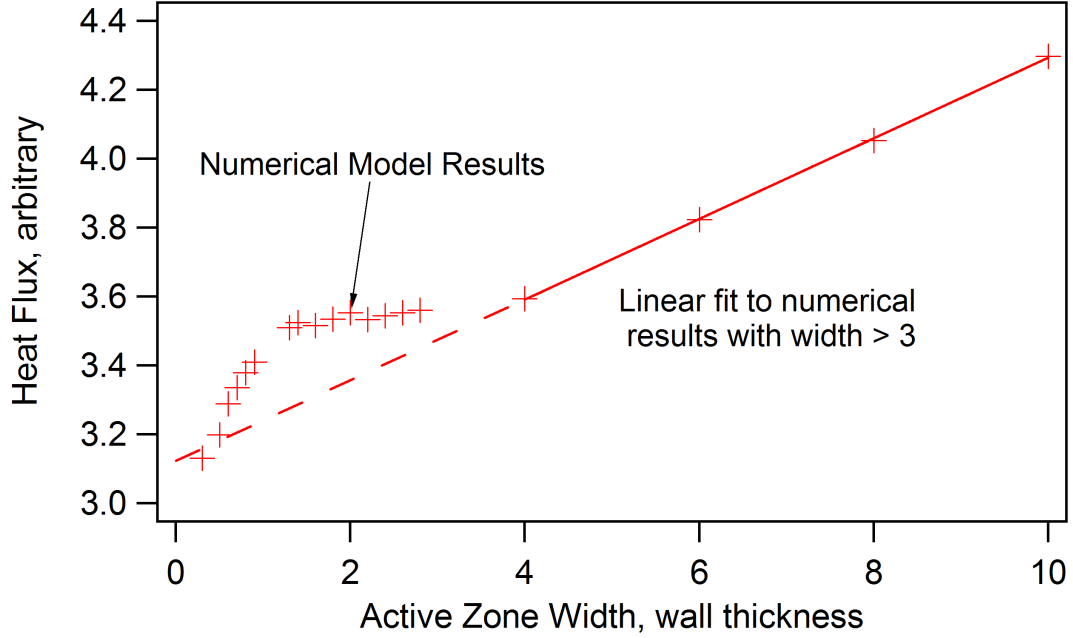


Figure 4.23: Heat flux from a localized active zone.

Active zone widths from 1 to 3 wall thicknesses have approximately the same loss of heat, which is greater than would occur with purely 1-dimensional conduction - this is shown in figure 4.23 by the numerical results in that range of widths having a heat flux greater than that represented by the dashed line, which is an extension of the linear fit of the large width results. From this analysis we can state that if the active zone width is less than 3 wall thicknesses, heat conduction occurs 2-dimensionally and, therefore, increases the power lost. For a minimum power loss configuration, we use 3 wall thicknesses in our analysis.

4.3.3 Ion Pressure in the Active Zone

Using the cathode temperature measurements and the estimated current density, we can determine the ion density within the active zone and the work function of the cathode. The ion pressure, p_i , is related to density through the equation of state,

$$p_i = n_i k_B T_c, \quad (4.3)$$

where n_i is the ion density and the temperature is taken to be equal to the cathode temperature, T_c . The ions collide and thermalize with the wall many times as they travel down the channel [20], therefore, setting the ion temperature to the cathode temperature is a good approximation. We include the most important processes at the cathode wall in the analysis, which are current conduction and power balance. The hot cathode surface emits electrons with a current density, j_{th} , as described by the Richardson-Dushman equation [93],

$$j_{th} = A_R T_c^2 \exp\left(-\frac{e\phi_o}{k_B T_c}\right), \quad (4.4)$$

where A_R is an empirical constant for the cathode material ($A_R = 70 \text{ A}\cdot\text{cm}^{-2}\text{K}^{-2}$ for tungsten), and ϕ_o is the material work function. The ion flux that impacts the wall after acceleration through the sheath contributes to the total current density,

$$j = j_{th} + v_B e n_i \exp(-1/2), \quad (4.5)$$

where v_B is the Bohm velocity, and $\exp(-1/2)$ accounts for the reduced density at the sheath edge due to presheath effects. The Bohm velocity is

$$v_B = \sqrt{\frac{k_B T_e}{m_{Li}}}, \quad (4.6)$$

which requires a presheath potential fall and density reduction to accelerate the ions. The potential drop through the presheath, $V_B = \frac{1}{2} \frac{k_B T_e}{e}$, is found from ion energy conservation. In turn, the ion density at the sheath/presheath boundary, $n_{i,s}$, is also reduced as described by the Boltzmann relation,

$$n_{i,s} = n_i \exp\left(-\frac{eV_B}{k_B T_e}\right) = n_i \exp(-1/2). \quad (4.7)$$

The power balance of an SCHC has three primary terms: the kinetic and potential energy delivered by the ions as they impact the wall, thermal radiation lost from the outer surface, and cooling via electron emission,

$$\epsilon_W \sigma_{SB} T_c^4 + j_{th} \left(\phi_o + \frac{3}{2} \frac{k_B T_c}{e} \right) = n_i v_B e (V_c - \phi_o + \phi_i) \exp(-1/2), \quad (4.8)$$

where ϵ_W is the emissivity of tungsten, σ_{SB} is the Stefan-Boltzmann radiation constant, and ϕ_i is the ionization energy. (The absorbed plasma radiation, field-enhancement of thermionic emission, and conduction along the cathode are neglected in this analysis.) An example of the calculated ion pressure and surface temperature as a function of current density based on the solution of equations (4.3), (4.4), (4.5), and (4.8) is shown in figure 4.24. The plasma potential, which is identical to the cathode voltage drop, and electron temperature are assumed to be 10 V and 0.5 eV, respectively, which are representative values of the SCHC, but they actually vary with operating conditions. Although, the results are insensitive to the electron temperature because the pressure and temperature are weakly dependent on that parameter. The predicted temperature dependence on current density has the same trends as the measured one, as shown in figure 4.25, which indicates that the most important processes have been included in the analysis.

The above equations give a unique relation between temperature, pressure, and current density, such that if one is known the others can be determined. Therefore, if the active zone temperatures of two different cathodes are the same, the ion pressure and current density are also the same. Consequently, the active zone occurs at a location of ion pressure that is sufficient to provide the heating required to balance the power losses of radiation and electron emission, which explains why the location depends on mass flow rate and channel diameter, but the temperature does not. The approximate power balance at the cathode wall demonstrates trends similar to the peak temperature versus current density data, as shown in figure 4.25. The temperature is less sensitive to current at high current because

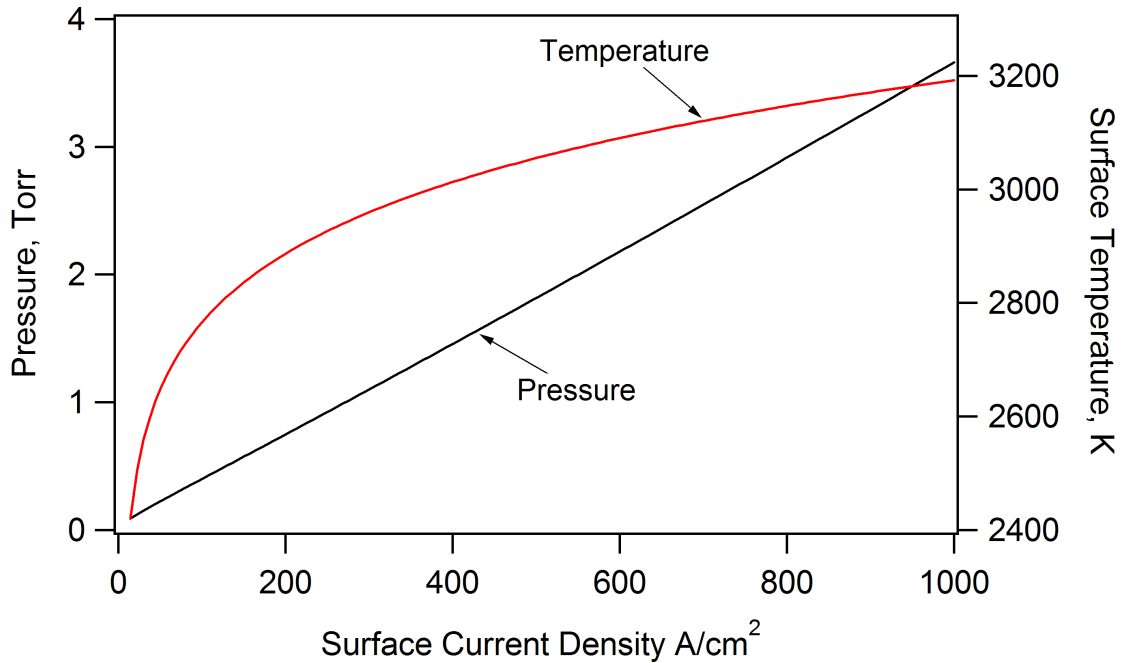


Figure 4.24: Ion pressure and cathode temperature as a function of current density assuming 10 V cathode voltage drop and 0.5 eV electron temperature and 3.8 eV tungsten work function.

thermionic emission is dominating.

The measured cathode temperatures were lower than the values expected of a pure tungsten surface, likely because of a lower work function. The work function could have been reduced by oxygen impurities within the lithium or on the feed system walls, as the work of Babkin and Potapov [25] suggested. The work function of the material can be estimated using the experimental data and equations (4.4), (4.5), and (4.8) to determine the value of the work function that best fits the data. The comparison of the calculated surface temperature and the experimental data is shown in figure 4.25. A calculation of thermal conduction through the cathode wall determined that the internal surface temperature was approximately 80 K hotter than the measured external temperature. The temperature curve that is about 80 K greater than the mean of the data is the one associated with 3.7 eV. Although, field enhancement of the thermionic emission reduced the work function by approximately 0.1 eV, as determined from calculations of the electric field within the sheath. Therefore, to

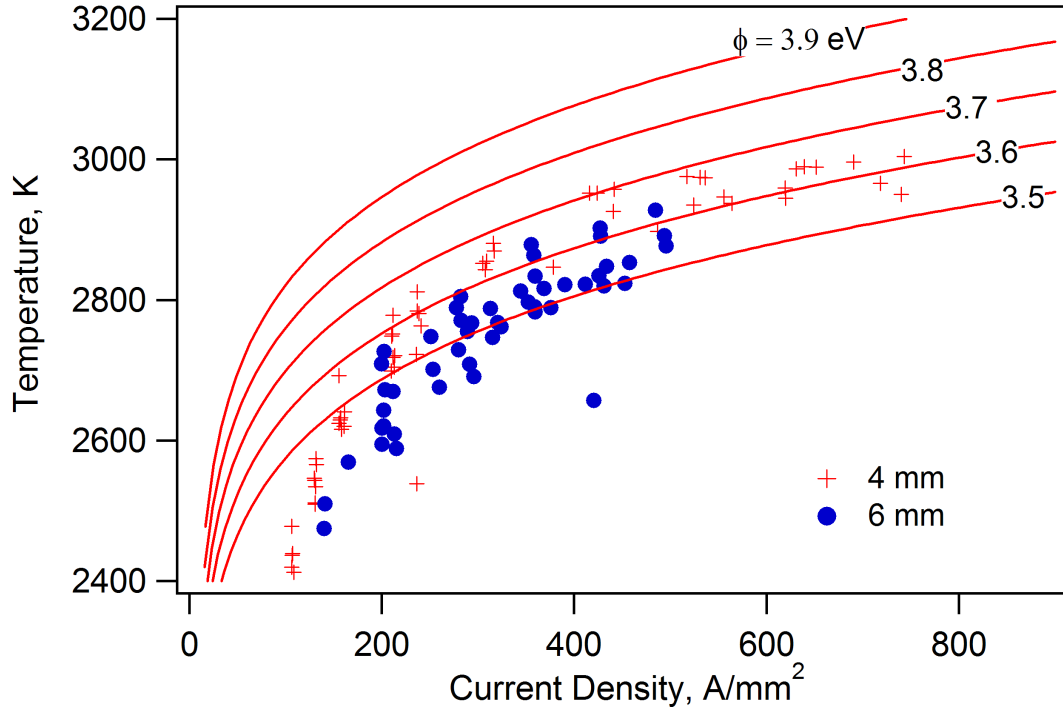


Figure 4.25: Temperature prediction as a function of work function, ϕ , and current density, assuming 1.5 mm active zone width compared to experimental data.

account for the reduction due to field enhancement, a work function of 3.8 eV is a logical choice.

4.3.4 Plasma Penetration Depth

The pressure within the channel is directly related to mass flow rate and distance from the channel exit. The pressure at the channel exit is determined by a choked flow condition, and it increases upstream of the exit due to frictional and kinetic effects. The details of determining the pressure are presented in section 5.1, of which an example of the results for a 4 mm channel are shown in figure 4.26. It can be seen that the pressure within the channel is approximately equal to that shown in figure 4.24, and that the dependence of penetration depth on mass flow rate is manifested in different pressure curves. Therefore, the active zone occurs at the location where the pressure matches that predicted in figure 4.24 for the given current and channel diameter.

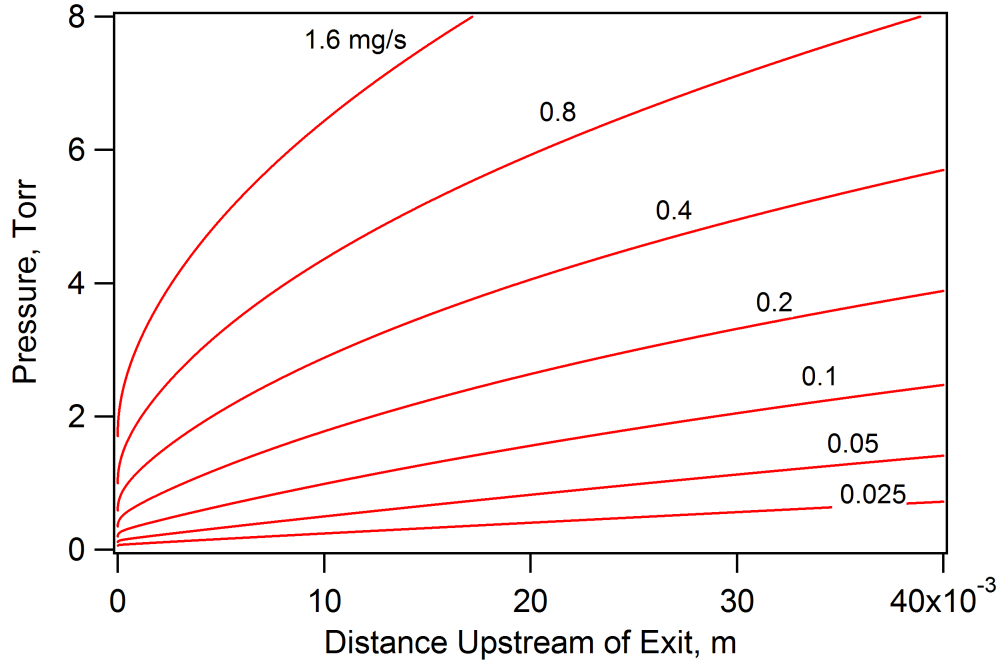


Figure 4.26: Pressure profile of a 4 mm diameter channel

The plasma penetration depth can be explained using physical arguments. If the active zone were downstream of the optimal pressure, i.e. at a lower density, the cathode voltage drop would have to be greater in order for the ions to supply heat for thermionic emission and thermal radiation. Conversely, there would be no advantage of the active zone being upstream of the optimal density location because energy is lost to de-excitation radiation from a partially ionized plasma, and the axial electric field would increase the overall cathode voltage drop. The active zone moves upstream with increasing current to obtain the higher plasma density required to conduct more current.

There was no experimental evidence that the region within the channel between the cathode tip and the active zone significantly contributed to current conduction or caused measurable power loss. The fact that the plasma potential at the cathode tip did not depend on penetration depth demonstrated that the processes that occur in the region downstream of the active zone did not consume much power. Also, since the peak temperature was independent of penetration depth, there must have been a negligible amount of current conducted from the region. Therefore, we feel justified in neglecting that region in our

analysis.

4.4 Analysis of MCHC Results

A qualitative analysis of the MCHC results is presented because the cathode was not operated in optimal mode, which is defined by the lack of a significant plasma penetration. An analysis of the pressure and current within the channels shows that the plasma could penetrate less than a millimeter at the highest current and lowest flow rate. (We did not operate at higher current because of equipment limitations.) The differences between the high and low mass flow rate data can be attributed to how near the cathode operation was to optimal. Calculations of pressure within the channel, see figure 5.3 in section 5.1, show that at high mass flow rate (0.05 mg/s per channel) the pressure is greater than 2 Torr throughout the entire channel. Using figure 4.24, one can see that at that ion pressure the cathode could have supported at least 600 A/cm², compared to the maximum 175 A/cm² that we operated at. The current density is based upon an active zone width of 2 mm, which we show how to calculate in section 5.11. The data recorded at a 0.4 mg/s mass flow rate (0.021 mg/s per channel) could have had a penetration depth of a few tenths of a millimeter according to our model, but we were not able to measure it.

The general insights that were found are that the MCHC did have a lower voltage and temperature than SCHCs that were operated at similar current and mass flow rates. The MCHC data also indicate that operation at a much higher current than the experiments were conducted at was possible.

4.5 Summary of Experimental Results

The experimental measurements and data analysis determined the dependence of plasma penetration depth and the plasma potential at the cathode tip on current, mass flow rate, and channel diameter - data required to develop an understanding of the SCHC and MCHC. The

SCHC experiments showed that

- the peak temperature was independent of mass flow rate
- the plasma penetration depth increased with current
- the cathode voltage drop decreased with increasing current
- the cathode voltage drop does *not* increase with penetration depth
- the peak temperature and voltage scaled with current density on the cathode wall
- the total voltage values and trends did not reflect those of the cathode voltage fall.

These results contradict the assertions of Delcroix and Trindade that the cathode voltage drop increases with penetration depth, and that the penetration depth is inversely related to current [20], although, their conclusions were likely due to the limited range of current over which their measurements were made.

The analysis of the SCHC results revealed that

- the cathode temperature and voltage drop clearly depend on current density at the active zone/cathode wall surface
- the active zone width primarily depends on cathode wall thickness
- the plasma pressure/density can be determined from cathode temperature
- the plasma penetrates to a location of optimal plasma density that depends on current and channel diameter
- in our experiments the surface work function was not equal to that of pure tungsten, but was 3.8 eV.

The MCHC experiments provided detailed cathode voltage fall and temperature measurements of the lithium-fed device and confirmed that the MCHC

- operates with a lower cathode voltage fall than an SCHC at similar current and mass flow rate
- operates at a lower temperature than an SCHC at similar current and mass flow rate
- can conduct higher currents than an SCHC and a solid cathode.

The above results and analysis greatly clarify the picture of the SCHC and MCHC operation and allow for the development of an accurate model, described in Chapter 5.

Chapter 5

Lithium-fed Hollow Cathode Theoretical Model

In this chapter we present a theoretical model that predicts the measurable properties of operating lithium-fed MCHCs and SCHCs as a function of the controllable parameters: the channel diameter, propellant mass flow rate, current, and, for the MCHC, the number of channels and overall cathode diameter. The relevant measurable properties that our model predicts are the cathode voltage drop (the plasma potential at the cathode tip), cathode temperature, and plasma penetration depth. We present the results and validation of the model, as well as discuss the physical insights that it provides at the end of this chapter.

Our goal was to develop a self-consistent model that, unlike any previous model, does not require experimental data as an input, but rather that the predictions of the model can be compared to experimental data. To attain that goal, we developed a model that directly calculates the ionization and excitation rates of the relevant states of the neutral atoms via both thermionic and thermal electron collisions, and determines the cathode voltage fall and plasma penetration depth. The SCHC model also includes the following processes, as shown in figure 5.1,

- gas flow through the channel

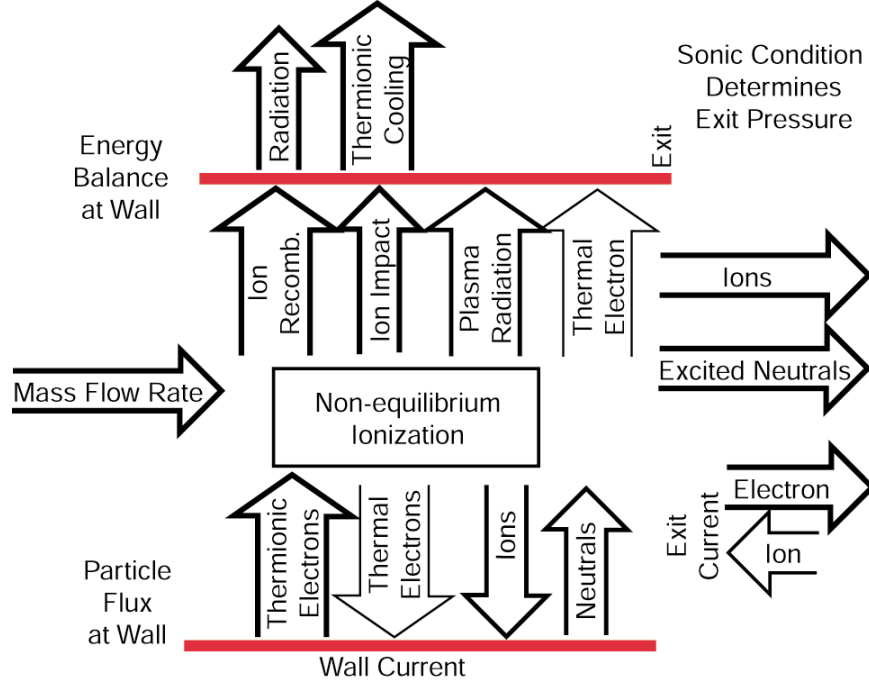


Figure 5.1: Diagram of some of the processes included in the SCHC model: the particle flux balance at the wall and through the channel, the energy balance at the wall, current conduction, and the ionization process.

- thermalization of thermionic electrons within the plasma
- work function reduction due to plasma sheath
- current conduction at the cathode
- cathode heating by ion impact and radiation
- thermionic electron emission cooling
- plasma electron heating.

The lithium-fed SCHC model was extended to include multiple channels. The MCHC model required the SCHC model, the inclusion of the thermal interaction of adjacent channels, and the division of current and mass flow rate.

The active zone of the hollow cathode is modeled as a cylinder of width w equal to $3t$, where t is the wall thickness, and diameter d_c , as shown in figure 5.2, within which the

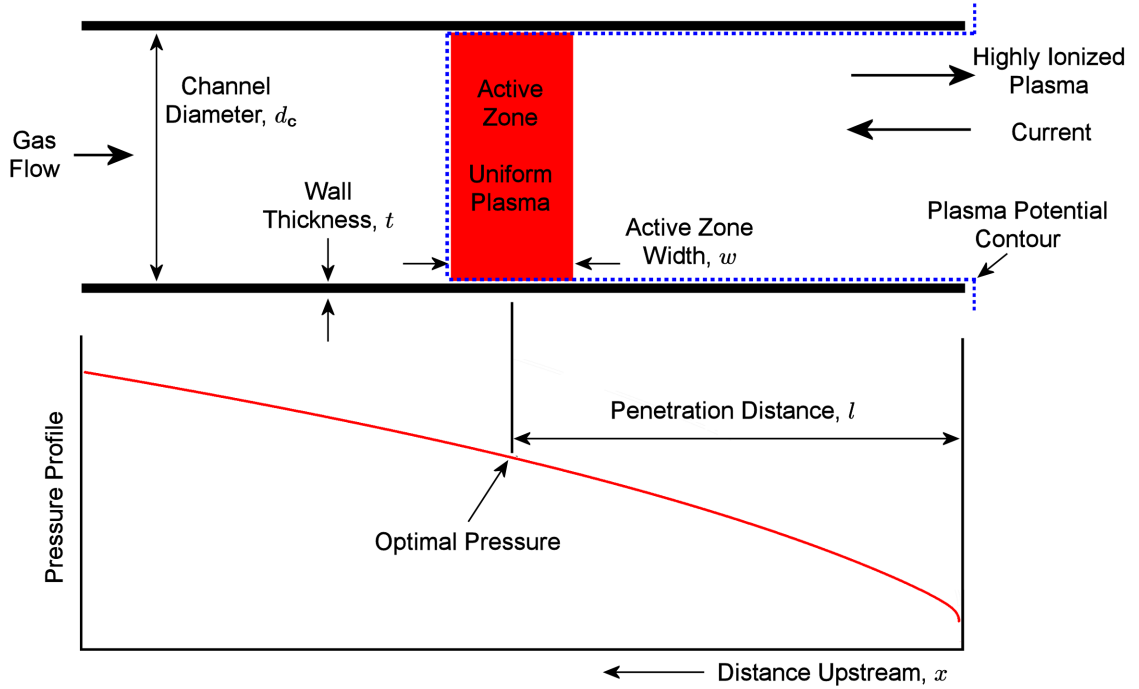


Figure 5.2: Schematic of the cylindrical SCHC adopted for the model.

plasma properties are assumed uniform. The width of the active zone was taken from the analysis of the SCHC data presented in section 4.3.2. The plasma penetrates upstream a distance l to the location of optimal pressure. The penetration distance is taken to be the axial center of the active zone. The radius is an independent parameter that we choose according to experiments. We assume that the thermionic electrons are emitted from a uniform temperature tungsten wall that surrounds the channel. The number densities of the excited states of lithium and the thermionic electrons are determined by a rate balance of all of the collision and flow processes, assuming steady state.

5.1 Gas Flow Through a Channel

The gas flow model determines the pressure along the channel so that the plasma penetration depth and density can be predicted. The density within the channel is determined by

the gas mass flow rate, channel diameter, and cathode temperature. Since the gas exhausts into a region of much lower pressure, the flow is choked at the channel exit. Unfortunately, the conditions are such that the flow is not solely viscous or molecular, but is a “transitional” combination of both. There are no universally agreed upon or validated theories for choked, transitional flow through a short tube; This forces us to find the best approximation for our conditions.

The flow regime is determined by the Knudsen number,

$$\text{Kn} = \frac{\lambda_m}{d_c}, \quad (5.1)$$

where d_c is the diameter of the channel and λ_m is the mean free path of the neutral atoms [81],

$$\lambda_m = \frac{1}{\sqrt{2}\pi n\delta^2}, \quad (5.2)$$

with an atom number density and atomic diameter of n and δ , respectively. A Knudsen number of less than 0.01 indicates that the flow is viscous, while a value of greater than unity indicates that the flow is molecular, otherwise the flow is considered to be transitional combination of both regimes. Hollow cathodes almost exclusively operate in the transitional regime, as corroborated by Ferreira and Delcroix [44].

The gas flow in the channel of a hollow cathode is most accurately described as flow through a short duct. This is because the viscous losses do not dominate the kinetic effects. It is suggested by Lafferty [71] that any channel less than $20d_c$ long should be considered “short” and the appropriate model applied. Hollow cathodes generally have a length of less than $20d_c$. The experiments discussed in this dissertation have channel lengths of approximately $10d_c$. Lafferty [71] presented a general formulation for transitional flow through a short duct with a large pressure ratio,

$$\dot{Q}_t = \theta\dot{Q}_m + (1 - \theta)\dot{Q}_v, \quad (5.3)$$

where \dot{Q}_t is the total gas flow throughput, in units of pressure-volume per time, through the channel, which is weighted between molecular, \dot{Q}_m , and viscous, \dot{Q}_v , throughput. The total throughput is related to mass flow rate by

$$\dot{Q}_t = \frac{k_B T_c}{m} \dot{m}, \quad (5.4)$$

where T_c is the cathode wall temperature, m is the molecular mass of the gas, and \dot{m} is the mass flow rate of the gas. The weighting factor is

$$\theta = \frac{k_s \text{Kn}}{k_s \text{Kn} + 1}, \quad (5.5)$$

where Santeler [94, 95] chose $k_s = 28$, which corresponds to an equal proportion of viscous and molecular flow when the Knudsen number is in the mid-range of transitional flow.

Since we are determining the density along the channel, which is directly related to pressure, we must re-write equation (5.3) in terms of pressure. The flow throughput is related to pressure through the conductance,

$$C = \frac{\dot{Q}}{p_u - p_d}, \quad (5.6)$$

where p_u and p_d are the upstream and downstream pressures, respectively. The pressure downstream of the channel exit can be neglected because it is at least one order of magnitude smaller than the pressure within the channel. In the case of choked viscous flow, the throughput is independent of p_d . Equation (5.3) becomes

$$\dot{Q}_t = [\theta C_m + (1 - \theta) C_v] p_u \quad (5.7)$$

when written in terms of the conductance of the viscous, C_v , and molecular, C_m , components of transitional flow. In order to find the upstream pressure the conductances as a

function of channel length are required, and are described in the following subsections.

The flow is considered to be isothermal with a temperature equal to the cathode temperature. The model will poorly predict the pressure upstream of the plasma because of the large heat addition that is ignored. Ignoring heat addition is acceptable because we are not concerned with the gas upstream of the active zone.

5.1.1 Molecular Flow Conductance

The molecular flow conductance is modeled as a short tube in series with an aperture at the exit. Here we use the molecular flow model presented by Lafferty [71]. The conductance is

$$C_m = \alpha C_a, \quad (5.8)$$

where α is called the transmission probability and C_a is the aperture conductance. The aperture conductance is

$$C_a = \frac{\pi d_c^2}{4} \sqrt{\frac{k_B T_c}{2\pi m}}. \quad (5.9)$$

The conductance is lower farther upstream from the aperture because the molecules have less of a chance to directly exit the channel and are slowed by collisions with the wall. This is accounted for with the transmission probability term

$$\alpha = \frac{1}{1 + \frac{3}{4} \frac{x_e}{d_c}}, \quad (5.10)$$

where x_e is the effective distance upstream of the channel exit defined by

$$x_e = x \left(1 + \frac{1}{3 + \frac{6}{7} \frac{x}{d_c}} \right) \quad (5.11)$$

and x is the distance upstream of the exit aperture.

5.1.2 Viscous Flow Conductance

The viscous conductance is best described as compressible, frictional flow. We use the viscous flow model presented by Lafferty [71]. The thermodynamic relation between throughput, pressure, and Mach number, M , is

$$\dot{Q}_v = p_u \sqrt{\gamma} C_z M \left[1 + \frac{1}{2}(\gamma - 1)M^2 \right]^{1/2}, \quad (5.12)$$

where γ is the ratio of specific heats of the gas and C_z is a conductance term commonly found in viscous flow models,

$$C_z = \sqrt{2\pi} C_a. \quad (5.13)$$

Ideally, the throughput is referenced to the stagnation conditions, but we will use the active zone temperature because the stagnation conditions cannot be determined.

The Mach number at the upstream location, M_x , is given by

$$\frac{1}{\gamma} \left\{ \frac{1}{M_x^2} - 1 - \frac{\gamma + 1}{2} \ln \left[\frac{1}{M_x^2} \frac{(\gamma - 1)M_x^2 + 2}{(\gamma + 1)} \right] \right\} = \frac{f_D x}{d_c}, \quad (5.14)$$

where f_D is the Darcy friction factor,

$$f_D = \frac{64}{\text{Re}}, \quad (5.15)$$

for viscous laminar flow, where Re is the Reynolds number for pipe flow. The viscous component of transition flow is always laminar, because the maximum possible Reynolds number is approximately 160 [71], which is less than the value of 2000 at which turbulent flow occurs. The Reynolds number is given by

$$\text{Re} = \frac{\rho_a v_a d_c}{\eta_v}, \quad (5.16)$$

where the fluid viscosity, η_v , depends on the gas type and temperature, and ρ_a and v_a are

the average density and velocity, respectively. We will use the kinetic-theory relation for viscosity [71, 96],

$$\eta_v = 0.499 \rho_a u \lambda_a = 0.998 \sqrt{\frac{k_B T m}{\pi}} \frac{1}{\pi \delta^2}, \quad (5.17)$$

where u is the gas molecule thermal speed and λ_a is the average mean free path.

5.1.3 Pressure and Velocity at the Channel Exit

The exit pressure must be determined from the choked flow condition because the pressure outside of the channel, p_d , is much less than that required to choke the flow. A simple sonic condition is not accurate because the flow is transitional at the exit, therefore we use a relation similar to equation (5.3) to describe the flow, but the conductances are those of choked flow through an aperture,

$$\dot{Q}_t = [\theta C_a + (1 - \theta) C_{v,a}] p_e. \quad (5.18)$$

The molecular flow component is simply described as the flow through an aperture [equation (5.9)]. The viscous flow conductance is

$$C_{v,a} = \left[\frac{\gamma(\gamma + 1)}{2} \right]^{1/2} C_z. \quad (5.19)$$

It is not possible to analytically solve for p_e in equation (5.18) because θ depends transcendently on pressure through the Knudsen Number. First, we calculate the exit pressure assuming purely viscous flow in order to find an initial guess for the Knudsen Number and θ . Then equations (5.18) and (5.5) are iteratively solved for p_e until the pressure converges.

The velocity at the exit, $v_{g,x}$, is determined from the mass flow rate, temperature and pressure at the exit,

$$v_{g,x} = \frac{\dot{m} k_B T_c}{p_e m_{Li} \pi r_c^2}. \quad (5.20)$$

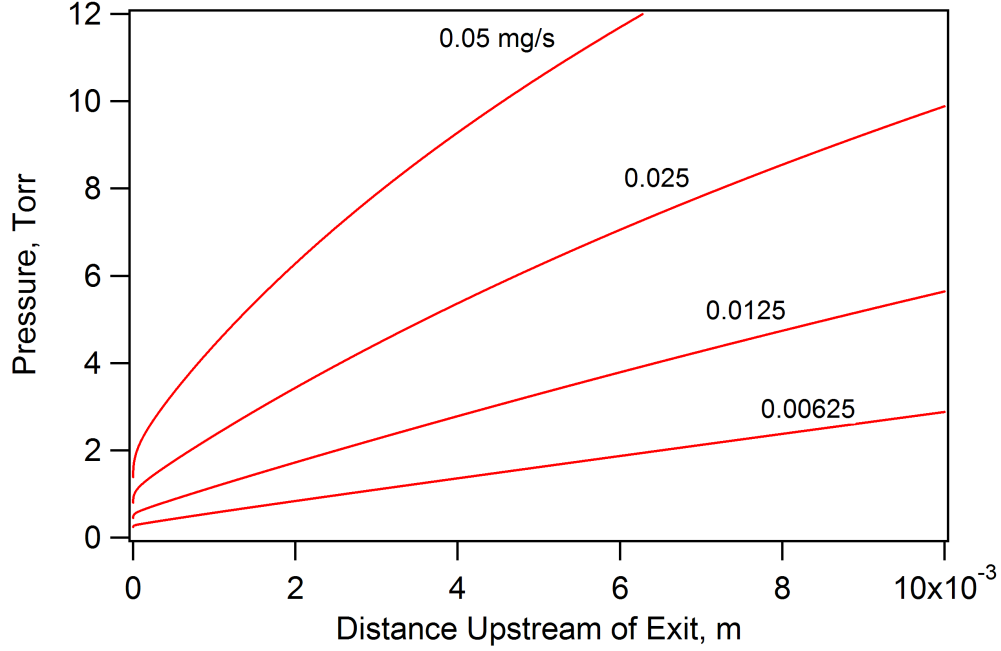


Figure 5.3: Pressure profile of a 1 mm diameter channel

5.1.4 Pressure Profiles Within Channels

A few characteristic pressure profiles (assuming a gas temperature of 3000 K) are presented in figures 5.3, 5.4, and 5.5 to illustrate their dependence on mass flow rate and channel diameter. The range of flow rates was chosen to represent values for which the cathode will operate optimally. This corresponds to pressures of a few Torr within the channel [20]. The pressure is taken to be only the partial pressure of the ions and neutrals within the theoretical model because the heavy particles dominate the flow calculations.

5.2 Plasma Penetration Depth

The penetration depth depends on the gas mass flow rate, current, channel diameter, and wall thickness. However, no previous theoretical model had been able to predict the depth. The trends found by Delcroix and Trindade [20] were that the depth increases with a decreasing value of the ratio of mass flow rate to channel cross-sectional area. As results from our experiments show, the penetration depth also increases with current for a given flow rate

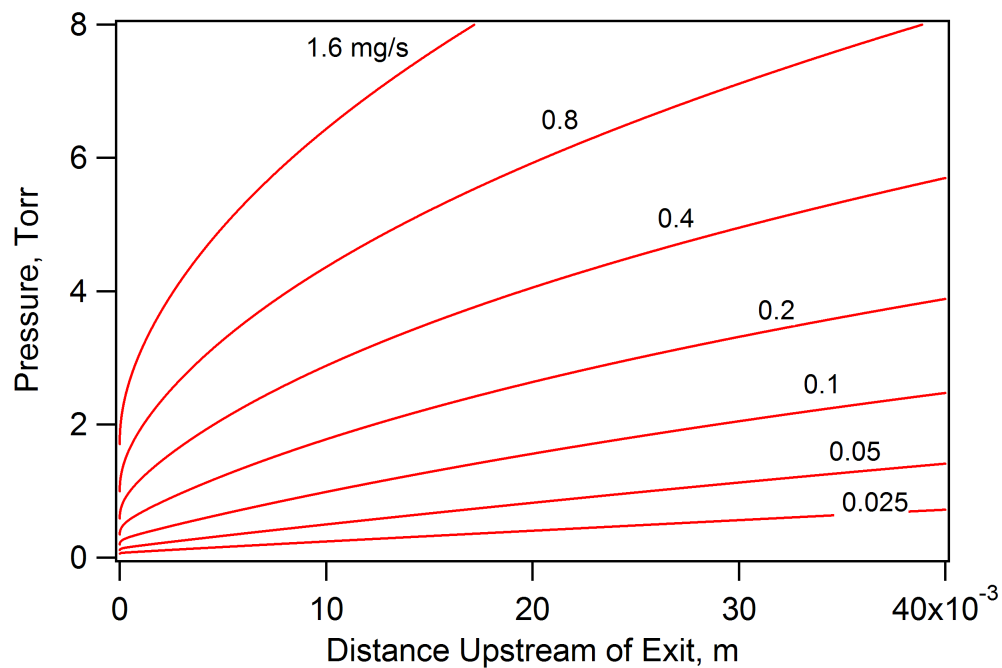


Figure 5.4: Pressure profile of a 4 mm diameter channel

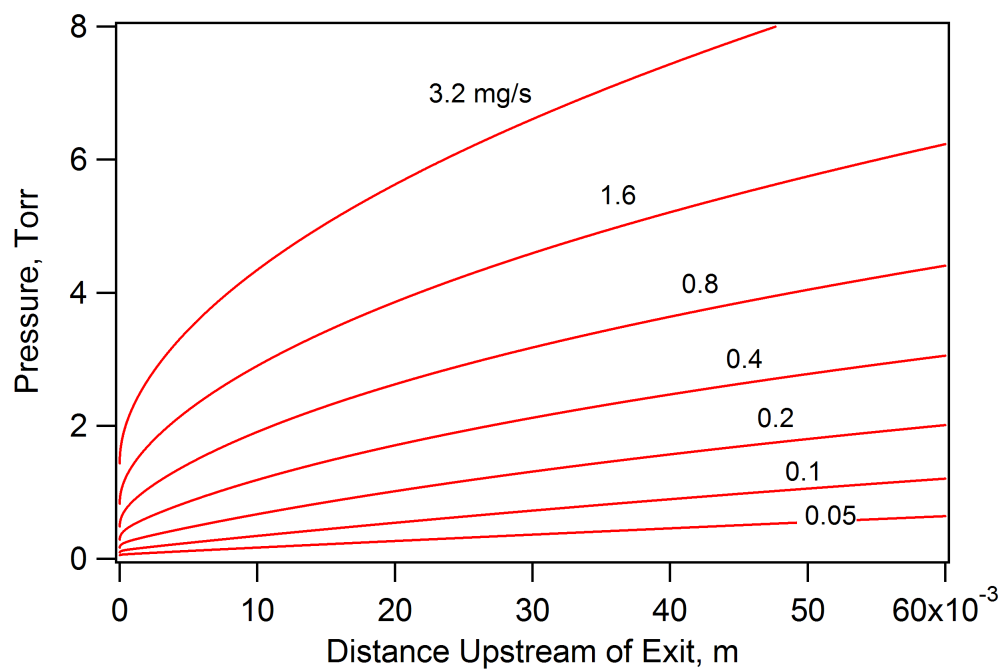


Figure 5.5: Pressure profile of a 6 mm diameter channel

and channel radius.

The guiding principle in determining the plasma penetration depth is that current follows the path of least resistance. We postulate that in a hollow cathode the plasma finds the location and extent of attachment that corresponds to the lowest value of cathode voltage fall divided by total current (the effective resistance). We solve the equations of the discharge model with various plasma penetration depths at fixed mass flow rate and thermionic electron current in order to find the result with the least resistance. The true penetration depth is taken to be the one associated with the minimum resistance.

5.3 Active Zone Width

As presented in section 4.3.2, the active zone width is best described as three times the wall thickness. When the active zone width is less than this, there is 2-dimensional thermal conduction of heat away from the active zone. The thermionic electron mean free path could also affect the active zone width because the active zone must contain the high energy electrons to efficiently ionize the gas. The plasma was determined to have a high density that limited the mean free path to approximately 0.2 mm. Therefore, since the minimum width determined from the thermal conduction analysis is much greater than the mean free path, the latter was not considered a relevant parameter.

5.4 Particle Conservation

Particle flux is conserved at the cathode wall and as the lithium vapor flows through the channel. The ions that impact the cathode wall are neutralized and return to the plasma volume as neutrals. The total flux of ions and neutrals leaving the cathode matches the flux of neutrals that enter the cathode.

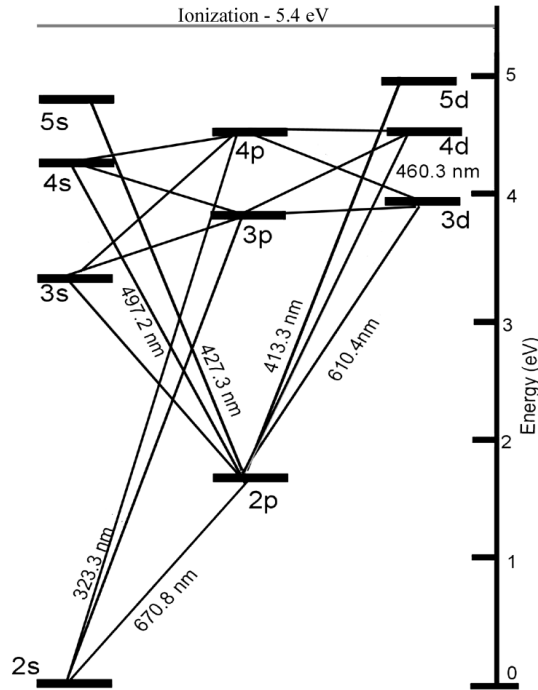


Figure 5.6: Electronic levels of Li I adopted in the SCHC model, based on [97].

5.5 Non-equilibrium Excitation/Ionization

Lithium is ionized via multi-step inelastic collisions with beam electrons thermionically emitted from the cathode surface as well as thermal electrons in the plasma. This forces a non-equilibrium model rather than a Saha-type equilibrium model. Our model is different from the non-equilibrium one presented by Ferreira and Delcroix [44] in that we include collisions of thermionic electrons with the excited states of the neutral atoms and it is specific to lithium atoms. The collision frequencies are modelled utilizing experimental or theoretical cross-section data. The lowest eight states of neutral lithium and singly ionized lithium are included, as shown in figure 5.6. The difference between the energies of the states above the 4d level is small compared to the energy associated with the electron temperature, therefore, we can assume that those states are easily ionized and do not require explicit modelling. A collision frequency is determined for each lithium state and beam electron energy.

Table 5.1: Allowed transitions of Lithium

Transition	$A_k(sec^{-1})$
2s-2p	3.72×10^7
2s-3p	1.17×10^6
2s-4p	1.42×10^6
2p-3s	3.49×10^7
2p-4s	1.01×10^7
2p-3d	7.16×10^7
2p-4d	2.30×10^7
3s-3p	3.77×10^6
3s-4p	3.69×10^3
3p-4s	7.46×10^6
3p-3d	3.81×10^3
3p-4d	6.85×10^6
3d-4p	5.52×10^5
4s-4p	7.72×10^5
4p-4d	1.28×10^3

5.5.1 Lithium Excitation Model

The state of the lithium neutral atom is modelled with electron-impact excitation transitions and spontaneous radiative emission of excited states of the atom. Published [88] values of the transition probability for spontaneous emission are used in the model and are presented in table 5.1. Since lithium has no metastable states, the forbidden transitions are not included in the excitation model. Also, no excited states of the lithium ion are considered since the first excited state is 59.0 eV.

The power radiated by spontaneous emission, P_{sp} , is partially trapped within the channel by the cathode walls. The radiated power that is not lost out of the end of the channel heats the cathode surface. The ratio of trapped to total radiated power is

$$R_{sp} = \frac{2\pi l r_c}{2\pi r_c l + 2\pi r_c^2} = \frac{l}{l + r_c}, \quad (5.21)$$

where r_c is the inner radius of the cathode. The amount of power transferred to the cathode

from the spontaneous emission process is

$$P_{sp,t} = R_{sp}P_{sp}, \quad (5.22)$$

which is utilized in the cathode wall power balance (section 5.9).

5.5.2 Excitation and Ionization Via Thermionic Electrons

One excitation and ionization process is that of inelastic collisions of mono-energetic electrons with the neutral lithium. Since we track the number density of thermionic electrons as a function of energy, we must calculate the collision frequency and change in energy associated with each collision process of the thermionic electrons at each energy. The thermionically emitted electrons are designated beam electrons because each energy group is mono-energetic. The frequency of the inelastic collision process, \hat{p} , between beam electrons and lithium atoms in state k is [59]

$$\nu_{b,k}^{\hat{p}}(\epsilon) = n_k \sqrt{\frac{2\epsilon}{m_e}} Q_k^{\hat{p}}(\epsilon), \quad (5.23)$$

where $Q_k^{\hat{p}}(\epsilon)$ is the cross section for inelastic collision processes of atoms in state k evaluated at the energy ϵ , n_k is the number density of the atoms in state k , and m_e is the electron mass. The processes are the various transitions between the states of lithium as well as ionization, which reduces the energy of the beam electrons by $\Delta\epsilon_k^{\hat{p}}$ as determined by the transition of excited electrons due to the process \hat{p} . We have used the cross sections provided by the International Atomic Energy Agency [98] because they provide standardized formulae for electron impact cross sections as a function of energy.

The total collision frequency of inelastic processes, \hat{p} , that the beam electrons undergo at each energy is

$$\nu_{b,\kappa}^{in}(\epsilon) = \sum_k \sum_{\hat{p}} \nu_{b,k}^{\hat{p}}(\epsilon), \quad (5.24)$$

where the subscript κ represents the discrete energies used in our calculations as explained in section 5.6.

5.5.3 Excitation and Ionization Via Thermal Electrons

The second excitation and ionization process is the collision of thermal electrons with lithium atoms. Electrons with a low temperature can contribute significantly to ionization because of the relatively low excitation energies of lithium. The average frequency of each process for atoms in state k is calculated from [59]

$$\bar{\nu}_{th,k}^{\hat{p}} = n_k \sqrt{\frac{2}{m_e}} \int_0^\infty \frac{2\epsilon Q_k^{\hat{p}}(\epsilon)}{\sqrt{\pi}(k_B T_e)^{3/2}} \exp\left(-\frac{\epsilon}{k_B T_e}\right) d\epsilon, \quad (5.25)$$

where T_e is the electron temperature. These inelastic collisions drain power from the thermal electrons, and thus reduce the electron temperature, as described in section 5.10. The total power is calculated from the sum of the energy lost in each collision process and atomic state,

$$P_{ex} = n_e \Upsilon \sum_k \sum_{\hat{p}} \bar{\nu}_{th,k}^{\hat{p}} \Delta\epsilon_k^{\hat{p}}, \quad (5.26)$$

where Υ is the volume of the active zone,

$$\Upsilon = \pi r_c^2 w. \quad (5.27)$$

5.6 Thermionic Electron Cascade

We must account for the decrease in kinetic energy of the thermionic electrons as they collide with the electrons and neutrals in the plasma in a “cascade”. The thermionic electrons enter the plasma with an energy equal to the sum of the sheath and presheath voltages,

which we take to be the same as the cathode voltage fall, V_c , plus the initial thermal energy associated with the cathode temperature,

$$\epsilon_{b,o} = V_c e + \frac{3}{2} k_B T_c. \quad (5.28)$$

As discussed in section 5.8, the thermionic electrons have a Maxwellian energy distribution normal to the surface with an average equal to the cathode temperature [99, 100, 101] as they leave the surface, before they enter the plasma. However, we approximate the energy of the thermionic electrons in the plasma as that of a mono-energetic beam because the energy gained by acceleration through the sheath is much greater than the energy associated with the surface temperature. Therefore, the energy spread due to the initial Maxwellian distribution is small compared to the energy gained by acceleration through the sheath and is neglected.

The model accounts for the change in energy of the beam electrons by dividing the energy space into finite groups of 0.1 or 0.2 eV depending on the magnitude of the cathode voltage drop. (Sensitivity studies we conducted demonstrated that division sizes of less than 0.2 eV do not significantly change the overall results.) Those bins are represented by the subscript κ and cover the range from $\frac{3}{2} k_B T_e$ to the initial energy, $\epsilon_{b,o}$.

5.6.1 Energy Exchange within the Active Zone

Inelastic collisions with neutral lithium and elastic collisions with plasma electrons reduce the energy of the thermionic electrons until it is equal to the energy corresponding to the plasma temperature, at which point they are considered to be thermal plasma electrons. The energy lost in each inelastic collision is assumed to be equal to the energy of the excited state transition caused by the collision. From reference [59], the energy lost through

collisions with plasma electrons is

$$\Delta\epsilon_{b,\kappa}^e = \frac{1}{2} \left(\epsilon_{b,\kappa} - \frac{3}{2} k_B T_e \right), \quad (5.29)$$

and the frequency of the collision of the beam electrons with the thermal electrons is

$$\nu_{b,\kappa}^e(\epsilon) = n_e v_{b,\kappa} 4\pi b_o^2 \ln \left(1 + \left(\frac{\lambda_D}{b_o} \right)^2 \right)^{1/2}, \quad (5.30)$$

where we use the Coulomb collision cross section with a mono-energetic beam of impacting electrons. The impact parameter, b_o , is given by

$$b_o = \frac{e^2}{4\pi\epsilon_0 m_e v_{b,\kappa}^2} \quad (5.31)$$

with the beam velocity given by

$$v_{b,\kappa} = \sqrt{\frac{2\epsilon_{b,\kappa}}{m_e}}. \quad (5.32)$$

The Debye length has the standard definition of

$$\lambda_D = \sqrt{\frac{\epsilon_0 k_B T_e}{n_e e^2}}. \quad (5.33)$$

The total power that heats the plasma electrons, P_h , described in section 5.10, is determined from the energy lost in each collision multiplied by the frequency of the occurrence

$$P_h = \Upsilon \sum_{\kappa} n_{b,\kappa} \nu_{b,\kappa}^e \Delta\epsilon_{b,\kappa}^e. \quad (5.34)$$

5.6.2 Direct Loss from the Active Zone

When the plasma is highly ionized and the density of beam electrons is high, the beam electrons can exit the channel without exchanging a significant amount of energy with the internal plasma. This is because the beam electrons will collide primarily with the ions, with which they cannot transfer energy. The collisions with the ions will change the direction of motion and allow them to exit the channel. To determine the fraction of beam electrons that escape the channel, we must calculate the mean free path of the beam electrons before they lose energy to thermal electrons or through inelastic collisions. To accomplish this the total collision frequency must be known. The sum of the energy exchange collision frequencies is

$$\nu_{b,\kappa}^{ex}(\epsilon) = \nu_{b,\kappa}^e(\epsilon) + \nu_{b,\kappa}^{in}(\epsilon), \quad (5.35)$$

where the frequencies are defined by equations (5.30) and (5.24), respectively. The only other significant collision type is that with the ions, where $\nu_{b,\kappa}^i(\epsilon)$ is the collision frequency [59],

$$\nu_{b,\kappa}^i(\epsilon) = n_i v_{b,\kappa} 4\pi b_o^2 \ln \left(1 + \left(\frac{\lambda_D}{b_o} \right)^2 \right)^{1/2}. \quad (5.36)$$

To calculate the mean free path of an individual process that does not dominate the collision we must use the concept of the random walk. The mean free path between successive energy exchange collisions is [59]

$$\lambda_{ex,\kappa} = \sqrt{\frac{\nu_{t,\kappa}}{\nu_{b,\kappa}^{ex}(\epsilon)}} \lambda_{t,\kappa}, \quad (5.37)$$

where $\nu_{t,\kappa} = \nu_{b,\kappa}^i(\epsilon) + \nu_{b,\kappa}^{ex}(\epsilon)$ and $\lambda_{t,\kappa}$ is the total mean free path defined as

$$\lambda_{t,\kappa} = \frac{v_{b,\kappa}}{\nu_{t,\kappa}}. \quad (5.38)$$

Next we calculate the fraction of beam electrons that undergo inelastic collisions before they can escape the channel. The primary electrons (those that have not collided yet, with $\kappa = 0$) are treated differently from the secondary electrons. Since the primary electrons are traveling perpendicular to the wall, they must undergo a collision to turn downstream before exchanging energy within the volume. Therefore, the fraction of primary electrons that lose energy within the channel is

$$\psi_0 = \frac{\nu_{b,0}^{ex}}{\nu_{t,0}} + \left(1 - \frac{\nu_{b,0}^{ex}}{\nu_{t,0}}\right) \frac{1}{2} \frac{l}{\lambda_{ex,0}}. \quad (5.39)$$

If the mean free path of a secondary beam electron is less than $l/2$ then there is little chance of the average electron leaving the volume. If $\lambda_{ex,\kappa}$ is greater than $l/2$ then we must calculate the fraction of electrons that leave the volume before transferring their energy. Since the probability of a collision is equal at every position along the path of travel, we can develop a relation for the fraction of collisions that occur within the channel. The fraction of secondary beam electrons that remain in the volume, ψ_κ , is summarized by

$$\begin{aligned} \psi_\kappa &= 1 && \text{if } \lambda_{ex,\kappa} < l/2 \\ \psi_\kappa &= \frac{1}{2} \frac{l}{\lambda_{ex,\kappa}} && \text{if } \lambda_{ex,\kappa} > l/2. \end{aligned} \quad (5.40)$$

Within the model, we know the rate at which electrons enter each energy group, S_κ . The rate the beam electrons leave the channel is $1 - \psi_\kappa$ times the entrance rate. The rest of the beam electrons collide with thermal electrons and the excited states of the lithium atom.

The beam electrons that leave carry current and energy directly out of the channel. For each group of electrons the power and current that directly exit the channel is

$$P_{d,\kappa} = S_\kappa (1 - \psi_\kappa) \epsilon \quad (5.41)$$

and

$$J_{d,\kappa} = S_\kappa (1 - \psi_\kappa) e. \quad (5.42)$$

The power and current carried from the channel by electrons that escaped is

$$P_d = \sum_{\kappa} P_{d,\kappa} \quad (5.43)$$

and

$$J_d = \sum_{\kappa} J_{d,\kappa}, \quad (5.44)$$

respectively.

5.7 Current Conduction at the Cathode Wall

Current is conducted from the plasma to the cathode wall via ions, j_i , thermionic electrons, j_{th} , and thermal electrons, j_{pe} ,

$$\frac{J}{A_z} = j = j_{th} + j_i - j_{pe}, \quad (5.45)$$

where J is the total current, j is current density, and A_z is the area of the active zone bounded by the cathode,

$$A_z = \pi d_c w. \quad (5.46)$$

.

5.7.1 Thermionic Electron Current

The thermionic current is described by the Richardson-Dushman equation [93],

$$j_{th} = A_R T_c^2 \exp \left(-\frac{e\phi_{eff}}{k_B T_c} \right), \quad (5.47)$$

where A_R is an empirical constant for the cathode material ($A_R = 70 \text{ A}\cdot\text{cm}^{-2}\text{K}^{-2}$ for tungsten), T_c is the cathode temperature, and ϕ_{eff} is the effective work function given by [93]

$$\phi_{eff} = \phi_o - \sqrt{\frac{eE_c}{4\pi\epsilon_0}}. \quad (5.48)$$

This relation describes how the effective work function of a material is affected by an electric field at the surface of the cathode (Schottky effect); ϕ_o is the work function of the cathode material ($\phi_o = 3.8 \text{ eV}$ in our experiments, see section 4.3.3), and E_c is the electric field at the cathode surface (see section 5.8).

5.7.2 Ion Current

The ion current is determined from the ion flux to the surface,

$$j_i = ev_{B,m}n_i \exp\left(-\frac{eV_{B,m}}{k_B T_e}\right), \quad (5.49)$$

where n_i is the plasma ion density and $v_{B,m}$ and $V_{B,M}$ are the modified Bohm velocity and voltage, respectively. The Bohm velocity is modified because the hollow cathode sheath is a double sheath due to the thermionic emission of electrons. The modified Bohm velocity and voltage are described in section 5.8.

5.7.3 Thermal Electron Current

Thermal electrons from the near-wall plasma can only reach the cathode wall if their energy perpendicular to the surface is greater than the sheath potential. Since the collisionality of the thermal electrons is high, we may assume that electron density follows a Boltzmann distribution determined by the potential in the sheath, as explained further in section 5.8. The flux of electrons to the wall is then $\frac{1}{4}n_{pe,c}\bar{v}$, where $n_{pe,c}$ is the number density at the cathode and \bar{v} is the average electron velocity as determined from the plasma electron

temperature [102], therefore,

$$j_{pe} = e \frac{1}{4} n_e \exp \left(-\frac{eV_c}{k_B T_e} \right) \left(\frac{8k_B T_e}{\pi m_e} \right)^{1/2}. \quad (5.50)$$

5.8 Electric Field at the Cathode Surface

The cathode wall and the internal plasma are separated by a sheath that accelerates the ions toward the wall and electrons into the plasma. The details of the sheath are not relevant, with the exception of the electric field at the cathode surface, because the field can reduce the effective work function of the cathode (see equation [5.48]). We use a sheath model that is sufficiently accurate to determine the electric field, yet simple enough for a solution to be found without much computation. Our model is based on the double sheath model developed by Prewett and Allen [103] modified to account for the finite energy of the thermionic electrons as they leave the cathode surface. Since our result is slightly different from previous researchers [104, 101], a derivation of the modified double sheath model is included in Appendix E. The electric field at the cathode surface, E_c , is determined by the relation

$$\begin{aligned} \frac{\epsilon_0}{2} E_c^2 &= -\frac{j_{th} m_e}{e} \left[\left(\frac{2e}{m_e} V_s + \frac{3k_B T_c}{m_e} \right)^{1/2} - \left(\frac{3k_B T_c}{m_e} \right)^{1/2} \right] \\ &+ 2n_{i,o} V_{B,m} e \left(\left(1 + \frac{V_s}{V_{B,m}} \right)^{1/2} - 1 \right) \\ &+ n_{e,o} k_B T_e \left(\exp \left(-\frac{eV_s}{k_B T_e} \right) - 1 \right), \end{aligned} \quad (5.51)$$

where $V_{B,m}$ represents the energy of the ions as they enter the sheath in terms of voltage, $n_{i,o}$ and $n_{e,o}$ are the number density of the ions and electrons at the sheath/plasma boundary, respectively, and ϵ_0 is the permittivity of free space. The sheath voltage, V_s , is different

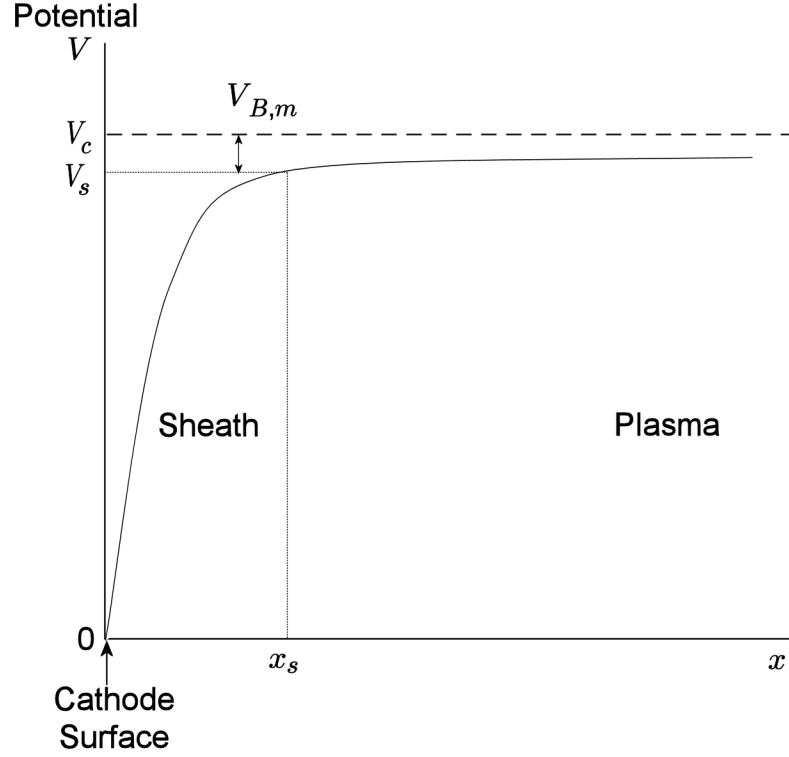


Figure 5.7: Schematic of the plasma potential profile near the cathode wall.

from the cathode voltage drop due to the presheath potential required to accelerate the ions

$$V_s = V_c - V_{B,m}. \quad (5.52)$$

A schematic of the potential profile near the cathode wall is shown in figure 5.7. We consider the sheath and presheath to be small compared to the channel diameter, so that the entire volume of the active zone is at a single potential relative to the cathode.

We use a simple approximation for the voltage across the presheath that is based solely on the modified Bohm velocity. There are two reasons for using this simple approximation: (1) no analytical solution is possible for the case of thermionically emitting cathode and (2) the presheath has little bearing on the processes within the cathode because its width is small compared to the channel diameter (see Ferreira and Delcroix [44]), and, therefore, only a small fraction of plasma volume is part of the presheath. The modified Bohm veloc-

ity is

$$v_{B,m} = \sqrt{2 \frac{V_{B,m} e}{m_{Li}}}, \quad (5.53)$$

where

$$V_{B,m} = \frac{1}{2} \frac{k_B T_e}{e} \frac{1 + j_{th} m_e^{1/2} n_{e,o}^{-1} e^{-1} (2eV_s + 3k_B T_c)^{-1/2}}{1 - j_{th} m_e^{1/2} n_{e,o}^{-1} e^{-1} k_B T_e (2eV_s + 3k_B T_c)^{-3/2}}. \quad (5.54)$$

It is difficult to develop an accurate model that describes the acceleration of the ions to the Bohm velocity because only a few simple cases are solvable analytically [105]. Presheaths that are dominated by collisions or ionization have voltages of $0.6 \frac{k_B T_e}{e}$ [106] or $0.69 \frac{k_B T_e}{e}$ [105, 107], respectively. Neither case is appropriate, but they demonstrate the small range of presheath potentials, and that our model is close to that range.

5.9 Cathode Material Heating

A power balance of the cathode wall is important because it determines the cathode temperature, which gives the thermionic current via the Richardson-Dushman expression, equation (5.47). Heat is supplied to the cathode wall by ions, P_i , and electrons, P_e , that bombard the surface with kinetic and potential energy and spontaneous radiation, $P_{sp,t}$. Thermal radiation from the surface in contact with the plasma, P_{rad} , conduction axially upstream along the cathode, P_c , and thermionic cooling, P_{th} , remove heat:

$$P_i + P_{pe} + P_{sp,t} = P_{rad} + P_c + P_{th}. \quad (5.55)$$

5.9.1 Ion Heating

The power delivered by the ions has two components, the kinetic energy of impact and the energy released when the ion recombines with a surface electron to become a neutral,

$$P_i = v_{B,m} e n_i \exp\left(-\frac{eV_{B,m}}{k_B T_e}\right) (V_c - \phi_{eff} + \phi_i) A_z, \quad (5.56)$$

where $v_{B,m}$ is the modified Bohm velocity defined by equation (5.53). The reduction from the ion density in the bulk, n_i , to that at the presheath/sheath boundary is accounted for with the exponential term, where the presheath potential drop is equal to that associated with the Bohm velocity.

5.9.2 Thermal Electron Heating

The electrons that reach the cathode surface by virtue of their energy, as described in section 5.7.3, heat the surface via their thermal energy and the energy released when they combine on the surface. The flux of electrons is the current determined by equation (5.50) divided by e . The kinetic energy that the electrons have when they reach the surface after traveling through the potential of the sheath must be determined. We begin by assuming a Maxwellian energy distribution (in terms of volts) of the electrons,

$$f(V) = 2\pi \left(\frac{e}{\pi k_B T_e}\right)^{3/2} V^{1/2} \exp\left(-\frac{eV}{k_B T_e}\right). \quad (5.57)$$

We then determine the average energy of the electrons that possess energy greater than V_c by

$$\bar{V}_{V_c} = \frac{N_{\bar{V}}}{D_{\bar{V}}} = \frac{\int_{V_c}^{\infty} V f(V) dV}{\int_{V_c}^{\infty} f(V) dV}. \quad (5.58)$$

If we assume that $V_c > \frac{k_B T_e}{e}$ (which is always true in the hollow cathode),

$$N_{\bar{V}} = \frac{2}{\sqrt{\pi}} \sqrt{\frac{V_c e}{k_B T_e}} \exp\left(-\frac{V_c e}{k_B T_e}\right) \left(V_c + \frac{3}{2} \frac{k_B T_e}{e}\right), \quad (5.59)$$

$$D_{\bar{V}} = \frac{2}{\sqrt{\pi}} \sqrt{\frac{V_c e}{k_B T_e}} \exp\left(-\frac{V_c e}{k_B T_e}\right), \quad (5.60)$$

and, finally,

$$\bar{V}_{V_c} = V_c + \frac{3}{2} \frac{k_B T_e}{e}. \quad (5.61)$$

Since this is the energy that the electrons possess in the plasma, they must lose V_c as they pass through the sheath. This leaves the electrons with an average energy at the cathode, $\bar{\epsilon}_c$, of

$$\bar{\epsilon}_c = \frac{3}{2} k_B T_e. \quad (5.62)$$

Therefore, the power delivered by the thermal electrons is

$$P_{pe} = \frac{j_{pe}}{e} \left(\frac{3}{2} k_B T_e + \phi_{eff} e \right) A_z, \quad (5.63)$$

where the energy released as the electrons recombine with the cathode material is included.

5.9.3 Heating via Spontaneous Radation

The spontaneous radiation emitted by the excited lithium atoms can be trapped within the channel, thus depositing power into the cathode wall. Using equation (5.21), we denote the spontaneous radiation power, $P_{sp,t}$, captured by the cathode as

$$P_{sp,t} = R_{sp} P_{sp}. \quad (5.64)$$

5.9.4 Cooling via Thermal Radiation and Conduction

Heat is conducted from the cathode surface at the active zone through the cathode walls, and is ultimately radiated away or conducted to the base of the cathode. The temperature profile is determined by the temperature gradient caused by heat conduction from the active zone. The base temperature is determined from experimental conditions, and the temperature

at the arc attachment location satisfies equation (5.47). Through a simple calculation we can determine the power conducted to the base (if any) and the power radiated along the cathode.

The thermal radiation is modeled using the Stefan-Boltzmann relation

$$P_{rad} = A_{os}\epsilon_W\sigma_{SB}T_c^4(x), \quad (5.65)$$

where A_{os} is the exposed external surface area, ϵ_W is the emissivity of tungsten, and σ_{SB} is the Stefan-Boltzmann constant. The temperature profile is calculated using standard thermal conduction relation

$$\frac{\delta T}{\delta x} = \frac{P_c(x)}{A_{xs}k_{th}}, \quad (5.66)$$

where A_{xs} is the cross-sectional area of the cathode, k_{th} is the thermal conductivity of the material ($k_{th} = 170 \text{ W}\cdot\text{m}^{-1}\text{K}^{-1}$ for tungsten), and $P_c(x)$ is thermal power conducted along the cathode that is ultimately lost as radiation or conducted to the base. A solution of the temperature profile determines the power conducted to the cathode base and the total power taken from the arc attachment region.

5.9.5 Cooling via Thermionic Electron Emission

Finally, we include the power removed by thermionic cooling. As the electrons leave the cathode material they take energy that is equal to the sum of their initial temperature and the effective work function,

$$P_{th} = j_{th} \left(\phi_{eff} + \frac{3}{2} \frac{k_B T_c}{e} \right) A_z. \quad (5.67)$$

5.10 Plasma Electron Heating

The temperature of the plasma electrons is determined by another power balance. The electron temperature is important because lithium excitation and ionization by thermal electrons depend strongly on that value. The plasma electrons gain energy through elastic collisions with the thermionic electrons. The energy is lost by transport out of the channel through current conduction, excitation and ionization of the lithium atoms, and conduction to the cathode wall,

$$P_h = P_{ex} + J_{e,x} \frac{3}{2} \frac{k_B T_e}{e} + j_{pe} A_z \frac{3}{2} \frac{k_B T_e}{e}, \quad (5.68)$$

where we note that the power lost to excitation, P_{ex} , is a function of electron temperature and J_e is the total current conducted by the electrons out of the channel. We use this relation to self-consistently determine T_e . The ions exiting the channel carry charge in the opposite direction of the current, and, therefore, the electron current must be greater than the total current,

$$J_{e,x} = J + n_i v_{g,x} \pi r_c^2 e - J_d. \quad (5.69)$$

5.11 MCHC Model Components

There are two primary differences between the operation of an MCHC and an SCHC: (1) in the former the current and mass flow rate are divided among the channels and (2) the thermal radiation and conduction are affected by adjacent channels. In an effort to keep a simple, yet effective, model of the MCHC, these processes are equally allocated to each channel. In order to accomplish this, the model assumes that all of the channels have the same diameter, and, therefore, the same mass flow rate and current. Hence, the mass flow rate and current in each channel is the total mass flow rate and current divided by the number of channels.

The power lost to thermal radiation and conduction is also equally attributed to each channel. This assumption does not explicitly capture all of the thermal effects, such as radiant heat transfer from the inner channels to adjacent channels of similar temperature and radial variations in the temperature of the channels, which have a portion of their surface exposed to the external environment. Nonetheless, this model captures the most relevant thermal processes. The power lost due to thermal radiation depends on the exposed outer surface area,

$$A_{M,e} = 2\pi r_{M,o}w, \quad (5.70)$$

where $A_{M,e}$ is the area of the exposed outer surface of an MCHC with a total outer radius of $r_{M,o}$ and w is the active zone width. The model decouples the radiation area from the individual channel radius so that each channel contributes equal portions to the exposed area of the MCHC,

$$A_{eff} = \frac{A_{M,e}}{N_c}, \quad (5.71)$$

where N_c is the number of channels in the cathode.

The active zone width and effective wall thickness are difficult to determine due to the complicated geometry of the MCHC. Therefore, we use an approximation of wall thickness based on the cross-sectional area of the cathode, which assumes each channel to be surrounded by an equal thickness of cathode material. This is accomplished by simply taking the cross sectional area of the cathode material left after the holes are created and assigning it equally to rings around each channel. The resulting thickness, t_c , is

$$t_c = \sqrt{\frac{r_{M,o}^2 - N_c r_c^2}{N_c} + r_c^2} - r_c, \quad (5.72)$$

from which the cross sectional area for axial thermal conduction for each channel is determined. The active zone width, w , is 3 times the thickness for an SCHC, as described in section 4.3.2. Since each channel is effectively separated by $2t_c$, we have $w = 6t_c$.

The MCHC model solves for the operation of a single channel using the SCHC formulation except for exchanging the exposed area, A_{os} , with the effective area, A_{eff} , in equation (5.65), and the cross-sectional area of the cathode for thermal conduction, $A_{xs} = \pi[(r_c + t_c)^2 - r_c^2]$, with the area of the MCHC in equation (5.66). Because each channel has an identical mass flow rate, current, and thermal power loss, we only have to solve the model of a single channel.

To illustrate the advantage of the MCHC, we give an example of the reduction in thermal radiation power loss as compared to the SCHC. With 2 concentric rings of holes around a central hole, 19 holes can fit in a tight pattern. The radius, $r_{M,o}$, is 5 times the radius of channels, which also increases the exposed area by a factor of 5. Yet there are 19 channels within the cathode providing heat to the surface area. The effective surface area will be $\frac{5}{19}$ or 26% of the area an SCHC would have. Since the radiated power is directly proportional to area, there is a 74% reduction in that power loss mechanism.

5.12 Neglected Processes

Here we comment on processes that are neglected in our theoretical model.

5.12.1 Axial Electric Field

The axial electric field is neglected because the data presented in sections 4.3.1 and 4.3.4 do not indicate that a significant field existed. The measured plasma potential at the cathode tip did not increase as the plasma penetration depth increased due to either an increasing current or decreasing mass flow rate. The Spitzer resistivity for a highly ionized plasma [59],

$$\eta_s \approx \frac{\pi e^2 m_e^{1/2}}{(4\pi\epsilon_0)^2 (k_B T_e)^{3/2}} \ln \Lambda, \quad (5.73)$$

predicts 1 to 5 Ω mm, depending on the electron temperature. At the high currents in our 4 mm cathode experiments, this corresponds 11-55 V/mm using the standard calculation

for electric field,

$$E = \eta_s j, \quad (5.74)$$

but this does not match our measurements. This deviation can be explained by the differences between the Spitzer resistivity calculation and the hollow cathode plasma conditions. The Spitzer resistivity derivation assumes a Maxwellian electron distribution [59], but hollow cathodes have a significant population of high energy electrons that are available to conduct the current. This population is only 0.01% to 1% of the electron population, but is significant in absolute terms ($10^{18} - 10^{20} \text{ m}^{-3}$). Also, the Spitzer resistivity derivation shows that most of the current is carried by the high energy electrons in the tail of the distribution. This indicates that the electric field would be lower in hollow cathodes. Therefore, the combination of experimental measurements and the above resistivity analysis justifies neglecting the electric field.

5.12.2 Electron-ion Three-Body Recombination

The electron-ion three-body recombination frequency, $\nu_{e,i}^{3b}$, can be calculated from the J.J. Thomson general theory of three-body recombination [59],

$$\nu_{e,i}^{3b} = 2.13 \times 10^{-20} \frac{n_e n_i}{T_e^{9/2}} \ln \Lambda, \quad (5.75)$$

in SI units. In the lithium hollow cathode plasmas studied here, this frequency is about 1 order of magnitude less than that of the ionization collision processes from the excited and ground states. Also, this type of recombination leaves the neutral atom in an excited state, which would then be quickly re-ionized by another thermal electron. This process is neglected because it is not a dominant process and it is difficult to predict the excited state of the resulting neutral atom.

5.12.3 Bremsstrahlung Radiation and Radiative Capture

The power radiated from the plasma due to *bremsstrahlung* radiation, P_{br} , is, in SI units, [59]

$$P_{br} \simeq 1.43 \times 10^{-40} n_e n_i T_e^{1/2}, \text{ W m}^3. \quad (5.76)$$

The SCHC and MCHC consume 10 - 1000 W, while this process radiates at most ≈ 0.1 W from the channel volume, therefore, it can be neglected. The power associated with radiative capture, P_{fb} , can be approximately expressed as a ratio of *bremsstrahlung* radiation,

$$\frac{P_{fb}}{P_{br}} \simeq \frac{2\epsilon_{m,i}}{k_B T_e m}, \quad (5.77)$$

where $\epsilon_{m,i}$ is the energy required for ionization from principal quantum level m . The highest radiated power ratio of ≈ 30 occurs with $m = 1$, $\epsilon_{m,i} = 5.4$ eV, and the approximate lowest electron temperature $\frac{k_B T_e}{e} = 0.4$ eV. Therefore, this process is justifiably neglected.

5.12.4 Collisional Deexcitation

Collisional deexcitation is the process of reducing the energy state of an excited electron through an inelastic collision with an electron or heavy particle. This process is usually important in highly collisional plasmas, such as the one studied here. The minimum electron density for the collisional deexcitation rate to equal that of radiation is given by [86]

$$n_e \geq 9 \times 10^{22} \left(\frac{\Delta E}{Ry} \right)^3 \sqrt{\frac{k_B T_e}{e Ry}}, \quad (5.78)$$

where Ry is the Rydberg constant, which is equal to 13.6 eV, and ΔE is the energy difference between the excited levels of the atom. For the electron temperatures in our plasma, 0.5 eV, and the energy level differences of about 1 eV in the lithium atom, the minimum plasma density for significant collisional deexcitation is $7 \times 10^{18} \text{ m}^{-3}$. As shown in section 4.3.3, the ion pressure was a few Torr, which corresponds to a density of approximately

$5 \times 10^{21} \text{ m}^{-3}$. This demonstrates that the excited states were populated through collisional deexcitation and excitation with the thermal electrons.

Unfortunately, we were not able to include this process in our theoretical model because the cross section for collisional deexcitation of the lithium atom is not well known. In fact, the IAEA only has the cross sections of Hydrogen and Helium tabulated [98]. In plasmas where collisional deexcitation is significant, a Saha equilibrium can normally be assumed for the ionization and excitation states.

Fortunately, neglecting collisional deexcitation had little effect on the optimal mode results because the plasma was highly ionized ($>80\%$). The population of the excited states is very small (two to three orders less than the LiII and neutral ground states) in a highly ionized plasma, and, therefore, excitation and deexcitation collisions with those states are limited. The theoretical results for the high-density, partially-ionized plasma in a non-optimal mode could have over predicted the ionization fraction and densities of the excited states because an important deexcitation process was neglected.

5.13 Solution Procedure

This theoretical model must be solved iteratively because the collision frequencies are a function of the densities of each state of the lithium atom, which are among the variables that we are solving for. The procedure for finding the solution is given below.

1. We set the following operational parameters:

- number of channels
- exposed surface area to that of the MCHC (A_{eff}) or SCHC (A_{os})
- channel inner diameter, d_c
- wall thickness, t
- active zone width, w

- penetration depth, l
- mass flow rate, \dot{m}
- thermionic electron current density, j_{th} .

We set the thermionic electron current, rather than the total current, because it allows for much faster convergence. The total current is determined by the model and is approximately twice the thermionic current. The penetration depth is varied while all other parameters are held constant to find the depth at which the most total current is conducted at the lowest cathode voltage fall. This is taken as the optimal penetration depth for those conditions.

2. We make the following initial guesses:

- cathode temperature, T_c , based on j_{th} without field-enhancement
- cathode voltage drop ($V_c = 20$ V)
- electron temperature ($T_e = 0.2$ eV)
- total density based on flow model
- densities of the excited states.

3. During the first iteration, we skip to step 6.

4. The cathode temperature, T_c , is determined, based on field-enhanced thermionic emission.

5. The ion pressure, p_u , is determined at the active zone based upon the new gas temperature, see section 5.1.

6. All collision frequencies are calculated using the densities determined in the previous iteration or, in the case of the first iteration, from the initial guesses.

7. The rates of collision for thermionic electron “cascade” are found, see section 5.6.

8. The rate balance of the states of lithium and the conservation of particles are solved in matrix form.
9. Steps 6 to 8 are repeated until the densities converge.
10. The cathode voltage drop is adjusted to balance equation (5.55).
11. Steps 4 to 10 are repeated until the voltage converges.
12. The electron temperature is adjusted to balance equation (5.68).
13. Steps 4 to 12 are repeated until the electron temperature converges.
14. All of the rates and powers are balanced giving the final solution for the given conditions.

5.14 Validation

A comparison of the theoretical and experimental results are presented in this section to demonstrate the validity of the SCHC and MCHC models. The cathode temperature, voltage drop, and penetration depth are compared over a wide range of currents and mass flow rates for the 4 and 6 mm SCHC and the MCHC. The comparisons are made with the 4 mm cathode operated at mass flow rates of 0.4 and 1.4 mg/s, the 6 mm cathode at 0.4, 1.0, and 1.4 mg/s, and the MCHC at 0.4 mg/s. The theoretical model was verified over a wide range of experimentally measured conditions to check its ability to predict the independent parameters over an extended range. In all cases the theoretical and experimental results were in good agreement, indicating that the model includes the relevant processes.

The comparisons of peak temperature on the outer surface and the penetration depths of the SCHC are shown in figures 5.8 to 5.12. The experimental and theoretical temperatures follow the same trend of increasing at a decreasing rate with current, and the predictions are within a few percent of the experimental error bars at currents where there was plasma

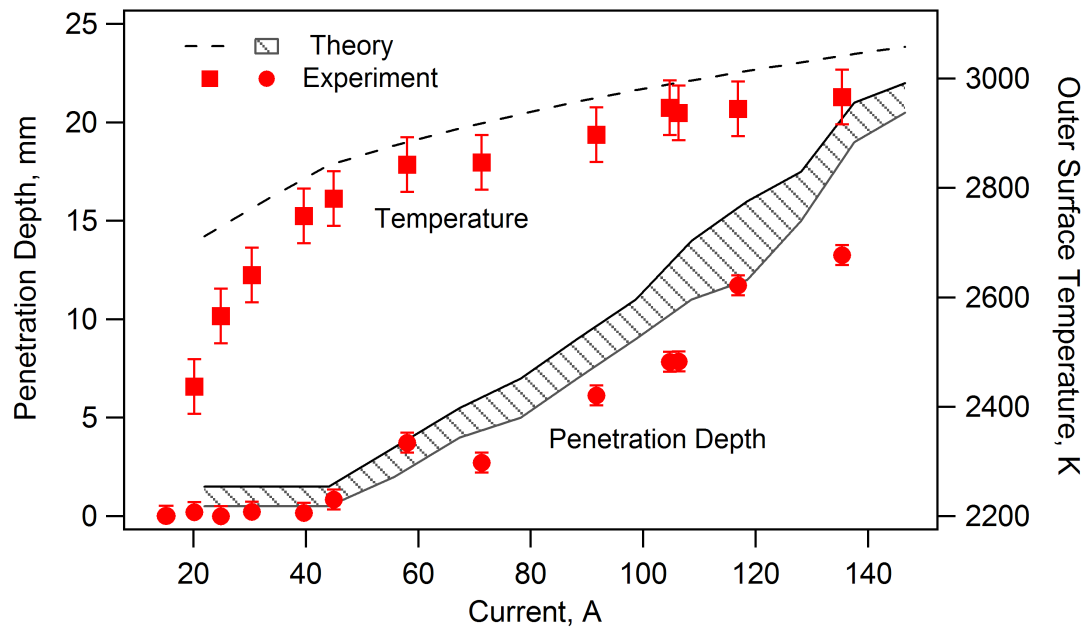


Figure 5.8: Comparison of cathode temperature and penetration depth as a function of current density for the 4 mm SCHCs operated at 0.4 mg/s.

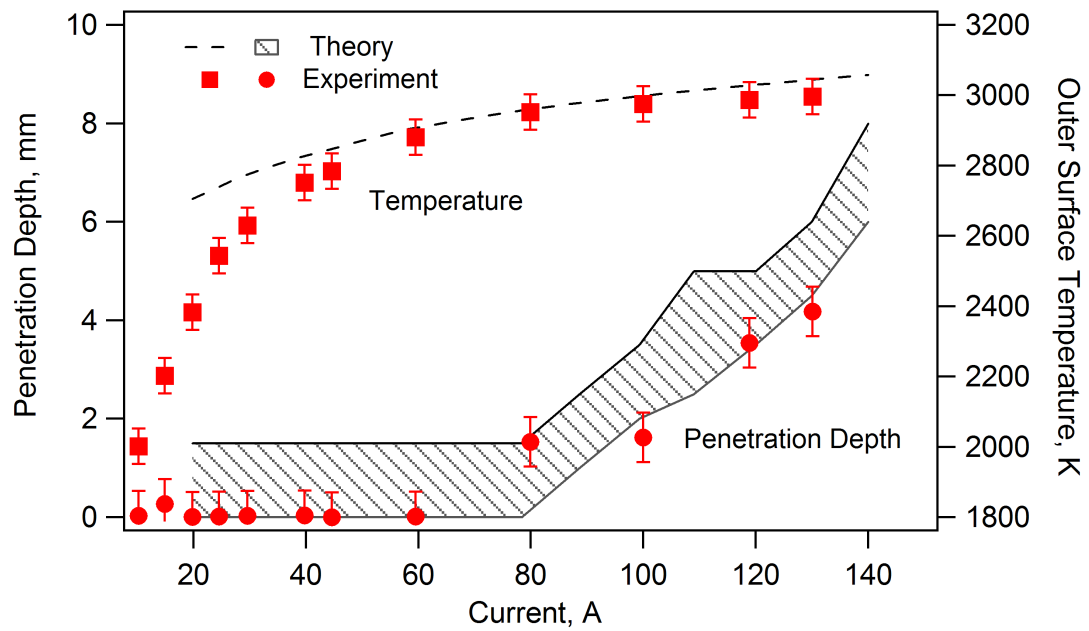


Figure 5.9: Comparison of cathode temperature and penetration depth as a function of current density for the 4 mm SCHCs operated at 0.8 mg/s.

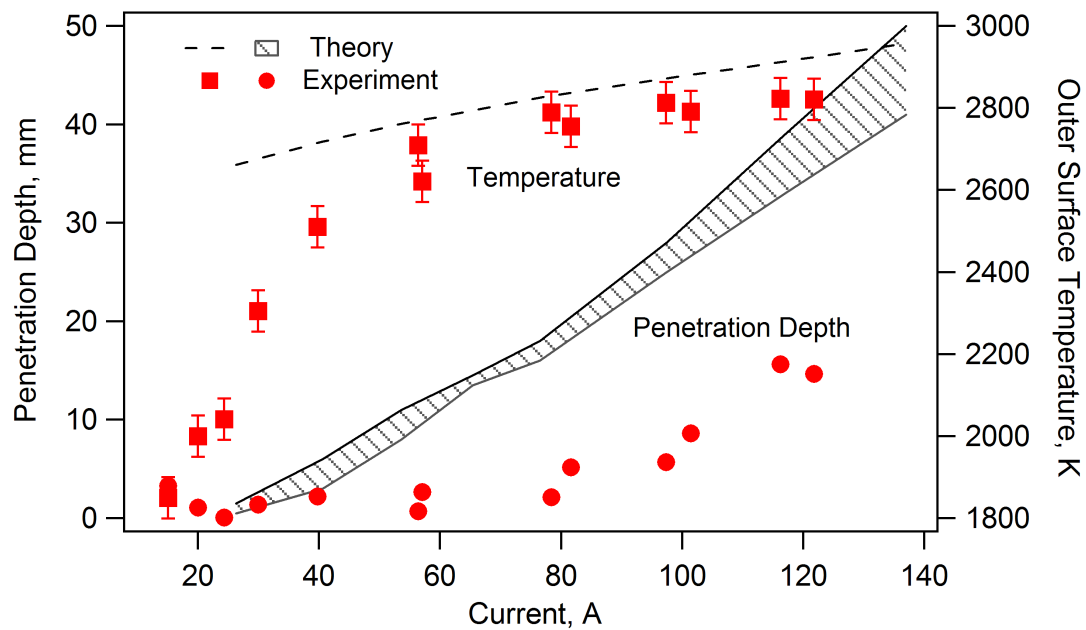


Figure 5.10: Comparison of cathode temperature and penetration depth as a function of current density for the 6 mm SCHCs operated at 0.4 mg/s.

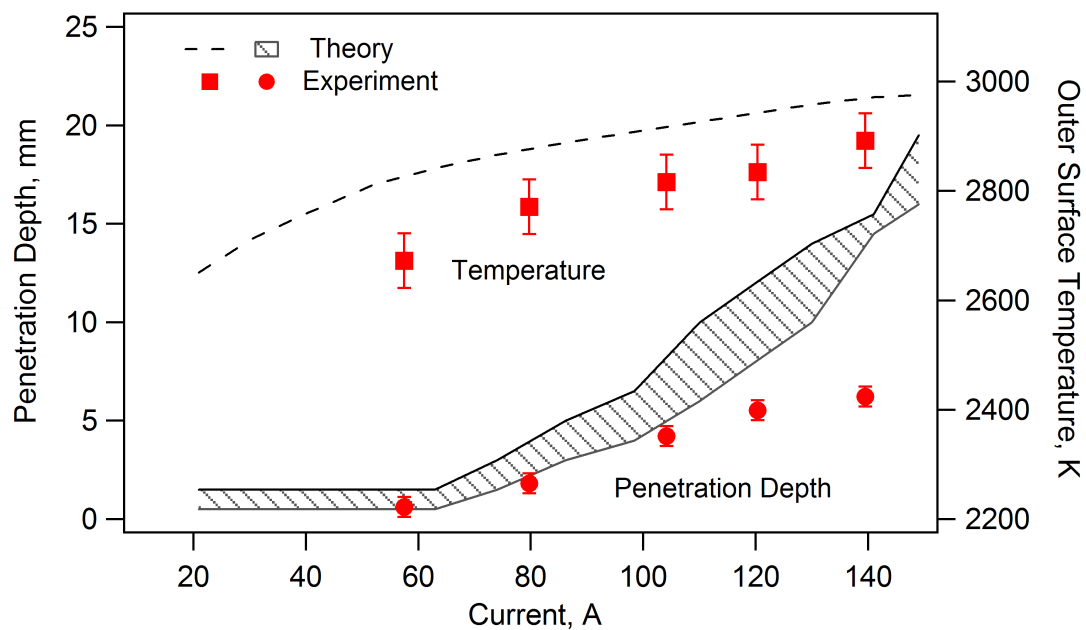


Figure 5.11: Comparison of cathode temperature and penetration depth as a function of current density for the 6 mm SCHCs operated at 1.0 mg/s.

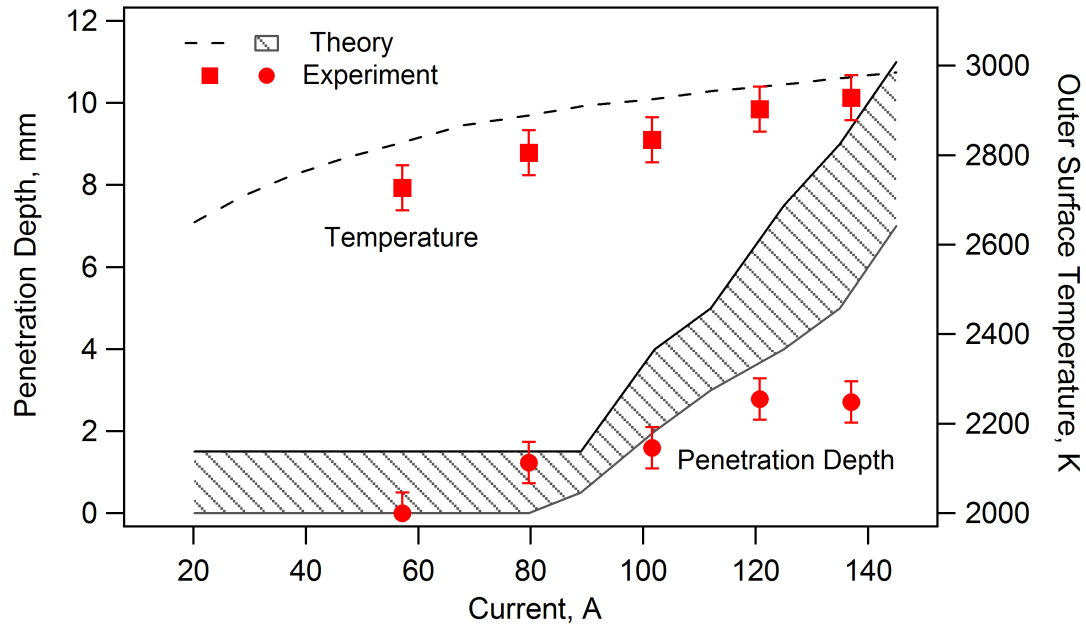


Figure 5.12: Comparison of cathode temperature and penetration depth as a function of current density for the 6 mm SCHCs operated at 1.4 mg/s.

penetration. The measured temperature of the data points without plasma penetration was much less than that predicted by the model. This could be because the active zone width was less than that required for 1-dimensional heat conduction, which would increase the temperature difference between the inner and outer sides of the cathode, or there might have been a lithium coating the cathode surface. The patterned areas in figures 5.8 to 5.12 represent the range of penetration distances that have an effective resistance within 1% of the minimum calculated one. This occurs because the pressure gradient is weak enough that the plasma density and arc resistance are similar over a range of penetration distances. The model over-predicts the penetration depth at high current, although it is more accurate at higher mass flow rates and smaller channel diameters. This indicates that for high Knudsen number flows the gas flow model could be improved.

The SCHC voltage drop predictions and measurements are compared in figures 5.13 to 5.17. Again, the model captures the trends of voltage as a function of current in all cases, with the voltage fall decreasing at a decreasing rate with increasing current. The predictions approximately match the experimental data of the 4 mm cathode operated at 0.4 mg/s,

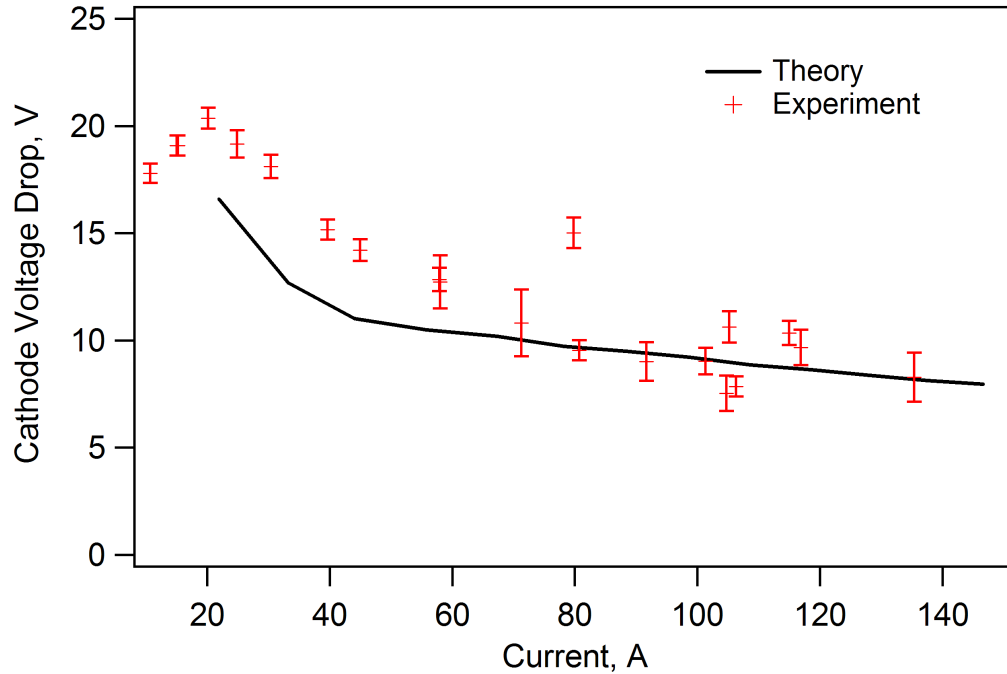


Figure 5.13: Comparison of cathode voltage drop as a function of current density for the 4 mm SCHCs operated at 0.4 mg/s.

although it ranges up to 30% below the measured voltage fall for the rest of the data. The model predicts the voltage drop reasonably well, even with negligible penetration depth, an indication that the model is applicable to discharges with mass flow rates greater, or currents less, than those that are optimal. At very low current, the experimentally measured voltage decreases with decreasing current, a phenomena that the model does not capture. This is likely because the cathode surface is coated with lithium, which can be inferred from the fact that the measured temperatures were less than 2500 K. A coating of the cathode with lithium reduces the work function, a process not included in our model.

The experimental and theoretical MCHC temperature and plasma penetration depth results agree well, as shown in figure 5.18. The predicted temperatures and depths are within the error of the experimental measurements. The cathode voltage was predicted to be 30% greater than the measured values, as shown in figure 5.19. This can be attributed to operation well out of optimal mode, which could have allowed for some surface coating with lithium and reduced the measured plasma potential.

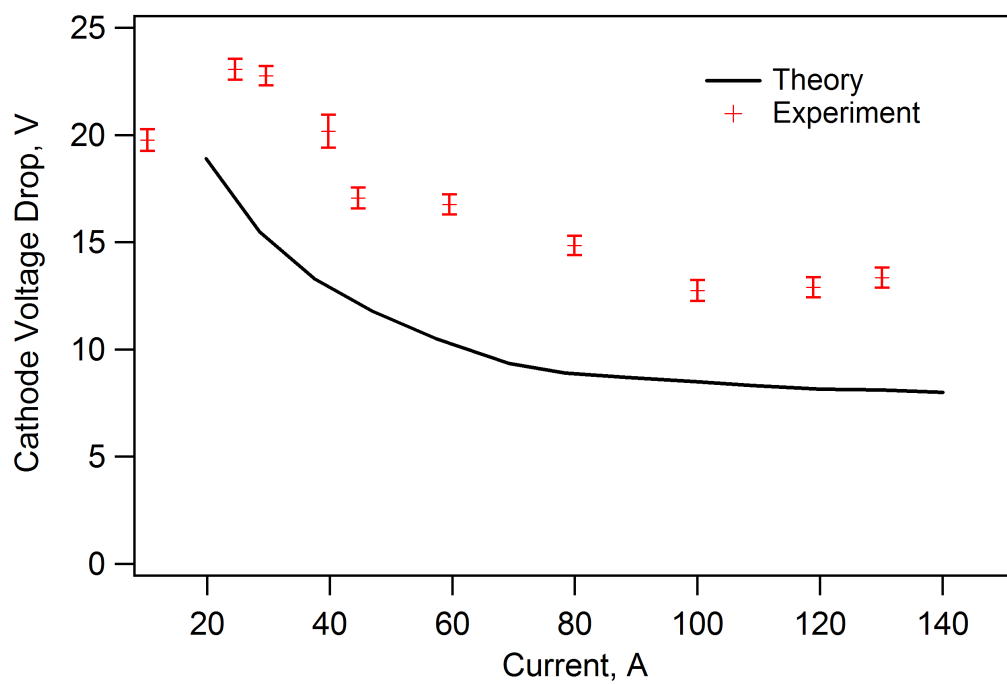


Figure 5.14: Comparison of cathode voltage drop as a function of current density for the 4 mm SCHCs operated at 0.8 mg/s.

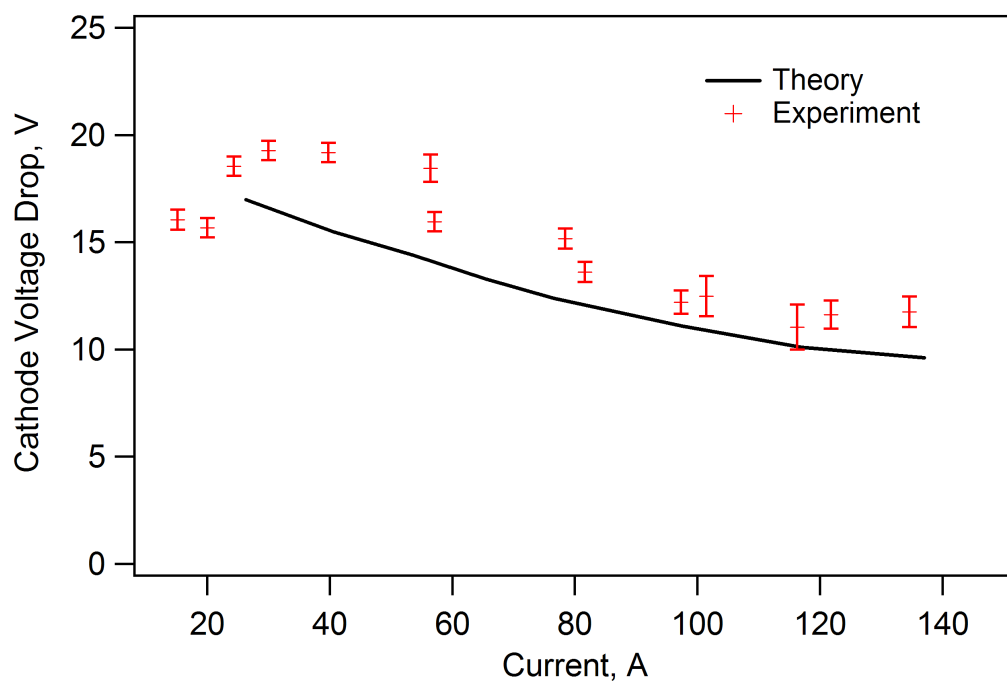


Figure 5.15: Comparison of cathode voltage drop as a function of current density for the 6 mm SCHCs operated at 0.4 mg/s.

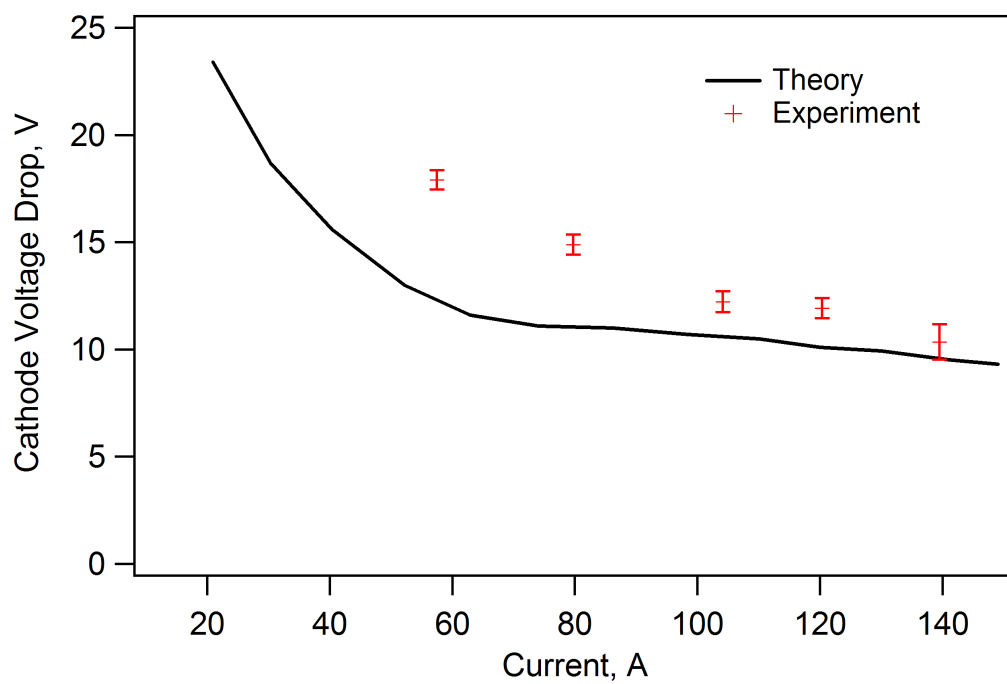


Figure 5.16: Comparison of cathode voltage drop as a function of current density for the 6 mm SCHCs operated at 1.0 mg/s.

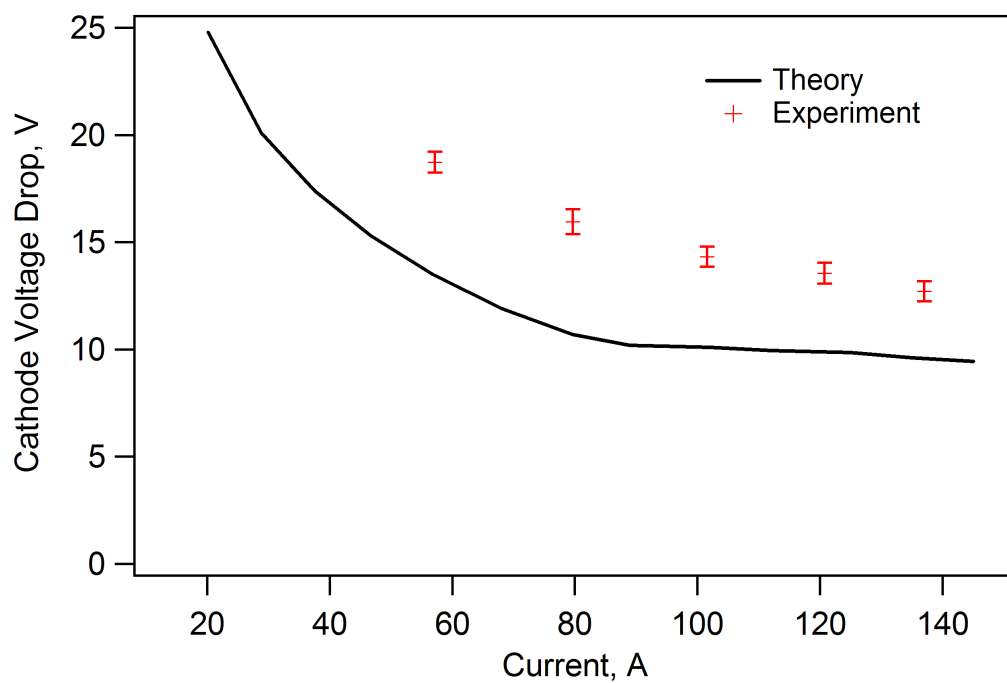


Figure 5.17: Comparison of cathode voltage drop as a function of current density for the 6 mm SCHCs operated at 1.4 mg/s.

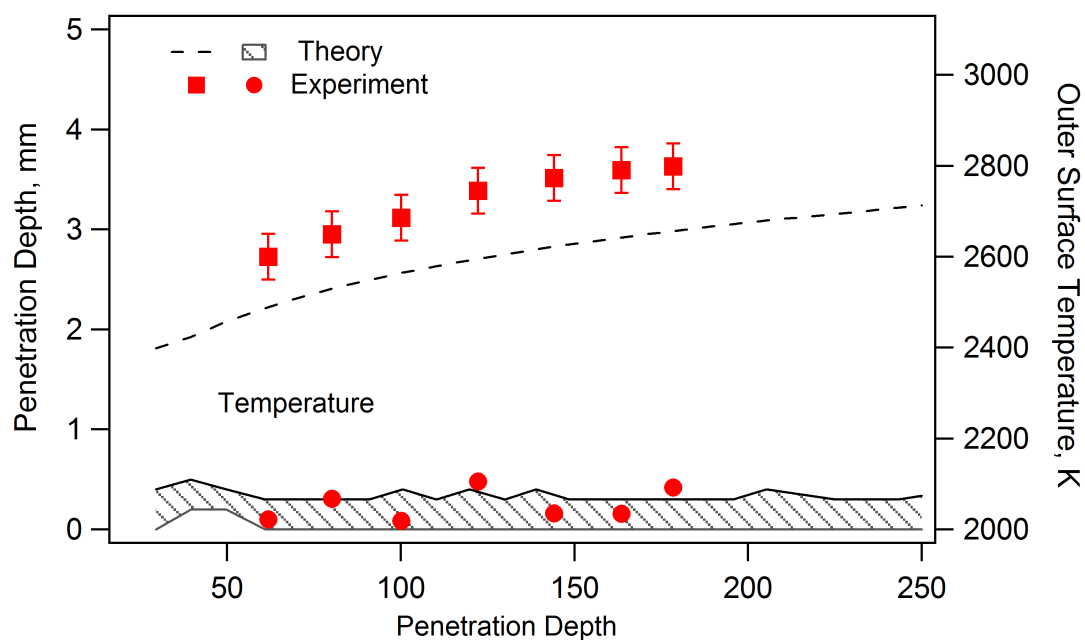


Figure 5.18: Comparison of cathode temperature and penetration depth as a function of current density for the MCHC operated at 0.4 mg/s.

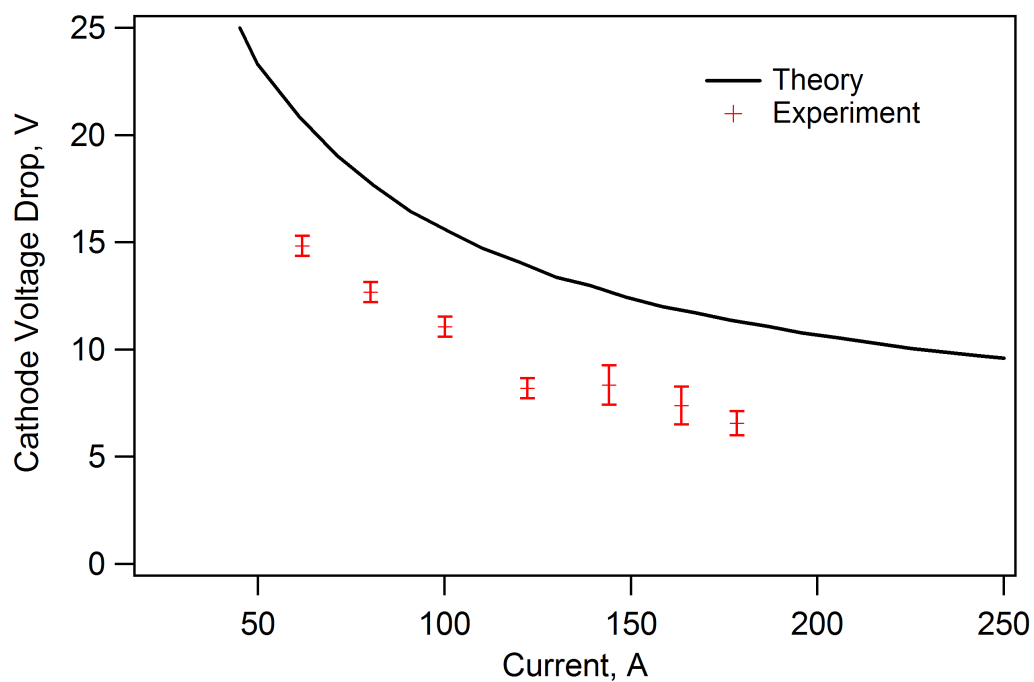


Figure 5.19: Comparison of cathode voltage drop as a function of current density for the MCHC operated at 0.4 mg/s.

5.15 Effect of Non-equilibrium Excitation and Ionization

Here we discuss the significance of the non-equilibrium excitation and ionization model. The function of this model is to *directly* calculate the ionization rate and ion density from the collisions with thermal and thermionic electrons, a method previously only applied to hollow cathodes by Ferreira and Delcroix [44]. However, they did not include collisions of electrons with all of the significantly populated excited states and they used an approximation for the collisions of thermal electrons with the excited states. In addition, their model could not be applied to the lithium plasma. Other researchers either indirectly calculated the ionization rate and ion density based on the ion flux to the cathode wall [52, 58, 32, 33] or assumed that the plasma was fully ionized [26, 47, 48].

Our desire was to model, as closely as possible, the effect the high-energy thermionic electrons have on the ionization rate and ion density. The non-equilibrium excitation and ionization model determines the collision rates for every populated state with thermal and thermionic electrons, which cannot be accomplished with equilibrium models or by assuming a fully ionized plasma. Our results determined that in a fully ionized plasma, 10% of the thermionic electrons contribute to excitation and ionization before colliding with thermal electrons or ions, and in a less than fully ionized plasma (near the lower current limit of optimal operation) the fraction of thermionic electrons that contribute to excitation and ionization increases with decreasing ionization fraction. This demonstrates the significance of non-equilibrium processes. Other benefits from our formulation are that the model includes spontaneous radiation calculations and that the formulation using rates can be consistently included in the relations for fluxes into and out of the channel, as well as into the cathode wall.

If the ionization fraction was determined by Saha equilibrium, the results likely would have been very similar, especially for cathodes operating in optimal mode. We know this because the collision rates for excitation and deexcitation between the thermal electrons and the neutral atoms are great enough for the assumption of equilibrium to be appropriate

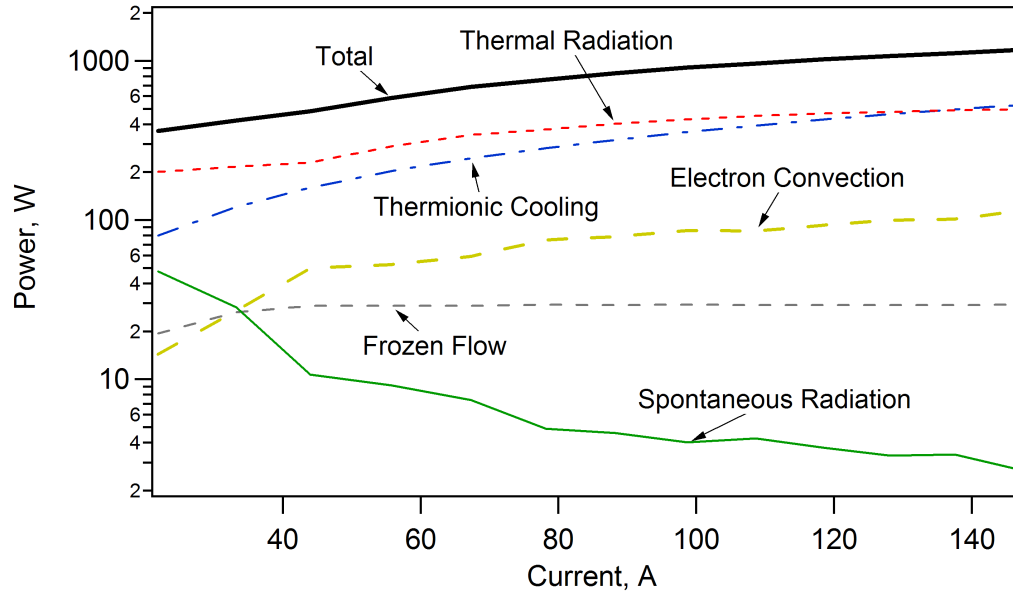


Figure 5.20: Power loss mechanisms of the 4 mm cathode operated at 0.4 mg/s.

if the thermionic electrons are neglected. The primary difference would be a slightly increased electron temperature (a few percent) because the inelastic collisions would have to be accomplished by only the thermal electrons to maintain full ionization. The secondary effects of this would be to increase the Bohm velocity, and, hence, decrease the required ion density. This would decrease the penetration depth and increase the cathode voltage drop, but would not affect the cathode temperature. The effects described above are all small (a few percent change from the non-equilibrium model) for hollow cathodes operating in optimal mode.

5.16 Theoretical Results and Insights

The theoretical model provides several insights into hollow cathode operation including those presented in section 5.14. Here, we briefly summarize other predictions from the model, including the electron temperature and ionization fraction. The insights include the relative importance of power loss mechanisms, the physical cause of lower voltage in an MCHC compared to an SCHC, and the minimum possible cathode voltage.

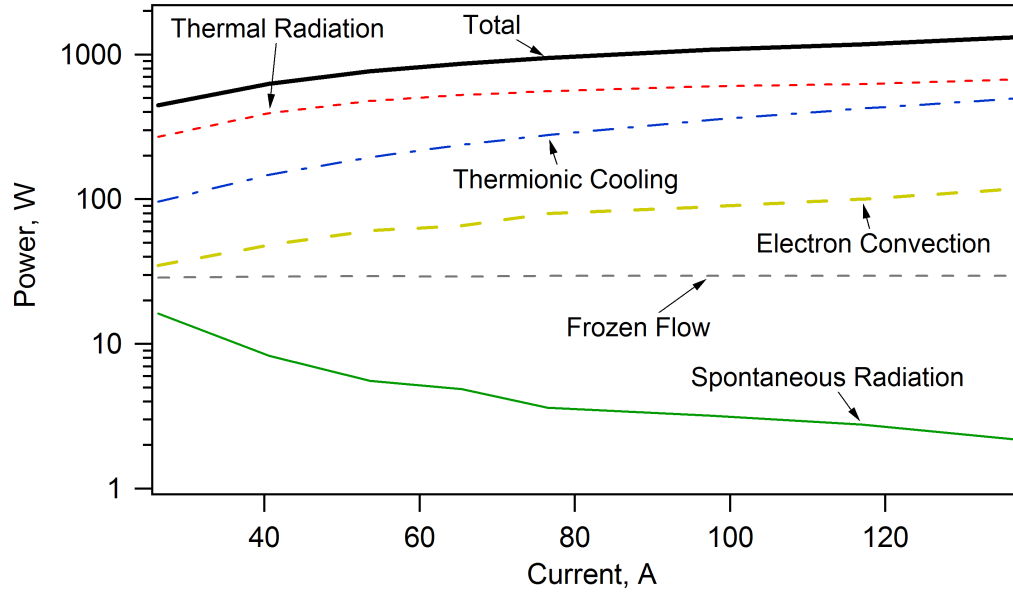


Figure 5.21: Power loss mechanisms of the 6 mm cathode operated at 0.4 mg/s.

The predicted electron temperature was 0.5 ± 0.1 eV in the cases of plasma penetration and slightly less with no penetration. This value is similar to the temperature measured via emission spectroscopy and the temperature that produces full ionization in a lithium plasma [108]. The ionization fraction was predicted to be greater than 95% in the cases with plasma penetration. These results validate the assumption of a fully ionized plasma with an electron temperature of 0.5 eV in the analysis of the experimental data (sections 4.3.3 and 4.3.4), which can be used for simplified analysis of lithium-fed hollow cathode operation by future researchers.

The model also demonstrated that the plasma electron reverse current was small in the active zone. The results also indicated that in optimal mode the thermionic electrons do not directly exit the active zone because of the high plasma density. Only at low current or high flow rate, where the ion density is low, is it possible for the thermionic electrons to escape before an inelastic collision.

The power consumed by the cathode is important because it decreases the overall efficiency of a thruster. The cathode voltage fall adds to the thruster discharge voltage without producing useful thrust. Therefore, it is worthwhile to evaluate the power loss mechanisms

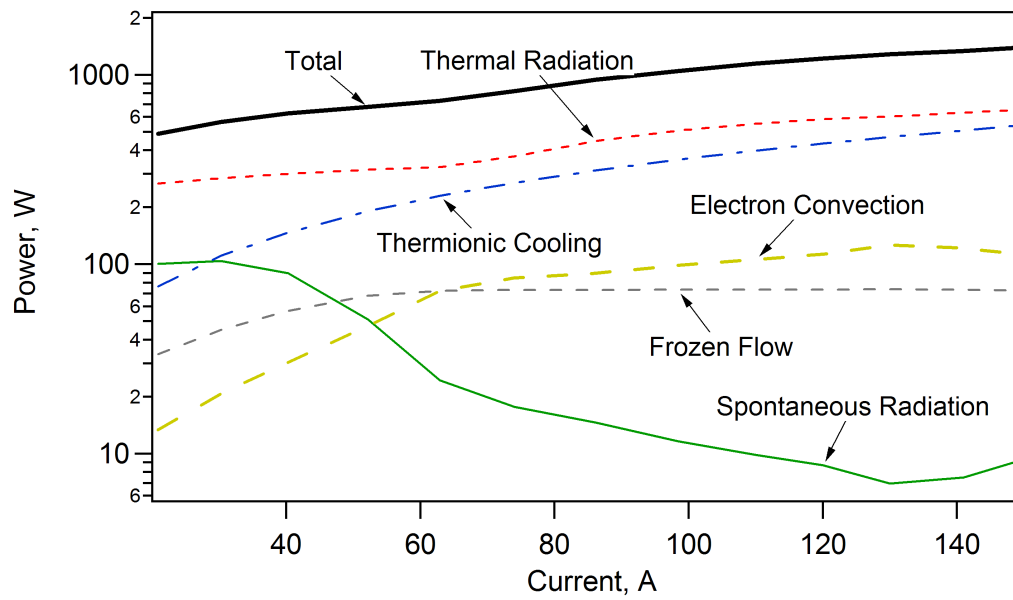


Figure 5.22: Power loss mechanisms of the 6 mm cathode operated at 1.0 mg/s.

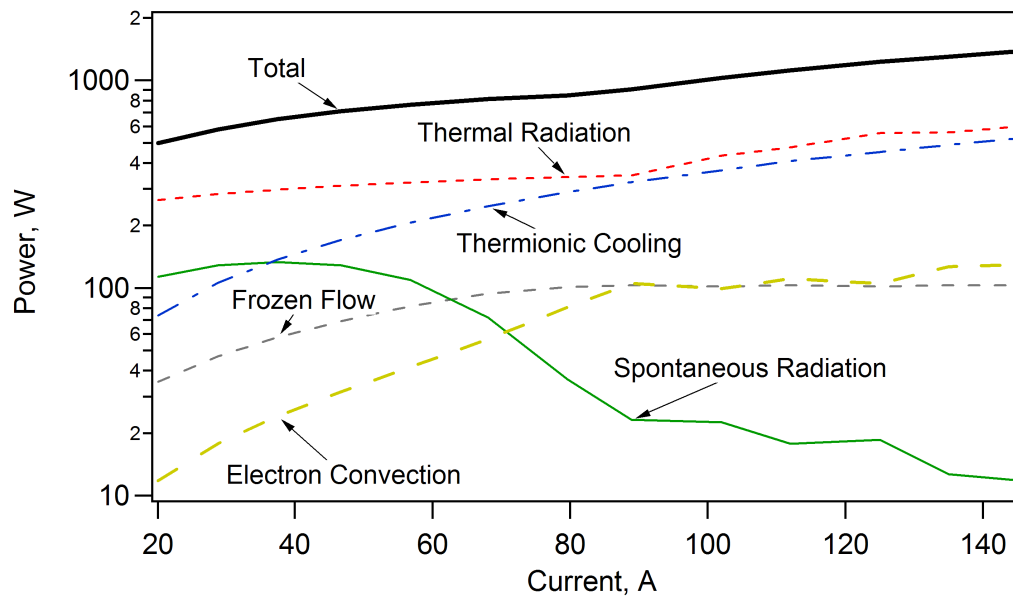


Figure 5.23: Power loss mechanisms of the 6 mm cathode operated at 1.4 mg/s.

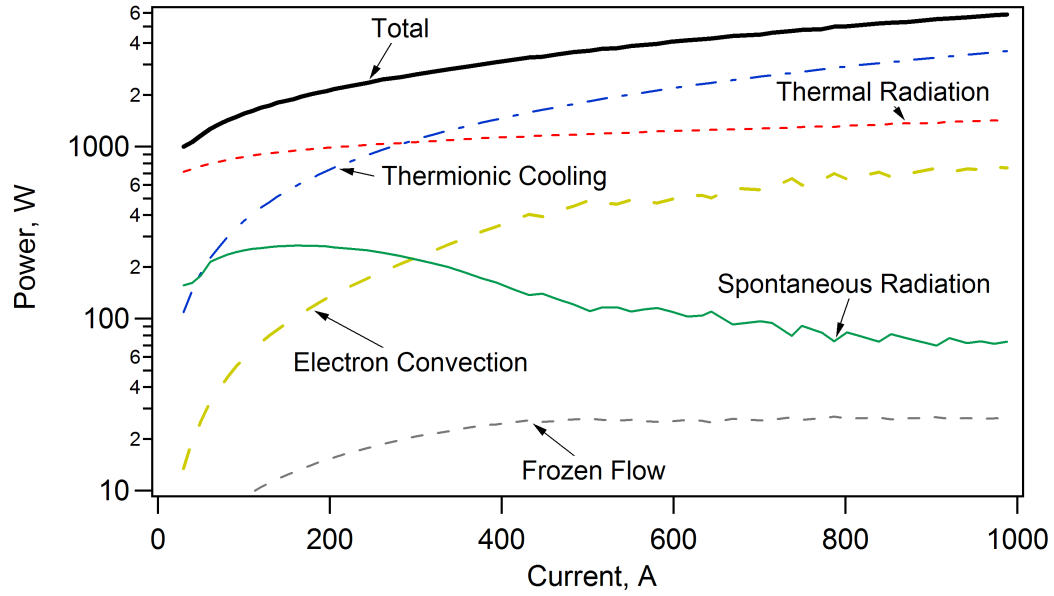


Figure 5.24: Power loss mechanisms of the MCHC operated at 0.4 mg/s.

in the SCHC and MCHC. The mechanisms are thermal radiation, thermionic electron cooling, electron convection, frozen flow, and spontaneous radiation, as shown in figures 5.20, 5.21, 5.22, 5.23, and 5.24. It can be seen that radiation and thermionic cooling are the primary power loss mechanisms. The electron convection and thermionic cooling power losses increase directly with current. This is because power of thermionic cooling is the product of current and effective work function, which varies by only a few percent over the range of operating parameters used in this analysis. The power lost to electron convection depends directly on current and electron temperature. The electron temperature is nearly constant at 0.5 eV. The power lost to electron convection and thermionic cooling cannot be reduced, except by coating the surface with a low work function material.

The frozen flow power loss increases with current until it reaches a constant value, as seen in figures 5.20, 5.21, 5.22, 5.23, and 5.24. The frozen flow power loss is greater at low current because the plasma is not fully ionized and the ionization fraction increases with current. There is no significant plasma penetration when the plasma is less than fully ionized, which corresponds to the cathode not operating in optimal mode. The power loss due to spontaneous radiation is also large when the plasma is less than fully ionized. This

is because the population of excited neutral states are large and the excitation collision rate of those states is less than the radiation rate, allowing spontaneous radiation. For cathodes operating in the optimal mode, the frozen flow and spontaneous radiation power losses are relatively small (less than a few percent).

The power lost to thermal radiation is weakly dependent on current. This is because the thermionic current density depends exponentially on cathode temperature, and, therefore, large current density increases result in small temperature increases. The increases seen in the figures are primarily due to the increased exposed area as the plasma penetration depth increases with current. A comparison of figures 5.20 and 5.21 shows that thermal radiation is greater in the 6 mm cathode than in the 4 mm one. This is because the larger surface area of the 6 mm SCHC radiates more power. The thermal radiation power lost in the MCHC, shown in figure 5.24, is relatively smaller than that lost in the SCHCs when compared to the total power. The MCHC decreases the power lost to radiation by having a reduced exposed area relative to the active zone area. The power lost to thermal radiation in the MCHC operating in optimal mode is less than 20% of the total power, rather than being about 50% in the SCHCs. This results in a lower cathode voltage fall in the MCHC.

The minimum possible cathode voltage fall of an MCHC can be determined by evaluating the power loss mechanisms as a function of increasing current. The primary power loss mechanism is thermionic cooling, which is the product of the current and effective work function, ϕ_{eff} . As shown in figure 5.24, the other mechanisms are relatively small. The next most significant power loss mechanisms are thermal radiation and electron convection, both being 10-20% of the total power. Therefore, the minimum cathode voltage fall is approximately $1-2\phi_{eff}$.

5.17 Summary of Theoretical Results

The general agreement between the theoretical and experimental results demonstrated that the most relevant processes were included in the model. We also demonstrated that the MCHC operates at a reduced voltage because of reduced power lost to thermal radiation, and has a lower temperature because of the increased area for the arc to attach to the cathode surface in the active zone. The models also were able to capture the trends of temperature, penetration depth and cathode voltage drop with channel diameter, mass flow rate, and current.

The SCHC and MCHC models successfully predicted the cathode temperature, cathode voltage drop, penetration depth, electron temperature, and ionization fraction as a function of mass flow rate, current, channel diameter, and, in the case of the MCHC, the number of channels. This accomplishes the goal set forth in the introduction: to predict the dependent operating parameters of the MCHC and SCHC.

Chapter 6

Design Procedure for an MCHC

In light of the insights gained from the experimental and theoretical studies presented in the previous chapters, we outline a procedure for designing the MCHC of an LiLFA, and illustrate the procedure on an application of practical interest. The current, J , mass flow rate, \dot{m} , and outer radius of the cathode, $r_{M,o}$, are assumed to be set by the thruster design, which leaves two remaining parameters: the individual channel diameters and their number. The cathode material is limited to tungsten for high-current operation with any significant lifetime. Of course, the number of channels is limited by the size of the cathode, their separation distance, and the minimum reasonable channel diameter. There are also two practical constraints on the design of an MCHC: (1) a maximum temperature that is determined by the melting point or an evaporation rate limitation of the cathode material, tungsten, and (2) the need to operate in the optimal hollow cathode mode. The maximum evaporation rate is determined by the desired lifetime of the thruster and the fraction of cathode material that can be lost without affecting performance. The MCHC must also operate in the optimal mode (i.e. have plasma penetration) to have a low cathode voltage drop and a fully ionized plasma exiting the channel.

First, we demonstrate that there is an optimal cross section of the channels for a given MCHC outer radius. This streamlines the cathode design process and makes it easy to

determine if the MCHC is capable of conducting the required current while operating at less than the maximum temperature. Next, we detail the procedure for designing an MCHC that meets the constraints. The procedure is applied to an LiLFA in section 6.3. Finally, we comment on the benefits and limitations of our design process.

6.1 Optimum Channel Cross Section

The optimum ratio of the cross section of all the channels to the total area encircled by the MCHC, Φ^* , can be determined independently of the design parameters. The general ratio is expressed as

$$\Phi = \frac{N_c \pi r_c^2}{\pi r_{M,o}^2}, \quad (6.1)$$

where N_c is the number of channels and r_c is the radius of the individual channels. The calculation of the arc attachment area in an MCHC results in a relation that is independent of N_c and r_c , from which an optimum Φ can be determined. The area of arc attachment, $A_{z,M}$, is a function of the channel circumference, the number of channels, and the active zone width, w ,

$$A_{z,M} = 2\pi r_c^2 N_c w = 2\pi r_c^2 N_c \Theta t_c, \quad (6.2)$$

where the active zone width is equal to Θ wall thicknesses, t_c , between the channels. The dependence of the active zone width on the wall thickness is supported by the theoretical and experimental findings of our research. Equation (6.2) reduces to

$$\frac{A_{z,M}}{\pi r_{M,o}^2} = 2\Theta (\Phi^{1/2} - \Phi) \quad (6.3)$$

when equations (5.72) and (6.1) are substituted for t_c and N_c , respectively. This expression is the ratio of attachment area to the total cross section of the MCHC, and depends only on Φ and Θ . This ratio has a maximum at $\Phi^* = \frac{1}{4}$, which is independent of Θ . This is a universal optimum that comes about because the active zone width directly depends on wall

thickness. There is a maximum channel radius that allows for an approximately uniform distribution of channels in the cathode, which we take to be approximately $\frac{1}{10}$ of the MCHC outer radius.

We can determine the maximum attachment area of an MCHC and show that an MCHC always operates at a lower temperature than an SCHC of the same outer diameter at the same current. The maximum attachment area is given by equation (6.3) using the value of Φ^* for Φ and taking $\Theta = 6$, which is shown to be the correct value in section 5.11,

$$A_{z,M}^* = 3\pi r_{M,o}^2. \quad (6.4)$$

It can be shown that for an SCHC ($N_c = 1$) to provide the surface area of an optimally designed MCHC, the wall thickness would have to be greater than the outer radius, clearly an impossibility. Therefore, an MCHC provides a greater area for the arc to attach to than the SCHC. This reduces the current density, and, hence, the temperature.

The range of Φ that can practically be used depends on how the holes are created. If many holes are drilled into a solid rod, the highest possible fraction occurs with the channels touching, which is approximately 0.7 - 0.8 [109]. Since the channels cannot touch, the maximum possible Φ is somewhat less than 0.7. A “spaghetti packet” MCHC, which is a tube filled with tungsten rods that has the gas flowing between the rods, has a maximum of $\Phi = 0.2 - 0.3$, very close to optimal.

6.2 MCHC Design Procedure

The MCHC design procedure provides a method for determining the number of channels and their diameter that leads to the longest lifetime and operation in optimal mode. It also determines if the current or mass flow rate are too great for the given cathode radius. The procedure is as follows:

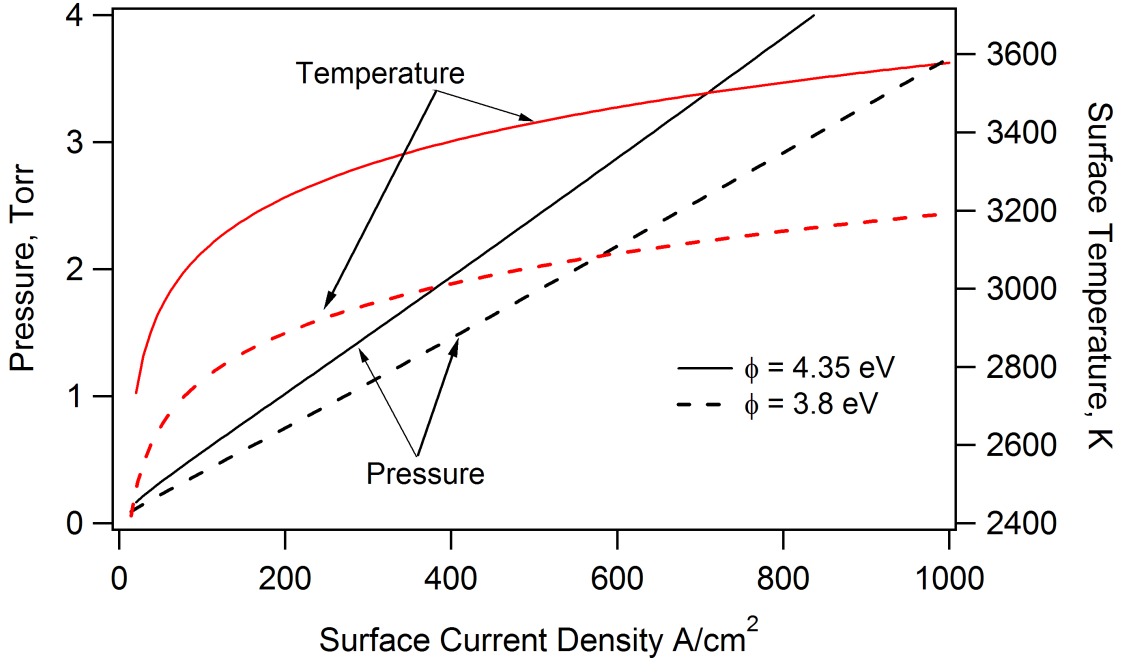


Figure 6.1: Plasma pressure and cathode temperature as a function of current density assuming 10 V cathode potential and 0.5 eV electron temperature and work functions of 3.8 eV and 4.35 eV.

1. Select the maximum operating temperature, T_{max} , based upon either the lifetime requirements of the cathode or the melting temperature of the cathode material (see ref. [13] or figure 1.2 for tungsten).
2. Calculate the maximum current attachment area, $A_{z,M}^*$, using equation (6.4) and the minimum current density,

$$j_{min} = \frac{J}{A_{z,M}^*}. \quad (6.5)$$

3. Calculate the cathode temperature, T_c , and plasma pressure, p_r , required for the minimum current density. This can be approximately calculated from a current and power balance of the cathode surface. The analysis is similar to that in section 4.3.3, except that thermal radiation is neglected because it is relatively small in high-current MCHCs. This approximation results in a slight overestimate of the temperature and

current density. The hot cathode surface emits electrons with a current density, j_{th} , following the Richardson-Dushman equation [93],

$$j_{th} = A_R T_c^2 \exp\left(-\frac{e\phi_o}{k_B T_c}\right), \quad (6.6)$$

where A_R is an empirical constant for the cathode material ($A_R = 70 \text{ A}\cdot\text{cm}^{-2}\text{K}^{-2}$ for tungsten) and ϕ_o is the material work function. The total current density, j , is given by

$$j = j_{th} + \frac{p_r}{k_B T_c} v_B \exp(-1/2), \quad (6.7)$$

where v_B is the Bohm velocity [equation (4.6)] and $\exp(-1/2)$ accounts for the reduced density at the sheath/presheath boundary. The power balance of an MCHC has two primary terms: the kinetic and potential energy delivered by the ions as they impact the wall and cooling via electron emission,

$$j_{th} e \left(\phi_o + \frac{3}{2} k_B T_c \right) = \frac{p_r}{k_B T_c} (V_c - \phi_o + \phi_i) v_B \exp(-1/2), \quad (6.8)$$

where ϕ_i is the ionization energy. The temperature and pressure cannot be found as a function of total current density, so we present the results in figure 6.1.

The physical parameters of work function, electron temperature, and cathode voltage drop must be based on previous experimental and theoretical results for lithium-fed cathodes, which are presented in chapters 4 and 5. The electron temperature within the channels and the cathode voltage drop are taken as approximately 0.5 eV and 10 V, respectively. The work function is more difficult to determine, because of lithium contamination effects. A conservative value would be that of pure tungsten, $\phi_o = 4.35 \text{ eV}$, but $\phi_o = 3.8 \text{ eV}$ could be appropriate for ground-based research devices, as was the case in our experimental results (see section 4.3.3). Also, the use of a propellant additive, such as barium, could reduce the work function.

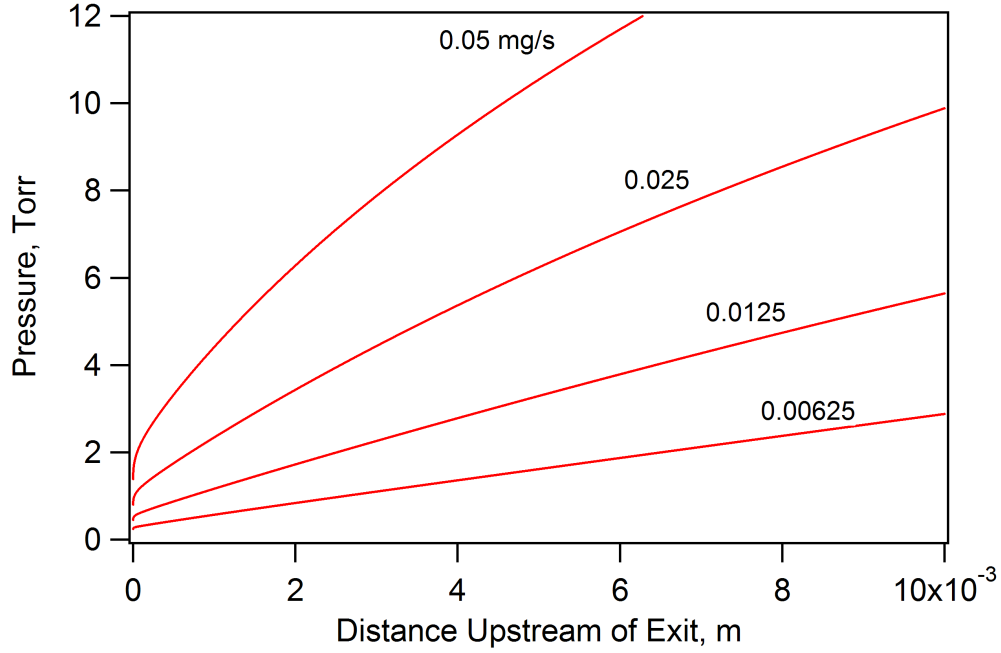


Figure 6.2: Pressure profile of a 1 mm diameter channel

4. Determine if the temperature constraint is met by comparing the maximum temperature, T_{max} , and that calculated at $j = j_{min}$, as found in figure 6.1. If the latter is greater than the former, it is not possible to design an MCHC to the given specifications. The design parameters of the MCHC, such as the outer radius, total current, or maximum temperature, must be changed or an additive must be mixed with the lithium to reduce the work function (see ref. [17]). If the temperature constraint is met, continue to the next step.
5. Select the individual channel radius and calculate the number of channels using equation (6.1) so that the pressure within the channels can be determined. The gas pressure, p , shown in figure 6.2 and the required pressure, p_r , must be equal within the channel at a location 1 to 10 channel radii upstream of the exit. The optimum number of channels depends on the mass flow rate because increasing the number of channels increases the pressure by restricting the flow. The mass flow rate through each

channel, \dot{m}_c , is equal to the total rate divided by the number of channels,

$$\dot{m}_c = \frac{\dot{m}}{N_c}. \quad (6.9)$$

This mass flow rate is used to determine the pressure within each channel. Since there is no “best” number of channels or radius, use figure 6.2 as a reference for deciding the on the radius. If the pressure at distances from 1-10 r_c , as shown in figure 6.2, is greater than p_r , select a smaller number of channels, or more channels for a lesser pressure. Next, calculate the pressure within the channel as described in section 5.1 using the new values for \dot{m}_c and r_c . If the pressure is less than that required, go to the next step. If the pressure is greater than that required, skip to step 7.

6. If the gas pressure is less than the required pressure, increase the number of channels and recalculate the gas pressure. Repeat this process until the channel size is too small to practically manufacture or the pressure condition is met. If the pressure is still too low, then decrease Φ , which decreases N_c , increases j , but does not affect r_c . The cathode temperature must be checked in figure 6.1 because j , p_r , and T_c will increase weakly with decreasing Φ . Repeat this process until the gas pressure matches the required pressure. Skip the next step.
7. If the gas pressure is greater than the required pressure, there are three possible methods for getting the correct pressure: (1) increase channel diameter, (2) increase Φ , and (3) reduce the mass flow rate through the MCHC channels. The first and second choices offer trades between cathode voltage drop and cathode temperature, while the third is an extreme choice that should be considered last. It is beneficial to use the largest possible number of channels because that configuration decreases the cathode voltage fall, as shown in section 5.11. Therefore, if the cathode temperature can be increased it would be better to increase Φ than decrease N_c . The value of Φ can be increased to a practical maximum of approximately 0.5, which increases the current

density by 17%. This both increases the required pressure and decreases the pressure within the channels. If increasing Φ did not result in the correct gas pressure, then the number of channels must be decreased or the mass flow rate must be changed. If possible, reduce the gas flow through the MCHC and allow it to enter the thruster elsewhere or design one large channel to reduce the flow through the smaller ones.

Finally, if you wish to refine your design, apply the complete theoretical model outlined in chapter 5 to determine the voltage and better estimate the cathode temperature and plasma penetration depth.

6.3 Application to an LiLFA

In this section present the application of the procedure outlined above to the MCHC proposed for a 250 kW LiLFA that was designed by a Princeton University-led research team. The cathode was specified to operate at 2750 A and 80 mg/s, have a diameter of 5.6 cm, and have a three year lifetime. The enumeration of the steps in this section directly corresponds to the step number in the procedure outlined in section 6.2.

1. We used the lifetime requirement and the cathode diameter to estimate the maximum temperature. Since the cathode has a diameter of many centimeters, we assumed that a maximum of a few tenths of a millimeter (~ 0.3 mm) should erode. Using figure 1.2 and the density of tungsten, 19.3 g/cm^3 , the maximum temperature, T_{max} , was calculated to be 2600 K.
2. The minimum current density, j_{min} , was determined to be 37 A/cm^2 .
3. The cathode temperature and ion pressure were found from figure 6.1 to be 2600 K and 0.2 Torr, respectively, when the surface work function was taken to be 3.8 eV. If the work function of pure tungsten would have been assumed, $\phi = 4.35$, then the temperature and pressure would have been 2900 K and 0.2 Torr, respectively.

Table 6.1: Number of channels and flow rate per channel for the LiLFA cathode.

Diameter (mm)	N_c	\dot{m}_c (mg/s)
1	783	0.10
2	195	0.41
3	87	0.92
4	48	1.67
5	31	2.58
6	21	3.81

4. It was necessary to assume a reduced work function to lower the surface temperature to match the requirement set in step 1. The LiLFA design calls for the addition of barium specifically to increase the cathode lifetime. The cathode would not meet the lifetime requirement without the addition of barium, as can be seen by the 300 K greater temperature that results from a pure tungsten surface, as shown in figure 6.1.
5. A channel diameter of 1 mm gives 783 channels and a mass flow rate of 0.1 mg/s through each channel. That mass flow rate exceeds those shown in figure 6.2 because the pressure is greater than 2 Torr throughout the channel. The number of channels, N_c , and the mass flow rate per channel, \dot{m}_c , are summarized in table 6.1 for channel diameters from 1 to 6 mm. The mass flow rate in the channels is also greater than that plotted in figures 5.4 and 5.5, although it is only 10% greater than the highest mass flow rate shown for a 6 mm channel. Therefore, none of these channel diameters will allow the cathode to operate in optimal mode. We continue the cathode design with step 7.
6. This step in the design procedure is skipped because pressure in the channels is greater than the required pressure.
7. Since the pressure within the channels was calculated to exceed the 0.2 Torr limit determined in step 3 for the channel diameters presented in table 6.1, we considered which of the three methods presented best fit the LiLFA application. The first

method involves decreasing the number of channels. The MCHC cannot have much less than 20 channels because the assumptions of even plasma penetration and the independence of Φ from N_c would not be valid, see section 6.1. Therefore, the maximum channel diameter is approximately 6 mm. The second method involves increasing the number of channels by increasing Φ . This increases the current density by decreasing the attachment area, an operational choice that should not be made when lifetime and temperature are very important. The third method, a reduction of the mass flow rate through the channels, was the best option. The extra lithium flow could be routed through a large central channel in the MCHC or to the anode or allowed to escape radially at a location upstream of the channels. The selection of the lithium flow path and the amount of flow depends on the overall thruster design and cannot be addressed here. As our MCHC data have shown, the MCHC can operate at low cathode voltage drop and temperature even when the internal pressure exceeds the optimal value. More research should be conducted on high-flow-rate MCHCs to determine how far above the optimal pressure these cathodes can operate without excessive erosion.

In summary, an MCHC can be designed for a 250 kW LiLFA that will operate for the required lifetime if the propellant has a low work function additive and some of the lithium is diverted from the main current carrying channels. The initial design of the cathode for the LiLFA has 5 or 6 mm channels, requires a barium additive, and possibly has to reroute a portion of the lithium flow through a large channel or away from the cathode. Further research on high-flow-rate MCHCs is required to determine the maximum lithium flow that gives near-optimal operation and accurate estimates of erosion near the cathode tip.

6.4 Comments

In this chapter we have shown that it is possible to design a cathode that has the maximum possible lifetime (i.e. lowest temperature). We also showed that in some cases the MCHC is unable to supply the required current at less than the desired temperature. In this case, changes must be made to the requirements placed on the cathode design or there must be low work function additives mixed into the propellant. In the case of high mass flow rate, there are many possible options for optimal cathode design. We do not discuss the details of how to reduce the gas flow through the channels or how to size a large channel to reduce the flow through the smaller ones. This is because the gas flow models are not accurate upstream of the active zone, and this makes it impossible to determine the division of the flow through different size cathodes. Most importantly, we do not know how far the internal pressure can be above optimal and still operate near the optimal mode.

Chapter 7

Conclusions

This lithium-fed MCHC and SCHC study has provided (1) measurements of the cathode potential at the cathode tip, cathode temperature, and plasma penetration depth, (2) insights into the plasma conditions within the cathode based on the experimental data, (3) a theoretical model of the physical processes in a hollow cathode, and (4) a procedure for designing an MCHC which was applied to a thruster cathode. The goal of the research presented in this dissertation was to develop a theoretical model of the lithium-fed multichannel hollow cathode that predicts cathode voltage drop, temperature, and plasma penetration depth depending on the physical conditions of gas mass flow rate, cathode material type, cathode outer radius, number of channels, diameter of channels, and current, and to use that model to create a procedure for designing an MCHC. To accomplish that goal we completed a series of lithium-fed hollow cathode experiments that determined the penetration depth, cathode temperature profile, and plasma potential at the cathode tip over an extended range of operating conditions. The experimental results provided new insights into the operation of lithium-fed hollow cathodes, which are summarized in the next section. The new data aided in the development and validation of SCHC and MCHC models capable of predicting cathode operation. We also presented a method for the design of an MCHC, which fulfilled the above mentioned goals. In this chapter, we summarize the experimental and theoretical

results as well as suggest improvements in the experimental diagnostics and different cathode geometries to further clarify the results presented in this study. Finally, we discuss the impact this research could have on LiLFA development.

7.1 Summary of Findings

The results of our lithium-fed SCHC and MCHC experimental campaigns provided data that greatly extended the range of cathode operation studied by previous researchers. Overall, our measurements of plasma potential at the cathode tip and cathode temperature are in the range of those presented in previous studies and the experimental results follow all of the trends found in our theoretical analysis. The significant lithium-fed SCHC and MCHC experimental results presented in this dissertation are:

- The peak temperature is independent of mass flow rate.
- The plasma penetration depth increases with current.
- The cathode voltage fall decreases with increasing current.
- The cathode voltage fall does *not* increase with penetration depth.
- The peak temperature and cathode voltage fall scale with current density at the active zone/cathode surface interface.
- The total voltage is not related directly to cathode voltage fall at high current.

The analysis of the results revealed that:

- The active zone width primarily depends on cathode wall thickness.
- The plasma pressure and density can be determined from cathode temperature.
- The plasma penetrates to a location of optimum plasma density that depends on current and channel diameter.

- In our experiments the surface work function was not equal to that of pure tungsten, but was 3.8 eV.

The detailed theoretical models of the SCHC and MCHC provided insights regarding the processes that occur within those cathodes. The model predicted the correct dependence of penetration depth on current and channel diameter (even though the scaling was not exact). This demonstrated that the plasma density within the channel drives the location of the active zone. The cathode voltage drop and temperature predictions of the model follow the experimental trends and generally match the measured values. Also, the results of the SCHC model demonstrated that radiative power loss is approximately half the total power loss in the cathode. This indicated that the MCHC, which has a reduced fraction of area that radiates relative to the SCHC, operates with a lower voltage because of reduced thermal power losses.

The validated theoretical model also allowed us to formulate a design procedure for the MCHC. The procedure showed that there is an optimal configuration and that an MCHC will always operate at a lower temperature than an SCHC with the same outer radius and current because of a larger surface area for arc attachment. Also, the reduction in radiative power losses decreases cathode voltage drop. The experimental results, theoretical model, and the design procedure have clearly shown why the MCHC operates at a lower voltage and temperature than the SCHC.

7.2 Future Work

Suggestions for future work include improvements in both the experimental apparatus and diagnostics, as well as the theoretical model.

The present study was the first to accomplish measurements of lithium-fed hollow cathodes operating over an extended range of conditions. Suggestions for future diagnostics include a high-speed reciprocating mechanism with accurate positioning of the Langmuir

probe. In our experiments, the plasma potential at the cathode tip measurements with the Langmuir probe were limited by the manual actuation of the probe position. A current-voltage trace could not be obtained because the probe would have melted due to its long residence time in the plasma. Also, lithium coating of the probe could be reduced with short residence times. Because the probe was manually inserted into the plasma, its location could not be accurately known. Therefore, with a high-speed reciprocating system and an accurate positioning mechanism the Langmuir probe would be in the plasma for a shorter time and a current-voltage trace could be obtained at precise locations.

The suggested improvements in the experimental apparatus include operating with a wider range of cathode geometries, greater currents, high-purity lithium, and lithium additives. Experiments with SCHCs should be conducted with various wall thicknesses between 1 - 10 mm, greater currents [$\mathcal{O}(100\text{ A})$], and larger inner radii. This will clarify the experimental trends reported in this dissertation by studying discharges with different active zone widths and greater penetration depths, and a large range of current. More MCHCs with a range of channel diameters should be tested at high current to complete the study of those cathodes. The experimental apparatus and the lithium should be purged of impurities, especially water and oxygen, to reduce the uncertainties caused by having to empirically determine the work function from the measurements. The cathode work function, and hence temperature, could be reduced by mixing additives that coat the surface (such as barium) with the lithium. This could further increase the lifetime of MCHCs, as shown by Ageyev [17].

The understanding of the maximum mass flow rate that allows for optimal cathode operation was not studied here. High mass flow rate pushes the active zone to the end of the cathode, and at some mass flow rate the active zone must decrease in width due to the high pressure and gas velocity. We do not know the details of this process, which could be important in thrusters where a high mass flow rate is required, and it should be studied in detail.

The theoretical model captures the most important characteristics of SCHC and MCHC operation, but improvements could be made to the gas flow model, calculations of the active zone width, especially at penetration depths less than one channel diameter, surface coating, additives to the gas, and contamination. The most important improvement is the calculation of the plasma density within the channel, which is very difficult because of the combination of transitional flow and the plasma effects. Our results over-predict plasma penetration at low mass flow rate and large channel diameters. Since optimal hollow cathode operation requires plasma penetration within the channel, a model of the discharge at high mass flow rate, where the penetration length is less than the active zone width, should be developed. Finally, there should be a detailed study of the effects of lithium contamination and of lithium - barium mixtures that reduce the surface work function.

7.3 Application to the LiLFA

We have shown how to design the MCHC for use in an LiLFA, a primary application of the MCHC. Our experimental results and analysis demonstrated that the MCHC is a better choice for high current operation than the SCHC because of the reduced cathode temperature due to the greater surface area available for arc attachment and lower voltage operation. These differences lead to lower operating temperatures, thus longer lifetime, and higher efficiency of the thruster.

We also found that there is an optimal geometry for an MCHC that provides the greatest surface area for arc attachment and, therefore, the minimum cathode temperature. This allows for an immediate determination of whether or not the MCHC can meet the lifetime and voltage requirements of the thruster and its mission.

Appendix A

Propulsion Options for Missions to Mars¹

In this appendix, high-power electric propulsion options are surveyed in the context of cargo and piloted missions to Mars. A low-thrust trajectory optimization program (RAPTOR) is utilized to analyze this mission. Candidate thrusters are chosen based upon demonstrated performance in the laboratory. Hall, self-field magnetoplasmadynamic (MPDT), self-field lithium Lorentz force accelerator (LiLFA), arcjet, and applied-field LiLFA systems are considered for this mission. In this first phase of the study, all thrusters are assumed to operate at a single power level (regardless of the efficiency-power curve), and the thruster specific mass and power plant specific mass are taken to be the same for all systems. Under these assumptions, for a 7.5 MW, 60 mT payload, piloted mission, the self-field LiLFA results in the shortest trip time (340 days) with a reasonable propellant mass fraction of 57% (129 mT). For a 150 kW, 9 mT payload, cargo mission, both the applied-field LiLFA and the Hall thruster seem reasonable choices with propellant mass fractions of 42 to 45% (7 to 8 mT). The Hall thrusters provide better trip times (530-570 days) compared to the applied-field LiLFA (710 days) for the relatively less demanding mission.

¹The work in this appendix was the contribution of the author and K. Sankaran, A. D. Kodys and E. Y. Choueiri of Princeton University.

A.1 Introduction

For the first time in over a decade NASA has been given the green light to pursue nuclear options for spacecraft propulsion. The Nuclear Space Initiative (NSI), approved under NASA's FY2003 budget, is a multi-year program expected to total \$2 billion with one goal being the development of space nuclear systems capable of 10-100 kW of power in space over the next ten years [110]. This initiative promises to open up the outer solar system to exploration by reducing spacecraft weight (propellant mass savings) and transit times (5 years versus 10 years to Pluto, with respect to chemical thrusters, at high power levels), and by providing a power supply to do science once the spacecraft arrives at the destination. As a result, the surface of Mars may now be accessible for long-term robotic and human exploration. This paper describes the first-phase of our study comparing near-term propulsion options for a two-stage (cargo & piloted) mission to Mars.

Because of their high exhaust velocities, electric propulsion (EP) systems can provide significant propellant savings over chemical thrusters for high Δv missions [10] like this one, and have been popular in such mission studies. With the success of the ion thruster as the primary propulsion system on the Deep Space 1 mission [111], and other recent EP enabled missions, the field of electric propulsion has now come of age as a reliable and efficient way of accomplishing relatively low energy missions. Currently, various types of EP devices, resistojets, arcjets, ion thrusters, Hall thrusters, and to a lesser extent, pulsed plasma thrusters, are routinely used for station keeping and maneuvering satellites. However, research on high-power electric propulsion has stagnated over the last two decades. As a consequence of the revival of interest in nuclear space systems, high-power propulsion options, first investigated in the 1960s to early 1980s (cf. ref. [9]) and then abandoned or continued at lower power levels due to lack of power in space, are receiving renewed attention.

A.1.1 Review of Previous Studies

Since the dawn of the space age, many mission studies have been performed on expeditions to Mars. Stuhlinger et al. [8] were among the first to propose the use of electric propulsion for missions of this kind. In the last two decades, several noteworthy studies have examined the advantages and disadvantages of various propulsion systems for a mission to Mars. We will briefly survey some piloted and cargo mission studies.

Coomes et al. [112] propose the use of a magnetoplasmadynamic thruster (MPDT - to be described in section A.3.2) operating at a power level of 6 MW for a piloted mission, and calculate a trip time of 600 days for Earth to Mars at this power level. King et al. [113] also examine the use of a MPDT for a similar mission and propose systems with input power up to 200 MW that can accomplish Earth-Mars round trip in less than a year. It is also suggested that MPDTs can offer trip time savings over chemical thrusters at power levels of 10 MW or higher. Gilland et al. [114] compare the use of MPDTs versus an array of ion thrusters for a similar mission, using a curve-fit for η_T vs. I_{sp} for the performance of these thrusters. Clark et al. [115] examine a 8 MW piloted (35 mT) fast trajectory mission for trip time, safety and reliability, abort options, and other costs. Pelaccio et al. [116] provide a technology readiness assessment of various thrusters for such a mission.

Clark et al. [115] also consider 4 MW minimum energy trajectory for a Mars cargo mission. They estimate that an array of ion thrusters offer significant mass savings over nuclear thermal systems, while maintaining comparable trip times. Frisbee et al. [117, 5] assess the technology readiness and development requirements for dynamic power conversion, power processing, and thrusters for Mars cargo mission. Polk et al. [118] examine the lithium Lorentz force accelerator technology (LiLFA - to be described in section A.3.2) for reusable orbit transfer vehicle with a parametric study of required power level, specific mass of power plant and performance to focus technology development. Noca et al. [119] consider robotic missions to outer planets with power levels ranging from 100 kW to 1 MW, using ion engines. Woodcock et al. [120] consider three outer planetary missions with small

payloads, and consider the use of various propulsion systems.

As described above, a lot of work has been done on investigating propulsion options for missions to Mars. However, the abovementioned studies either perform the analysis with *extrapolated data*, and/or look at the problem from the perspective of research guidelines for a *specific thruster*. Therefore, there is a need for a comparison of multiple propulsion options for this mission using measured performance data only, and that is the goal of this paper.

A.1.2 Outline

The two-stage human Mars mission, chosen for this study, is described in detail in section A.2. This mission will benefit from nuclear power by yielding mass savings and reduced trip time, due to the ability to operate at higher power than would be otherwise available. In section A.3, we will examine some of the existing EP devices capable of taking advantage of near-future nuclear power systems, and we will discuss the current status of the technology and current trends in research. As will be described in section A.3.1, we will limit this study to thrusters that have been successfully operated (thrust measured) in the laboratory to keep with the near-term (10-20 years) spirit of the study and to perhaps provide some insight into technology drivers. The results of the mission analysis will be presented in section A.4. Following that, in section A.5, we will briefly discuss the propulsion options that were not considered in this analysis.

A.2 Mission Description

In this study we consider a two-stage mission to Mars. The power available for each stage of the mission was chosen in accordance with the near-term technology assessment of the thrusters, though many of the studies mentioned in section A.1.1 consider missions with larger power supplies.

In the first stage, 90 metric tons of cargo would be transported from Earth orbit to Mars orbit. The propulsion systems for this mission would have a total power supply of $\mathcal{O}(100 \text{ kW})$ available, and the trip time is expected to be approximately two years. Because of the relatively low power available in this mission, the total payload of 90 mT would be transported in ten vehicles (each with a payload of 9 mT) to accomplish the trip within two years. The propulsion system for this stage of the mission should accomplish this with minimum propellant mass.

The second stage would carry the crew and supplies, totaling 60 metric tons of payload, and would be launched approximately two years after the launch of the cargo stage. The propulsion systems for this mission would have a total power supply of $\mathcal{O}(1 \text{ MW})$ available, and the trip time must be less than one year, due to human health factors.

A.2.1 Trajectory Calculations

The mission simulation is accomplished with RAPTOR (RAPid Trajectory Optimization Resource), an optimization program developed at NASA-Johnson Space Center for low-thrust, interplanetary missions [121]. The code analyzes the three parts of an interplanetary mission: the spiral to escape from low Earth orbit, the heliocentric transfer, and the spiral to a circular orbit about the arrival planet. In the spiral phase, the code merely propagates the position of the spacecraft, without optimizing the trajectory. Throughout the spirals, thrust is directed along the velocity vector. The escape spiral begins with a circular orbit and is propagated until the vehicle has acquired a positive energy. The capture spiral is modeled in the reverse manner. The heliocentric portion is an optimization code based on the Davidon-Fletcher-Powell Penalty Function Method [122].

The position and velocity of the departure and arrival planets are the boundary conditions. Given these, the code minimizes the total acceleration of the interplanetary trajectory. RAPTOR contains a genetic algorithm to converge on the proper Lagrange multipliers, trip length and departure date for the heliocentric code.

More details of how the code was used for this mission analysis will be given in section A.4.2.

A.3 Propulsion Options

In this section we will briefly describe the propulsion systems that may be suitable for this mission. Because of their high I_{sp} , EP systems are naturally attractive candidates for this type of mission. Within the family of electric propulsion devices, several types of thrusters, conceptually, have the ability to process 100s of kilowatts to megawatts of power at reasonably high efficiencies. We list them in table (A.3), and in section A.3.1, we narrow down the field to a few thrusters which will be considered in the mission analysis. Further information on these devices can be obtained from recent surveys, such as refs. [123, 15]. First, we will describe the criteria we used to select the thrusters.

A.3.1 Selection Criteria

While a variety of propulsion systems have been proposed for interplanetary missions, we restrict our analysis only to those that have:

1. been successfully characterized in a laboratory as a thruster (i.e., thrust and efficiency have been measured directly),
2. demonstrated a *potential* for attaining a significant lifetime ($\mathcal{O}(100 \text{ hours})$),
3. the ability process at least:
 - 25 kW per thruster for the cargo mission,
 - 500 kW per thruster for the piloted mission,

so that the number of thrusters per spacecraft is reasonable.

Since, at present, there do not exist conclusive lifetime assessment tests of *any* of the devices, we consider those that have operated with tolerable erosion for 100 hours.

At high power levels, measured thrust and efficiency data is available for only three main classes of thrusters, Hall thrusters, thermal arcjets, and magnetoplasmadynamic thrusters (MPDT). Hall thrusters and thermal arcjets have been operated at power levels up to 150 kW, and are therefore well suited for the cargo phase of the mission. Some Hall thrusters examined in this study have operated only at lower power levels (25-75 kW) and therefore a cluster of 2-6 thrusters will be required to accomplish the mission. The only EP device to date to have demonstrated the ability to operate at megawatt power levels with a single (or reasonably small number of) thruster is the MPDT. For the MPDT two distinct variations exist differing in propellant and electrode design, both of which have been operated in the laboratory and will be discussed here.

Other promising thruster concepts, such as the ion thruster, Pulsed Inductive Thruster (PIT), and the VArable Specific Impulse Magnetoplasma Rocket (VASIMR), that did not meet our selection criteria are discussed in section A.5.

A.3.2 Piloted Mission

Few thrusters have demonstrated performance at power levels of $\mathcal{O}(\text{MW})$, and have survived many hours of laboratory testing. Consequently, the field narrowed down to gas-fed magnetoplasmadynamic thrusters (MPDT) and lithium Lorentz force accelerators (LiLFA). They will be briefly described in the subsequent sections.

Magnetoplasmadynamic Thrusters

In the magnetoplasmadynamic thruster (MPDT), a voltage applied between concentric electrodes breaks down a propellant gas, creating a quasi-neutral plasma within the thruster chamber. A high current ($\mathcal{O}(10^2 - 10^4)$ A) carried by the plasma to the electrodes induces an azimuthal magnetic field, causing a Lorentz force ($\mathbf{j} \times \mathbf{B}$) to accelerate the plasma out

of the thruster at velocities of $\mathcal{O}(10 \text{ km/s})$ [9]. As shown in figure A.1, this body force accelerates the fluid in the direction perpendicular to both the electric and the magnetic fields.

The MPDT has a unique place among electric thrusters in its ability to process megawatts of electrical power in a small, simple, compact device and produce thrust densities (thrust per unit exhaust area) of $\mathcal{O}(10^5) \text{ N/m}^2$ [15]. However, this major advantage of the MPDT has also been the disadvantage to its development. Since high efficiencies ($>30\%$) are only reached at high power levels ($>200 \text{ kW}$), MPDTs require power levels that are an order of magnitude higher than what is currently available on spacecraft in order to be competitive with other propulsion options. Therefore, research on MPDTs was largely sidelined, in favor of thrusters that have higher efficiencies at lower power levels. Renewed interest in high-power MPDTs led to a flight-test of a quasi-steady MPDT in 1996 aboard the Japanese Space Flyer Unit, which was operated successfully at 1 kW [124].

Still, steady-state testing at the megawatt level is difficult, and to date all data in the 1 to 6 MW range has been taken in quasi-steady mode. In this mode, the thruster is operated for current pulse length of $\mathcal{O}(1 \text{ ms})$, and data from this mode is expected to be a good indication of its steady-state performance [125]. Databases of measured quasi-steady thruster performance have been compiled in Japan [126] and at Princeton University [14]. A MW-class pulsed facility at the NASA-Glenn Research Center began operation in 2001, with plans to develop it to a steady-state facility [127]. So far, steady-state data is limited to less than 1 MW , and has been obtained mostly at the NASA Glenn (formerly Lewis) Research Center [128], and at the University of Stuttgart [129]. The NASA-Lewis test facility had the capability to operate at steady-state power level of up to 600 kW , but research was discontinued by the early 1990s. The focus of the research at University of Stuttgart is on investigating arc and plasma instabilities at power levels from 0.1 to 1 MW . At 0.5 MW , efficiencies of 28% at 1099 s were achieved during steady-state operation.

To date, the best gas-fed MPDT data has been achieved with hydrogen in quasi-steady

mode, 43% efficiency at 5000 s has been reported [130]. In general, however, results have been in the 10 - 35% in range at 1000 - 4500 s specific impulse using Ar, NH₃, and N₂ as propellants [131].

A major concern about the MPDT technology is the erosion of its cathode (cf. ref. [12]), which has often limited the lifetime of laboratory studies. However, there are some indications from recent research [129, 132] that this problem may be manageable.

To summarize, the three major technological issues exist in the development of the MPDT are: accurate performance measurements at steady state, characterization and optimization of the thruster's stable operating range, and demonstration of lifetimes of the order of mission requirements (8,000-10,000 hours).

Lithium Lorentz Force Accelerators

The lithium Lorentz Force Accelerator (LiLFA) can be considered the next-generation MPDT [15]. Its operating principle is essentially identical to that of the MPDT. The name is a result of largely historical reasons. However, two major differences between the LiLFA and the MPDT are to be noted. First is the choice of propellant. Whereas the MPDT traditionally uses inert gas propellants, such as argon, helium, and hydrogen, the LiLFA, as its name indicates, uses lithium vapor. Furthermore, the central electrode of the LiLFA differs from the single rod design common to most gas-fed MPDTs. Instead, the LiLFA employs multiple rods, tightly packed within a hollow tube. Propellant flow (see figure 1.1) is through the channels in the cathode that are created in between these smaller rods, rather than from the electrode base, as in the MPDT (figure A.1).

These two major differences address some of the fundamental limitations of the MPDT uncovered during extensive testing in the 1960s and 70s. First, the choice of a low-ionization energy propellant (lithium) reduces the non-recoverable energy lost in ionizing the propellant, thus improving efficiency, especially at low power levels (<200 kW) where the ionization sink can approach 50% of the total input power. The use of lithium also

Table A.1: Summary of Propulsion Options for Two-Phase Mars Mission.

Thruster	Laboratory Models	Measured Thrust at P >25 kW	Lifetime >100 hrs
Arcjet	✓	✓	✓
Hall	✓	✓	✓
Ion	✓		✓
LFA	✓	✓	✓
MPDT	✓	✓	✓
PIT	✓	✓	
VASIMR	✓		

precludes the need for high-voltage ignition capacitors and hardware required to achieve breakdown in inert gas systems. Moreover, lithium can be stored in solid form onboard the spacecraft, leading to potential mass savings. However, no space-qualified system exists for feeding lithium propellant. The multi-channel design for the central electrode, combined with the lithium propellant, has been shown to improve efficiency and increase thruster lifetime by reducing electrode erosion [133]. The role of the electrode design in increasing efficiency and lifetime is, however, poorly understood.

The possibility of the LiLFA as a high-power propulsion option was shown nearly a decade ago with the demonstration of 500 hours of erosion-free operation, at a power level of 500 kW. At this power level, an exhaust velocity of 40 km/s, thrust of 12 N, and thrust efficiency of 60% were reported [133]. Due to its high efficiency and high thrust-to-power ratio, the LiLFA has emerged as a promising candidate for the piloted mission. However, since very little data is available on this thruster aside from what has been cited in ref. [133], there is a need for further verification of this performance. To this end, NASA-JPL is in the process of developing a high-power steady state test facility for LiLFA at MW power level.

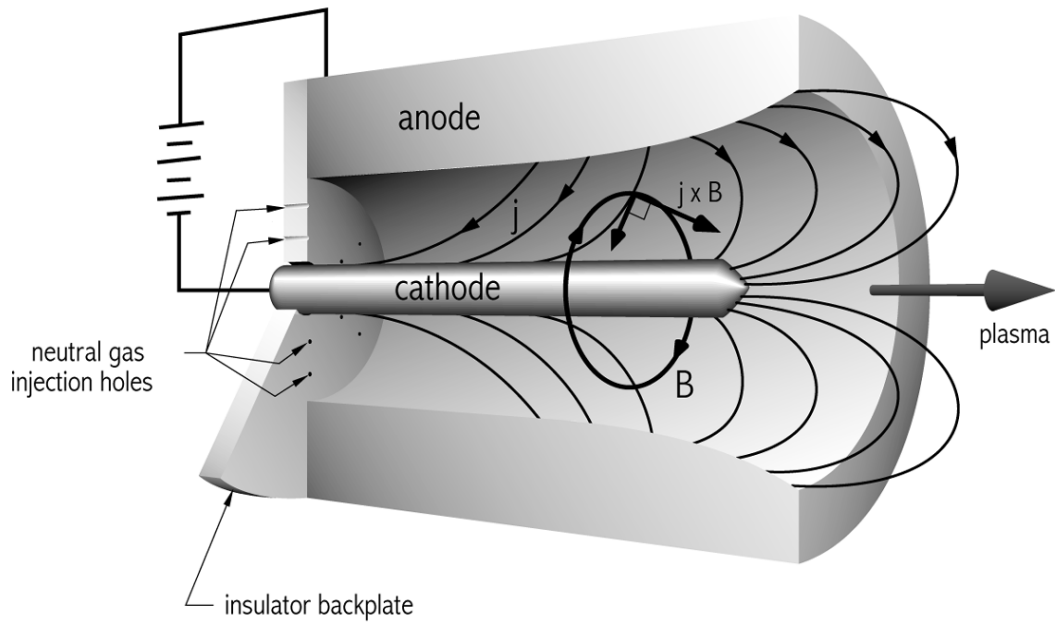


Figure A.1: Schematic of the operation of the MPDT.

A.3.3 Cargo Mission

As mentioned earlier, there has been more research done on relatively low power propulsion than on MW-class propulsion required for the piloted mission. Hence, for the cargo mission, more thrusters are available for consideration. The thrusters that have met our selection criteria will be briefly described in the subsequent sections.

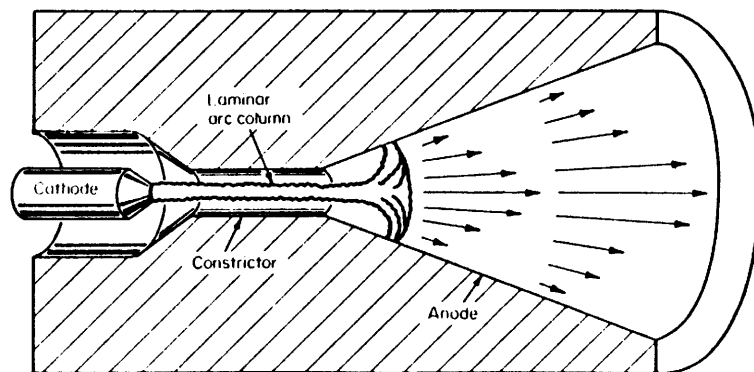


Figure A.2: Schematic of the operation of the arcjet.

Arcjets

In this class of thrusters, an electric arc is used to add enthalpy to the propellant. Akin to a chemical thruster, part of the enthalpy in the flow is converted to directed kinetic energy using a nozzle.

As shown in figure A.2, a tightly constricted electric arc, carrying currents up to $\mathcal{O}(100)$ A, heats the core of the propellant stream to temperatures up to 10000 K, while the walls of the thruster are maintained at much lower temperatures (<3000 K) to prevent melting. Because of the higher temperatures in the core, and consequently, higher specific enthalpy, the exhaust velocity of an arcjet can reach, or even exceed, 10 km/s, as opposed to only 4 km/s for a chemical thruster. Its simple design and its high thrust density are some of the attractive features of the arcjet.

We will see in section A.4.3, however, that arcjets tend not to be competitive as our other option at the power levels considered.

Hall Thrusters

Hall thrusters derive their thrust by accelerating heavy ions, using an electric field, to high exhaust velocities.

Under high magnetic fields, and low densities, the current in the direction perpendicular (specifically, in the $\mathbf{E} \times \mathbf{B}$ direction) to the electric field (commonly called the Hall current) can exceed the current along the electric field. As implied by their name, Hall thrusters utilize this Hall current to lock electrons into a nearly collisionless cross-stream drift, leaving the positive ions free to be accelerated by the applied electric field (cf. figure A.3). In a sense, these devices are hybrid electrostatic-electromagnetic accelerators with space-charge neutralization automatically provided by the background of drifting electrons. Because of this, the Hall thrusters are not affected by space-charge limitations. Therefore, Hall thrusters produce higher thrust densities than space-charge limited devices, such as ion thrusters.

Because the magnetic fields in these devices are externally supplied, and because the mass flow densities are intrinsically low, these thrusters optimize their performance at considerably lower powers than those of the self-field MPDTs. In fact, the requirement of low mass density (to maintain significant Hall effect) precludes the Hall thruster from producing thrust densities comparable to the MPDT and the LiLFA at a given power level.

The first Hall thrusters were developed in the US in the 1960s, but the research was discontinued in favor of ion engines [15]. However, research in the former Soviet Union picked up in the late 1960s, and by 1990s they had demonstrated efficiencies greater than 50%.

Hall accelerators of the closed-drift type are at present the most commonly used plasma thrusters. Since 1972, more than 100 Hall thrusters have been flown on Russian spacecraft. They are developed and used by the commercial sector for orbit insertion, attitude control, and drag compensation of satellites.

The Hall thrusters chosen for this study were the NASA-457M high power model [134] using xenon propellant, and the thruster with anode layer (Bi-TAL) from TsNIIMASH [135] using bismuth propellant.

The NASA-457M has been tested for power levels up to 75 kW. At this power level, its measured efficiency was 58%, specific impulse 2900 s, and thrust 2.95 N. A variant of this thruster [136] had an efficiency of 62%, specific impulse of 3250 s, and thrust 0.95 N at 25 kW of input power.

The Bi-TAL had efficiency greater than 70%, and a specific impulse of 8000 s at 140 kW input power. A variant of this thruster (designated TAL-200) had an efficiency of 67%, specific impulse of 3000 s, thrust of 1.13 N, at an input power level of 25 kW [135]. As a result of its high I_{sp} and high efficiency, this thruster has emerged as a promising candidate for the cargo mission. However, very little data is available on this device, and therefore, there is a need for further verification of its performance and lifetime.

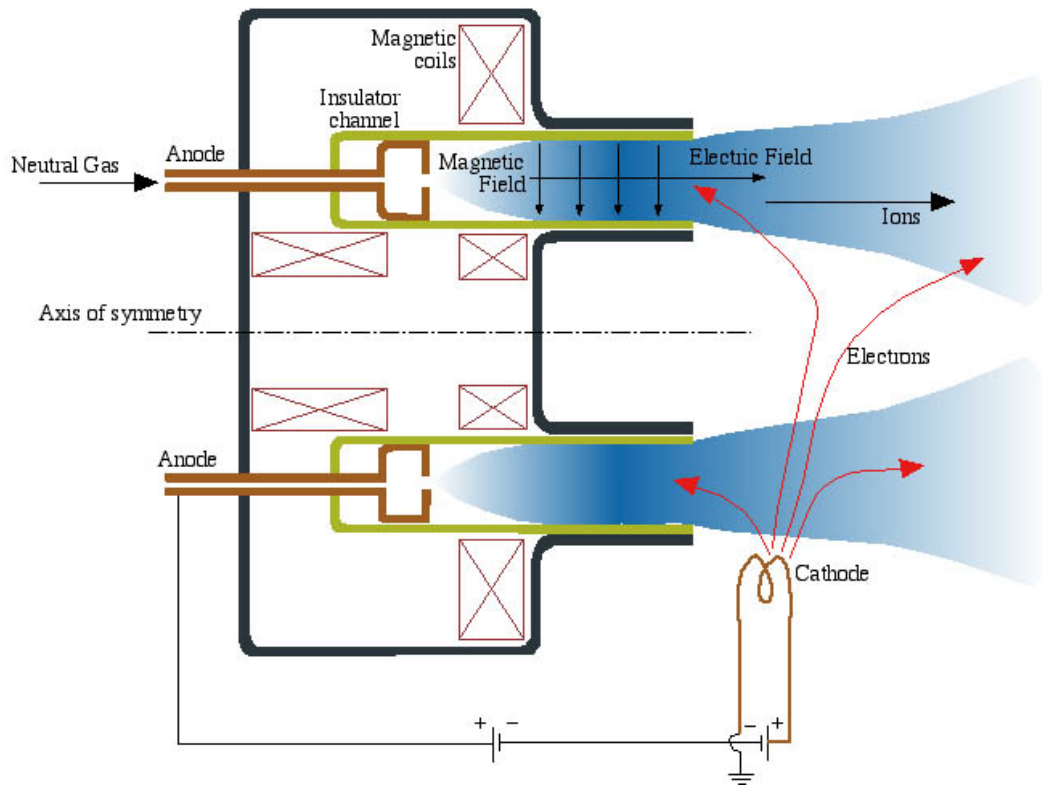


Figure A.3: Schematic of the operation of the Hall thruster. (From ref. [137])

Applied Field LiLFA

Stated simply, the applied field LiLFA (AF-LFA) is a design to increase MPDT/LiLFA efficiency at power levels less than 200 kW, by adding an additional source of magnetic field. By using an external solenoid to enhance the magnetic field, efficient electromagnetic acceleration can occur at power levels where the current is too low to induce a substantial magnetic field. The AF-LFA offers the advantage higher efficiencies ($\geq 40\%$) at lower power (< 200 kW) compared to MPDT and LiLFA, while maintaining exhaust velocities (10-35 km/s) that are comparable. Apart from high-energy planetary missions, potential applications of the AF-LiLFA include missions requiring high thrust-to-power ratios, such as orbit transfer, N-S stationkeeping, and drag compensation.

At the power levels considered for cargo missions, the applied field lithium Lorentz force accelerator, jointly developed by the Moscow Aviation Institute (MAI) and NASA-JPL was a suitable candidate for consideration. The conclusion of a 5 year AF-LiLFA

Table A.2: Summary of performance of thrusters for cargo phase of mission

Thruster	Power (kW)	Thrust (N)	I_{sp}	Efficiency (%)	Reference
H ₂ Arcjet	75	2.5	1715	29	[138]
Bi Hall	25	1.13	3000	67	[135]
	150	2.5	8000	70	[135]
Xe Hall-1	25	0.95	3250	60	[136]
Xe Hall-2	75	2.9	2900	56	[134]
AF-LiLFA	150	4.0	3290	40	[11]
Argon MPDT	150	6.7	849	19	[129]

Table A.3: Summary of performance of thrusters for piloted phase of mission (* denotes quasi-steady data.)

Thruster	Power (MW)	Thrust (N)	I_{sp}	Efficiency (%)	Reference
LiLFA	0.5	12	4077	60	[133]
H-MPDT-1*	1.5	26.3	4900	43	[130]
H-MPDT-2*	3.75	88.5	3500	43	[130]
H-MPDT-3*	7.5	60.0	6000	25	[14]
Argon MPDT	0.5	25.5	1099	28	[129]

research program at the MAI [11] was the design of a 48% efficient thruster operating at 185 kW with 4200 s and 4.5 N. For 130 kW of input power, this thruster has demonstrated 40% efficiency, 3290 s specific impulse, and 4.0 N of thrust in their study [11]. However, like in the case of its self-field variant, very little data is available on this thruster, and hence there is a need for further verification of its performance. Therefore, the collaborative effort by NASA-JPL and Princeton University is aimed at testing the applied-field LFA at power levels $\mathcal{O}(10 - 100 \text{ kW})$.

A.4 Mission Analysis

A.4.1 Assumptions

In order to simplify our analysis, we have made the following assumptions for the present study, some of which will be relaxed in future studies.

1. The specific mass of the power supply, α_p , is assumed to be 4.0 kg/kW for all the cases. This is within the range of previous studies such as ref. [5] and ref. [114].
2. The specific mass of the thrusters for the piloted mission were all assumed to be 0.35 kg/kW [118]. Since many of the thruster considered in this study are still laboratory models, it is not easy to arrive at an accurate estimate for α_t . The influence of this assumption on the result is yet to be determined, since the mass of the thruster is expected to be only a small fraction of the total mass.
3. For the cargo mission, the mass of the thruster system was assumed to be negligible compared to the total mass, and was hence neglected.
4. The arrival date on Mars orbit was fixed to be the same for all cases of each of the two (cargo and piloted) missions.
5. The cargo mission was analyzed at a power level of 150 kW, irrespective of the optimum power level of the thruster. The piloted mission was analyzed at a power level of 7.5 MW, irrespective of the optimum power level of the thruster.
6. For the cargo mission, the total payload of 90 mT was evenly distributed among ten spacecraft. This was done in order to ensure a reasonable trip time, given the limited (150 kW) power supply.

A.4.2 Calculations

For the thrusters that met our selection criteria (section A.3.1), we selected the highest measured performance data that was available and used it as input into the RAPTOR code. A summary of the thruster data is presented in tables (A.2 & A.3). As noted in table (A.3), the data for the three types of hydrogen MPDT were obtained in a quasi-steady mode of operation, and it is expected to be a good indication of the steady-state performance as well [9].

For this study, we did not use the genetic algorithm, described in section A.2.1 to optimize the departure date due to the large amount time required to calculate the shortest trip. The dates of 12/1/2016 for the cargo, and 12/1/2018 for the piloted missions, were chosen as the arrival date at Mars (before the spiral) because those dates are expected to be near the minimum for those missions. The genetic algorithm was used to find the Lagrange multipliers and trip length that best satisfied the mission.

Given an initial mass in Earth orbit, the RAPTOR code can determine the final mass, or given a payload to Mars, the code can find the initial mass required. Since we have chosen a payload, RAPTOR will be run in latter mode. First, RAPTOR executes the spiral in to Mars orbit to determine that portion's duration and the propellant the maneuver requires. The heliocentric code then uses the mass of the payload and propellant to begin its optimizations. In this mode the date of arrival in Mars' sphere of influence is the only controllable date, all else is referenced to that date. The heliocentric code optimizes "backward" in time to find the minimum acceleration (i.e., minimum propellant) trajectory. Finally, the spiral to escape from Earth is executed and the mass at escape is matched with that at the beginning of the heliocentric transfer. The genetic algorithm is used only with the heliocentric portion of the code.

A.4.3 Results

The results of the RAPTOR code under the assumptions of this study are given in figures A.4 and A.5. The results for the trip time can be considered accurate to within ± 10 days, and for the propellant mass within ± 1 mT for both stages of the mission. The accuracy of the trip time is based on the sum of the round offs in the convergence calculation of various phases of the trip, and the accuracy of the mass estimate is based on the sum of the uncertainty associated with estimating the mass of the components such as the tank mass, and other structural mass.

The RAPTOR code does not explicitly optimize for trip time, rather it finds the trajec-

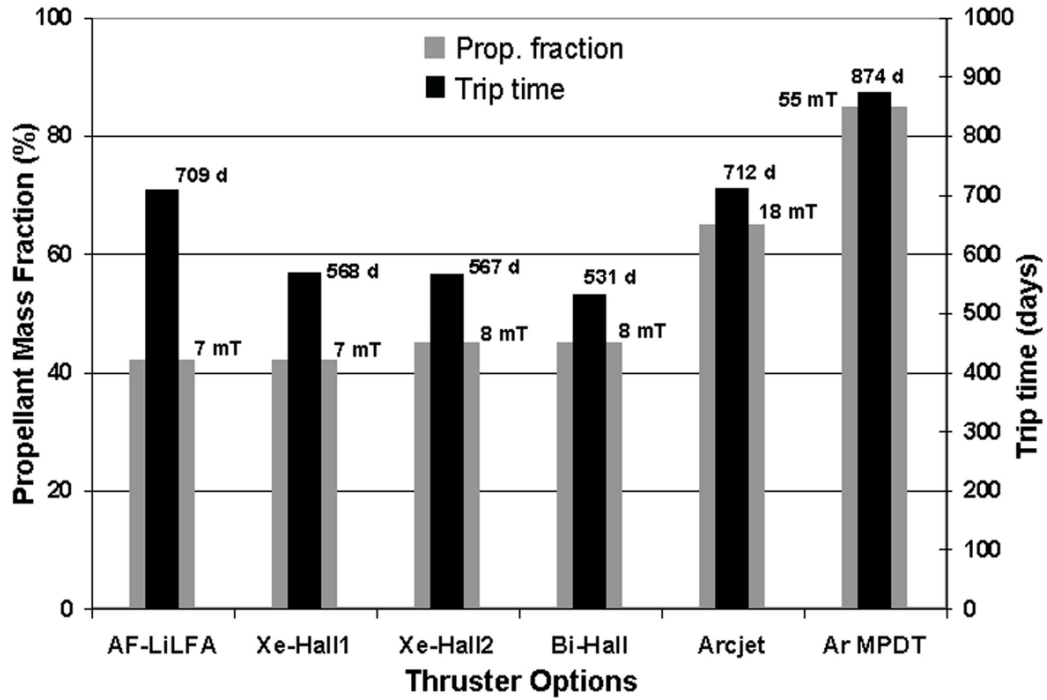


Figure A.4: Results of the cargo mission analysis (all set to arrive on 12/1/2016), with increasing propellant consumption from left to right.

tory that minimizes acceleration. This amounts to minimizing the required initial mass in nuclear-safe earth orbit. Since the thruster mass, payload mass, and power supply masses were assumed to be constant for each stage of the mission, the initial mass is a function of propellant mass alone. The minimum acceleration trajectory will result in the minimum propellant used and hence the minimum initial mass.

A.4.4 Cargo Mission

The cargo mission was restricted to a power level of 150 kW in order to utilize measured thruster data in this study rather than projections of performance. Our power restriction was found to place two major constraints on the analysis. First, as was discussed in the assumptions (section A.4.1), we found it necessary to divide the 90 mT of cargo into 10 smaller payload missions to reduce the trip times to something reasonable (in the neighborhood of 2 years). Second, even with the lower payload mass, the heliocentric portion

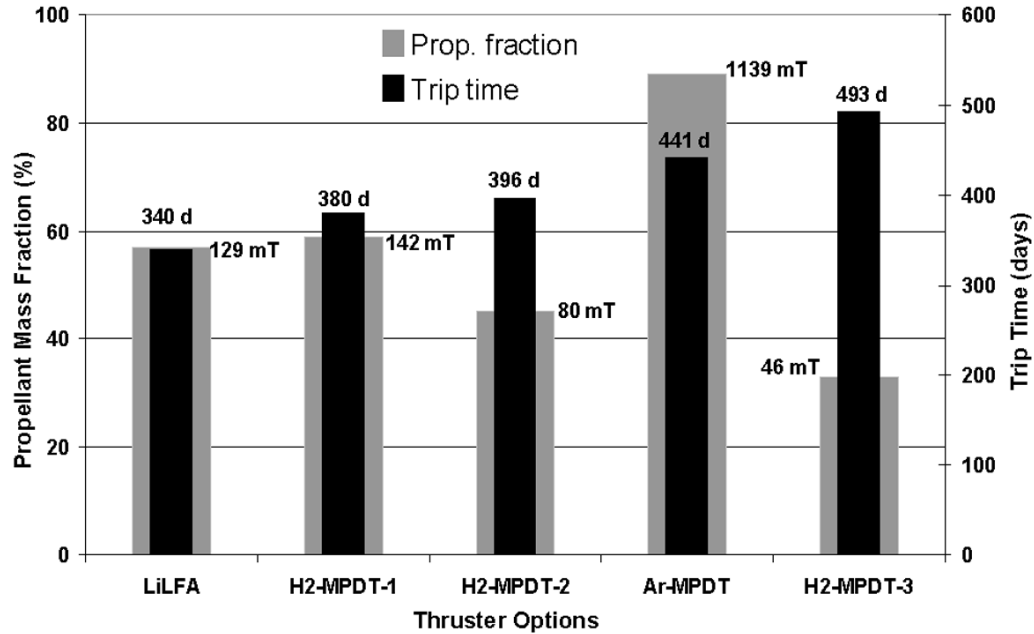


Figure A.5: Results of the piloted mission analysis (all set to arrive on 12/1/2018), with increasing trip time from left to right.

of the mission was being optimized for trip times much longer than two years. To limit the mission length, 300 days was chosen for the heliocentric portion. Essentially, we picked the trip time and power available and from that allowed the code to find which thruster would use the least propellant to accomplish the mission. The differences in trip time come largely from the different times requires to spiral out of earth orbit. The assumption of restricting the heliocentric trip time did have one significant drawback. The code did not converge for the high-power bismuth Hall thruster in table (A.2), since its thrust-to-power ratio was too low to complete the heliocentric trip in 300 days.

Within the accuracy limits of our calculation, the AF-LiLFA and the Xe-Hall thrusters required the lowest launch mass fraction (42 to 45%, i.e., 7 to 8 mT). However, the time to spiral out of earth orbit for the AF-LiLFA is 140 to 178 days longer for a savings of only 1 to 2 mT over the Hall thrusters. Since this is close to our estimated error (± 1 mT) it is not clear that the AF-LiLFA would provide significant mass savings over any of the Hall thrusters. From this analysis, the arcjet would not be the preferred choice for this mission.

With a propellant mass fraction of 65% (18 mT), it required significantly more propellant mass and took longer time to arrive at Mars (712 days) than the AF-LiLFA or the Xe-Hall thrusters. The argon MPDT required the highest propellant fraction, 85% (55 mT), and took the longest (874 days) of the options considered.

A.4.5 Piloted Mission

For the piloted portion of the mission, the desired propulsion option would be the one which accomplishes the mission in the least amount of time. Trip times ranged from 490 days for the H-MPDT-3 [14] to just under 340 days for the LiLFA. The 3.75 MW H-MPDT-2 [130] had a trip time of only about one month longer (380 days) than the LiLFA. However, the initial mass required was also higher than the LiLFA. Due to its high specific impulse, the MPDT-3 required the least propellant mass fraction, 33% (45 mT), for the mission. However, its low efficiency (25%), and its lower thrust-to-power (compared to other choices at the same power level), prevented it from being competitive because of long trip time.

The range of trip times (340-490 days) depends upon the power level chosen (7.5 MW) for this stage of the mission. At that power level, the LiLFA is the best option, with the minimum trip time and a moderate propellant requirement (57% = 129 mT lithium) compared to other choices.

A.5 Other Viable Candidates

As mentioned in section A.3.1, we restricted our analysis to thrusters that have measured performance data, and have demonstrated significant lifetime. This eliminated many thruster concepts that may be promising for this mission.

Ion propulsion has demonstrated the in-space performance and lifetime necessary to be incorporated into future mission design and planning [139]. Good power throttling

over a rather broad power range make ion propulsion ideal for solar electric propulsion missions where the electric power available varies with distance from the sun. In fact, the next-generation ion thrusters are being developed for such missions. NEXT, NASA's Evolutionary Xenon Ion Thruster, will provide higher power capabilities and lower specific mass with slightly increased exhaust velocities over Deep Space 1 technology [140]. These advances will meet the requirements of several near-term planetary missions including a Neptune orbiter and a Titan explorer [140].

Due to the electrostatic nature of ion propulsion, increased power (exhaust velocities) and propellant throughput (thrust) require corresponding increases in thruster size. The 30-cm DS1 thruster was capable of operation at up to 2.5 kW. The NEXT thruster will increase the effective area by 2, by moving to 40 cm diameter optics, and power capabilities near 10 kW. NASA's long-range goal for the development of ion engine technology is the demonstration of operation at 30 kW and above [139]. Work in 1968 investigated the feasibility of much higher power (>100 kW) ion thrusters. Preliminary tests on a 150-cm engineering model showed that operation at 177 kW was possible with exhaust velocities in excess of 7000 s and calculated efficiencies of 76%. Thruster conditioning and grid stability issues arose at this size and power, as well as a need for higher power electron sources [141]. Lack of potential missions at that time caused the research program to end before these issues were solved or thrust measurements could be obtained. However, there appears to be no fundamental limit on thrusters of this size and power [139].

Another thruster concept that could be promising is the pulsed inductive thruster (PIT) [142]. Using ammonia as propellant, this thruster demonstrated 48% efficiency, with Isp of 4000 s at discharge energy of 2 kJ per pulse. If this thruster can be operated at a pulsing frequency of ($\mathcal{O}(100\text{-}1000$ Hz)), it would be competitive with the LiLFA for the piloted mission. However, the PIT has yet to show potential for lifetime of the order of the mission duration for it to be a serious candidate.

In addition, there are other thruster concepts, such as the VArIable Specific Impulse

Magnetoplasma Rocket (VASIMR) [143], that may be suited for this mission. The VASIMR is a two-stage plasma propulsion device: the production of the plasma is accomplished in the first stage, and the heating and acceleration in the second. It is hoped that the separation of these two processes would allow for better control of the exhaust velocity, while utilizing maximum available power. This device is intended to operate at power levels ranging from 10 kW to 100 MW. If proven, its ability to vary specific impulse independent of power (which will likely require varying the propellant), can reduce both trip time and propellant utilization. However, this device has not yet been successfully operated in the laboratory as a thruster, and propulsive characteristics and performance have not been directly measured.

A.6 Concluding Remarks

The goal of this study was to examine electric propulsion options for near-term (10-20 years) cargo and piloted missions to Mars. Thrusters for the study were chosen from the highest performance data available, subject to the following constraints: that they had demonstrated operation at power levels of 25 kW (cargo) or 500 kW (piloted) in a *single* laboratory thruster, that thrust measurements at this power level had been published, and has demonstrated a *potential* for lifetimes on the order of at least 100 hours. Power levels chosen for this study were 150 kW for the cargo mission and 7.5 MW for the piloted mission. Trajectory analysis was performed by the NASA-JSC RAPTOR code which optimized acceleration for the heliocentric portion of the mission.

The cargo mission results showed that several of the thrusters we considered are promising candidates. For a chosen power level of 150 kW, the AF-LiLFA and all three of Hall thrusters considered could deliver the 9 mT payload with nearly the same mass in earth orbit.

For the piloted mission at 7.5 MW, the lithium Lorentz force accelerator (LiLFA) pro-

vided trip times savings of at least one month over any of the MPDTs in the study. The initial mass required to accomplish this was in the middle of the range of the thrusters considered. Overall, the LiLFA seems to be a promising technology for high-power, high Δv missions of this type. Because the power available for this mission is fixed at 7.5 MW, the range of trip times (340-490 days) is longer than the estimates in other studies that consider much higher power levels.

This study provides a survey of electric propulsion options for cargo and piloted Mars missions. In order to more completely determine the relative strengths and weaknesses of each system considered, several of our assumptions need to be addressed in future work. So far, we have completed only the first phase of this study, with strong assumptions on specific mass of components, and thruster operation at a single power level only. The next step would be to perform trajectory analysis for each mission stage at a range of power levels. This would allow for the determination on of the optimum thruster and power level for a given mission. In addition, the assumptions of constant thruster and power supply specific mass for all thruster options might have influenced our results, given the large variations in power requirements of each thruster. Obtaining better estimates of these values would increase the relevance of our results. Finally, in the next phase of this work, a parametric study of thruster efficiency and specific impulse will be undertaken, which could provide guidelines for future research in thruster design and optimization.

Appendix B

Least-squares Multi-color Pyrometry

Least-squares multi-color pyrometry is a method of analysis of pyrometric measurements at multiple wavelengths that determines the temperature and emissivity of a surface radiated a gray body spectrum. If a surface could be coated by a second material or the emissivity is unknown this method enables the use pyrometry under conditions where the measurements would otherwise lead to unacceptably large errors. We were interested in developing this method in case the working gas (lithium in the present experiments and barium in the near future) coated the cathode surface. Our lithium-fed experiments and calculations of lithium coverage of tungsten (see Appendix D) determined that lithium did not coat the outer cathode surface, and, therefore, we did not utilize this method for data analysis because it produces greater uncertainties than assuming a fixed emissivity (as described in section 3.11.3).

An evaluation of previously proposed least-squares multi-color pyrometry methods is presented here to determine their highest achievable accuracy, including a new analysis method that increases their accuracy. The study was limited to the visible spectrum and the temperature range of 1700 to 3000 K. A Monte-Carlo simulation of the various methods showed the effects that the number of colors of the pyrometer, the errors associated with noise and calibration, and the number of measurements have on the uncertainty of the

predicted temperature. Some of these methods were found to lead to inaccurate results, an underestimate of the uncertainty of the predicted temperature, or yield larger uncertainties than single-color pyrometry. The two methods that were found to yield the highest accuracy without underestimating the uncertainty are based on fitting the intensity versus wavelength data with three free parameters (temperature and the two coefficients of the emissivity versus wavelength model). Adding complementary measurements, at the price of spatial or temporal resolution, is shown to allow a reduction of the uncertainty in the predicted temperature well below that associated with single-color pyrometry.

B.1 Introduction

The intent of least-squares multi-color pyrometry (LSMCP) is to accurately determine the temperature of a heated surface that has an unknown emissivity. Emissivity is a material property that is sensitive to roughness, oxidation, contamination, radiation wavelength, and the angle of observation; factors that are difficult to determine accurately for a given surface *a priori*. The intensity of thermal radiation is measured at discrete, multiple wavelengths to determine the intensity as a function of wavelength. The intensity data are fit to an appropriate radiation intensity model, Planck's law or Wien's approximation, and to an emissivity model to determine the temperature and emissivity. LSMCP reduces the uncertainty in the predicted temperature by measuring the intensity more times than there are free parameters in the intensity and emissivity models.

B.1.1 Review of Previous Research

During the past two and a half decades researchers have proposed a variety of methods capable of determining temperature with the use of least-squares multi-color pyrometry, yet there is no consensus on which methods are the most accurate. In 1979 LSMCP was first utilized in a three-color pyrometer that determined the temperature of a flame assumed

to have constant emissivity [144]. The first analysis assuming a non-constant emissivity was a computer simulation of a six-color pyrometer [145]. It was developed to compare the temperature determination accuracy of both linear and nonlinear least-squares fitting routines. Two emissivity models were used in the simulation, the first assumed the emissivity had a linear dependence on wavelength while the second assumed the same for the natural logarithm of the emissivity, described by equations (B.6) and (B.7), respectively. The analysis determined that the predicted temperature was less than 3% from the true temperature when measuring intensity in the infrared spectrum. Using the methods in that analysis, an experimental six-color pyrometer determined the temperature of many metallic surfaces [146]. The metals that gave satisfactory results, less than 3% deviation from the true temperature, had a linear variation of emissivity with wavelength throughout the visible and infrared spectra. These initial papers demonstrated that LSMCP can determine the temperature of many surfaces and proposed the emissivity models and fitting routines evaluated in this paper.

Various methods that fit the intensity data to Wien's approximation were later developed with the goal of reducing the uncertainty of the predicted temperature. Modeling the natural logarithm of the emissivity as a line or polynomial, the relations between intensity measurements, temperature, and emissivity can be algebraically manipulated into many forms [147, 148]. Simulations and experimental pyrometers determined the temperature of many surfaces using those methods.

The most recently developed method assumes the radiance temperature to be a linear function of wavelength [149]. The constant term of the line fit in equation (B.11) is interpreted as the true temperature.

In references [150, 151] a Monte-Carlo simulation studied the effects of noise in the intensity data on two different temperature determination methods. One hundred simulations of the intensity measurements, with a 2% uniformly distributed random error added to the intensity, demonstrated that temperatures would be predicted with a reasonably small

deviation from the true temperature.

B.1.2 Motivation

Two primary obstacles still exist in developing pyrometers for experimental use. First, since no comparative evaluation of the temperature determination methods has been published, there is no standard method in the field of multi-color pyrometry. Second, the effects of errors associated with noise and calibration on the predicted temperature uncertainty have not been clearly demonstrated to guarantee a required accuracy from a multi-color pyrometer.

After a brief review of pyrometric relations in Section B.2, we will compare the various proposed temperature determination methods in an effort to determine which methods are redundant or consistently produce a large deviation in predicted the temperature from the true temperature. A disparity in the uncertainties in the temperature determined by each method motivated our investigation of the dependence of the uncertainty on the errors associated with noise and calibration via a Monte-Carlo simulation, discussed in Section B.4. The goals are to show that the uncertainty in each predicted temperature agrees with the range of temperatures in the Monte-Carlo simulation, that the true temperature of the surface lies within the predicted error bars, and which methods yield the smallest uncertainty in the predicted temperature. In many cases the resulting uncertainty could be larger than that of single-color pyrometry. A method based on adding complementary measurements to reduce the uncertainty in predicted temperature below that of single-color pyrometry is presented in Section B.5.

B.2 Fundamental Relations

Pyrometry is based on the fact that all surfaces at temperatures above absolute zero emit thermal radiation. Planck's radiation law, modified to include surface emissivity, is the

fundamental relation of thermal radiation:

$$I(\lambda, T) = \epsilon_\lambda \frac{C_1}{\lambda^5} \left(\frac{1}{e^{\frac{C_2}{T\lambda}} - 1} \right) \quad (\text{B.1})$$

where u is the intensity, ϵ_λ is the emissivity as a function of wavelength, $C_1 = 1.191 \times 10^{16} \text{ W}\cdot\text{nm}^4\text{cm}^{-2}\text{Sr}^{-1}$ and $C_2 = 1.4384 \times 10^7 \text{ nm}\cdot\text{K}$ are the first and second radiation constants, T is the absolute temperature in Kelvin, and λ is the wavelength of the radiation in nm. With knowledge of the emissivity, the temperature of any surface can be determined by fitting the intensities measured at various wavelengths to the above relation.

Wien's approximation to Planck's law,

$$I(\lambda, T) = \epsilon_\lambda \frac{C_1}{\lambda^5} e^{\frac{-C_2}{T\lambda}}, \quad (\text{B.2})$$

and the appropriate choice of ϵ_λ allows approximating Planck's law as a linear relation in wavelength. Within the visible spectrum and temperatures less than 3200 K the temperature determined from the approximation will deviate by less than 0.025% from Planck's law. The common form used in pyrometry is

$$\frac{-C_2}{T_r\lambda} = \ln \epsilon_\lambda - \frac{C_2}{T\lambda}, \quad (\text{B.3})$$

where T_r is called the radiance or brightness temperature and is defined as the temperature determined from the intensity assuming an emissivity of unity

$$\frac{1}{T_r} = \frac{-\lambda}{C_2} \ln \frac{I\lambda^5}{C_1}. \quad (\text{B.4})$$

The emissivity dependence on wavelength can be expressed in many forms, but we will consider those that fit experimental measurements or simplify the analysis. Most surfaces

have an emissivity that varies with wavelength and temperature, but we ignore the temperature dependence based on the assumption that each observed location is at the same temperature. The emissivity of metallic surfaces in the visible and near-infrared wavelengths often exhibit a polynomial dependence on wavelength

$$\epsilon_{\lambda} = c_1 + c_2\lambda + \dots + c_n\lambda^n. \quad (\text{B.5})$$

This emissivity dependence can also be interpreted as a Taylor expansion of the emissivity for a narrow range of wavelengths. The number of terms in the expansion is chosen by comparing the increase in uncertainty caused by having more free parameters to the systematic error induced by using a less accurate model. We consider two forms, the linear dependence of emissivity on wavelength,

$$\epsilon_{\lambda} = a + b\lambda, \quad (\text{B.6})$$

and the linear dependence of the natural logarithm of emissivity on wavelength,

$$\ln \epsilon_{\lambda} = a' + b'\lambda. \quad (\text{B.7})$$

Two factors must be considered when choosing between the two emissivity models: (1) which model best represents the emissivity as a function of wavelength for the heated surface and (2) if the possible reduction in the uncertainty in the predicted temperature yielded by the linear fitting methods, as shown in section B.4, is more important than the first factor.

In order to limit the uncertainty in the predicted temperature, the emissivity models are limited to two terms. An analysis in reference [152] determined that emissivity models for six-color pyrometers should not contain more than two free parameters. We have used this guideline for pyrometers of four to ten colors.

B.3 Method Comparison

Material & Temperature	Method						
	1	2	3	4	5	6	7
Tantalum 1700 K	0.7±12.6	3.9±2.5	-0.6±4.1	-0.5±6.9	-0.6±17.3	0.3±2.5	3.0±0.9
Tantalum 2200 K	-0.1±17.0	4.4±3.3	0.5±5.4	0.5±9.1	0.5±22.6	1.0±3.6	3.2±1.1
Tantalum 2400 K	-0.1±18.7	3.7±3.4	4.1±6.1	4.0±10.7	4.1±25.6	4.2±5.9	2.7±1.2
Tantalum 2800 K	-0.2±22.2	3.8±4.1	1.8±7.0	1.8±11.9	1.8±29.2	1.9±5.5	2.4±1.4
Molybdenum 2000 K	-0.8±14.8	2.1±2.9	0.1±5.6	-0.0±9.5	0.1±23.5	0.3±4.2	1.4±1.0
Molybdenum 2800 K	-2.3±22.0	2.3±4.2	-2.0±6.9	-2.2±11.4	-2.0±29.0	-1.5±4.7	0.7±1.3
Rhenium 1810 K	-0.5±12.7	0.8±2.6	-2.2±4.3	-2.1±7.1	-2.2±18.1	-1.7±2.9	0.2±0.9
Tungsten 1800 K	-0.0±12.8	1.0±2.5	0.5±4.4	0.5±7.4	0.5±18.5	0.5±3.8	0.6±0.9
Tungsten 2000 K	-0.1±14.4	1.3±2.8	0.4±4.9	0.4±8.3	0.4±20.6	0.4±4.1	0.7±1.0
Tungsten 2200 K	-0.2±16.2	1.5±3.1	0.4±5.4	0.4±9.1	0.4±22.6	0.5±4.4	0.9±1.1
Tungsten 2400 K	-0.2±17.9	1.8±3.4	0.1±5.9	0.1±9.9	0.1±24.6	0.3±4.6	1.0±1.2
Tungsten 2900 K	-0.6±22.8	3.1±4.3	-0.8±7.0	-0.9±11.7	-0.8±29.4	-0.4±5.0	1.6±1.4

Table B.1: Deviation of predicted temperature from the true temperature and the uncertainty in the predicted temperature for the seven pyrometric methods. (Percent of true temperature.)

A comparison of the ability of the various methods to accurately determine temperature is shown here with the goal of determining which methods are redundant or produce a large deviation between the true and predicted temperatures. LSMCP methods are differentiated by the relation used in the fitting routine and whether the routine is linear or nonlinear least-squares. The linear least-squares fitting routines lead to analytical solutions while the nonlinear fit require an initial guess and many iterations and is thus more computationally intensive. The results of seven types of pyrometry (ratio pyrometry, single-color pyrometry, and five LSMCP methods) are compared. The LSMCP relations are listed here:

- Linear two-term temperature fitting method [147]:

$$\frac{(1/\lambda_n T_{r_n}) - (1/\lambda_m T_{r_m})}{\lambda_m - \lambda_n} = \frac{1}{T} \frac{1}{\lambda_m \lambda_n} + \frac{b'}{C_2}. \quad (\text{B.8})$$

- Linear two-term emissivity fitting method [148]:

$$\frac{1/T_{r_n} - 1/T_{r_m}}{\lambda_m - \lambda_n} = \frac{a'}{C_2} + \frac{b'(\lambda_m + \lambda_n)}{C_2} \quad (\text{B.9})$$

- Linear three-term fitting method [148]:

$$-\frac{1}{T_{r_n}} = -\frac{1}{T_0} + \frac{a'\lambda_n}{C_2} + \frac{b'\lambda_n^2}{C_2} \quad (\text{B.10})$$

- Radiance temperature fitting [149]:

$$T_{r_n} = T_0 + g\lambda_n \quad (\text{B.11})$$

- Non-linear fitting method [146]:

$$I(\lambda, T) = (a + b\lambda) \frac{C_1}{\lambda^5} \left(\frac{1}{e^{\frac{C_2}{T\lambda}} - 1} \right) \quad (\text{B.12})$$

Ratio pyrometry assumes a constant emissivity, which results in an analytical temperature determination

$$T = \frac{1 - \lambda_1/\lambda_2}{\frac{1}{T_{r_1}} - \frac{\lambda_1/\lambda_2}{T_{r_2}}}. \quad (\text{B.13})$$

This method is often used with intensity measurements made at wavelengths within a few percent of each other. Ratio pyrometry is included in this study to determine its accuracy when measuring intensity over the relatively wide range of the visible spectrum.

B.3.1 Discussion

An appropriate procedure to determine the accuracy of each method would be to measure the thermal radiation of many calibrated surfaces and compare the departure of the temperature predicted by each method from the known temperature. Unfortunately, only refractory metals (tantalum, molybdenum, rhenium, and tungsten) are in the solid state over the entire range of temperatures used in this study; and of those only tungsten lamps have been calibrated for pyrometric studies. In order to consider various surfaces, we simulated the intensity radiating from refractory metals using Planck's law and emissivity values found

in reference [74]. The extent of the existing data limits the possible number of different simulations to 12. In order for the fitting routines to determine an appropriate uncertainty in the predicted temperature there must be an uncertainty associated with the simulated intensity data; we assumed 3%. The resulting deviation of the predicted temperature and its uncertainty (both expressed as percent of the true temperature) are shown in Table B.1, where each column number corresponds to one of the seven methods discussed below.

Single-color pyrometry (Method 1)

Single-color pyrometry, with an assumed emissivity of 0.45, predicted the temperature to within 1% of the actual temperature in eleven of the twelve cases. Published values of emissivity in the visible spectrum for refractory metals lie between 0.3 and 0.7, providing bounds to determine the uncertainty in temperature. The uncertainty was calculated to be between 4% and 7% in all cases. However, any oxidation or surface contamination could effect the emissivity to a greater degree and thus increase the uncertainty.

Ratio pyrometry (Method 2)

The temperature predicted by Ratio pyrometry gave a relatively large deviation from the true temperature, yielding the worst results of all methods in ten of the cases. The assumption of constant emissivity across the visible spectrum is thus unjustifiable.

Linear fitting methods (Methods 3,4 & 5)

The three linear fitting methods yield temperature predictions to within 0.1% of each other. Because the relations in the two-term fitting methods are reformulations of the relation in linear three-term method, we expected the predictions to be similar. The only difference between the predictions of the methods is the uncertainty they assign to the temperature. Fitting only two of the three terms in the radiation model reduces the uncertainty in the fit because the least-squares routine fits four data points to a two-parameter model, when

three parameters exist. The linear two-term temperature fitting method (Method 3) gives the smallest uncertainty because the temperature is directly determined from the two-term fit. The linear two-term emissivity fitting method (Method 4) has a larger uncertainty because both terms of the emissivity model are fit and the error in the fit is propagated to the temperature. The linear three-term fitting method (Method 5) fits all radiation model parameters directly and thus leads to a higher uncertainty. Each method is equally valid for determining the temperature in cases where the uncertainty is not underestimated by eliminating terms from the fit; however, we will show in section B.4 that the uncertainty is often under-predicted.

Nonlinear fitting method (Method 6)

The non-linear fitting method has the least deviation of predicted temperature from the true value for six of the cases and is within 0.1% of the best prediction of temperature in three more cases. This method is well suited to determining the temperature of refractory metal surfaces.

Radiance temperature fitting (Method 7)

The radiance temperature fitting method produces the largest or second largest deviation in nine of the cases, and in many of those cases the deviations are two to three times larger than the lowest values obtained. Also, the uncertainty is less than the deviation in five cases, implying that the relative accuracy is not satisfactory.

B.3.2 Recommendations

We compared the performance of six multi-color pyrometry techniques and found that the one nonlinear method and the three linear ones determine the smallest deviation from the true temperature with a reasonable uncertainty. The radiance temperature fitting method and ratio pyrometry do not accurately predict the temperature. One must be cautious when

using the linear two-term fitting routines because the uncertainty could be under-predicted, as discussed in the next section.

B.4 Effect of errors associated with noise and calibration

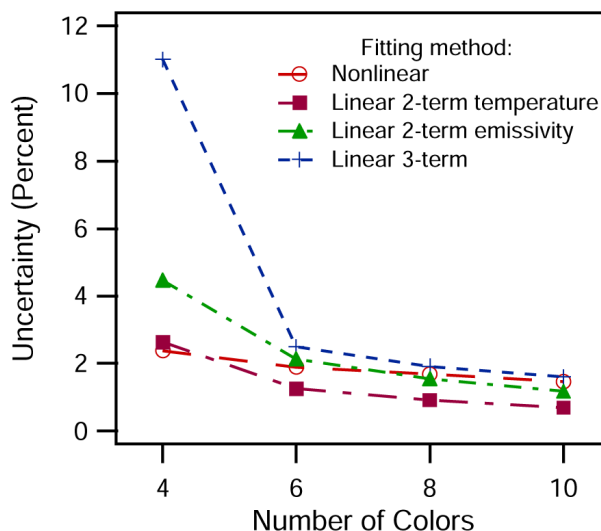


Figure B.1: The predicted temperature uncertainty of four LSMCP methods subject to 1% error associated with noise and calibration.

The LSMCP methods that were shown to perform well in the previous section were further analyzed to determine the effect of errors associated with noise and calibration on the predicted temperature uncertainty. We used a Monte-Carlo simulation to determine the range of temperatures and uncertainties to be expected from the LSMCP methods when the intensity measurements are subject to random noise. The deviation in the simulated intensity from the nominal value was limited to the magnitude of the errors associated with noise and calibration; chosen to be 1%, 3% or 5%. (The standard deviation was 60% of the error.) We determined that the predicted temperatures and uncertainties of the Monte-Carlo simulation change by less than 2% when more than 1000 cases are included, thus we used 1000 cases throughout the analysis.

A Monte-Carlo analysis was conducted for each combination of 4, 6, 8, and 10 color

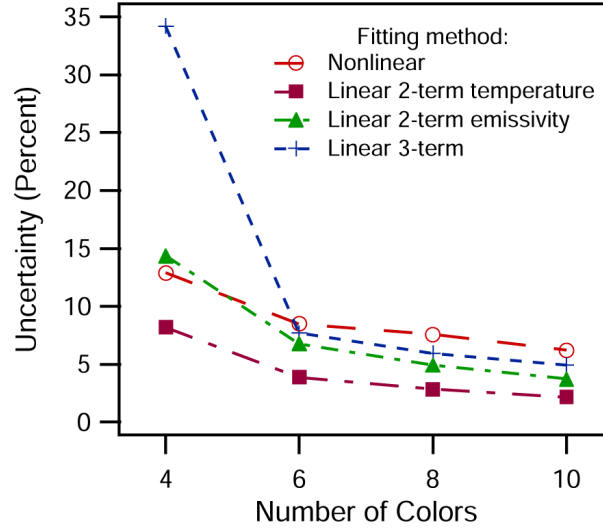


Figure B.2: The predicted temperature uncertainty of four LSMCP methods subject to 3% error associated with noise and calibration.

pyrometers and for noise and calibration errors of 1%, 3%, and 5%. The intensity of the radiation from a 2700 K surface was calculated using Planck's law (B.1) with the artificial emissivity model

$$\epsilon_{\lambda} = 0.5 - 0.0001\lambda. \quad (\text{B.14})$$

The values of the coefficients were chosen to be similar to those determined experimentally for many metallic surfaces to ensure that the results of the simulations are applicable to the temperature measurement of metal surfaces.

B.4.1 Discussion

The dependence of the uncertainty of the predicted temperature on the number of colors of the pyrometer is presented for each fitting method in figures B.1, B.2, and B.3; where the plots show the uncertainty resulting from errors associated with noise and calibration of 1%, 3%, and 5%, respectively. For pyrometers of greater than four colors and errors of 1% or 3%, both the linear three-term and nonlinear methods have similar uncertainties in the predicted temperature. 5% errors associated with noise and calibration cause the

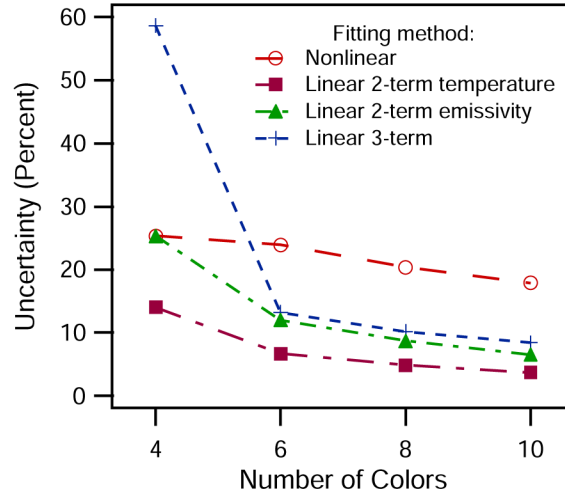


Figure B.3: The predicted temperature uncertainty of four LSMCP methods subject to 5% error associated with noise and calibration.

nonlinear fitting method to predict large uncertainties in temperature, shown in figure B.3. The linear two-term fitting methods yield smaller uncertainties than that of the linear three-term method in all cases, with the two-term temperature fitting method being the smallest.

With the exception of the four-color pyrometer, a general comparison of the uncertainty in the predicted temperature of the LSMCP methods and that of single-color pyrometry can be made. Figure B.1 shows that a 1% error associated with noise and calibration generally results in an uncertainty in predicted temperature of less than 2%, while a single-color pyrometer has approximately a 5% uncertainty for all magnitudes of error. The uncertainty in temperature determined by the LSMCP methods when there is a 3% and 5% error (figures B.2 and B.3) is similar to or larger than that of single-color pyrometry. In order to circumvent the difficulties of lowering the noise of the detector and optics below 3% we developed a method of increasing the accuracy through complementary measurements (Section B.5).

The Monte-Carlo analysis also determined that the uncertainty is under-estimated for both ten-color pyrometers using the two-term emissivity fitting method and greater than four-color pyrometers using the two-term temperature fit. The curves labelled “calculated uncertainty” in figures B.4 and B.5 represent the uncertainty in the predicted temperature

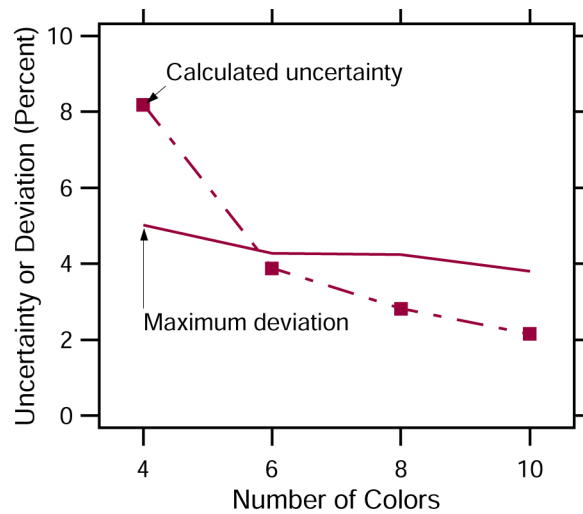


Figure B.4: Demonstration of the under-predicted uncertainty of the linear 2-term temperature fitting method.

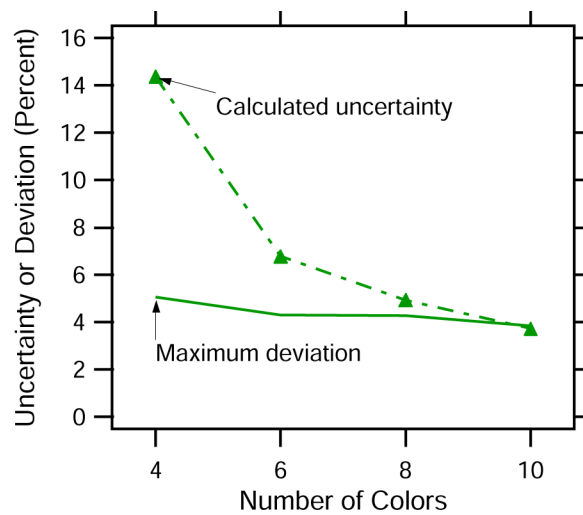
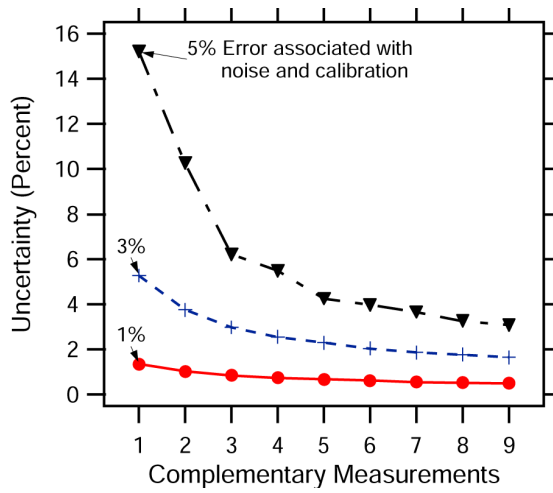
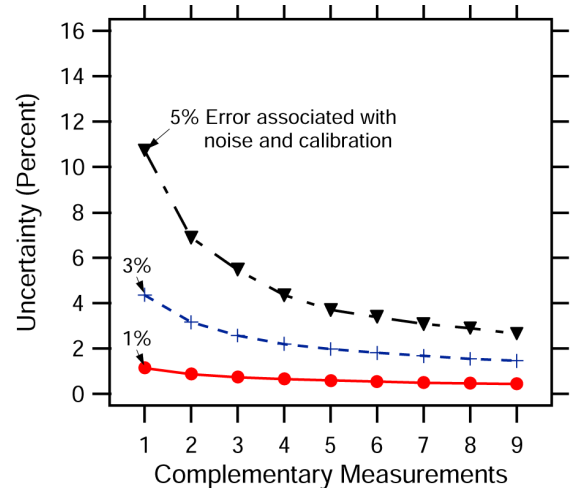


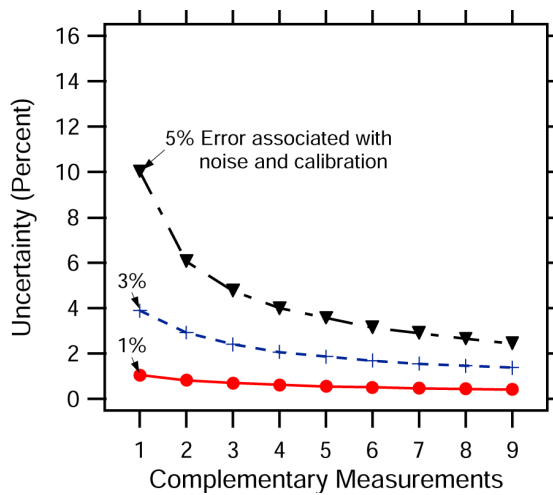
Figure B.5: Demonstration of a under-predicted uncertainty of the linear 2-term emissivity fitting method.



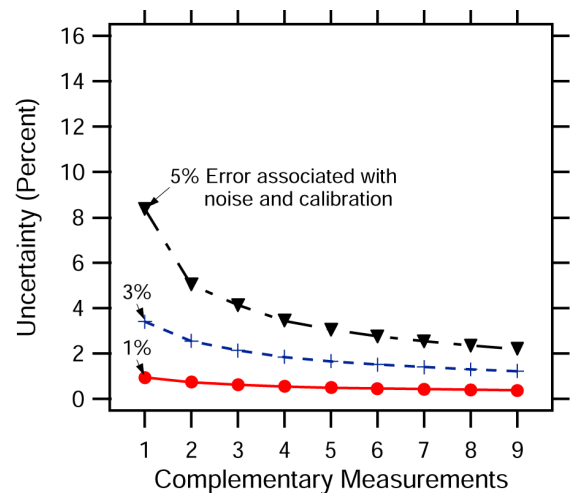
B.6a. 4-color pyrometer



B.6b. 6-color pyrometer

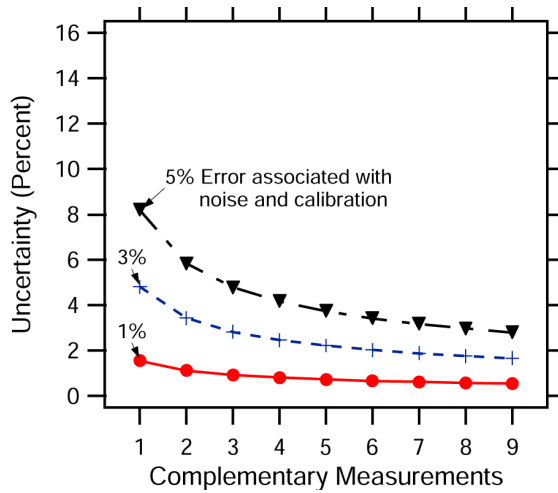


B.6c. 8-color pyrometer

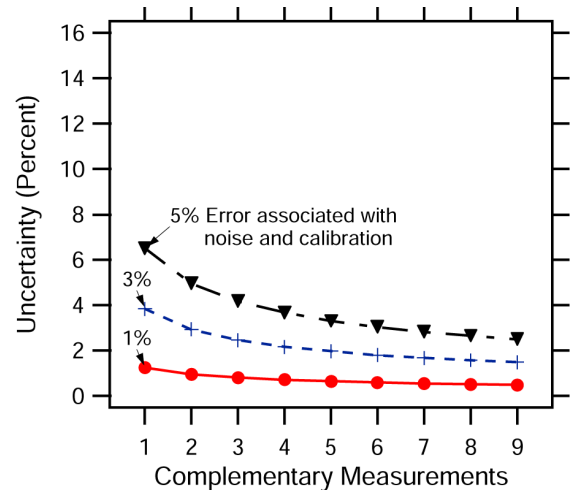


B.6d. 10-color pyrometer

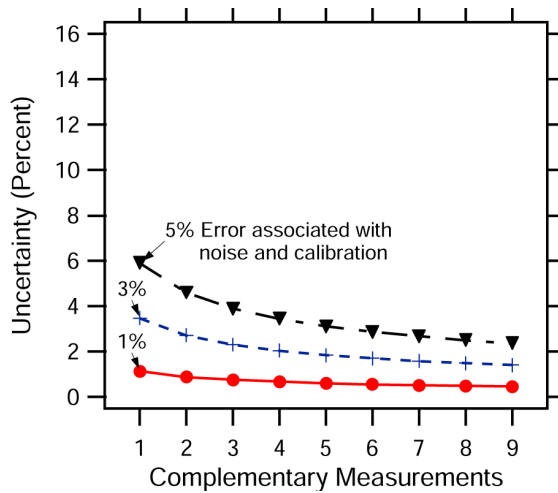
Figure B.6: The uncertainty in the predicted temperature as a function of complementary measurements for the nonlinear fitting method.



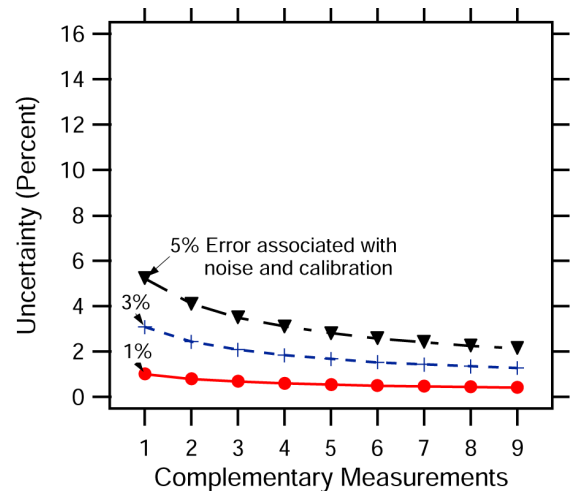
B.7a. 4-color pyrometer



B.7b. 6-color pyrometer



B.7c. 8-color pyrometer



B.7d. 10-color pyrometer

Figure B.7: The uncertainty in the predicted temperature as a function of complementary measurements for the linear three-term fitting method.

of the two-term fitting methods; the same as in the previous figures. The “maximum deviation” curves represent the magnitude of the maximum deviation of the predicted temperature from the true temperature. If the “calculated uncertainty” curve has a larger value than the “maximum deviation” curve, the method has determined an appropriate uncertainty; i.e. the true temperature will lie within the error bars. As can be seen in figures B.4 and B.5, the curves cross indicating that the methods under-predict the uncertainty. Although only the cases of 3% error associated with noise and calibration are shown, the trends are identical in the other cases.

B.4.2 Recommendations

The results of the Monte-Carlo analysis demonstrate that fitting the intensity data using either the linear three-term or nonlinear fitting methods will always predict the appropriate uncertainty in the temperature, but the uncertainty may not be the smallest when compared to that of the linear two-term fits. When the error associated with noise and calibration is less than 5%, the linear three-term and nonlinear fits yield approximately the same uncertainty in the predicted temperature. This allows a method to be selected based solely on the emissivity model that best represents the surface being measured. The two-term temperature fitting method should only be used with 4-color pyrometers, while the linear two-term temperature emissivity fitting method can be used with 4, 6, and 8-color pyrometers.

B.5 Complementary Measurements

The uncertainties in the predicted temperature found for the linear three-term and nonlinear fitting methods are larger than those of single-color pyrometry when the errors associated with noise and calibration are greater than 1%, making single-color pyrometry more accurate in many cases. A new method for LSMCP, designated complementary measurements, was developed to reduce the uncertainty below that of single-color pyrometry. We define

complementary measurements as additional intensity data measured at each wavelength of the pyrometer. For a pyrometer with a fixed number of colors this implies using adjacent pixels on a CCD array or including measurements taken at successive times.

A Monte-Carlo analysis, similar to that used in section B.4, of the linear three-term and nonlinear fitting routines determined the predicted temperature and its uncertainty when complementary measurements are included. The linear two-term fitting methods underestimate the uncertainty of the predicted temperature in the majority of the cases and thus are ignored. The analysis included one to nine complementary measurements, 1%, 3%, and 5% error associated with noise and uncertainty, and 4, 6, 8, and 10-color pyrometers.

It can be seen in figures B.6 and B.7 that the uncertainty in the predicted temperature is always less than the 5% associated with single-color pyrometry when the number of complementary measurements is greater than three or four. For example, a four-color pyrometer with a 3% error requires two complementary measurements with the nonlinear fitting method and one complementary measurement with the linear fit. The figures also show that the uncertainty in the predicted temperature asymptotes to the same value for each fitting method and error. This yields the minimum uncertainty attainable by that method given an error associated with noise and calibration.

B.6 Conclusions

We have addressed the obstacles that exist for developing multi-color pyrometers for experimental use by comparing the ability of five LSMCP methods to determine temperature and the uncertainty of that prediction. We showed that:

1. The radiance temperature fitting method does not accurately predict the temperature.
2. The linear two-term temperature fitting method accurately predicts the temperature only with four-color pyrometers.

3. The linear two-term emissivity fitting method accurately predicts the temperature with 4, 6, and 8-color pyrometers.
4. The linear three-term and nonlinear methods accurately predict the temperature with pyrometers of any number of colors.

These conclusions indicate that the linear three-term and nonlinear fitting methods could be considered the standards in LSMCP, with the linear 2-term fitting methods being used only in certain circumstances.

Except when the errors associated with noise and calibration are at or below 1%, single-color pyrometers, with a modest assumption of the range of the emissivity, offer a higher accuracy than LSMCP. The method of complementary measurements was introduced to reduce the uncertainty in the results of LSMCP. This method can be used with linear three-term and nonlinear fitting methods to reduce the uncertainty in the predicted temperature well below that of single-color pyrometers, with the price of reduced temporal or spatial resolution.

Appendix C

Spectroscopy Data

The raw spectroscopy data is presented in figures C.1 to C.20. The MCHC data presented in figures C.19 and C.20 are not from the same cathode described in section 3.4. This cathode has a larger outer diameter (12.7 mm) at the cathode tip and one of the 1 mm channels was clogged. We did not record spectroscopy data with the other MCHC because the experiment was unexpectedly terminated before that was accomplished.

The weighted emission intensity of the line at $E_m = 3 \times 10^{-19}$ J (6708 Å) was at least one order of magnitude less than that expected for reasonable temperatures. It is possible that the lower energy level of atom could be underpopulated compared to the Boltzmann distribution while higher levels fit the LTE model [86, 153, 154]. A study conducted by Goodfellow and Polk [155] also discarded data from lower energy levels; however, no clear explanation or rationale is given for doing so. Since the transition that produced the 6708 Å line involves the lowest energy level of lithium, it is reasonable to ignore that data.

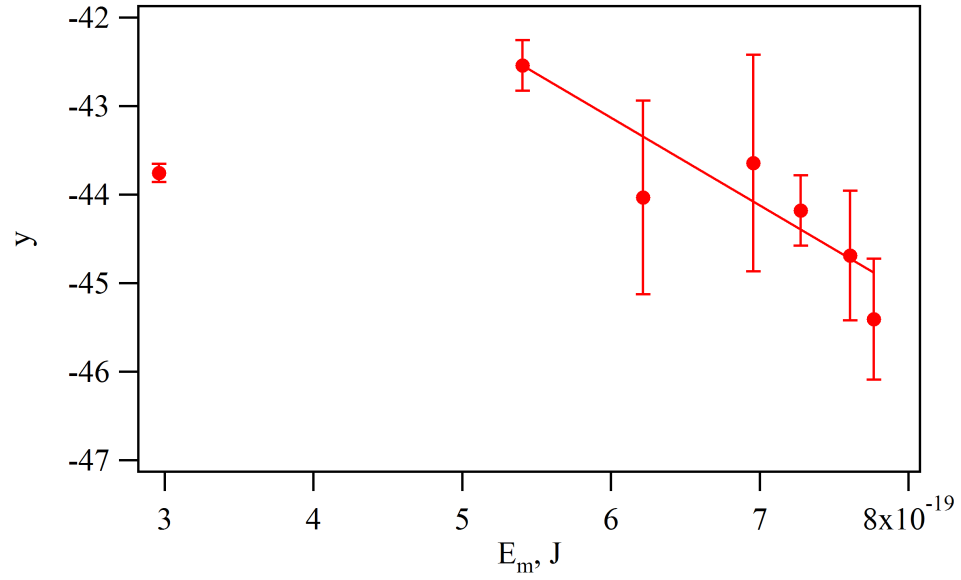


Figure C.1: Weighted dimensionless spectral emission intensity, y , versus upper state energy, E_m , of the 2 mm SCHC operated at 5 A and 1.0 mg/s lithium flow rate. The electron temperature is calculated to be: $T_e = 0.63 \pm 0.12$ eV

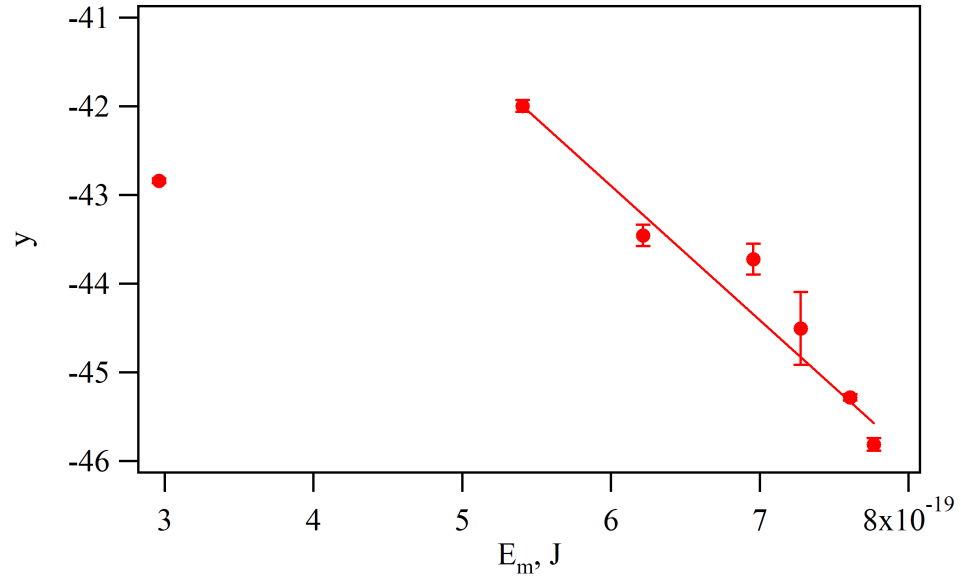


Figure C.2: Weighted dimensionless spectral emission intensity, y , versus upper state energy, E_m , of the 2 mm SCHC operated at 20 A and 1.0 mg/s lithium flow rate. The electron temperature is calculated to be: $T_e = 0.41 \pm 0.008$ eV

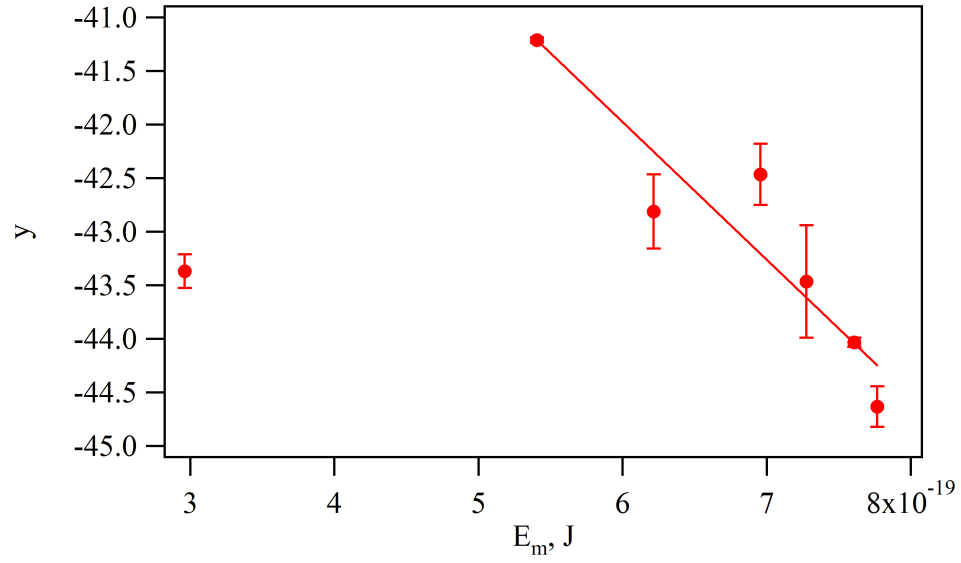


Figure C.3: Weighted dimensionless spectral emission intensity, y , versus upper state energy, E_m , of the 2 mm SCHC operated at 10 A and 2.0 mg/s lithium flow rate. The electron temperature is calculated to be: $T_e = 0.49 \pm 0.008$ eV

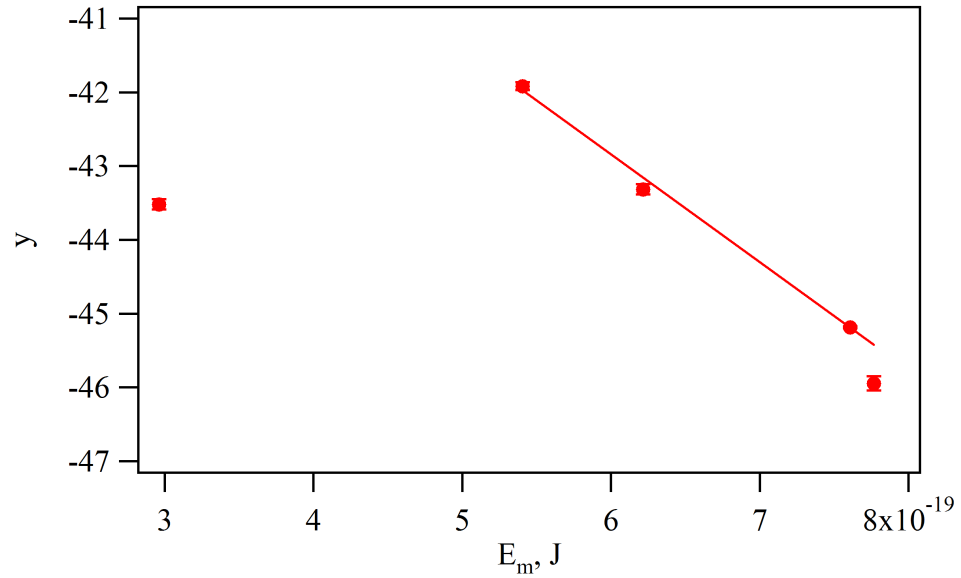


Figure C.4: Weighted dimensionless spectral emission intensity, y , versus upper state energy, E_m , of the 2 mm SCHC operated at 20 A and 2.0 mg/s lithium flow rate. The electron temperature is calculated to be: $T_e = 0.43 \pm 0.007$ eV

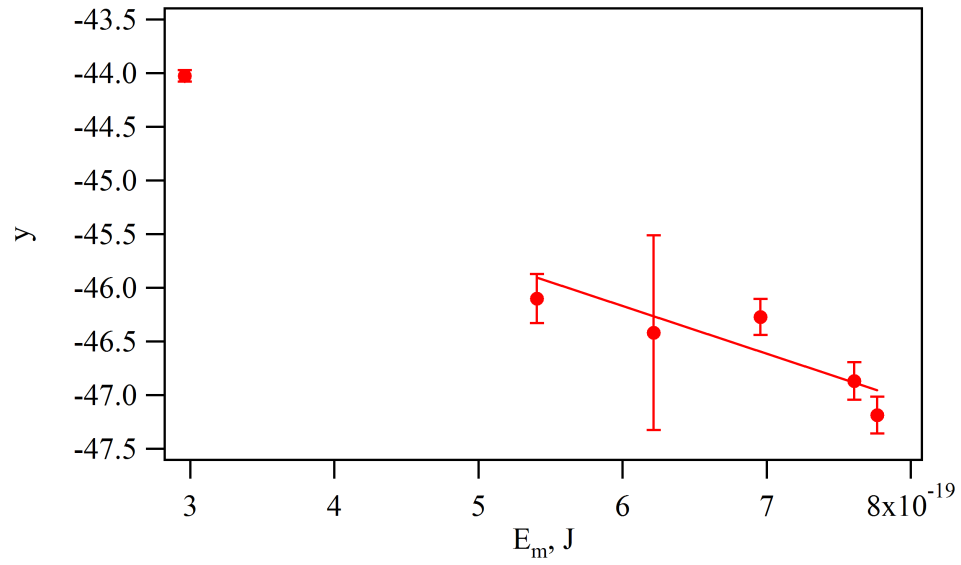


Figure C.5: Weighted dimensionless spectral emission intensity, y , versus upper state energy, E_m , of the 2 mm SCHC operated at 10 A and 0.5 mg/s lithium flow rate. The electron temperature is calculated to be: $T_e = 1.40 \pm 0.43$ eV

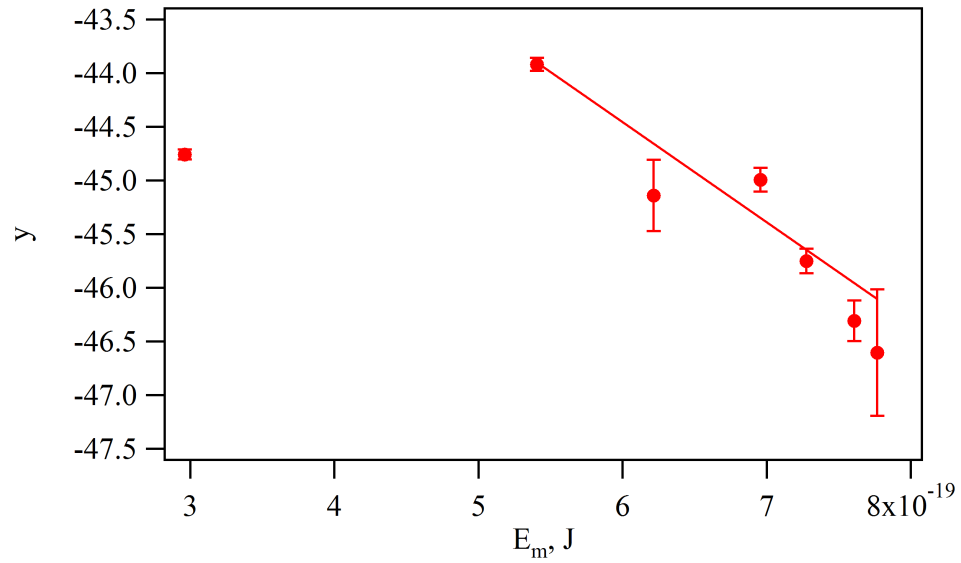


Figure C.6: Weighted dimensionless spectral emission intensity, y , versus upper state energy, E_m , of the 2 mm SCHC operated at 10 A and 4.0 mg/s lithium flow rate. The electron temperature is calculated to be: $T_e = 0.67 \pm 0.04$ eV

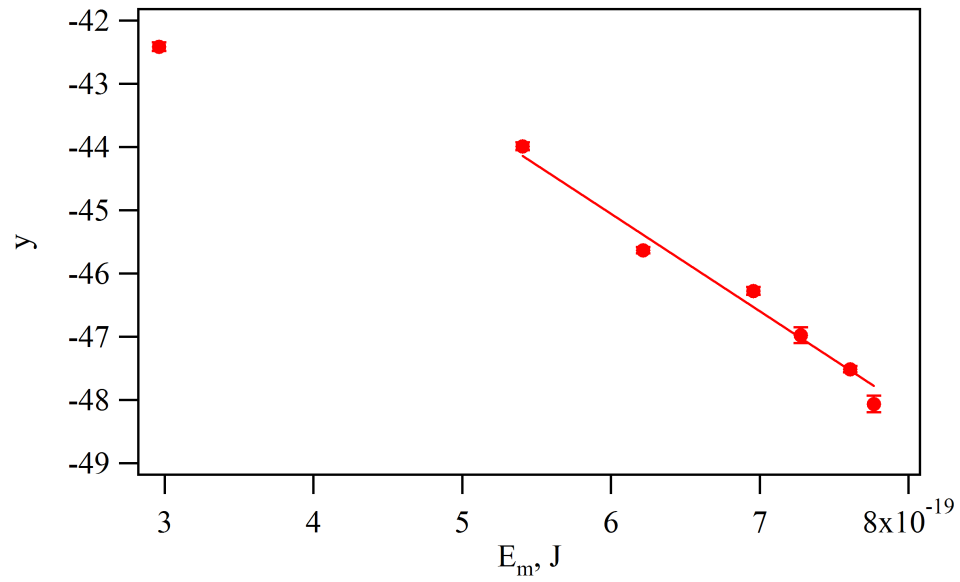


Figure C.7: Weighted dimensionless spectral emission intensity, y , versus upper state energy, E_m , of the 2 mm SCHC operated at 40 A and 1.0 mg/s lithium flow rate. The electron temperature is calculated to be: $T_e = 0.41 \pm 0.01$ eV

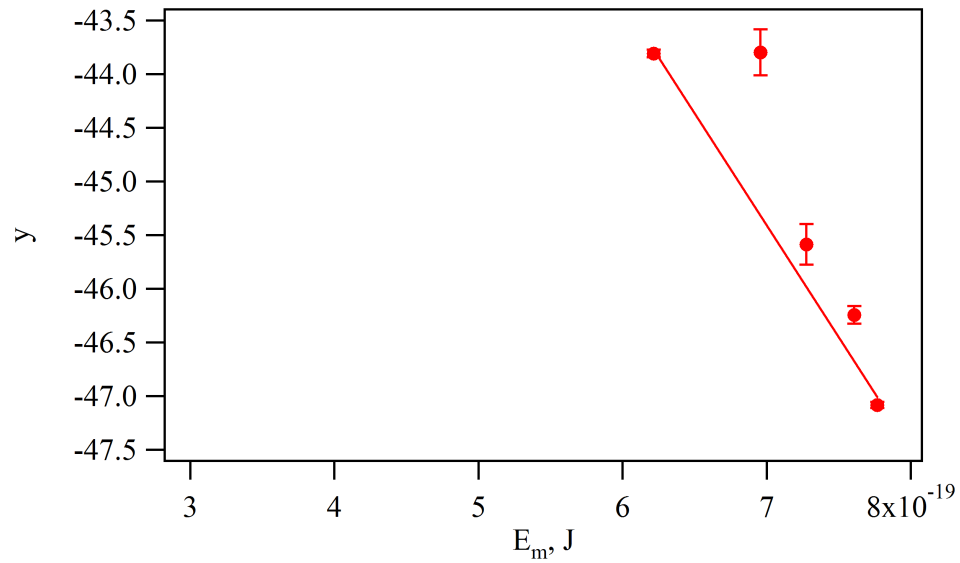


Figure C.8: Weighted dimensionless spectral emission intensity, y , versus upper state energy, E_m , of the 8 mm SCHC operated at 20 A and 1.0 mg/s lithium flow rate. The electron temperature is calculated to be: $T_e = 0.30 \pm 0.005$ eV

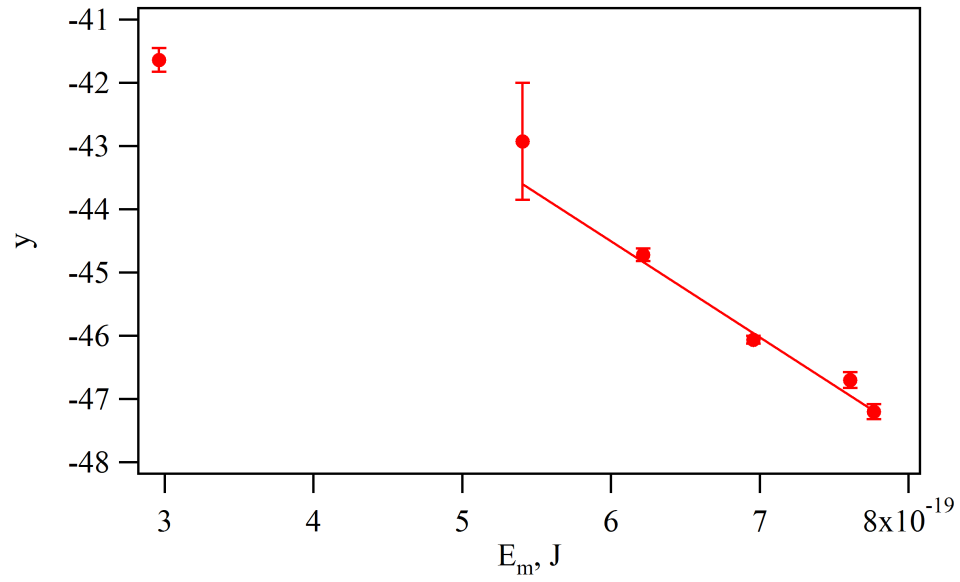


Figure C.9: Weighted dimensionless spectral emission intensity, y , versus upper state energy, E_m , of the 8 mm SCHC operated at 20 A and 0.8 mg/s lithium flow rate. The electron temperature is calculated to be: $T_e = 0.41 \pm 0.03$ eV

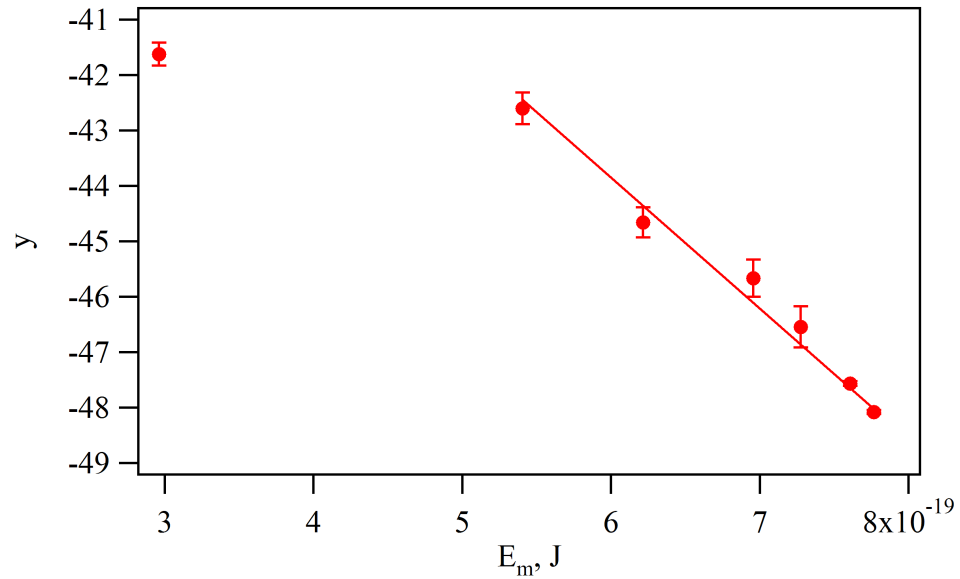


Figure C.10: Weighted dimensionless spectral emission intensity, y , versus upper state energy, E_m , of the 8 mm SCHC operated at 30 A and 0.8 mg/s lithium flow rate. The electron temperature is calculated to be: $T_e = 0.26 \pm 0.01$ eV

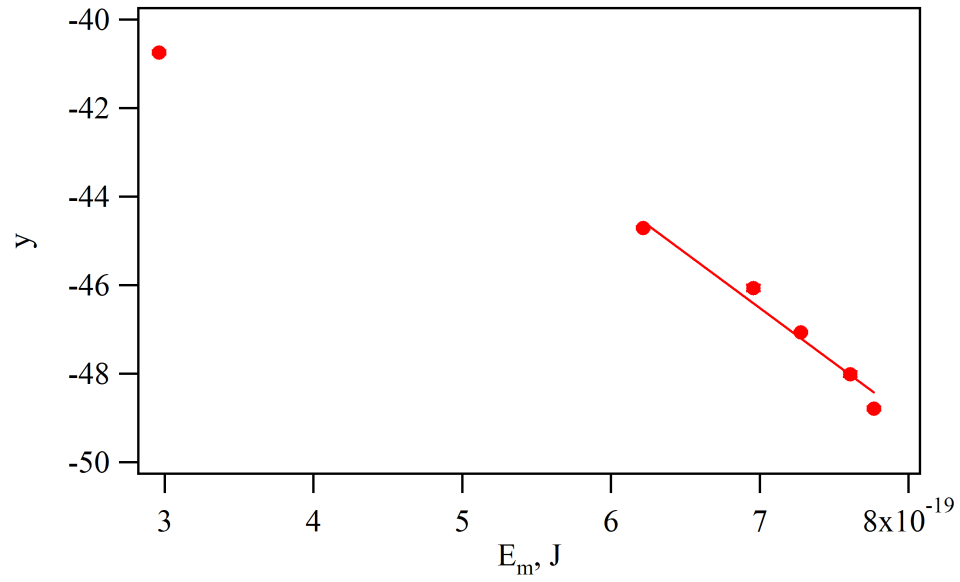


Figure C.11: Weighted dimensionless spectral emission intensity, y , versus upper state energy, E_m , of the 4 mm SCHC operated at 25 A and 0.4 mg/s lithium flow rate. The electron temperature is calculated to be: $T_e = 0.25 \pm 0.004$ eV

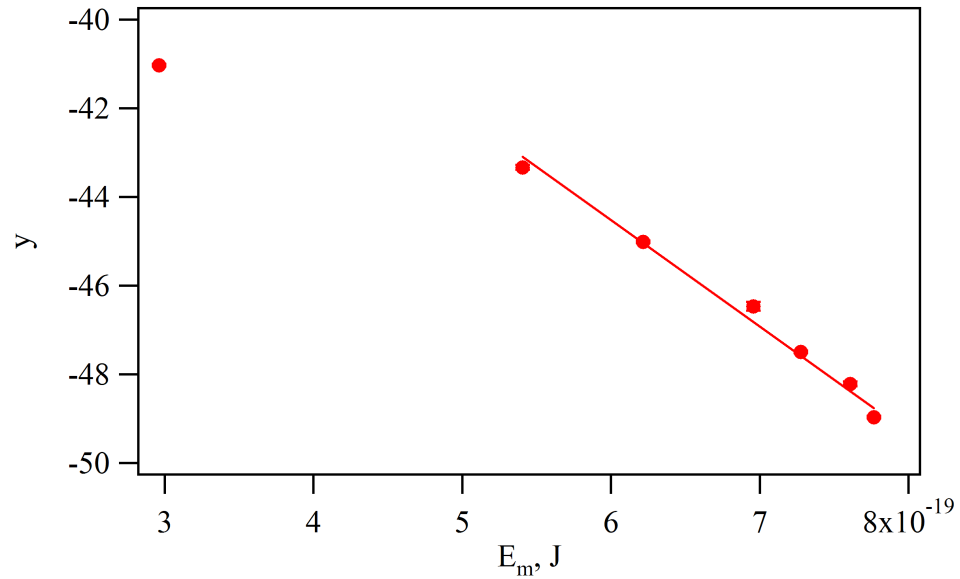


Figure C.12: Weighted dimensionless spectral emission intensity, y , versus upper state energy, E_m , of the 4 mm SCHC operated at 25 A and 0.8 mg/s lithium flow rate. The electron temperature is calculated to be: $T_e = 0.26 \pm 0.002$ eV

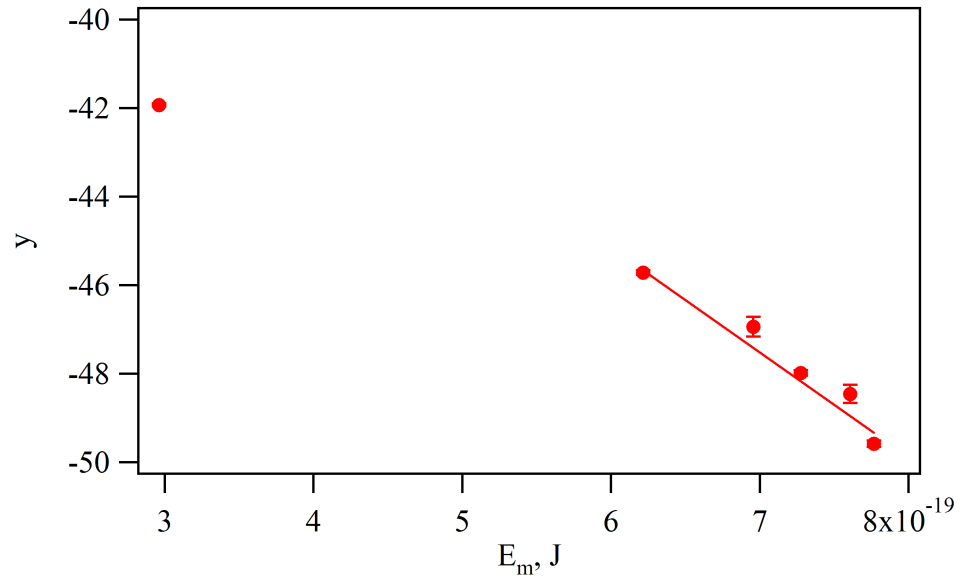


Figure C.13: Weighted dimensionless spectral emission intensity, y , versus upper state energy, E_m , of the 4 mm SCHC operated at 60 A and 0.8 mg/s lithium flow rate. The electron temperature is calculated to be: $T_e = 0.260 \pm 0.007$ eV

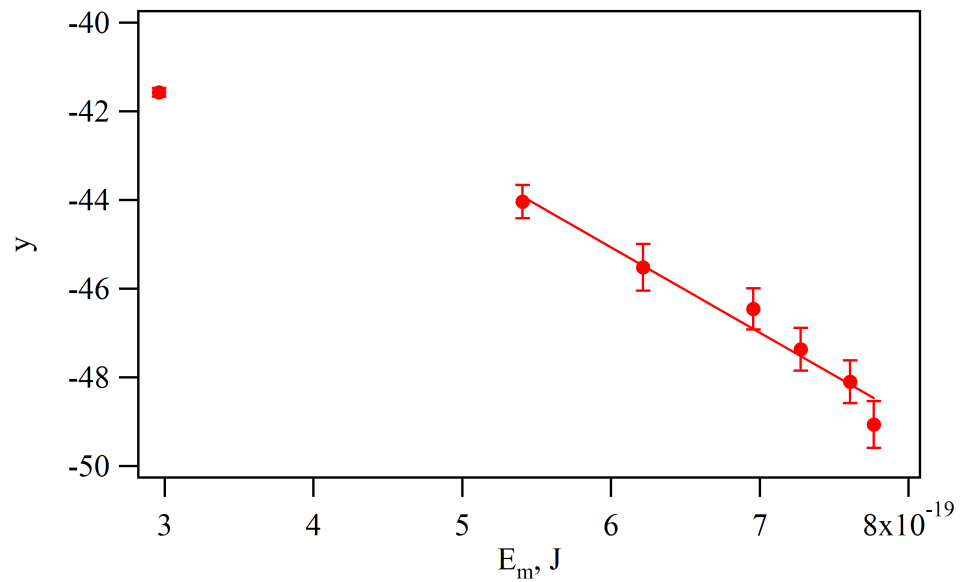


Figure C.14: Weighted dimensionless spectral emission intensity, y , versus upper state energy, E_m , of the 4 mm SCHC operated at 60 A and 0.4 mg/s lithium flow rate. The electron temperature is calculated to be: $T_e = 0.32 \pm 0.04$ eV

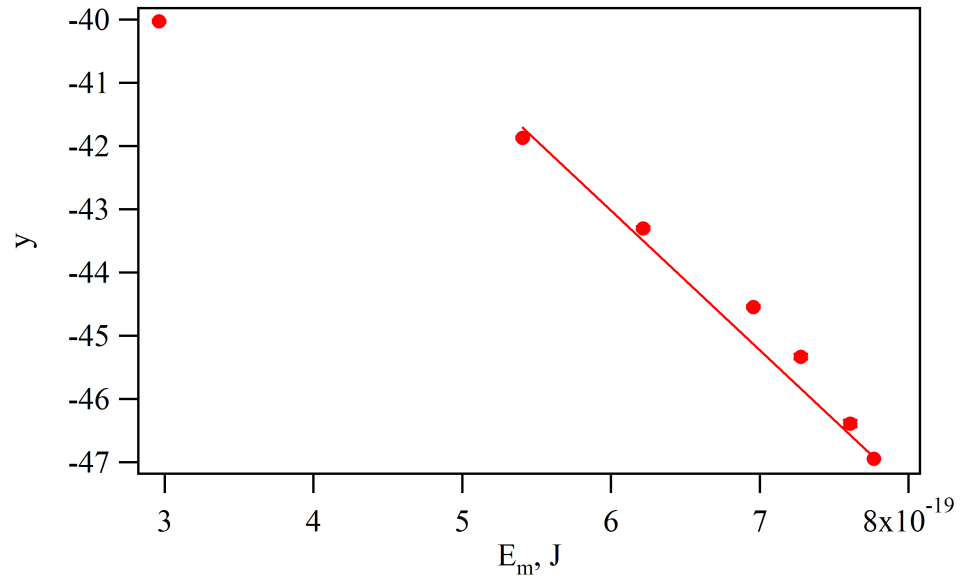


Figure C.15: Weighted dimensionless spectral emission intensity, y , versus upper state energy, E_m , of the 6 mm SCHC operated at 100 A and 0.8 mg/s lithium flow rate. The electron temperature is calculated to be: $T_e = 0.28 \pm 0.001$ eV

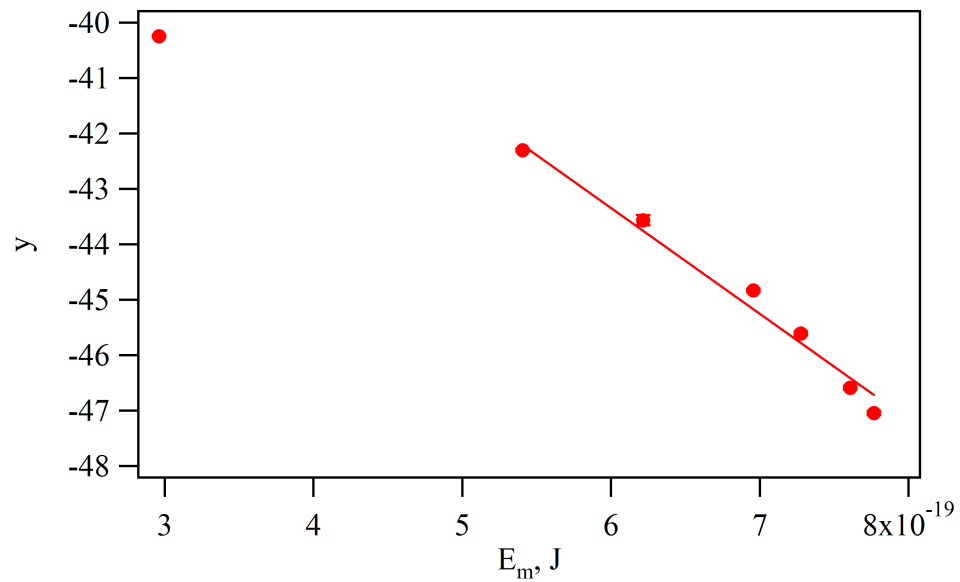


Figure C.16: Weighted dimensionless spectral emission intensity, y , versus upper state energy, E_m , of the 6 mm SCHC operated at 100 A and 0.4 mg/s lithium flow rate. The electron temperature is calculated to be: $T_e = 0.33 \pm 0.003$ eV

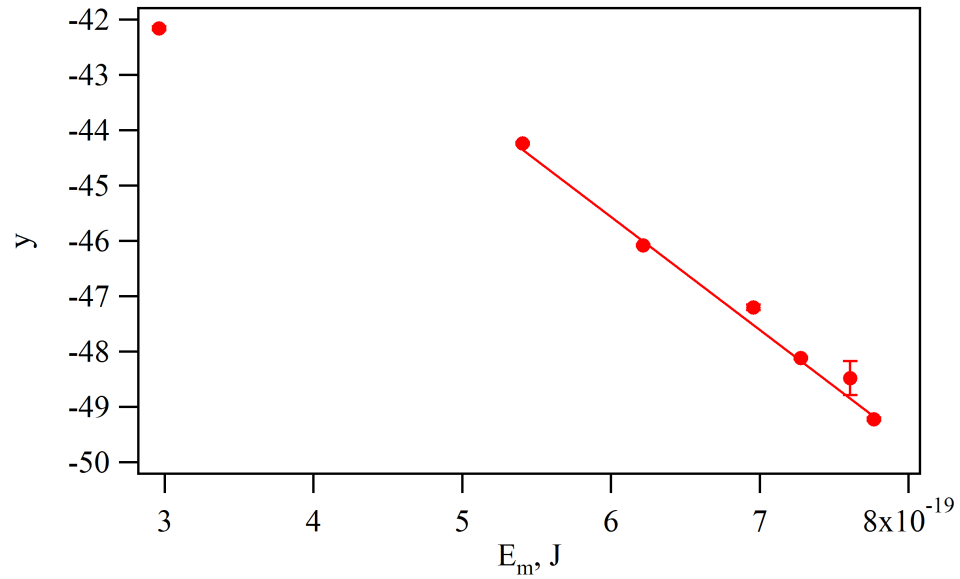


Figure C.17: Weighted dimensionless spectral emission intensity, y , versus upper state energy, E_m , of the 6 mm SCHC operated at 25 A and 0.8 mg/s lithium flow rate. The electron temperature is calculated to be: $T_e = 0.31 \pm 0.002 \text{ eV}$

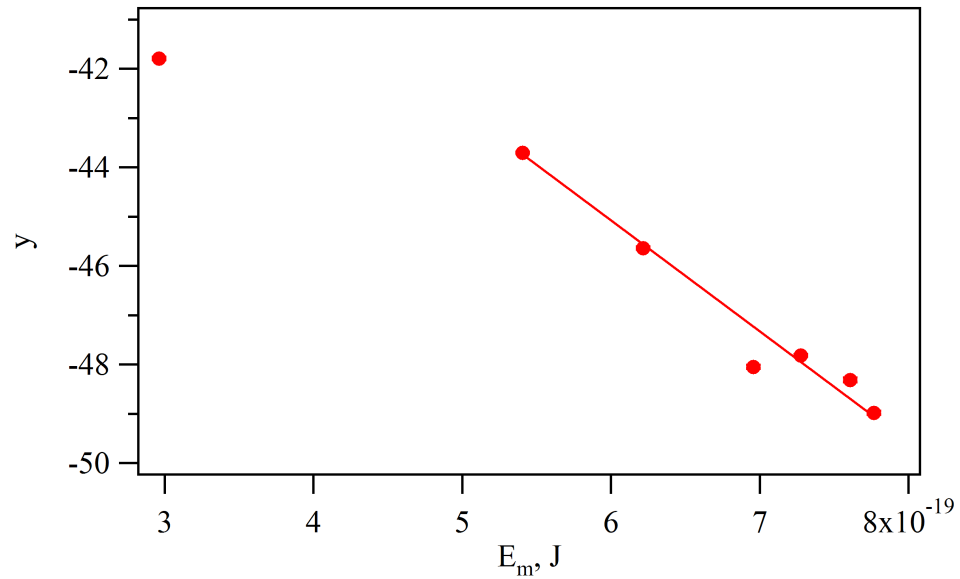


Figure C.18: Weighted dimensionless spectral emission intensity, y , versus upper state energy, E_m , of the 6 mm SCHC operated at 30 A and 0.4 mg/s lithium flow rate. The electron temperature is calculated to be: $T_e = 0.28 \pm 0.002 \text{ eV}$

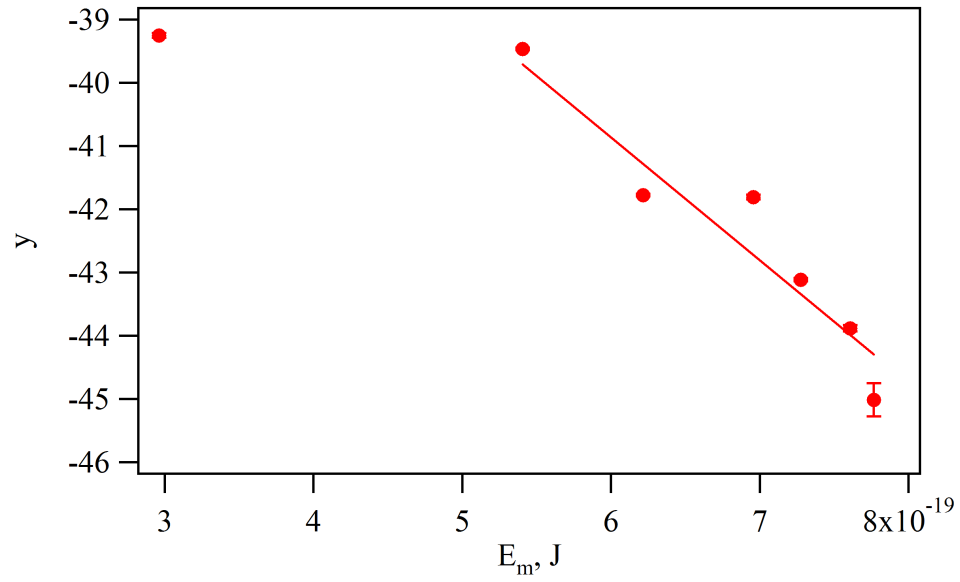


Figure C.19: Weighted dimensionless spectral emission intensity, y , versus upper state energy, E_m , of an 18 channel MCHC operated at 100 A and 2.0 mg/s lithium flow rate. The electron temperature is calculated to be: $T_e = 0.32 \pm 0.003$ eV

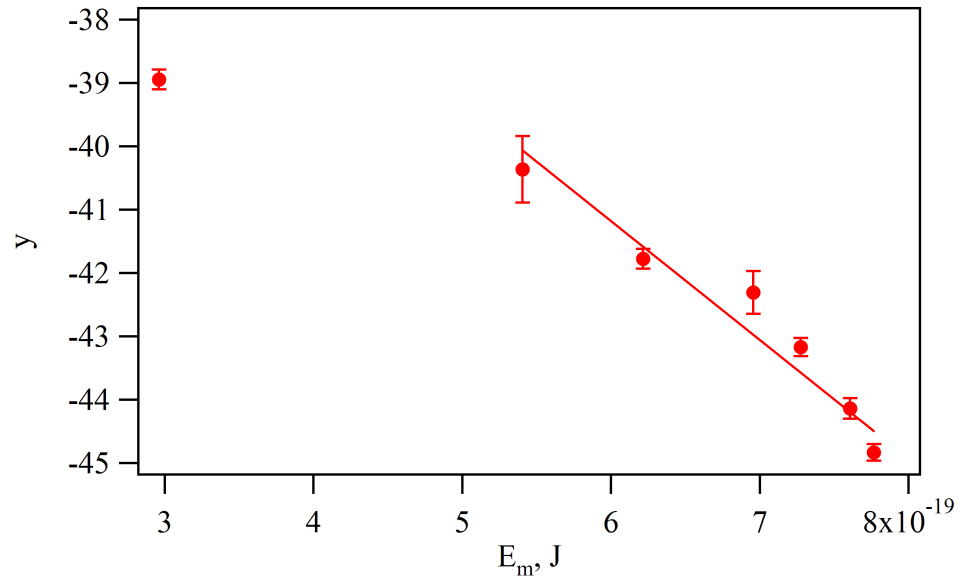


Figure C.20: Weighted dimensionless spectral emission intensity, y , versus upper state energy, E_m , of an 18 channel MCHC operated at 140 A and 0.8 mg/s lithium flow rate. The electron temperature is calculated to be: $T_e = 0.33 \pm 0.02$ eV

Appendix D

Lithium Surface Coverage ¹

The equilibrium surface coverage of lithium on the cathode that is due to a flux from the gas or ions from the plasma is given by

$$k_a n_{Li} = k_d N_{Li}, \quad (\text{D.1})$$

where k_a is the condensation rate coefficient, n_{Li} is the gas or ion density near the cathode surface, k_d is the desorption rate coefficient, and N_{Li} is the surface density. Assuming that the adsorption process is non-activated, the adsorption sites are non-localized, and there are no competing adsorbate species

$$k_d N_{Li} = \omega_{Li} \exp \left[\frac{-E_d^{Li}}{k_B T_c} \right] N_{min}^{Li} f_{Li}, \quad (\text{D.2})$$

where k_B is the Boltzmann constant, T_c is the cathode wall temperature, ω_{Li} is an experimentally determined pre-exponential coefficient, E_d^{Li} is the desorption energy, N_{min}^{Li} is the surface density with the minimum work function, and f_{Li} is the fractional surface coverage, N_{Li}/N_{min}^{Li} . The lithium surface density with minimum work function is $5 \times 10^{-14} \text{ cm}^{-2}$. The flux of the lithium toward the surface depends on if it is a neutral or an ion. If it is a

¹The analysis in this appendix is based upon Appendix E of J. Polk's dissertation. [12]

neutral, then the flux depends on the random thermal velocity. If it is an ion, then the flux is determined by the Bohm velocity. The total flux is given by

$$k_a n_{li} = \alpha_i \frac{p}{k_B T_c} \sqrt{\frac{k_B T_e}{m_{Li}}} + \frac{(1 - \alpha_i)p}{(2\pi m_{Li} k_B T_c)^{1/2}}, \quad (\text{D.3})$$

where α_i is the ionization fraction, T_e is the electron temperature, p is the vapor pressure, and m_{Li} is the lithium molecular weight. The gas temperature is assumed to be equal to the cathode wall temperature.

The material coefficients ω_{Li} and E_d^{Li} were determined experimentally by Medvedev and Smereka [156] as a function of temperature and coverage, f_{Li} on the (110) crystal face of the tungsten crystal. This face is the most likely to be exposed after extended heating because it is the lowest surface energy state [12]. The surface coverage can be calculated as a function of surface temperature and ionization fraction. The isotherms of lithium at 0%, 50%, and 100% ionization fraction are shown in figures D.1, D.2, and D.3, respectively. Coverage fractions of less than approximately 0.05 do not significantly change the surface work function and therefore do not affect the discharge. The pressure within the channel is at most a few Torr (500 Pa), therefore a weakly ionized discharge would be affected by surface coating at less than 2400 K. This temperature climbs to approximately 2600 K in the case of a fully ionized plasma. We will take 2500 K as the minimum temperature at which lithium adsorption on the cathode surface must be considered.

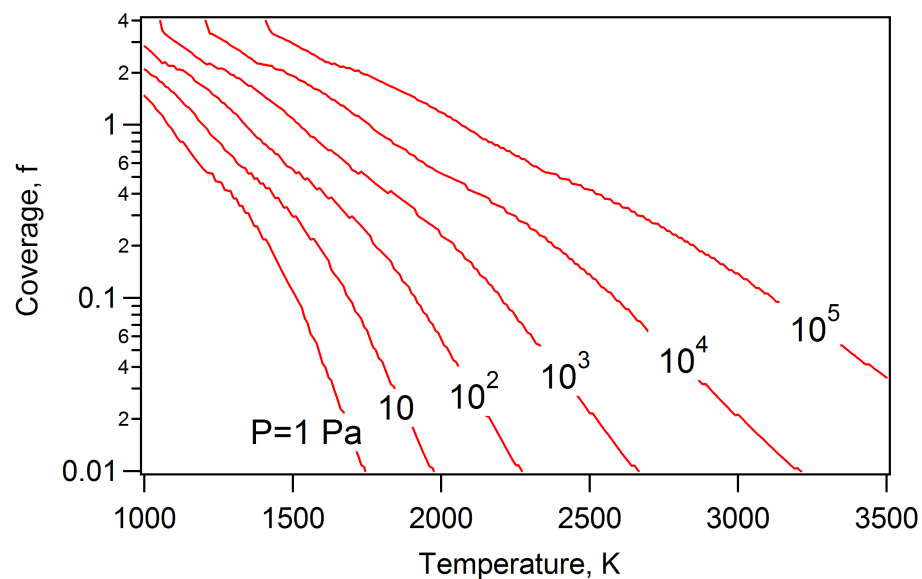


Figure D.1: Surface coverage as a function of temperature and gas pressure for a plasma with a 0% ionization fraction.

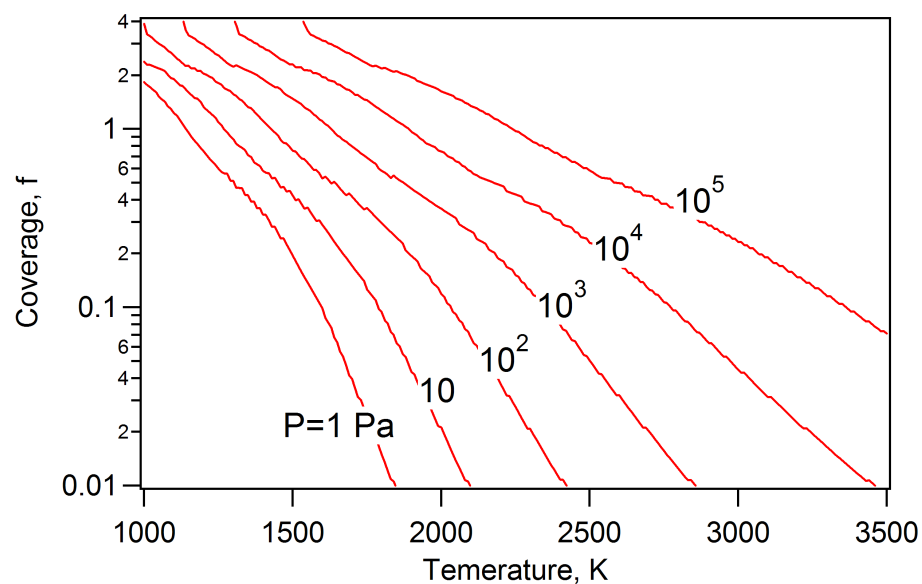


Figure D.2: Surface coverage as a function of temperature and gas pressure for a plasma with a 50% ionization fraction.

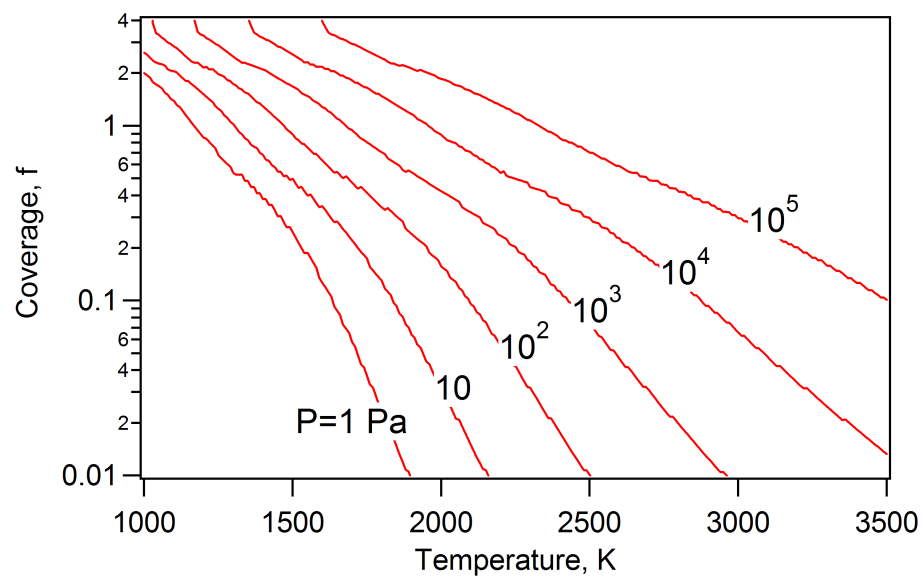


Figure D.3: Surface coverage as a function of temperature and gas pressure for a plasma with a 100% ionization fraction.

Appendix E

Double Sheath Derivation

We begin by deriving a model of the double sheath, similar to that of Prewett and Allen [103]. At the high currents of a hollow cathode discharge the double sheath model of Prewett and Allen can predict a space charge limited current, which is not consistent with experimental results. Including a finite thermal energy gives a more accurate model of the sheath that results in larger values of the electric field at the cathode surface [104]. The sheath will be modeled as collisionless. A beam of electrons exit the cathode with a thermal energy equal to the cathode temperature and are accelerated through the sheath. Ions enter the sheath from the plasma and are accelerated until they reach the surface where they recombine to form neutrals. The contribution of the thermal electrons from the plasma is included as well. The cathode will be considered the origin and the sheath/presheath boundary will be considered to have zero potential to clarify the derivation. Therefore, the sheath voltage V_s is related to the cathode voltage V_c as $V_s = V_c - V_o$, where V_o is the presheath potential required to accelerate the ions to the energy eV_o , which will also be determined in this appendix.

E.1 Thermionic Electrons

The thermionic electron flux is a fixed value determined by the temperature of the cathode. The electrons possess an initial thermal energy that is accurately described as a Maxwellian distribution [99, 100]. The average initial energy is thus directly related to the cathode temperature as $\frac{3}{2}k_B T_c$ [59, 101]. We can approximate the energy of the thermionic electrons as a mono-energetic beam because the energy gained by acceleration through the sheath is much greater than the energy associated with the surface temperature. Therefore, the energy differences due to the initial Maxwellian distribution are small compared to the energy gained by acceleration through the sheath and can be neglected. Energy conservation (assuming no collisions) gives the velocity of the thermionic electrons as they pass through the sheath

$$\frac{1}{2}m_e v_b^2 = e(V_s - V) + \frac{3}{2}k_B T_c, \quad (\text{E.1})$$

where $-V_s$ is the potential at the cathode, $-V$ is the potential through the sheath, e is the charge of an electron, m_e is the mass of an electron, and v_b is the velocity of the electron as it moves through the sheath.

The number density of the thermionic electrons can be found from continuity

$$n_b v_b = \frac{j_{th}}{e}, \quad (\text{E.2})$$

where n_b is the number density of thermionic electrons and j_{th} is the current density of the thermionic electrons. The number density is

$$n_b = \frac{j_{th}}{e} m_e^{1/2} [2e(V_s - V) + 3k_B T_c]^{-1/2}. \quad (\text{E.3})$$

An important feature of this model is that there is not an infinite density at the surface, as in most other models. This factor will increase the maximum thermionic current predicted by this model as compared to the others.

E.2 Ions

The Bohm condition applies to the boundary between the sheath and the bulk plasma. The condition specifies that the ions enter the sheath with a velocity equal to the ion sound speed in the plasma. We will express the initial velocity, $v_{i,o}$, in terms of an equivalent potential, V_o ,

$$\frac{1}{2}m_i v_{i,o}^2 = eV_o \quad (\text{E.4})$$

The energy of the ions can be expressed using the energy conservation equation,

$$\frac{1}{2}m_i v_i^2 = \frac{1}{2}m_i v_{i,o}^2 + eV \quad (\text{E.5})$$

as they travel through the sheath without collisions. Combining equations (E.4) and (E.5) gives the ion velocity as a function of sheath potential

$$v_i = \left(\frac{2e}{m_i} \right)^{1/2} (V_o + V)^{1/2}. \quad (\text{E.6})$$

Again, continuity of the electrons must be conserved across the sheath

$$n_i v_i = n_{i,o} v_{i,o}, \quad (\text{E.7})$$

where $n_{i,o}$ is the number density of ions at the sheath edge. Combining equations (E.6) and (E.7) we get the relation for ion number density throughout the sheath

$$n_i = n_{i,o} (1 + V/V_o)^{-1/2} \quad (\text{E.8})$$

E.3 Thermal Electrons

The thermal electrons within the plasma will penetrate into the sheath by virtue of their high thermal energy. This is especially important for a lithium plasma sheath because the potential can be as little as 5 times the energy associated with the electron temperature. We will use a Boltzmann distribution to describe their energy distribution

$$n_e = n_{e,o} \exp(-eV/k_B T_e). \quad (\text{E.9})$$

E.4 Sheath Relations

Since we assumed that the sheath is not quasi-neutral we can use Poisson's equation to determine the potential within the sheath,

$$\epsilon_0 \frac{d^2 V}{dx^2} = \rho_c, \quad (\text{E.10})$$

where ϵ_0 is the permittivity of free space and ρ_c is the space charge density. The space charge density in the sheath is determined by the sum of the relations we derived above for the thermionic electrons, equation (E.3), ions, equation (E.8), and thermal electrons, equation (E.9), multiplied by the electron charge,

$$\begin{aligned} \epsilon_0 \frac{d^2 V}{dx^2} &= -j_{th} m_e^{1/2} [2e(V_s - V) + 3k_B T_c]^{-1/2} \\ &+ n_{i,o} e (1 + V/V_o)^{-1/2} \\ &- n_{e,o} e \exp(-eV/k_B T_e). \end{aligned} \quad (\text{E.11})$$

We normalize the relation to clarify the fundamentals of the problem using the following normalized quantities:

$$\beta = \frac{eV}{k_B T_e} \quad (\text{E.12})$$

$$\tau = \frac{3T_c}{T_e} \quad (\text{E.13})$$

$$\hat{\nu}_i = \frac{n_{i,o}}{n_{e,o}} \quad (\text{E.14})$$

$$\chi_{th} = \frac{j_{th}}{n_{e,o}e(k_B T_e/m_e)^{1/2}} \quad (\text{E.15})$$

$$\xi = x/\lambda_D \quad (\text{E.16})$$

$$\lambda_D = \left(\frac{\epsilon_0 k_B T_e}{n_{e,o} e^2} \right)^{1/2}. \quad (\text{E.17})$$

The normalized equation is

$$\begin{aligned} \frac{d^2 \beta}{d\xi^2} = \varrho = & -\chi_{th} [2(\beta_s - \beta) + \tau]^{-1/2} \\ & + \hat{\nu}_i (1 + \beta/\beta_o)^{-1/2} - \exp(-\beta). \end{aligned} \quad (\text{E.18})$$

We can apply a boundary condition to the above equation to determine the value of one of the free parameters $\hat{\nu}_i$ and β_o . Our first boundary condition is quasineutrality at the sheath-presheath boundary,

$$\varrho = 0 \text{ at } \beta = 0. \quad (\text{E.19})$$

This determines the value of the normalized ion density

$$\hat{\nu}_i = 1 + \chi_{th} (2\beta_s + \tau)^{-1/2}. \quad (\text{E.20})$$

It can be seen that if there is no thermionic current the normalized ion density is unity,

exactly the value predicted by Bohm for a space charge sheath.

The second boundary condition is derived by Andrews and Allen [103]

$$\frac{d\varrho}{d\beta} = 0 \text{ at } \beta = 0 \quad (\text{E.21})$$

and determines β_o

$$\beta_o = \frac{1}{2} \frac{1 + \chi_{th}(2\beta_s + \tau)^{-1/2}}{1 - \chi_{th}(2\beta_s + \tau)^{-3/2}}. \quad (\text{E.22})$$

Again, it can be seen that the Bohm condition is satisfied when the thermionic current is zero. These two boundary conditions can be thought of as modified Bohm conditions for an electron emitting cathode with a double sheath,

$$v_{B,m} = \sqrt{2\beta_o \frac{k_B T_e}{m_i}}. \quad (\text{E.23})$$

The solution of the electric field is found by multiplying by dV/dx and integrating from x to the sheath edge. Setting $E = -dV/dx$, the result is

$$\begin{aligned} \epsilon_c^2 &= -2\chi_{th}[(2\beta_s + \tau)^{1/2} - \tau^{1/2}] \\ &+ 4\hat{\nu}_i\beta_o[(1 + \beta_s/\beta_o)^{1/2} - 1] \\ &+ 2\exp(-\beta_s) - 2 + \epsilon_e^2. \end{aligned} \quad (\text{E.24})$$

An analysis of the normalized electric field will show that the ϵ_e term can be neglected. First, let's approximate the electric field E as $\Delta V/\Delta L$, where ΔL is the characteristic length of the presheath region

$$\epsilon_e = \frac{E\lambda_D}{k_B T_e/e} = \frac{\Delta V}{k_B T_e/e} \frac{\lambda_D}{\Delta L}. \quad (\text{E.25})$$

The characteristic length is defined by the mean free path of the ions, which is normally 10^2 to 10^3 times greater than the Debye length. If we consider that the field in the presheath

is the largest near the sheath, conservatively an order of magnitude larger, we can approximate $\Delta L \approx 10\lambda_D$. The voltage fall in the presheath is approximately half of the electron temperature

$$\frac{\Delta V}{k_B T_e / e} \approx \frac{1}{2}, \quad (\text{E.26})$$

which gives

$$\epsilon_e = \frac{\lambda_D}{2 \Delta L} \approx \frac{1}{20}. \quad (\text{E.27})$$

In equation (E.24) the electric field at the presheath boundary is squared. The square of our approximation of $\epsilon_e^2 = 1/400$ is much smaller than 2, thus it will be neglected.

The electric field at the cathode surface is determined from

$$\begin{aligned} \epsilon_c^2 &= -2\chi_{th}[(2\beta_s + \tau)^{1/2} - \tau^{1/2}] \\ &+ 4\hat{\nu}_i\beta_o[(1 + \beta_s/\beta_o)^{1/2} - 1] \\ &+ 2 \exp(-\beta_s) - 2. \end{aligned} \quad (\text{E.28})$$

Bibliography

- [1] The vision for space exploration. Technical report, NASA, February 2004.
- [2] NASA JPL. Cassini-huygens: Operations-gravity assists, December 20 2004.
<<http://saturn.jpl.nasa.gov/mission/gravity-assists.cfm>>.
- [3] Encyclopedia Astronautica. Saturn v, 2004.
<<http://www.astronautix.com/lvs/saturnv.htm>>.
- [4] R. Frisbee. SP-100 nuclear electric propulsion for mars cargo missions. In *29th AIAA/SAE/ASME/ASEE Joint Propulsion Conference*, Monterey, CA, USA, June 1993. AIAA-93-2092.
- [5] R. Frisbee. Electric propulsion options for mars cargo missions. In *32nd AIAA/ASME/SAE/ASEE Joint Propulsion Conference and Exhibit*, Lake Buena Vista, FL, USA, July 1996. AIAA-96-3173.
- [6] J.E. Polk and T.J. Pivrotto. Alkali metal propellants for MPD thrusters. In *AIAA/NASA/OAI Conference on Advanced SEI Technologies*, Cleveland, OH, USA, September 1991. AIAA-91-3572.
- [7] K. Sankaran, L.D. Cassady, A.D. Kodys, and E.Y. Choueiri. A survey of propulsion options for cargo and piloted missions to mars. In E. Belbruno, D. Folta, and P Gurfil, editors, *Astrodynamics Space Missions and Chaos*, volume 1017, pages 450–567, New York, NY, USA, 2004. Annals of the New York Academy of Sciences.

- [8] E. Stuhlinger. *Ion propulsion for Space Flight*. McGraw-Hill, New York, 1964.
- [9] R.G. Jahn. *Physics of Electric Propulsion*. McGraw-Hill, 1968.
- [10] K.E. Tsiolkovsky. Exploration of the Universe with Reaction Machines. *The Science Review*, 5, 1903. English translation from the website of *Tsiolkovsky State Museum of the History of Cosmonautics*.
- [11] G. Popov, V. Kim, V. Tikhonov, S. Semenikhin, and M. Tibrina. The Fourth (Final) Quarterly Report on the Milestones (a)(4) and (a)(5)(D) of SoW of Contract No 960938 Between RIAME-MAI and JPL to NASA-JPL (Items 8 and 9 of Delivery Schedule). *RIAME-MAI Technical Report, Moscow, Russia*, 1998.
- [12] J.E. Polk. *Mechanisms of Cathode Erosion in Plasma Thrusters*. Ph.D. Thesis, Princeton University, 1996. PRIN 685 1996.7300.
- [13] J.E. Polk, A.J. Kelly, R.G. Jahn, H.L. Kurtz, M. Auweter-Kurtz, and H.O. Schrade. Mechanisms of hot cathode erosion in plasma thrusters. In *21st International Electric Propulsion Conference*, Orlando, FL, USA, July 1990. AIAA/DGLR/JSASS. AIAA-90-2673.
- [14] E.Y. Choueiri and J.K. Ziemer. Quasi-Steady Magnetoplasmadynamic Thruster Performance Database. *Journal of Propulsion and Power*, 17:967–976, 2001. September-October.
- [15] R.G. Jahn and E.Y. Choueiri. *Academic Press Encyclopedia of Science & Technology*, chapter Electric Propulsion. Number 5. 3 edition, 2002.
- [16] C.E. Moore. *Atomic Energy Levels*. National Standard Reference Data System, 1971.
- [17] V.P. Ageyev, V.G. Ostrovsky, and V.A. Petrosov. High-current stationary plasma accelerator of high power. In *23rd International Electric Propulsion Conference*, pages

1071–1075, Seattle, WA, USA, September 1993. AIAA/AIDAA/DGLR/JSASS. IEPC-93-117.

- [18] K.D. Goodfellow. *A Theoretical and Experimental Investigation of Cathode Processes in Electric Thrusters*. PhD thesis, University of Southern California, 1992.
- [19] J.L. Delcroix, H. Minoo, and A.R. Trindade. Gas fed multichannel hollow cathode arcs. *Review of Scientific Instruments*, 40(12):1555–1562, December 1969.
- [20] J.L. Delcroix and A.R. Trindade. *Advances in Electronics and Electron Physics*, volume 35, chapter Hollow Cathode Arcs, pages 87–190. Acedemia Press, New York, NY, USA, 1974.
- [21] M. Krishnan, R.G. Jahn, W.F. von Jaskowsky, and K.E. Clark. Physical processes in hollow cathodes. *AIAA Journal*, 15(9):1217–1223, September 1977.
- [22] H. Minoo. *Etude des décharges à cathode creuse à flux de gaz en régime d’arc*. Thèse d’état, Orsay, 1969.
- [23] G.V. Babkin, V.G. Mikhalev, E.P. Morozov, and A.V. Potapov. An experimental investigation of a plasma in a multichannel cathode. *Journal of Applied Mechanics and Technical Physics*, 17(6):767–770, 1976.
- [24] G.V. Babkin, V.G. Mikhalev, S.N. Ogorodnikov, R.V. Orlov, and A.V. Potapov. High-current coaxial plasma source. *Soviet Physics - Technical Physics*, 20(9):1175–1178, 1976.
- [25] G.V. Babkin and A.V. Potapov. An experimental investigaion of the effect of oxygen on the erosion of a multichannel tungsten cathode. *Journal Of Applied Mechanics And Technical Physics*, 3, 1979.

- [26] V.M. Ogarkov, S.N. Ogorodnikov, and V.N. Stepanov. The design of the multirod cathode of a high-current plasma source. *Radio Engineering and Electronic Physics-USSR*, 21(12):98–103, 1976.
- [27] V.M. Ogarkov, S.N. Ogorodnikov, and V.N. Stepanov. The influence adsorption effects on the characteristics of a high-current multirod cathode. *Radio Engineering and Electronic Physics-USSR*, 23(8):123–127, 1979.
- [28] S.D. Grishin, A.K. Litvak, S.N. Ogorodnikov, and V.N. Stepanov. Intermediate-power steady-state plasma accelerator. *Soviet Physics - Technical Physics*, 22(2):280–285, February 1977.
- [29] G.A. Dyuzhev, E.A. Startsev, S.M. Shkol'nik, and V.G. Yur'ev. Low-temperature erosionless cathode for high current densities. *Soviet Physics - Technical Physics*, 23(10):1207–1209, October 1978.
- [30] E.P. Vaulin, M.V. Kirushkina, V.B. Tikhonov, and E.A. Filatova. Calculation of hollow cathode erosion. In *2nd Russian-German Conference on EP Engines and Their Technical Applications*, Moscow, Russia, July 1993.
- [31] S.A. Semenikhin and V.B. Tikhonov. The influence of cathode design on the performance and characteristics of MPD thrusters with applied magnetic field. In *3rd Russian-German Conference on Electric Propulsion Engines and their technical applications*, Stuttgart, Germany, June 1994.
- [32] P. Rossetti, F. Paganucci, M. Andrenucci, and M. Signori. Centropazio progress on mpdt hollow cathodes. In *40th AIAA/ASME/SAE/ASEE Joint Propulsion Conference and Exhibit*, Fort Lauderdale, FL, USA, July 2004. AIAA-2004-3429.
- [33] P. Rossetti, M. Signori, M. Andrenucci, and F. Paganucci. Hollow cathodes study at alta-centropazio. In *29th International Electric Propulsion Conference*, Princeton University, NJ, USA, October-November 2005. IEPC-2005-277.

- [34] L.M. Lidsky, S.D. Rothleder, D.J. Rose, S. Yoshikawa, C. Michelson, and R.J. Mackin. Highly ionized hollow cathode discharge. *Journal of Applied Physics*, 33(8):2490–2497, August 1962.
- [35] A. von Engel. *Ionized Gases*. Oxford University Press, London, United Kingdom, second edition, 1965.
- [36] A. Lorente-Arcas. A model for the hollow cathode discharge. *Plasma Physics*, 14:651–659, 1972.
- [37] A. Brunet. Characteristics of interior positive-column of a hollow cathode discharge deduced from probe measurements. *C.R. Acad. Sc. Paris*, 21:813–816, May 1973. (In French).
- [38] A. Brunet. Hollow-cathode arc - experimental study of plasma column inside cathode. *Revue de Physique Appliquee*, 12(8):1105–1110, August 1977. (In French).
- [39] J.L. Delcroix. Establishing general rules for a hollow cathode arc discharge. *Journal of Physics - Paris*, 29(7):605–610, 1968.
- [40] J.L. Delcroix, H. Minoo, and A.R. Trindade. Hollow cathode arc discharge and gas flow. *Revue Roumaine De Physique*, 13(5):401–422, 1968. (In French).
- [41] J.L. Delcroix, H. Minoo, and A.R. Trindade. A novel function an arc-discharge at a hollow cathode. *Comptes Rendus Hebdomadaires Des Seances De L Academie Des Sciences Serie B*, 266(12):762–764, March 1968. (In French).
- [42] J.L. Delcroix, H. Minoo, and A.R. Trindade. Establishing general rules for a hollow cathode arc discharge. *Journal of Physics - Paris*, 29(7):605–610, July 1968. (In French).

- [43] A.R. Trindade and J.L. Delcroix. Theoretical evaluation of metastable production in a gas-fed hollow cathode arc. In *Proceedings of the International Conference on Gas Discharges - 2nd*, pages 105–106, 1972.
- [44] C.M. Ferreira and J.L. Delcroix. Theory of the hollow cathode arc. *Journal of Applied Physics*, 49(4):2380–2395, April 1978.
- [45] S. Dushman. *Scientific Foundations of Vacuum Technique*. John Wiley, New York, NY, USA, 1949.
- [46] S.D. Grishin, V.I. Lisitsin, K.K. Marakhtanov, and M.K. Marakhtanov. Emission current-density in a hollow arc cathode. *High Temperature*, 15(4):767–769, 1977.
- [47] F.G. Baksht and A.B. Rybakov. Fully ionized dense plasma in a hollow-cathode arc. *Soviet Physics - Technical Physics*, 23(2):141–146, February 1978.
- [48] F.G. Baksht and A.B. Rybakov. Arc mode in a flow-through hollow cathode. *Soviet Physics - Technical Physics*, 23(4):412–415, April 1978.
- [49] F.G. Baksht and A.B. Rybakov. Influence of surface emission properties on the characteristics of a hollow arc cathode in a cesium plasma. *Soviet Physics - Technical Physics*, 26(9):1070–1072, September 1981.
- [50] G.A. Dyuzhev, E.A. Startsev, and V.G. Yur'ev. Physics of a hollow arc cathode with a highly ionized dense plasma. *Soviet Physics - Technical Physics*, 23(10):1157–1163, October 1978.
- [51] N.N. Rykalin, A.V. Nikolaev, and A.P. Borzhov. Temperature of heavy-current cylindrical hollow-cathode. *Journal de Physique*, 40(7):229–230, July 1979.
- [52] E.P. Vaulin, M.V. Kiryushkina, V.A. Obukhov, and F. Scortecci. Mathematical modelling of arc hollow cathodes. In *32nd AIAA/ASME/SAE/ASEE Joint Propulsion Conference and Exhibit*, Lake Buena Vista, FL, USA, July 1996. AIAA-1996-3184.

- [53] R.V. Kennedy. Theory of the arc hollow cathode. *Journal of Physics D: Applied Physics*, 34:787–793, 2001.
- [54] M. Krishnan. Physical processes in hollow cathodes. In *12th International Electric Propulsion Conference*, Key Biscayne, FL, USA, November 1976. AIAA. AIAA-76-984.
- [55] F.R. Chamberlain. Electropositive surface layer mpd thruster cathodes. Master’s thesis, Princeton University, 1989.
- [56] F.R. Chamberlain, A.J. Kelly, and R.G. Jahn. Electropositive surface layer MPD thruster cathodes. In *25th AIAA/ASME/SAE/ASEE Joint Propulsion Conference*, Monterey, CA, USA, July 1989. AIAA-89-2706.
- [57] J.S. Fillmore. An experimental study of lithium dispenser cathodes in the MPD thruster. Master’s thesis, Princeton University, 1997.
- [58] P. Rossetti, F. Paganucci, and M. Andrenucci. A hollow cathode model for application to the electric propulsion. In *38th AIAA/ASME/SAE/ASEE Joint Propulsion Conference and Exhibit*, Indianapolis, IN, USA, July 2002. AIAA-2002-4239.
- [59] M. Mitchner and C.H Kruger. *Partially Ionized Gases*. John Wiley & Sons, Inc., New York, NY, USA, 1973.
- [60] M.A. Mantenieks and R.M. Myers. Preliminary test results of hollow cathode MPD thruster. In *22st International Electric Propulsion Conference*, Viareggio, Italy, October 1991. AIDAA/AIAA/DGLR/JSASS. IEPC-91-076.
- [61] D.B. Fradkin, A.W. Blackstock, D.J. Roehling, T.F. Stratton, M. Williams, and K.W. Liewer. Experiments using a 25 kW hollow cathode lithium vapor MPD arcjet. *AIAA Journal*, 8(5):886–894, May 1970.

- [62] L.I. Ageyev, S.D. Grishin, V.G. Mikhalev, S.N. Ogorodnikov, and V.N. Stepanov. Characteristics of high-current plasma sources with a hollow cathode. *Radio Engineering and Electronic Physics-USSR*, 20(9):67–71, 1975.
- [63] D.E. Siegfried and P.J. Wilbur. A model for mercury orificed hollow cathodes: Theory and experiment. *AIAA Journal*, 22(10):1405–1411, October 1984.
- [64] D.E. Siegfried. Investigation of mercury hollow-cathode phenomena. *Astronautics and Aeronautics*, 16(12):B22–B22, 1978.
- [65] A. Salhi and P.J. Turchi. A first-principles model for orificed hollow cathode operation. In *28th AIAA/ASME/SAE/ASEE Joint Propulsion Conference*, Nashville, TN, USA, July 1992. AIAA-92-3742.
- [66] A. Salhi and P.J. Turchi. Theoretical modeling of orificed, hollow cathodes discharges. In *23rd International Electric Propulsion Conference*, Seattle, WA, USA, September 1993. AIAA/AIDAA/DGLR/JSASS. IEPC-93-024.
- [67] A. Salhi and P.J. Turchi. Scaling relations for design and operation of orificed-hollow cathodes. In *30th AIAA/ASME/SAE/ASEE Joint Propulsion Conference*, Indianapolis, IN, USA, June 1994. AIAA-94-3133.
- [68] I. Katz, J. Polk, I.G. Mikellides, D.M. Goebel, and S.E. Hornbeck. Combined plasma and thermal hollow cathode insert model. In *29th International Electric Propulsion Conference*, Princeton University, NJ, USA, October-November 2005. IEPC-2005-228.
- [69] I.G. Mikellides, I. Katz, D. Goebel, and J.E. Polk. Theoretical model of a hollow cathode insert plasma. In *40th AIAA/ASME/SAE/ASEE Joint Propulsion Conference and Exhibit*, Fort Lauderdale, FL, USA, July 2004. AIAA-2004-3817.

- [70] I.G. Mikellides, I. Katz, D. Goebel, and J.E. Polk. Theoretical modeling of a hollow cathode plasma for the assessment of insert and keeper lifetimes. In *41st AIAA/ASME/SAE/ASEE Joint Propulsion Conference and Exhibit*, Tucson, AZ, USA, July 2005. AIAA-2005-4234.
- [71] J. Lafferty. *Vacuum Science and Technology*. John Wiley & sons, New York, NY, USA, 1998.
- [72] C. Yaws. *Handbook of Vapor Pressure*, volume 4. Gulf Publishing Co., Houston, TX, USA, 1994.
- [73] *National Institute of Standards and Technology Standard Reference Database 69*. United State Government, release: nist chemistry webbook edition, March 2003.
- [74] Y.S. Touloukian and D.P. DeWitt, editors. *Thermophysical Properties of Matter, Thermal Radiative Properties: Metallic Elements and Alloys*, volume 7. Plenum, New York, 1970.
- [75] D.R. Lide, editor. *CRC Handbood of Chemistry and Physics*. CRC Press, Boca Raton, FL, USA, 77 edition, 1997.
- [76] L. Barleon and C. Wong. The transpiration cooled first wall blanket concept. *Fusion Engineering and Design*, 61(62):477–482, 2002.
- [77] V.A. Evtikhin, A.V. Vertkov, I.E. Lyublinski, B.I. Khripunov, V.B. Petrov, and S.V. Mirnov. Research of lithium capillary-pore systems for fusion reactor plasma facing components. *Journal of Nuclear Materials*, 307(311):1664–1669, 2002.
- [78] B.I. Khripunov, V.B. Petrov, V.V. Shapkin, N.V. Antonov, A.S. Pleshakov, A.S. Rupyshev, D.Yu. Prokhorov, V.A. Evtikhin, I.E. Lyublinsky, and V.V. Vertkov. Lithium surface operating under steady-state power load. *Fusion Engineering and Design*, 65:449–454, 2003.

- [79] R. Majeski et al. The lithium tokamak - results from CDX-U and the design of LTX. In *Innovative Confinement Concepts Workshop*, Madison, WI, USA, May 2004.
- [80] A.D. Kodys, G. Emsellem, L.D. Cassady, J.E. Polk, and E.Y. Choueiri. Lithium mass flow control for high power Lorentz force accelerators. In *Space Technology and Applications International Forum*, Albuquerque, NM, USA, February 2001. STAIF Paper 195.
- [81] W.G. Vincenti and Jr. C.H. Kruger. *Introduction to Physical Gas Dynamics*. Krieger Publishing Company, Malabar, FL, USA, 1965.
- [82] Y. Vargaftik. *Handbook of Thermodynamic and Transport Properties of Alkali Metals*. Inter. Union of Pure and Applied Chemistry Chemical Data Series No. 30. Blackwell Scientific Publishing, Oxford, UK, 1985.
- [83] A. Bondi. van der Waals volumes and radii. *The Journal of Physical Chemistry*, 68(3):441–451, March 1964.
- [84] R. Larrabee. Spectral emissivity of tungsten. *Journal of the Optical Society of America*, 49(6):619–625, June 1959.
- [85] T.E. Markusic. *Current Sheet Canting in Pulsed Electromagnetic Accelerators*. Ph.D. thesis, Princeton University, 2002.
- [86] H.R. Griem. *Plasma Spectroscopy*. McGraw-Hill Book Company, 1964.
- [87] I.H. Hutchinson. *Principles of Plasma Diagnostics*. Cambridge University Press, New York, NY, USA, 1987.
- [88] W.L. Wiese, M.W. Smith, and B.M. Glennon. *Atomic Transition Probabilities*. Number 4 in National Standard Reference Data Series. National Bureau of Standards, Washington, DC, May 1966.

- [89] National Institute of Standards and Technology. NIST atomic spectra database. http://physics.nist.gov/cgi-bin/AtData/main_asd, 2005.
- [90] L.D. Cassady and E.Y. Choueiri. Experimental and theoretical studies of the lithium-fed multichannel and single-channel hollow cathode. In *29th International Electric Propulsion Conference*, Princeton University, NJ, USA, October-November 2005. IEPC-2005-094.
- [91] D.E. Siegfried. *A Phenomenological Model for Orificed Hollow Cathodes*. PhD thesis, Colorado State University, 1983.
- [92] R.H. Huddleston and S.L. Leonard. *Plasma Diagnostic Techniques*. Academic Press Inc., New York, NY, USA, 1965.
- [93] J.D. Cobine. *Gaseous Conductors*. Dover, New York, 1958.
- [94] D. Santeler. Exit loss in viscous tube flow. *Journal of Vacuum Science and Technology A*, 4(3):348–352, 1986.
- [95] D. Santeler. Gas-flow experiments in the transition region. *Journal of Vacuum Science and Technology A*, 12(4):1744–1749, July/August 1994.
- [96] S. Chapman and T.G. Cowling. *The Mathematical Theory of Non-uniform Gases*. University Press, Cambridge, UK, 3rd edition, 1970.
- [97] J.W. Turkstra. *Hot Recoils from Cold Atoms*. Ph.d. thesis, RIJKSUNIVERSITEIT GRONINGEN, October 2001.
- [98] Nuclear Data Section/Atomic International Atomic Energy Agency and Molecular Data Unit. ALLADIN database. Web Site: <http://gap3.lpgp.u-psud.fr/GENIE/>, 2004.
- [99] T.J. Jones. *Thermionic Emission*. Methuen & Co, Ltd., London, England, 1936.

- [100] A.L. Reimann. *Thermionic Emission*. John Wiley & Sons, Inc., New York, NY, USA, 1934.
- [101] X. Zhou and J. Heberlein. Analysis of the arc-cathode interaction of free-burning arcs. *Plasma Sources Science and Technology*, 3(4):564–574, November 1994.
- [102] B. Rethfeld, J. Wendelstorf, T. Klein, and G. Simon. A self-consistent model for the cathode fall region of an electric arc. *Journal of Physics D: Applied Physics*, 29(1):121–128, January 1996.
- [103] P.D. Prewett and J.E. Allen. The double sheath associated with a hot cathode. *Proceedings of the Royal Society of London Series A, Mathematical and Physical Sciences*, 348(1655):435–446, 1976.
- [104] K.D. Goodfellow and J.E. Polk. High current cathode thermal behavior, part 1: Theory. In *23rd International Electric Propulsion Conference*, Seattle, WA, USA, September 1993. AIAA/AIDAA/DGLR/JSASS. IEPC-93-030.
- [105] K.U. Riemann. The Bohm criterion and sheath formation. *Journal of Physics D: Applied Physics*, 24(4):493–517, April 1991.
- [106] K.U. Riemann. Kinetic theory of the plasma sheath transition in a weakly ionized plasma. *Physics of Fluids*, 24(12):2163–2172, December 1981.
- [107] G.S. Kino and E.K. Shaw. Two-dimensional low-pressure discharge theory. *The Physics of Fluids*, 9(3):587–593, March 1966.
- [108] K. Sankaran. *Simulation of Plasma Flows in Self-field Lorentz Force Accelerators*. PhD thesis, Princeton University, 2005.
- [109] E. Oberg, F. Jones, H. Horton, and H. Ryffel. *Machinery's Handbook*. Industrial Press, Inc, New York, NY, USA, 27 edition, 2004.

- [110] Nuclear space initiative: A planetary society white paper. The planetary report, The Planetary Society, 2002.
- [111] J.E. Polk, R.Y. Kakuda, J. R. Anderson, J. R. Brophy, V. K. Rawlin, M. J. Patterson, J. Sovey, and J. Hamley. Validation of the NSTAR Ion Propulsion System on the Deep Space 1 Mission. *AIAA-99-2274*, 1999.
- [112] E.P. Coomes, D.Q. King, and M.J. Patterson. PEGASUS: A Multi-Megawatt Nuclear Electric Propulsion System. *Third Annual Symposium on Space Nuclear Power*, 1986.
- [113] D.Q. King and J.C. Sercel. A Review of the Multi-Megawatt MPD Thruster and Current Mission Applications. *AIAA-86-1437*, 1986.
- [114] J.H. Gilland and R.M. Myers. Multimegawatt Electric Propulsion System Design Considerations. *AIAA-90-2552*, 1990.
- [115] J.S. Clark et al. Nuclear electric propulsion: A “better, safer, cheaper” transportation system for human exploration of mars. In *Space Technology and Application International Forum*, Albuquerque, NM, USA, 1994. January 9-13.
- [116] D.G. Pelaccio, G.A. Rauwolf, G. Maggio, S. Patel, and K. Sorenson. An Examination of Emerging In-Space Propulsion Concepts for One-Year Crewed Mars Missions. *Annual Symposium on Space Nuclear Power*, 2002.
- [117] R.H. Frisbee, N.J. Hoffman, and K.H. Murray. Sp-100 dynamic power and lithium propellant MPD nuclear electric propulsion technology requirements. In *Space Technology and Application International Forum*, Albuquerque, NM, USA, 1994. January 9-13.

- [118] J.E. Polk et al. Technology requirements for high-power lithium lorentz force accelerators. In *Space Technology and Application International Forum*, Albuquerque, NM, USA, 2001.
- [119] M. Noca, J.E. Polk, and R. Lenard. An Evolutionary Strategy for the Use of Nuclear Electric Propulsion. *Annual Symposium on Space Nuclear Power*, 2000.
- [120] G. Woodcock et al. Benefits of nuclear electric propulsion for outer planet exploration. *AIAA-02-3548*, 2002.
- [121] E. Braden, I. Johnson, and T. Crain. RAPTOR: (RAPid Trajectory Optimization Resource). *Personal communication*, 2002.
- [122] I. Johnson. The Davidon-Fletcher-Powell Penalty Function Method: A Generalized Iterative Technique for Solving Parameter Optimization Problems. *NASA-TN-D-8251*, 1976.
- [123] M. Martnez-Sanchez and J.E. Pollard. Spacecraft electric propulsion- an overview. *Journal of Propulsion and Power*, 14:688–699, 1998. September-October.
- [124] K. Toki, Y. Shimuzu, and K. Kuriki. Electric Propulsion Experiment (EPEX) of a Repetitively Pulsed MPD Thruster System Onboard Space Flyer Unit (SFU). In *International Electric Propulsion Conference*, 1997. IEPC 97-120.
- [125] K.E. Clark and R.G. Jahn. Quasi-Steady Plasma Acceleration. *AIAA Journal*, 8:216–220, 1970.
- [126] Akihiro Sasoh and Y. Arakawa. Electromagnetic Effects in an Applied-Field Magnetoplasma dynamic Thruster. *Journal of Propulsion and Power*, 8:98–102, 1992. January-February.

- [127] M.R. LaPointe and P.G. Mikellides. Design and operation of mw-class mpd thrusters at the nasa glenn research center. In *Joint Propulsion Conference*, Indianapolis, IN, USA, July, 2002. AIAA 2002-4113.
- [128] R. Myers, M. Mantentiek, and M. LaPointe. MPD Thruster Technology. *Conference on Advanced SEI Technologies*, AIAA-91-3568, September, 1991.
- [129] T. Wegmann et al. Experimental comparison of steady-state nozzle type and cylindrical MPD thrusters at high current levels. In *International Electric Propulsion Conference*, Seattle, WA, USA, 1993. IEPC 93-122.
- [130] H. Tahara, H. Yasui, Y. Kagaya, and T. Yoshikawa. Development of a Quasi-Steady MPD Arcjet Thruster for Near-Earth Missions. *AIAA-87-1001*, 1987.
- [131] James S. Sovey and Maris A. Manteniaks. Performance and Lifetime Assessment of Magnetoplasdynamic Arc Thruster Technology. *Journal of Propulsion and Power*, 7:71–83, 1991. January-February.
- [132] H.L. Kurtz, M. Auweter-Kurtz, W. Merke, and H.O. Schrade. Experimental MPD Thruster Investigations. *Journal of the British Interplanetary Society*, 41:223–232, 1998.
- [133] V.P. Ageyev and V.G. Ostrovsky. High-current stationary plasma accelerator of high power. In *Proceedings of the 23rd International Electric Propulsion Conference*, Seattle, WA, USA, 1993. IEPC-93-117.
- [134] D.H. Manzella, R.S. Jankovsky, and R.R. Hofer. Laboratory Model 50 kW Hall Thruster. *AIAA-2002-3676*, 2002.
- [135] S. Tverdokhlebov, A. Semenkin, and J. Polk. Bismuth Propellant Option for Very High Power TAL Thruster. *AIAA-2002-0348*, 2002.

- [136] D.T. Jacobson and R.S. Jankovsky. Performance Evaluation of a 50 kW Hall Thruster. *NASA-TM-1999-209447*, 1999.
- [137] E.Y. Choueiri. Fundamental difference between the two Hall thruster variants. *Physics of Plasmas*, 8:5025–5033, 2001.
- [138] M. Auweter-Kurtz, T. Golz, H. Habiger, F. Hammer, H. Kurtz, M. Riehle, and C. Sleziona. High-Power Hydrogen Arcjet Thrusters. *Journal of Propulsion and Power*, 14:764–773, 1998.
- [139] Matthew T. Domonkos, Michael J. Patterson, and Robert S. Jankovsky. Ion engine and hall thruster development at the NASA Glenn Research Center. In *International Mechanical Engineering Congress*, New Orleans, LA, USA, November 17-22 2002. IMECE 2002-34444.
- [140] Steven Oleson et al. Mission Advantages of NEXT: NASA’s Evolutionary Xenon Thruster. In *AIAA Joint Propulsion Conference*, Indianapolis, IN, July 7-10 2002. AIAA 2002-3969.
- [141] S. Nakanishi and E.V. Pawlik. Experimental Investigation of a 1.5-m-diam Kaufman Thruster. *Journal of Spacecraft and Rockets*, 5:801–807, 1968. July.
- [142] C.L. Dailey and R.H. Lovberg. Pulsed Inductive Thrusters Performance Database for Megawatt Class Engine Applications. *AIAA-93-0103*, 1993.
- [143] F. R. Chang Diaz, J. P. Squire, R. D. Bengston, B. N. Breizman, F. W. Baity, and M. D. Carter. The Physics and Engineering of the VASIMR Engine. *AIAA-00-3756*, 2000.
- [144] K. Cashdollar. Three-wavelength pyrometer for measuring flame temperature. *Applied Optics*, 18:2595–2597, 1979.

- [145] J.L. Gardner and T.P. Jones. Multi-wavelength radiation pyrometry where reflectance is measured to estimate emissivity. *Phys.E: Sci. Instrum.*, 13:306–319, 1980.
- [146] J.L. Gardner. Computer modelling of a multiwavelength pyrometer for measuring true surface temperature. *High Temperatures - High Pressures*, 12:699–705, 1980.
- [147] Jean-Pol Hiernaut, Rutger Beukers, Michael Hoch, Tsuneo Matsui, and Roland W. Ohse. Submillisecond six-wavelength pyrometer for high-temperature measurements in the range of 2000 to 5000 k. *High Temperatures - High Pressures*, 18:627–633, 1986.
- [148] Michael Hoch. The integral six-color pyrometer: A new general method of temperature determination. *High Temperatures - High Pressures*, 24:607–623, 1992.
- [149] Michael Hoch. Multiwavelength pyrometry: Radiance temperature versus wavelength curve should be used for temperature measurement. *Review of Scientific Instruments*, 63:4205–4207, 1992.
- [150] G. R. Gathers. Monte carlo studies of multiwavelength pyrometry using linearized equations. *International Journal of Thermophysics*, 13:361–382, 1992.
- [151] G. R. Gathers. Analysis of multiwavelength pyrometry using nonlinear chi-square fits and monte carlo methods. *International Journal of Thermophysics*, 13:539–554, 1992.
- [152] C. Ronchi, J.P. Hiernaut, and G.J. Hyland. Emissivity x points in solid and liquid refractory transition metals. *Metrologia*, 29:261–271, 1992.
- [153] T. Fujimoto and R.W.P. McWhirter. Validity criteria for local thermodynamic equilibrium in plasma spectroscopy. *Physical Review A*, 42:6588–6601, 1990.

- [154] W.L. Wiese. Spectroscopic diagnostics of low temperature plasmas, techniques and required data. *Spectrochimica Acta Part B: Atomic Spectroscopy*, 46:831–841, 1991.
- [155] K.D. Goodfellow and J.E. Polk. Experimental verification of a high current cathode thermal mode. In *31st AIAA/ASME/SAE/ASEE Joint Propulsion Conference and Exhibit*, San Diego, CA, USA, July 10-12 1995.
- [156] V.K. Medvedev and T.P. Smereka. Lithium adsorption onto the fundamental faces of a tungsten single crystal. *Soviet Physics - Solid State*, 16(6):1046–1049, December 1974.